BOSTON UNIVERSITY

GRADUATE SCHOOL OF ARTS AND SCIENCES

Dissertation

WWW PRODUCTION AT THE LHC (VERSION 1.7)

by

BRIAN ALEXANDER LONG

B.S., The University of North Carolina, 2010
M.A., Boston University, 2015

Submitted in partial fulfillment of the

requirements for the degree of

Doctor of Philosophy

2016

Approved by

First Reader

John M. Butler, PhD
Professor of Physics

Second Reader

Kevin M. Black, PhD
Assistant Professor of Physics

Acknowledgments

John and Kevin

Committee

BU ATLAS and collaborators

Friends in physics department

Kate and Caitlin ("the Ckaitelyns"), this wouldn't have even gotten off the ground if you both didn't have the guts to take this journey up to Boston with me. And you're still stuck up here! Sorry about that. You can always go back home, but I'd miss you if you did. Clare, I owe you so much for taking me under your wing. It's because of you that I had such a great experience in Geneva. Here's to many more in Boston! Grant, thanks for putting up with me even though I made you feel old. I miss our debates over red wine and reindeer meat. Bonnie, Grant, Michal, and Michelle, here's to Michal not driving off that cliff in Rapallo while dancing to Daft Punk on the radio. You made my time in Geneva too much fun. Luke, John, all these years since I first set up my drums on Painted Tree Rd and we still don't have a band. It probably has something to do with this thing... Sorry about that, but you managed to keep the metal alive without me. Anyway, it's meant so much to me that I can fly down to NC and see you... Ryan, thanks for keeping the spirit of North Carolina alive in Massachusetts. ... Jeff, looks like we made it. Look how far we've come my baby. We mighta took the long way. We knew we'd get there someday. They said, "I bet they'll never make it". But just look at us holding on. We're still together still going strong. Also, I still hate Garrison Keillor. Chynna, Katie, April,... Mom, Dad, Paul, Susan, how could I ever truly thank you? I know this at least, I wouldn't have made it anywhere without your love and I would never have made it this far without your belief in me. Mom, Dad, I love you all.

WWW PRODUCTION AT THE LHC (VERSION 1.7)

BRIAN ALEXANDER LONG

Boston University, Graduate School of Arts and Sciences, 2016

Major Professor: John M. Butler, Professor of Physics

ABSTRACT

In 2012 a resonance with a mass of 125 GeV resembling the elusive Higgs boson was discovered simultaneously by the ATLAS and CMS experiments using data collected from the Large Hadron Collider (LHC) at CERN. Its observation finally confirms the mechanism for Spontaneous Electroweak Symmetry Breaking (EWSB) necessary for describing the mass structure of the electroweak (EW) gauge bosons. In 2013, Peter Higgs and Francois Englert were awarded the Nobel Prize in physics for their work in developing this theory of EWSB now referred to as the Higgs mechanism. The explanation for EWSB is often referred to as the last piece of the puzzle required to build a consistent theory of particle physics known as the Standard Model. But does that mean that there are no new surprises to be found? Many EW processes have yet to be measured and are just starting to become accessible with the data collected at the LHC. Indeed, this unexplored region of EW physics may provide clues to as yet unknown new physics processes at higher energy scales. Using the 2012 LHC data recorded by the ATLAS experiment, we seek to make the first observation of one such EW process, the massive tri-boson final state: WWW. It represents one of the first searches to probe the Standard Model WWWW coupling directly at a collider. This search looks specifically at the channel where each W boson decays to a charged lepton and a neutrino, offering the best sensitivity for making such a measurement. In addition to testing the Standard Model directly, we also use an effective field theory approach to test for the existence of anomalous quartic gauge couplings which could offer evidence for new physics at higher energies than those produced by the LHC.

Contents

1 Introduction **1**

2 Theory **5**

2.1 The Standard Model 5

2.1.1 Quantum Chromodynamics 8

2.1.2 Parton Distribution Functions 11

2.1.3 The Electroweak Theory 15

2.2 WWW Production 23

2.3 Effective Field Theory 27

2.4 Status of QGC Measurements and aQGC Limits 31

3 Collider Physics and The Large Hadron Collider **32**

3.1 Collider Physics 33

3.2 The LHC Accelerator Complex 37

3.3 Data Collection 38

4 The ATLAS Detector **42**

4.1 Inner Detector 46

4.2 Calorimeters 50

4.3 Muon Spectrometer 56

4.4 Trigger 65

5 Search for $WWW \to \ell\nu\ \ell\nu\ \ell\nu$ **68**

5.1 Data and Simulation Samples 69

5.1.1 Data . . . 69
5.1.2 Simulation samples . . . 70
5.2 Physics Object Definition and Selection . . . 79
5.3 Event Selection . . . 82
5.3.1 Pre-selection . . . 83
5.3.2 Signal Region Selection . . . 83
5.3.3 Fiducial Region Selection . . . 86
5.4 Background Estimates . . . 88
5.4.1 Monte Carlo Backgrounds . . . 88
5.4.2 Electron Charge Mis-identification . . . 99
5.4.3 Fake lepton background . . . 109
5.5 Event Yields . . . 129
5.5.1 Event Pre-selection . . . 129
5.5.2 Optimization . . . 131
5.5.3 Signal Region Yields . . . 134
5.5.4 Fiducial Cross-sections and Correction Factors . . . 154
5.6 Corrections and Systematic Uncertainties . . . 155
5.6.1 Theoretical Uncertainties . . . 156
5.6.2 Methodological Uncertainties . . . 158
5.6.3 Experimental Corrections and Uncertainties . . . 159
5.6.4 Luminosity Uncertainty . . . 163
5.7 Cross-section Measurement . . . 163
5.7.1 Profile Likelihood Ratio . . . 164
5.7.2 Testing for Discovery Significance . . . 165
5.7.3 Measurement and Uncertainty using Profile Likelihood Interval . . . 166
5.8 Anomalous Quartic Gauge Couplings . . . 168
5.8.1 aQGC Signal Yields . . . 168
5.8.2 Confidence limits . . . 171

6 Combination of $WWW \rightarrow \ell\nu\ \ell\nu\ \ell\nu$ and $WWW \rightarrow \ell\nu\ \ell\nu\ jj$ 175

6.1 Search for $WWW \rightarrow \ell\nu\ \ell\nu\ jj$ . . . 175

6.2 Combined Cross-section Measurement . . . 179

6.3 Combined aQGC Limits . . . 181

7 Conclusions 186

7.1 Summary . . . 186

7.2 Outlook . . . 187

List of Journal Abbreviations 188

Bibliography 189

Curriculum Vitae 201

List of Tables

2.1 Summary of the electric charge, Q (in unites of e), and masses of the SM fermions. Masses are taken from the Particle Data Group [1] and are shown to the best precision available within their uncertainties. Particles are also organized by their generation. The limits on the electron neutrino and muon neutrino masses are set at a 90% confidence level while the tau neutrino limits are set at a 95% confidence level. 7

2.2 The charges of the SM fermions in units of the electric charge, e. The charges are the same for each generation, so only the first generation of quarks and leptons are shown. 17

2.3 Measured branching fractions of the W and Z bosons as reported by the Particle Data Group [1]. Only the inclusive branching fraction of the W and Z decay to all quark generations is reported. The invisible branching fraction of the Z boson comes from the decay of the Z to neutrinos. The branching fractions sum to 100% separately for the W and Z bosons within their uncertainties. 23

5.1 Inclusive and common fiducial cross-sections at NLO for VBFNLO and MadGraph samples. The sum of the inclusive cross-sections are different because of the different branching fractions in the two cases. The sum of the fiducial cross-sections, however, are expected to be similar because they are computed for the same phase space, as described in Sec. 5.3.3. Only statistical uncertainties are shown. 72

5.2 Summary of PDF uncertainties estimated on NLO MadGraph cross-sections in both the fiducial and total phase space. 72

5.3 The relative variation of the NLO cross sections corresponding to different choices of factorization and renormalization scales for the $W^+W^+W^-$and $W^-W^+W^-$processes. 74

5.4 Optimized signal selection split by number of Same-Flavor Opposite-Sign (SFOS) lepton pairs. 84

5.5 Fiducial regions based on optimized selection. 87

5.6 All of the inputs used to constrain the system of five equations from Eq. (5.4) and Eq. (5.6). The values are derived in the signal region and three sideband regions described in the text. $N_{A,B}^{\mathrm{Data}}$ are determined directly from the data; $N_{A,B}^{\mathrm{Electroweak}}$ and $N_{A,B}^{WZ}$ are determined in MC. The value for $N_{\mathrm{With}\ Z,\mathrm{Isolated}}^{WZ}$ is not used as an input and is instead solved for as the the main parameter of interest. Still, the value is determined in MC to be 498 ± 1. Only statistical uncertainties are shown. 92

5.7 Outputs from the system of five equations from Eq. (5.4) and Eq. (5.6) after including the numbers from Table 5.6 as input. The value for $N_{\mathrm{With}\ Z,\ \mathrm{Isolated}}^{WZ}$ is the value of primary interest. Only statistical uncertainties are shown. . . 92

5.8 Number of data and predicted events in the ZZ control region. The error quoted on the MC samples, except for ZZ, represents only the statistical error. The systematic error due to the k-factor on the ZZ sample is also shown. 95

5.9 Expected and observed event yields for the Zγ control region. Only statistical uncertainties are shown. 99

5.10 Contribution of individual terms to the overall fake lepton prediction in the fake three lepton pre-selection region. The term called “Other” includes events with more than three leptons. 120

5.11 Measured real efficiencies for electrons including statistical and systematic absolute uncertainties. Systematic is calculated by taking the difference between the efficiencies measured in data and MC. The efficiency measured in data is used as the nominal central value. 125

5.12 Measured real efficiencies for muons including statistical and systematic absolute uncertainties. Systematic is calculated by taking the difference between the efficiencies measured in data and MC. The efficiency measured in data is used as the nominal central value. 126

5.13 Calculation of fake rate for electrons when $N_{b-\mathrm{Jet}} > 0$. 128

5.14 Calculation of fake rate for muons when $N_{b-\mathrm{Jet}} > 0$. 128

5.15 Expected and observed yields for the fake lepton control region. Only statistical uncertainties are shown. 129

5.16 A summary of the expected yields compared to data for all three signal regions. Statistical uncertainties are shown as a symmetric uncertainty on the central value. Systematic uncertainties are shown as an asymmetric uncertainty and are shown after taking the quadrature sum of all individual uncertainties. In the actual analysis, each systematic uncertainty is treated as an individual nuisance parameter and are NOT added in quadrature. The presentation here serves only as a demonstration of the overall size of the systematic uncertainties for each source in the individual signal regions. . . 135

5.17 Categorized systematic uncertainties for signal and background predictions in all three signal regions. All uncertainties are shown as a percentage of the nominal prediction. 135

5.18 Cut-flows showing the event yields and efficiencies for each cut in the 0 SFOS signal region starting from event pre-selection separately for the total signal and total background predictions, along with the observed data. Event yields for MC backgrounds and signal include all weights and are normalized to an integrated luminosity of 20.3 fb^{-1}. The fake lepton background only includes the matrix method weights. The data is unweighted. Efficiencies show the ratio of the yield with respect to the previous cut. The efficiency is first calculated at the first cut after event pre-selection. 146

5.19 Cut-flows showing the event yields and efficiencies for each cut in the 0 SFOS signal region starting from event pre-selection and binned by background category. Event yields for MC backgrounds and signal include all weights and are normalized to an integrated luminosity of 20.3 fb^{-1}. The fake lepton background only includes the matrix method weights. The data is unweighted. Efficiencies show the ratio of the yield with respect to the previous cut. The efficiency is first calculated at the first cut after event pre-selection. 147

5.20 Cut-flows showing the event yields and efficiencies for each cut in the 1 SFOS signal region starting from event pre-selection separately for the total signal and total background predictions, along with the observed by data. Event yields for MC backgrounds and signal include all weights and are normalized to an integrated luminosity of 20.3 fb^{-1}. The fake lepton background only includes the matrix method weights. The data is unweighted. Efficiencies show the ratio of the yield with respect to the previous cut. The efficiency is first calculated at the first cut after event pre-selection. 149

5.21 Cut-flows showing the event yields and efficiencies for each cut in the 1 SFOS signal region starting from event pre-selection and binned by background category. Event yields for MC backgrounds and signal include all weights and are normalized to an integrated luminosity of 20.3 fb^{-1}. The fake lepton background only includes the matrix method weights. The data is unweighted. Efficiencies show the ratio of the yield with respect to the previous cut. The efficiency is first calculated at the first cut after event pre-selection. 150

5.22 Cut-flows showing the event yields and efficiencies for each cut in the 2 SFOS signal region starting from event pre-selection separately for the total signal and total background predictions, along with the observed data. Event yields for MC backgrounds and signal include all weights and are normalized to an integrated luminosity of 20.3 fb^{-1}. The fake lepton background only includes the matrix method weights. The data is unweighted. Efficiencies show the ratio of the yield with respect to the previous cut. The efficiency is first calculated at the first cut after event pre-selection. 152

5.23 Cut-flows showing the event yields and efficiencies for each cut in the 2 SFOS signal region starting from event pre-selection and binned by background category. Event yields for MC backgrounds and signal include all weights and are normalized to an integrated luminosity of 20.3 fb^{-1}. The fake lepton background only includes the matrix method weights. The data is unweighted. Efficiencies show the ratio of the yield with respect to the previous cut. The efficiency is first calculated at the first cut after event pre-selection. 152

5.24 Correction factors, C_i, and fiducial cross-sections derived separately for each signal region. Correction factors are determined using VBFNLO ; fiducial cross-sections are determined using MadGraph. 155

5.25 Size of theoretical uncertainties in percent for the 0 SFOS signal region. The background uncertainties are shown for the individual background components as well as the total. The signal uncertainty is shown separately. Those marked — are either not applicable or below 0.02 % and thus considered to be negligible . . . 156
5.26 Size of theoretical uncertainties in percent for the 1 SFOS signal region. The background uncertainties are shown for the individual background components as well as the total. The signal uncertainty is shown separately. Those marked — are either not applicable or below 0.02 % and thus considered to be negligible . . . 156
5.27 Size of theoretical uncertainties in percent for the 2 SFOS signal region. The background uncertainties are shown for the individual background components as well as the total. The signal uncertainty is shown separately. Those marked — are either not applicable or below 0.02 % and thus considered to be negligible . . . 157
5.28 Size of the methodological uncertainties in percent for the 0 SFOS signal region. The background uncertainties are shown for the individual background components as well as the total. The signal uncertainty is shown separately. Those marked — are either not applicable or below 0.02 % and thus considered to be negligible . . . 158
5.29 Size of the methodological uncertainties in percent for the 1 SFOS signal region. The background uncertainties are shown for the individual background components as well as the total. The signal uncertainty is shown separately. Those marked — are either not applicable or below 0.02 % and thus considered to be negligible . . . 158

5.30 Size of the methodological uncertainties in percent for the 2 SFOS signal region. The background uncertainties are shown for the individual background components as well as the total. The signal uncertainty is shown separately. Those marked — are either not applicable or below 0.02 % and thus considered to be negligible 158

5.31 Size of the experimental uncertainties in percent for the 0 SFOS signal region. The background uncertainties are shown for the individual background components as well as the total. The signal uncertainty is shown separately. Those marked — are either not applicable or below 0.02 % and thus considered to be negligible 159

5.32 Size of the experimental uncertainties in percent for the 1 SFOS signal region. The background uncertainties are shown for the individual background components as well as the total. The signal uncertainty is shown separately. Those marked — are either not applicable or below 0.02 % and thus considered to be negligible 160

5.33 Size of the experimental uncertainties in percent for the 2 SFOS signal region. The background uncertainties are shown for the individual background components as well as the total. The signal uncertainty is shown separately. Those marked — are either not applicable or below 0.02 % and thus considered to be negligible 161

5.34 Expected and observed one-dimensional limits on the $f_{s,0}$ vs $f_{s,1}$. The non-unitarized case is when $\Lambda = \infty$. 174

6.1 Selection criteria for the semi-leptonic channel. 176

6.2 Description of fiducial selection for each of the semi-leptonic channels. . . . 176

6.3 A summary of the expected yields compared to data for all three signal regions in the semi-leptonic analysis channel. Statistical uncertainties are shown as a symmetric uncertainty on the central value. Systematic uncertainties are shown as an asymmetric uncertainty and are shown after taking the quadrature sum of all individual uncertainties. In the actual analysis, each systematic uncertainty is treated as an individual nuisance parameter and are NOT added in quadrature. The presentation here serves only as a demonstration of the overall size of the systematic uncertainties for each source in the individual signal regions. 178

6.4 Categorized systematic uncertainties for signal and background predictions in all three signal regions of the semi-leptonic analysis channel. All uncertainties are shown as a percentage of the nominal prediction. 178

6.5 Correction factors, C_i, and fiducial cross-sections derived separately for each signal region in the semi-leptonic analysis channel. Correction factors and fiducial cross-sections are determined using MadGraph. 179

6.6 Acceptance values, A_i, derived separately for each signal region. The sum of all of the acceptance in each bin is used to compute the overall acceptance, A. Only statistical uncertainties are shown. 180

6.7 Expected and observed one-dimensional limits on $f_{s,0}$ vs $f_{s,1}$. 181

6.8 Expected and observed one-dimensional limits on α_4 vs α_5. 181

List of Figures

2.1 Feynman diagrams of QCD describing the interactions between gluon and quark fields. The gluons and quarks can in general have different colors. . . 9

2.2 Plot of $xf_i(x, Q^2)$ vs x for the MSTW 2008 NLO PDF sets [2] with 68% CL eigenvector uncertainties for two different scales, $Q^2 = \mu_R^2 = \mu_F^2$. The peaks in the f_u and f_d distributions are due to the valence quark requirements in the proton. The sea quark PDF distributions are shown, as is the large gluon PDF, which is scaled down by a factor of 10. At high Q^2, the sea quark PDFs become more important, as do the contribution from heavy quarks. . 13

2.3 Plot of $k_{\mathrm{QCD}} = \sigma(\mathrm{NNLO})/\sigma(\mathrm{NLO})$ for charged Drell-Yan production using various PDF sets as a function of the invariant mass of the W when it decays leptonically, $m_{l\nu}$, as studied for the background estimate in a search for leptonically decaying exotic W' bosons [3, 4]. Several different PDFs are compared: MSTW 2008 [2] (solid red line), CT10 [5] (narrow dashed blue line), NNPDF 2.3 [6] (wide dashed purple line), ABM 11 [7] (wide dashed-dotted green line), and HERA 1.5 [8] (narrow dashed-dotted orange line). Ratios are shown of the various PDFs at NNLO with respect to the CT10 PDF set at NLO. All PDF sets use a strong coupling constant of $\alpha_s = 0.117$. The 90% CL uncertainty on the MSTW 2008 NNLO PDF set is also shown (hashed red band). 14

2.4 Feynman diagrams of the couplings of the W boson to the first generation of leptons (top) and quarks (bottom). The quark generations can mix while the lepton generations do not. 19

2.5 Feynman diagrams of the Higgs couplings with the W and Z gauge bosons. 21

2.6 Feynman diagrams of EW QGC couplings 22

2.7 The tree level Feynman diagrams for WWW production. The incoming fermion lines in each diagram consist of an up-type quark (anti-quark) and down-type anti-quark (quark). In this case, the charge of the initial state quarks is assumed to sum to +1, leading to the same charge in the final state. It is also possible for the initial and final states to sum to -1 via charge conjugation. 24

2.8 Invariant mass distribution of two opposite-sign W bosons in WWW events at truth level. The Higgs mass peak is clearly visible around 125 GeV. . . . 25

2.9 Pie chart showing the different decay modes contributing to the total cross-section for the WWW process. The dotted areas indicate the portion of each decay mode which is due to the production of tau leptons. 26

2.10 The unitarized and non-unitarized differential cross sections as a function of $\sqrt{s}$ for the EFT prediction with $f_{S,0}/\Lambda^4 = 6 \times 10^{-7}$ GeV^{-4} divided by the SM values. The form-factor function from Eq. (2.43) with $n = 1$ and $\Lambda_U =$ 180 GeV is used for unitarization. The choice of parameters here serves merely as a demonstration. 30

3.1 Instantaneous luminosity as a function of time as recorded by ATLAS for several runs in 2010. 34

3.2 An event display of 20 pileup interactions in a single bunch crossing. The resulting tracks are shown, along with two high energy muons extrapolated back to a single primary vertex. The upper left shows a cross-section of the whole detector in the transverse plane, the upper right shows the detector viewed along the $r - z$ plane, and the bottom portion is zoomed in to the length of the bunch crossing. The average bunch crossing length at the LHC is around 10 cm [1]. 36

3.3 Diagram of the different accelerators in the CERN accelerator complex [9]. Those relevant for the LHC are the LINAC2, PSB, PS, SPS, and the LHC itself. The ATLAS detector is labeled at the bottom of the LHC ring. . . . 39

3.4 (Top) The peak luminosity from the LHC as a function of time for 2010, 2011, and 2012 data-taking periods and (Bottom) the peak number of pileup interactions as a function of time as recorded by ATLAS. The peak luminosity and pileup interactions have both increased since the LHC began operation in 2010. The gaps in recorded values are due to technical stops and long shutdowns for maintenance and upgrade work. 40

3.5 (Top) The integrated luminosity as a function of time in 2012. The amount delivered by the LHC is shown in green while the amount recorded by ATLAS is overlayed in yellow. More than 93 % of the integrated luminosity delivered by the LHC in 2012 was recorded by ATLAS. (Bottom) The distribution of pileup interactions, parameterized as the mean number of interactions per crossing, $<\mu>$, recorded by ATLAS in 2011 and 2012. . . 41

4.1 A diagram of the ATLAS detector where the detector has been artificially opened up to reveal the LHC beam line and the various sub-detector components within. The sub-detector components are labeled as such. 42

4.2 A diagram of one wedge of the ATLAS detector as viewed from looking down the LHC beam line. The sub-detector components are shown along with the particles that typically come from the collision. The paths of the particles are shown to indicate how each particle interacts with the detector. 44

4.3 Diagram of the ATLAS Inner Detector (ID) showing a wedge of the barrel system. The three detector systems are clearly labeled. The LHC beam pipe is axial to the system and is shown at the bottom of the diagram. . . . 47

4.4 Diagram of the ATLAS Inner Detector (ID) showing a wedge of the end-cap system as well as a part of the SCT and Pixel barrel systems. The detector systems are clearly labeled. The LHC beam pipe is axial to the system but is not shown. Trajectories of two charged tracks with a $p_{\mathrm{T}} = 10\mathrm{GeV}$ are shown along $\eta = 1.4$ and $\eta = 2.2$ as indicated by the solid bright red lines. . 48

4.5 A cut-out diagram of the ATLAS pixel detector showing the arrangement of the pixel modules (green) in three layers of the barrel and three layers of one end-cap system. Some of the support structure is also shown. 49

4.6 Diagram of ATLAS calorimeter system with cut-out portion to allow a view of the nested sub-components. 51

4.7 Photo of three ECAL sampling layers showing its accordion-like structure. In the picture, the horizontal directions corresponds to the radial direction when the detector is in position, which is the direction the LHC products would follow. 52

4.8 A diagram of one ECAL barrel module covering 22.5° in azimuth. When inside the detector, it is oriented as indicated by the axes. 53

4.9 A diagram of one tile HCAL module covering 5.625° in azimuth. The radial direction when positioned in the detector corresponds to the vertical direction in the image. 54

4.10 A schematic showing one quadrant of the HEC system in the R-z plane. The dashed lines indicate the pointing direction achieved by the segmentation of the readouts. Dimensions are in mm. 55

4.11 A schematic showing the end-cap of the ECAL, the two HEC modules, and the three FCAL modules, as well as additional shielding, in one quadrant of the ATLAS detector, as viewed in the R-z plane. The R-direction is shown with a larger scale than in the Z-direction. 56

4.12 A cross-section of the MS in the transverse ($r - \phi$) plane viewed from one end of the detector. The MDT chambers, RPCs, and barrel and end-cap toroids of the MS system are clearly labeled. The barrel toroid coils extend in to and out of the page while only half of the end-cap toroid is shown to reveal the ID and calorimeter systems. The LHC beam pipe runs through the center. 57

4.13 One quadrant of the MS as viewed in the $R - z$ plane. The MDT chambers, RPCs, TGCs, CSCs are clearly indicated, as are the the end-cap and barrel toroids. Support structures, shielding and the calorimeter and ID systems are also drawn. The LHC beam pipe runs from left to right along the bottom. 58

4.14 (Left) Diagram of MS toroid magnet geometry shown in red. The tile calorimeter is also shown. (Right) Predicted field strength of the MS magnet system as a function of $|\eta|$ for $\phi = 0$ in red and $\phi = \pi/8$ in black. 59

4.15 (Left) Cross-section of single MDT tube with muon track passing through. Ionized electrons (black dots) collect on the anode wire due to the applied electric field. (Right) Muon track reconstructed from array of MDT tubes. . 59

4.16 Schematic of a single MDT chamber. 60

4.17 Diagram showing the arrangement of the CSCs in the end-cap. 62

4.18 Layout of the trigger components for one quadrant in the $r - z$ plane. RPC and TGC chambers are clearly labeled. Possible muon trajectories are seen for low and high p_{T} roads formed by the trigger algorithm (see Sec. 4.4). . . 63

5.1 The signal cross-sections for different PDFs along with their uncertainties are shown on the MadGraph WWW signal samples for the total WWW phase space and branching fraction for the $W^+W^+W^-$ (top left) and $W^+W^-W^-$ (top right) charge modes and in the fiducial region for $W^+W^+W^-$ (bottom left) and $W^+W^-W^-$ (bottom right). The bands show the PDF uncertainty for CT10 NLO (solid yellow), MSTW 2008 NLO (hashed blue), and NNPDF 3.0 NLO (hashed red). The solid line shows the envelope of all uncertainty bands used as the final PDF uncertainty estimate. The central value of CT10 NLO is taken as the central value of the estimate. The dashed-line shows the cross-section and statistical uncertainty for the CTEQ6L1 pdf sets used in the original generation step. 73

5.2 Total cross-section for non-unitarized aQGC signal samples as a function of $f_{s,0}$ vs $f_{s,1}$. The total SM cross-section is shown at $f_{s,0} = f_{s,1} = 0$ for comparison. 75

5.3 Total cross-section for unitarized aQGC signal samples as a function of $f_{s,0}$ vs $f_{s,1}$. Four different values of the unitarization scale, Λ, are chosen: 3 TeV (Top Left), 2 TeV (Top Right), 1 TeV (Bottom Left), and 0.5 TeV (Bottom Right). The total SM cross-section is shown at $f_{s,0} = f_{s,1} = 0$ for comparison. 76

5.4 Diagram of the four different regions used in the ABCD method as defined from cuts on the 2D plane of isolation versus the Z boson SFOS mass parameter. 90

5.5 WZ control region with 3 lepton pre-selection plus 2 SFOS requirement. Distributions show leading lepton p_T, $E_{\mathrm{T}}^{\mathrm{miss}}$, m_{12}, and jet multiplicity. The systematic band shows the uncertainty on the WZ k-factor. 94

5.6 $ZZ \to llll$ control region with two separate SFOS pairs. Distributions are shown for the lepton p_{T}, the leading di-lepton mass (m_{12}), the minimum di-lepton mass (m_{34}), and the four lepton mass (m_{4l}). 96

5.7 Three lepton $Z\gamma$ control region. Distribution are shown for the lepton p_T, three lepton invariant mass ($m_{\mu\mu e}$), electron η, and jet multiplicity. 98

5.8 Feynman diagram showing combination of bremsstrahlung and pair-production processes that lead to electron charge mis-identification. In this case, we start with an electron and end with two electrons and a positron. For electron charge mis-identification to occur, the positron would have to be the only final state particle that is reconstructed. 99

5.9 Electron charge mis-identification rates as a function of the electron p_{T} and η extracted using the MC truth method (left) and the likelihood method in data (right). 104

5.10 Summary of electron charge mis-identification rates using the likelihood method in data with background subtraction (black points) and without background subtraction (black line), the MC truth method (blue line), and the likelihood method in MC (red). Systematic uncertainties are extracted as described in the text and are shown in the gray hashed band pointing from bottom left to top right. The systematic uncertainties are combined with the statistical uncertainties on the black points to arrive at a total uncertainty on the rates, shown in the hashed band pointing from bottom right to top left. 105

5.11 Plots of the different branching fractions of the WZ process as a function of the leading lepton p_{T} at pre-selection (left) and after also applying a requirement that events have 0 SFOS lepton pairs (right). The individual decays of W and Z are split up into whether they decay into taus (τ) or into electrons and muons (denoted l). The taus also subsequently decay. The contributions from $WZ \to l\nu ll$ and $WZ \to \tau\nu ll$ after applying the 0 SFOS selection are due purely to charge mis-identification. 109

5.12 Validation of the charge mis-ID rates comparing MC $WZ \to \ell ee$ ($\ell = e, \mu$) samples re-weighted with the charge mis-ID rates measured in the MC $Z \to ee$ sample to the original MC predictions. Distribution of lepton p_T, η, $\Delta\phi(3l, E_T^{Miss})$,$E_{\mathrm{T}}^{\mathrm{miss}}$, Same-sign di-electron invariant mass, and jet multiplicity. 110

5.13 Validation of the charge mis-ID rates comparing MC $ZZ \to \ell\ell ee$ ($\ell = e, \mu$) samples re-weighted with the charge mis-ID rates measured in the MC $Z \to ee$ sample to the original MC predictions. Distribution of lepton p_T, η, $\Delta\phi(3l, E_T^{Miss})$,$E_{\mathrm{T}}^{\mathrm{miss}}$, Same-sign di-electron invariant mass, and jet multiplicity. 111

5.14 Probe lepton p_{T} distributions in SFOS tag and probe control regions used to derive real rates. Electron (left) and muon (right) are shown when the probe lepton is either tight (top) or no additional selection (besides the pre-selection) is required (bottom) 124

5.15 Real lepton efficiency as a function of p_{T} and measured in data (red) and MC (blue) for electrons (left) and muons (right). 125

5.16 Transverse momentum distributions p_{T} of tight probe muons (top) and loose OR tight probe muons (bottom) passing signal selection criteria in the control Same-Sign $\mu - \mu$ control region without any additional requirement on b-jets in the event (left) and at least one b-jet (right). The amount observed in data (black points) corresponds to $N_T^{\mathrm{Data},i} + N_L^{\mathrm{Data},i}$ (bottom) and $N_T^{\mathrm{Data},i}$ (top) following the notation in Eq. 5.42. Meanwhile, the contribution determined in MC to come from real leptons (blue line) and from photon conversion (red line) are shown separately; they are not stacked. The real lepton contribution corresponds to $N_T^{\mathrm{Real},i} + N_L^{\mathrm{Real},i}$ (bottom) and $N_T^{\mathrm{Real},i}$ (top) and the photon conversion contribution corresponds to $N_T^{\mathrm{PC},i} + N_L^{\mathrm{PC},i}$ (bottom) and $N_T^{\mathrm{PC},i}$ (top) again using the notation in Eq. 5.41. The photon conversion is observed to be negligible for muons. 136

5.17 Transverse momentum distributions p_{T} of tight probe electrons (top) and loose OR tight probe muons (bottom) passing signal selection criteria in the control Same-Sign $e - \mu$ control region without any additional requirement on b-jets in the event (left) and at least one b-jet (right). The amount observed in data (black points) corresponds to $N_T^{\mathrm{Data},i} + N_L^{\mathrm{Data},i}$ (bottom) and $N_T^{\mathrm{Data},i}$ (top) following the notation in Eq. 5.42. Meanwhile, the contribution determined in MC to come from real leptons (blue line) and from photon conversion (red line) are shown separately; they are not stacked. The real lepton contribution corresponds to $N_T^{\mathrm{Real},i} + N_L^{\mathrm{Real},i}$ (bottom) and $N_T^{\mathrm{Real},i}$ (top) and the photon conversion contribution corresponds to $N_T^{\mathrm{PC},i} + N_L^{\mathrm{PC},i}$ (bottom) and $N_T^{\mathrm{PC},i}$ (top) again using the notation in Eq. 5.41. 137

5.18 Distributions in a control region designed to study the data-driven fake lepton background estimate. 138

5.19 Distributions showing the observed data compared to the background estimate at event pre-selection. From top to bottom and left to right, these distributions are: the leading, sub-leading, and minimum lepton p_{T} (ordered by their p_{T}), $E_{\mathrm{T}}^{\mathrm{miss}}$, $\Delta\varphi(lll, E_T^{\mathrm{Miss}})$, m_{SFOS}, N_{Jet}, $N_{b-\mathrm{Jet}}$, and N_{μ}. 139

5.20 Yields at event pre-selection in the 0, 1 and 2 SFOS regions. The most important systematic uncertainties (discussed in section 5.6) are shown, namely from the fake estimates and the uncertainties on the WZ and ZZ k-factors. 140

5.21 Plots of the $E_{\mathrm{T}}^{\mathrm{miss}}$(left) and m_{SFOS} (right) distributions in the 1 SFOS (top) and 2 SFOS (bottom) regions after pre-selection plus the b-veto requirement. 141

5.22 Signal and background efficiencies for the selection $E_{\mathrm{T}}^{\mathrm{miss}} > X$ as a function of the $E_{\mathrm{T}}^{\mathrm{miss}}$ selection threshold, X, in both the 0 SFOS (left) and pre-selection (right) regions. 142

5.23 Signal and background efficiencies for the selection $N_{\mathrm{Jet}} \leq X$ as a function of the N_{Jet} selection threshold, X, in both the 0 SFOS (left) and pre-selection (right) regions. 142

5.24 Signal and background efficiencies for the selection $N_{b-\text{Jet}} \leq X$ as a function of the $N_{b-\text{Jet}}$ selection threshold, X, in both the 0 SFOS (left) and pre-selection (right) regions. 143

5.25 Signal and background efficiencies for the selection $|\Delta\varphi(lll, E_T^{\text{Miss}})| > X$ as a function of the $\Delta\varphi(lll, E_T^{\text{Miss}})$ selection threshold, X, in both the 0 SFOS (left) and pre-selection (right) regions. 143

5.26 Signal and background efficiencies for the selection Lepton $p_{\text{T}} > X$ as a function of the p_{T} selection threshold, X, in both the 0 SFOS (left) and pre-selection (right) regions. 144

5.27 Yields after full selection in the 0, 1 and 2 SFOS regions. The most important systematic uncertainties are shown, namely from the fake estimates and the uncertainties on the WZ and ZZ k-factors. 145

5.28 Distributions showing data compared to the signal plus background estimate in the 0 SFOS region at each stage of the selection before the cuts are applied to the given distribution. Plots should be read sequentially from left to right and from top to bottom. Referring to Table 5.18, the top left plot is shown before cut #3 is applied, top middle is before cut #5, and so on until the bottom right which is after all cuts are applied. 148

5.29 Distributions showing data compared to the signal plus background estimate in the 1 SFOS region at each stage of the selection before the cuts are applied to the given distribution. Plots should be read sequentially from left to right and from top to bottom. Referring to Table 5.20, the top left plot is shown before cut #3 is applied, top middle is before cut #4, and so on until the bottom right which is after all cuts are applied. 151

5.30 Distributions showing data compared to the signal plus background estimate in the 2 SFOS region at each stage of the selection before the cuts are applied to the given distribution. Plots should be read sequentially from left to right and from top to bottom. Referring to Table 5.22, the top left plot is shown before cut #3 is applied, the top middle is before cut #4, and so on until the bottom right which is after all cuts are applied. 153

5.31 Probability distribution of the background-only hypothesis as a function of q_0 for the combination of all three channels. The probability distributions are determined using toy MC. The solid black line represents the observed value of q_0 seen in the data. The shaded area above this line represents the null p-value or the integral of the background hypothesis in the signal-like region. The dotted black curve shows a χ^2 distribution for 1 degree of freedom with which it can be seen is a good approximation of the the background-only PDF. 167

5.32 The profile likelihood contours evaluated as a function of the signal strength for the combination of all three channels. The observed (black) and expected (red) contours are shown when considering only statistical uncertainty (dashed line) and when considering both statistical and systematic uncertainties (solid line). The dotted black lines pinpoint the location of the 1 σ and 2 σ total Gaussian uncertainties on the measurement of the signal strength which corresponds to the minimum value of the contour. 169

5.33 Fiducial cross-section for unitarized and non-unitarized aQGC signal samples as a function of $f_{s,0}$ vs $f_{s,1}$. The non-unitarized samples (Top Left) are shown along with the unitarization with four different unitarization scales, Λ: 3 TeV (Top Right), 2 TeV (Middle Left), 1 TeV (Middle Right), and 0.5 TeV (Bottom Center). The total SM cross-section is shown at $f_{s,0} = f_{s,1} = 0$ for comparison. 170

5.34 Correction factor for non-unitarized aQGC signal samples as a function of $f_{s,0}$ vs $f_{s,1}$. The SM correction factor is shown at $f_{s,0} = f_{s,1} = 0$ for comparison. 172

5.35 Two-dimensional limits at 95% CL for the non-unitarized case (Top Left) and three different choices of the unitarization scale, Λ: 3 TeV (Top Right), 2 TeV (Middle Left), 1 TeV (Middle Right), and 0.5 TeV (Bottom Center). 173

6.1 Comparison of $\Delta Y(jj)$ and M_{jj} distributions between VBFNLO and MadGraph LO events with two same-sign leptons and two jets in the final state. 177

6.2 Fiducial cross-sections for unitarized and non-unitarized semi-leptonic aQGC signal samples as a function of $f_{s,0}$ vs $f_{s,1}$. The non-unitarized samples (Top Left) are shown along with the unitarization with four different unitarization scales, Λ: 3 TeV (Top Right), 2 TeV (Middle Left), 1 TeV (Middle Right), and 0.5 TeV (Bottom Center). The total SM cross-section is shown at $f_{s,0} = f_{s,1} = 0$ for comparison. 182

6.3 PDF of the background only hypothesis as a function of q_0 for the combination of all three channels. PDFs are determined using toy MC. The dashed black line represents the expected value of q_0 while the solid black line represents the observed value of q_0 seen in the data. The shaded area to the right of this line represents the null p-value or the integral of the background hypothesis in the signal-like region. The dotted black curve shows a χ^2 distribution for 1 degree of freedom with which it can be seen is a good approximation of the the background only PDF. 183

6.4 The profile likelihood contours evaluated as a function of the signal strength for the combination of all three channels. The observed (black) and expected (red) contours are shown when considering only statistical uncertainty (dashed line) and when considering both statistical and systematic uncertainties (solid line). The dotted black lines pinpoint the location of the 1 σ and 2 σ total Gaussian uncertainties on the measurement of the signal strength which corresponds to the minimum value of the contour. 184

6.5 Two-dimensional limits at 95% CL on the combination for the non-unitarized case (Top Left) and three different choices of the unitarization scale, Λ: 3 TeV (Top Right), 2 TeV (Middle Left), 1 TeV (Middle Right), and 0.5 TeV (Bottom Center). 185

List of Symbols

aQGC	....	anomalous Quartic Gauge Coupling
aTGC	....	anomalous Triple Gauge Coupling
ATLAS	....	A Toroidal LHC ApparatuS
CSC	....	Cathode Strip Chamber
DPS	....	Double Parton Scattering
ECAL	....	Electromagnetic Calorimeter
EF	....	Event Filter
EFT	....	Effective Field Theory
EW	....	Electroweak
EWSB	....	Electroweak Symmetry Breaking
FCAL	....	Forward Calorimeter
HCAL	....	Hadronic Calorimeter
HEC	....	Hadronic End-cap Calorimeter
HLT	....	High-Level Trigger
ID	....	Inner Detector
L1	....	Level-1
L2	....	Level-2
LAr	....	Liquid Argon
LHC	....	Large Hadron Collider
LO	....	Leading-Order

MC	....	Monte Carlo simulation
MDT	....	Muon Drift Tube
ML	....	Maximum Likelihood
MS	....	Muon Spectrometer
NLO	....	Next-to-Leading-Order
NNLO	....	Next-to-Next-to-Leading-Order
PC	....	Photon Conversion
PDF	....	Parton Distribution Function
PS	....	Proton Synchrotron
PSB	....	Proton Synchrotron Booster
QCD	....	Quantum Chromodynamics
QGC	....	Quartic Gauge Coupling
RoI	....	Region-of-Interest
RPC	....	Resistive Plate Chambers
SFOS	....	Same-Flavor Opposite-Sign
SM	....	Standard Model
SPS	....	Super Proton Synchrotron
TGC	....	Thin Gap Chambers
VBF	....	Vector Boson Fusion

Chapter 1

Introduction

There was a moment when the world thought they knew everything about the matter of the universe. That was in February of 1932, when Chadwick discovered the neutron [10]. By that point the proton had already been well established by Rutherford a decade prior as making up the nucleus of the Hydrogen atom [11]. Plus, the electron had been known to be positioned in the atom since Thompson established its particle nature a couple of decades before that [12]. The neutron helped to explain the extra mass in the nucleus of heavier atoms, like Helium, and that was it. There was the peculiar discovery by Compton in 1923 [13] that light had a particle nature, in the form of photons and there was apparently no need for anything else.

But then things began to unravel. On August 2$^{\text{nd}}$, 1932, Anderson discovered what appeared to be the positive electron (now the positron), and in March of 1933 published the photograph to prove it [14][1]. Well, that could be explained nicely by Dirac's relativistic equations for the electron. But then in 1936, Anderson and Neddermeyer discovered what is now know to be the muon [15], leading one famous Nobel Laureate to proclaim "Who ordered that?"

And there were more. In 1947, the charged pion was shown to be distinct from the muon [16]. Another brief moment where they thought they were done. But then the unstable charged and neutral Kaons were discovered in the same year [17] implying the existence of some new class of particles (now associated with the discovery of the strange quark). By this point things were getting messy with new particles being discovered regularly and

[1] If only it were still so easy.

efforts being taken to classify them all.

Then came the *November Revolution* with the discovery of the J/ψ in November of 1974 [18, 19]. Its existence couldn't be explained by the standard class of models. This lead to the confirmation of the quark model to describe the hadrons and the proposal of a new particle: the charm. It predicted an entirely new slew of composite particles, but at least they could be explained now by a short list of constituent particles, now known as the quarks: the up, down, strange, and charm, as well as the bottom and top discovered later in 1977 [20] and 1995 [21, 22], respectively.

A whirlwind of theoretical progress occurred in the mid-20$^{\text{th}}$ century to explain all of the new particles popping up in experiments. But it was the unification of the weak and electromagnetic interactions by Glashow, Weinberg, and Salam [23, 24, 25] as well as the proposal for giving mass to the weak gauge bosons by Englert, Brout, Higgs, Guralnik, Hagen, and Kibble [26, 27, 28] in the 1960s that has informed much of the experimental effort in particle physics ever since. The W and Z bosons predicted by the theory were discovered in 1983 at CERN [29, 30]. And most recently, the Higgs boson was discovered in 2012 [31, 32], nearly 50 years after it was first proposed. Together with the theory of Quantum Chromodynamics, this ostensibly completes the Standard Model (SM) of particle physics. So are we done? Just like they thought in 1932?

Perhaps not. There are experimental hints of entirely new realms of the universe, so mysterious we refer to them as dark matter and dark energy. If we could only find a new particle, this generation's version of the positron or the J/ψ, we could potentially open the door to this new realm. Perhaps the key is lurking somewhere in the observations of the SM and we just haven't been able to find it yet. Much of the structure of the SM, like why there are three generations of leptons and quarks, are not understood. And there is still uncharted territory within the SM itself.

We seek to explore this uncharted territory by looking for a process which is predicted by the SM but it is too rare to have yet been observed; namely, the production of three W bosons simultaneously from proton-proton collisions. The massive nature of the W

($m_W = 80.385 \pm 0.015$ GeV [1]) requires a large amount of energy to produce it. This is why it was not observed until 1983, when a collider with sufficient energy (540 GeV) could be built. So naturally, producing more than one requires even more energy. Production of two W bosons has been measured most recently by ATLAS [33] and CMS [34], but the production of three W bosons has remained out of reach.

The high energy and collision rate of the Large Hadron Collider (LHC) at CERN provides an opportunity to look for this process for the first time. Indeed, the data collected from the LHC in 2012 should have produced around 150 of collisions of this type on average. These could potentially be measured by any of the detectors at the LHC, though we will use the ATLAS detector, which is particularly well suited for this type of measurement. There are, however, many other processes that are produced far more copiously and can easily swamp out sensitivity to this process. Thus, we must carefully sift through the data, trying to separate our signal from the background. Once we think we've done our best, we assess whether or not the signal is present by measuring the cross-section of the process. We also use these results to assess whether or not new physics processes have been observed. If not, we ask whether or not we can rule out any class of new physics models. In the words of my esteemed Professor John Butler, "What could go wrong?"

As this thesis describes an attempt to measure a prediction of the SM, it starts with a discussion of the details of the SM itself and a description of the WWW process in Chapter 2. It introduces both the theory of Quantum Chromodynamics (QCD) and Parton Distribution Functions (PDF), both of which are important at a proton-proton collider like the LHC. This is followed by a description of the Electroweak (EW) theory, with a particular emphasis on how it leads to the predictions of the WWW process. The experimental tools of the LHC and ATLAS are described in Chapters 3 and 4, respectively. Chapter 3 describes the general principles of particle physics performed at a hadron collider as well as specifics of the LHC. Chapter 4 describes the different components of the ATLAS detector and how they are used to identify and measure the properties of the products of the collisions of the LHC.

Once these tools have been described, we get to the main thrust of the thesis, which is how we use them to search for the WWW process. Chapter 5 goes into precise detail about how we search for the WWW process in one particular decay channel where each W decays into electrons or muons plus neutrinos, denoted $WWW \to \ell\nu\ \ell\nu\ \ell\nu$, and referred to as the "fully-leptonic" channel. It begins by introducing the LHC dataset and the simulation datasets that are used in the predictions of the signal and background. It then talks about how the collisions are selected to obtain a good collection of signal. One of the most challenging aspects of an analysis of this type is being sure that one understands all of the backgrounds to the signal process. Thus, we next devote attention to how the backgrounds are estimated. This is followed by a presentation of the observed data after final selection and how this compares to the signal plus background estimates. These results are then interpreted to extract a cross-section measurement and uncertainty on the signal process and to extract information about new physics as predicted from anomalous Quartic Gauge Couplings (aQGC) in an Effective Field Theory (EFT) approach. In Chapter 6, this is followed by a re-interpretation of the sensitivity to the WWW process after combining with another decay channel where one of the W bosons decays instead to quarks, denoted $WWW \to \ell\nu\ \ell\nu\ jj$ and referred to as the "semi-leptonic" channel. This decay channel is not the focus of this thesis, but its inclusion can improve the sensitivity to the WWW process. Thus, the decay channel along with the results of the search in this individual channel are briefly introduced, followed by a presentation of an updated interpretation of the cross-section measurement and limits on new physics similar to that which is presented in Chapter 5. Finally, we conclude in Chapter 7 with a summary of the results and a prediction for the outlook of this search using future LHC data.

Throughout the thesis we use natural units where $c = \hbar = 1$. This takes advantage of the relativistic relationship between energy, momentum, and mass so that they are all in units of the energy, measured in electron volts, or eV. The electric charge, e, is related to the fine structure constant, $\alpha \approx 1/137$, by $e = \sqrt{4\pi\alpha}$.

Chapter 2

Theory

The focus of this thesis is to probe the production of the Standard Model (SM) process with three W bosons produced in proton-proton collisions with each decaying leptonically. To that end, an introduction to the SM is in order. This is presented below with particular emphasis on those things which are relevant for the understanding of this process; namely Quantum Chromodynamics (QCD) and Parton Distribution Functions (PDFs), describing the interactions at a proton-proton collider, and the Electroweak (EW) theory which describes the mechanisms of WWW production and decay. The SM is well established and has been written about thoroughly since the mid-20$^{\text{th}}$ century. So while the WWW process has never been observed, the SM building blocks of this process are not new. The descriptions below thus rely mostly on those in [35], [36], and [37].

We also seek to assess our sensitivity to new physics using a contemporary approach to Effective Field Theory (EFT) in the context of modifying the SM, with a particular focus on anomalous Quartic Gauge Couplings (aQGC). A discussion of this approach is described following the description of the SM process.

2.1 The Standard Model

The Standard Model (SM) is a theory which describes all of the observed matter and interactions in the universe, except for gravity. It is built from a quantum field theory where the constituent particles and interactions fit into a non-Abelian SU(3) $\times$ SU(2) $\times$ U(1) gauge symmetry. From these symmetries come the spin-1/2 matter fermions, split into the quarks and leptons, and the force-carrying bosons that mediate their interactions. The SU(3) symmetry describes the theory of Quantum Chromodynamics (QCD) which explains the interaction of the quarks via the gluons, the gauge bosons that mediate the strong force. The remaining SU(2)$\times$U(1) symmetry describes the Electroweak (EW) theory which explains the interactions of the quarks and leptons via the electroweak gauge bosons that mediate the electroweak force: W, Z, and γ (i.e. the photon). The EW theory is itself a unified description of the weak force, involving the W and Z, and the electromagnetic force, involving just the photon. The W and Z gauge bosons (as well as the quarks and leptons) receive their non-zero masses through the process of electroweak symmetry breaking (EWSB), while keeping γ massless. The simplest form of EWSB introduces an additional 'Higgs' field that predicts a single new fundamental scalar boson. This boson is the famous Higgs boson which was discovered recently at the LHC [31, 32], thereby confirming this last component of the SM.

All of the observed fundamental matter particles in the universe are described by the quarks and leptons of the SM. Their properties are listed in Table 2.1. The quarks and leptons can each be divided up into three "generations" composed of pairs of particles with identical charges but whose masses increase with each generation. The generations are labeled in Table 2.1. Even though there are three generations in both the lepton and quark sectors, there are no observed direct interactions between the two, thus the quarks and lepton generations should be thought of as separate. The particles can be distinguished by their charges and masses. The charges describe how (and if) the particles participate in different interactions. Those fermions with electric charge participate in the electromagnetic interactions. The quarks have color charge (sometimes just called color), which allows them to participate in the QCD interactions. All fermions also participate in the weak interactions. The types of allowed weak interactions are determined by a combination of the electric charge as well as the weak isospin and weak hypercharge, described in Sec. 2.1.3. The masses of the particles are not predicted by the theory, but are essential for understanding their stability and decay properties as well as their kinematic behavior. Each particle also has a corresponding anti-particle with the same mass but whose electric charge has opposite sign. The neutrinos, with zero electric charge, could possibly be their own anti-particle (so-called Majorana fermions), but this has yet to be confirmed.

	Generation	Name	Symbol	Q	Mass [MeV]
Quarks	First	Up	u	$2/3$	$2.3^{+0.7}_{-0.5}$
		Down	d	$-1/3$	$4.8^{+0.5}_{-0.3}$
	Second	Charm	c	$2/3$	1275 ± 25
		Strange	s	$-1/3$	95 ± 5
	Third	Top	t	$2/3$	173210 ± 874
		Bottom	b	$-1/3$	4180 ± 30
Leptons	First	Electron	e	-1	$0.510998928 \pm 0.000000011$
		Electron Neutrino	ν_e	0	< 0.002
	Second	Muon	μ	-1	$105.6583715 \pm 0.0000035$
		Muon Neutrino	ν_μ	0	< 0.19
	Third	Tau	τ	-1	1776.86 ± 0.12
		Tau Neutrino	ν_τ	0	< 18.2

Table 2.1: Summary of the electric charge, Q (in unites of e), and masses of the SM fermions. Masses are taken from the Particle Data Group [1] and are shown to the best precision available within their uncertainties. Particles are also organized by their generation. The limits on the electron neutrino and muon neutrino masses are set at a 90% confidence level while the tau neutrino limits are set at a 95% confidence level.

The SM can be written down using a lagrangian of the form

$$\mathcal{L}_{\text{SM}} = \mathcal{L}_{\text{QCD}} + \mathcal{L}_{\text{EW}} + \mathcal{L}_{\text{EWSB}}, \tag{2.1}$$

which is gauge invariant. From this, one can calculate all of the fundamental interactions of the SM. As written, the SM lagrangian can be split up into separate terms describing the QCD, EW, and EWSB interations; these are discussed in Sec. 2.1.1 and Sec. 2.1.3. The interactions, each with their own coupling parameters, can be used (like the pieces of a puzzle) to build quantum mechanical amplitudes for some process with a given initial and final state. This amplitude, along with phase space considerations, can then be used to determine the cross-section, σ, for the process. The cross-section is the observable which we measure.

In general there are an infinite number of configurations of the fundamental interactions which can be used to describe a given initial and final state, where each configuration contributes a separate term to the amplitude. Fortunately, as long as the coupling parameters of the fundamental interactions are small (as is usually the case) then only the simplest terms are important. This is the method of perturbation theory. Most predictions of quantum field theory phenomena rely on approximate calculations using perturbation theory. For instance, say that a given fundamental interaction has a coupling parameter, $0 < \alpha < 1$. Since $0 < \alpha < 1$, terms with higher powers of α are suppressed and can be ignored if one is willing to sacrifice some precision. The simplest "tree-level" interactions involve just one factor of the coupling. These are referred to as Leading-Order (LO) interactions. Higher order interactions involving two powers of the coupling, α^2 are referred to as Next-to-Leading-Order (NLO). This can be continued to Next-to-Next-to-Leading-Order (NNLO), which is proportional to α^3, and so on *ad infinitum*. In fact, usually the LO prediction is good enough. This applies separately to both the EW and QCD[1] interactions as well as combinations of the two.

2.1.1 Quantum Chromodynamics

The theory of Quantum Chromodynamics (QCD) is a non-Abelian SU(3) gauge theory describing the "strong" interactions which result in hadronic bound states (for example, the proton). To participate in QCD a particle must possess color charge. Quarks possess color charge, as do the gluons, which are the gauge boson mediators of the "strong" interactions. The quarks can possess one color charge: red, green, or blue (for example, there exist red quarks and blue quarks but no red blue quarks). The anti-quarks possess anti-color charge (for example, there exist anti-red anti-quarks but no red anti-quarks). Thus, there are three colors of quarks and three colors of anti-quarks. Colorless objects, meaning those that don't possess color charge, can be formed from colored objects either by pairing a color with its anti-color (for example, red plus anti-red cancel out) or by combining the

[1] Though this can break down for some regimes in QCD as described in Sec. 2.1.1.

three colors or three anti-colors (for example, red plus blue pus green makes white). One consequence of the theory being non-Abelian is that the gluons are also colored, though not in the same way as the quarks. Each gluon possesses one color and one anti-color (for example, there exist anti-red blue gluons). This results in eight independent colored gluons[2].

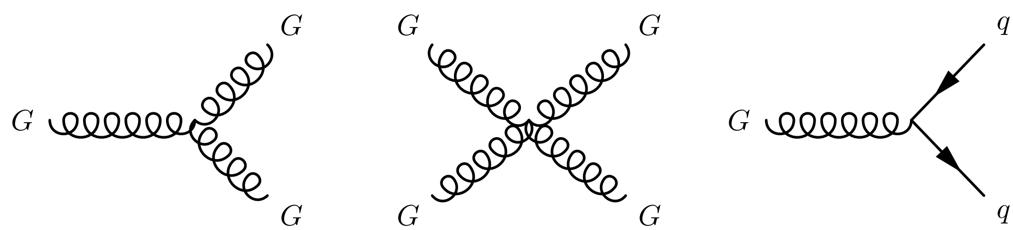

Figure 2.1: Feynman diagrams of QCD describing the interactions between gluon and quark fields. The gluons and quarks can in general have different colors.

The QCD term in the SM lagrangian can be written as

$$\begin{aligned} \mathcal{L}_{\mathrm{QCD}} = &- \frac{1}{4} G^a_{\mu\nu} G^{\mu\nu}_a - g_s \Big(\overline{q}_{\overline{c}} \gamma^\mu T_a q_c \Big) G^a_\mu \\ &+ \overline{q}_{\overline{c}} \Big(i\gamma^\mu \partial_\mu - m \Big) q_c. \end{aligned} \tag{2.2}$$

The first term describes the kinetic energies of the gluons and their self-interactions while the second term describes the interactions between the the gluons and quarks. These interactions can be identified with the Feynman diagrams in Fig. 2.1. The last term describes the kinetic energy and masses of the quarks. The quark fields are represented by q_c, with an implied sum over the three different colors, indexed by c. There is also an implied sum over the quark flavors. The gluon fields are represented by G^a_μ, where there is also an implied sum over the eight different gluon fields, indexed by a. The gluon fields are four-vectors of the Lorentz group and thus undergo Lorentz transformations as indicated by their Lorentz index, μ. The T_a are the generators of SU(3), represented by the eight Gell-Mann matrices. Because the theory is non-Abelian, the generators obey the

[2]The anti-red red, anti-blue blue, and anti-green green configurations form three independent linear combinations, two of which possess color and a third which does not. This reduces the number of gluons from the naive value of nine when considering just the permutations, down to eight when eliminating the colorless configuration.

commutation relation,

$$\Big[T_a, T_b\Big] = i f_{abc} T_c, \tag{2.3}$$

where f_{abc} are the anti-symmetric SU(3) structure constants that are completely determined by the specification of T_a. $G^a_{\mu\nu}$ is the gluon field strength,

$$G^a_{\mu\nu} = \partial_\mu G^a_\nu - \partial_\nu G^a_\mu - g_s f_{abc} G^b_\mu G^c_\nu, \tag{2.4}$$

where the ∂_μ is the four-dimensional partial derivative of the Lorentz group and the γ^μ are the Dirac matrices. Finally, g_s is the strong coupling and m represents the quark masses, which are both parameters of the theory that must be determined by experiment.

The strong coupling parameter, g_s, is not constant, but instead changes as a function of the energy of the interaction. The self-interactions of the gluons, seen in Fig. 2.1, and the number of quark flavors, listed in Table 2.1, result in the peculiar property that g_s decreases with increasing energy (or equivalently, decreasing distance). This is the property of asymptotic freedom [38, 39], where when probing a proton or other hadronic bound state at high energy, the quarks behave essentially as free particles. On the other hand, if in isolation at low energy, they do not behave as free particles but instead interact strongly with the vacuum. This has tremendous consequences, since the strong coupling parameter can grown until perturbative QCD breaks down at low energy and since it is believed to be the cause of "color confinement". The principle of "color confinement" states that only colorless objects can be observed in nature. Thus, quarks and gluons can never be observed directly. Furthermore, hadronic bound states, themselves comprised of colored quarks and gluons, are restricted to colorless configurations. The simplest colorless hadronic configurations are mesons (for example, the π^0) and baryons (for example, the proton and neutron), although more complex configurations have been discovered (most recently, the pentaquark at LHCb [40]). Any attempt to split up a hadron into its constituent quarks will fail, with the quarks forming new hadrons from quark-antiquark pairs pulled from the vacuum. This cascade of hadrons breaking up into more hadrons is referred to as "hadronization". At the

LHC, hadronization frequently occurs at a high momentum where the resulting objects are Lorentz boosted into highly collimated collections of hadrons and other particles, called jets. Jets are thus one of the main observables for probing QCD at the LHC.

2.1.2 Parton Distribution Functions

Despite color confinement, the constituent quarks and gluons of the hadrons, also known as partons, can still be probed, although indirectly. Indeed, in the high energy proton-proton collisions of the LHC, the partons inside the proton participate directly in the interactions under study. However, while the momentum and energy of the protons can be known with great precision, this is not true of the partons. Instead, the individual parton momenta can only be known with some probability. These are governed by the parton distribution functions (PDF), $f_i(x,\ \mu_R^2,\ \mu_F^2)$, where x ranges from $0 < x < 1$ and is the fraction of the parton momentum with respect to the total proton momentum, i indexes the parton that the PDF refers to, μ_R is the renormalization scale which is necessary for removing divergences inherent in perturbation theory applied to QCD, and μ_F is the factorization scale which separates the non-perturbative regime describing the hadronization from the perturbative regime relevant for the partonic hard-scattering cross-section. The two scales are both in units of energy and are usually chosen to be equal to the characteristic energy in the interaction[3], though this choice does introduce an additional uncertainty which is usually tested by varying both scales independently.

The overall probability must of course sum to unity, such that for some given choice of scales,

$$\sum_i \int_0^1 \mathrm{d}x\ x f_i(x,\ \mu_R^2,\ \mu_F^2) = 1, \tag{2.5}$$

where note that the sum over i is taken over all possible partons; this includes all quark (and anti-quark) flavors (though the more massive quarks are less important) as well as the gluons. A hadron is characterized by its valence quark composition, which places additional

[3] For example, in Drell-Yan production ($pp \to Z\ \to l^+l^-$ or $pp \to Z \to q^+q^-$) a natural scale to choose would be $\mu_R = \mu_F = m_Z$.

requirements on the PDFs. In the case of the proton, the valence quark composition is charactized by two up quarks and a down quark. This translates into the requirements

$$\int \mathrm{dx}(f_u(x,\ \mu_R^2,\ \mu_F^2) - f_{\overline{u}}(x,\ \mu_R^2,\ \mu_F^2)) = 2 \tag{2.6}$$

and

$$\int \mathrm{dx}(f_d(x,\ \mu_R^2,\ \mu_F^2) - f_{\overline{d}}(x,\ \mu_R^2,\ \mu_F^2)) = 1, \tag{2.7}$$

while the other quark flavors are referred to as sea quarks and follow the requirement

$$\int \mathrm{dx}(f_i(x,\ \mu_R^2,\ \mu_F^2) - f_{\overline{i}}(x,\ \mu_R^2,\ \mu_F^2)) = 0, \quad \text{where } i \neq d, u. \tag{2.8}$$

After these requirements, the remaining momentum fraction of the proton comes from the gluon PDF, which in the end typically contributes to most of the momentum of the proton.

The PDFs can then be used along with the partonic cross-section for the given process, $\hat{\sigma}$, to determine an overall cross-section for its production in proton-proton scattering. To achieve this, the PDFs are convoluted with the partonic cross-section, which is also a function of the parton momenta and the renormalization and factorization scales, in order to obtain an overall cross-section of the form

$$\sigma = \sum_i \sum_j \int_0^1 \mathrm{d}x_1\ \mathrm{d}x_2\ f_i(x_1,\ \mu_R^2,\ \mu_F^2)\ f_j(x_2,\ \mu_R^2,\ \mu_F^2)\ \hat{\sigma}_{ij}(x_1,\ x_2,\ \mu_R^2,\ \mu_F^2), \tag{2.9}$$

where x_1 and x_2 are the separate momentum fractions of the partons in the two incoming protons with partons indexed by i and j, respectively.

The PDFs are ultimately determined experimentally using fits to the data collected from deep inelastic scattering and hadron collider experiments. There isn't one perfect way to determine the PDFs. As a result there are many different PDF sets available to choose from, with updates being churned out regularly by different physics groups. An example for one particular PDF set is shown using two different scales, $Q^2 = \mu_R^2 = \mu_F^2$,

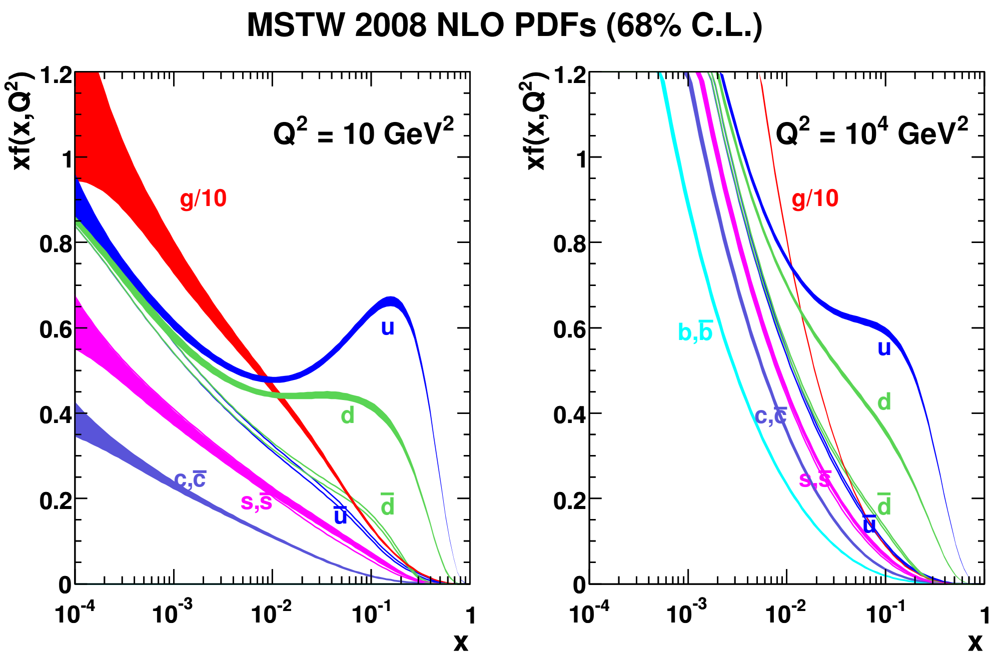

Figure 2.2: Plot of $xf_i(x, Q^2)$ vs x for the MSTW 2008 NLO PDF sets [2] with 68% CL eigenvector uncertainties for two different scales, $Q^2 = \mu_R^2 = \mu_F^2$. The peaks in the f_u and f_d distributions are due to the valence quark requirements in the proton. The sea quark PDF distributions are shown, as is the large gluon PDF, which is scaled down by a factor of 10. At high Q^2, the sea quark PDFs become more important, as do the contribution from heavy quarks.

in Fig. 2.2. In general, the predictions from different PDFs agree within a few percent. Differences can arise, however, in particular at high energy (high x) where it is difficult to measure. When making predictions, one usually compares multiple PDFs following some prescription such as in [41]. This can be seen, for instance, in a comparison I performed on the variation of different PDF predictions on the charged Drell-Yan process seen in Fig. 2.3.

For this thesis, three different PDF sets are compared for the signal process: MSTW 2008 [2], CT10 [5], and NNPDF 3.0 [42]. All PDF sets are evaluated at NLO. All three PDF sets include data from deep inelastic scattering studies during Run-I at HERA, vector boson production and inclusive jet studies at the Tevatron, as well as data from fixed target experiments. NNPDF 3.0 is the most up-to-date with additional data from deep inelastic scattering studies in Run-II at HERA, and from recent LHC measurements at

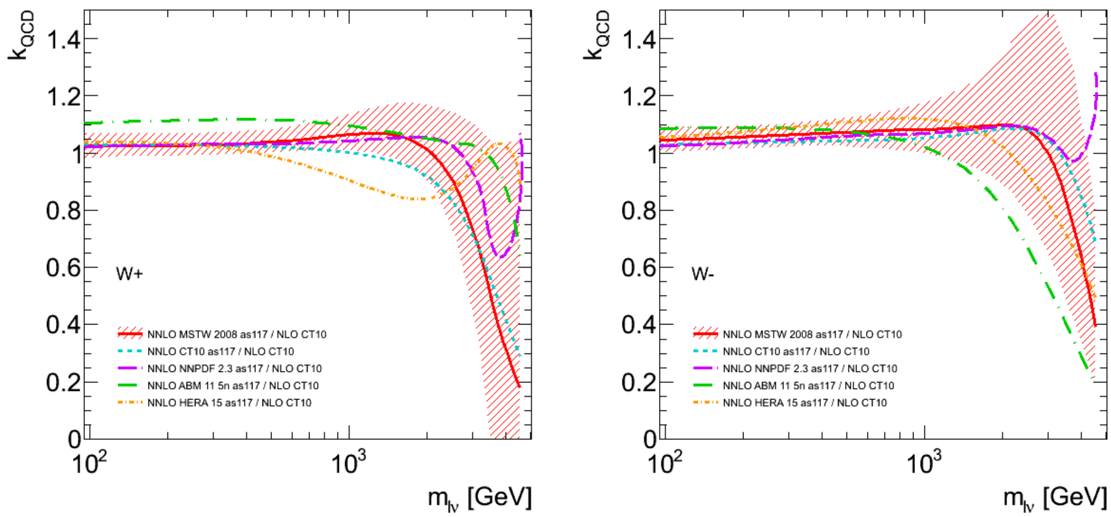

Figure 2.3: Plot of $k_{\mathrm{QCD}} = \sigma(\mathrm{NNLO})/\sigma(\mathrm{NLO})$ for charged Drell-Yan production using various PDF sets as a function of the invariant mass of the W when it decays leptonically, $m_{l\nu}$, as studied for the background estimate in a search for leptonically decaying exotic W' bosons [3, 4]. Several different PDFs are compared: MSTW 2008 [2] (solid red line), CT10 [5] (narrow dashed blue line), NNPDF 2.3 [6] (wide dashed purple line), ABM 11 [7] (wide dashed-dotted green line), and HERA 1.5 [8] (narrow dashed-dotted orange line). Ratios are shown of the various PDFs at NNLO with respect to the CT10 PDF set at NLO. All PDF sets use a strong coupling constant of $\alpha_s = 0.117$. The 90% CL uncertainty on the MSTW 2008 NNLO PDF set is also shown (hashed red band).

ATLAS, CMS, and LHCb. The uncertainties on the MSTW 2008 and CT10 PDF sets are determined using a Hessian approach while the NNPDF 3.0 PDF set uses a Monte Carlo approach as described in [41]. The Hessian approach constructs a likelihood to determine the PDF central value while the uncertainty is taken from a confidence interval that is built from an orthonormal representation of the covariance matrix at the minimum of the likelihood. The Monte Carlo approach produces PDF set replicas that capture variations on the input data which can then be used to calculate distributions for extracting the central value and uncertainties. In general, each of the PDF sets considered are in good agreement with the LHC data.

2.1.3 The Electroweak Theory

The electroweak (EW) theory of Glashow, Weinberg, and Salam [23, 24, 25] is a renormalizable [43, 44] non-Abelian gauge theory that successfully unifies the theories of the U(1) electromagnetism and SU(2) weak interactions. It incorporates the observed charge conjugation (C) and parity (P) violating V-A structure of the weak interactions [45, 46, 47] while simultaneously preserving these symmetries for electromagnetism. It also explains the presence of the massive EW gauge bosons while maintaining gauge invariance using spontaneous symmetry breaking.

The EW term in the SM lagrangian can be written as

$$\mathcal{L}_{\mathrm{EW}} = -\frac{1}{4}\mathbf{W}_{\mu\nu} \cdot \mathbf{W}^{\mu\nu} - \frac{1}{4}B_{\mu\nu}B^{\mu\nu} + \overline{\psi}\gamma^{\mu}D_{\mu}\psi, \tag{2.10}$$

where the first two terms describe the kinetic energies and self-interactions of the EW gauge bosons and the last term describes the fermion kinetic energies and their interactions with the EW gauge bosons, with an implied sum over the fermion fields denoted as ψ. The kinetic energies are described by the field strength tensors,

$$\mathbf{W}_{\mu\nu} = \partial_{\mu}\mathbf{W}_{\nu} - \partial_{\nu}\mathbf{W}_{\mu} - g\mathbf{W}_{\mu} \times \mathbf{W}_{\nu} \tag{2.11}$$

and

$$B_{\mu\nu} = \partial_{\mu}B_{\nu} - \partial_{\nu}B_{\mu}. \tag{2.12}$$

The gauge fields, $\mathbf{W}_{\mu}$ and B_{μ}, represent the massless EW gauge bosons before EWSB. Like the gluon fields, they are four-vectors of the Lorentz group as indicated by their Lorentz index, μ. The $\mathbf{W}_{\mu} = (W_{\mu}^{1}, W_{\mu}^{2}, W_{\mu}^{3})$ describe two charged gauge bosons and a neutral gauge boson as a triplet of weak isospin in SU(2) with its generators being the famous Pauli matrices, $\boldsymbol{\tau}$, that follow the commutation relation

$$\left[\tau_a, \tau_b\right] = i\varepsilon_{abc}\tau_c, \tag{2.13}$$

where ε_{abc} is the Levi-Civita symbol. The charged gauge bosons are represented by a superposition of the first two components of the isotriplet, $W_\mu^\pm = \sqrt{\frac{1}{2}}\left(W_\mu^1 \mp iW_\mu^2\right)$, while the neutral gauge boson is represented by the third component, W_μ^3. The B_μ is a singlet of U(1) and describes a single neutral gauge boson using a single vector field with generator Y, referred to as the weak hypercharge. By construction, the weak hypercharge is related to the electric charge of U(1) electromagnetism, Q, and the charge of the third component of weak SU(2), T^3, by

$$Q = T^3 + Y/2. \tag{2.14}$$

The ∂_μ is the four-dimensional partial derivative of the Lorentz group and the γ^μ are the Dirac matrices. The EW covariant derivative, D_μ, is

$$D_\mu = i\partial_\mu - g\frac{1}{2}\boldsymbol{\tau}\cdot\mathbf{W}_\mu - g'\frac{Y}{2}B_\mu. \tag{2.15}$$

The coupling constants g and g' describe the strength of the interactions of the fermions with the gauge boson fields before EWSB.

The fermion fields, ψ, (and their conjugates, $\overline{\psi}$) can be split up into the left-handed fermion isospin doublets, L, and the right-handed fermion isospin singlets, R, which are described in more detail below. Putting it all together, we end up with

$$\begin{aligned}\mathcal{L}_{\mathrm{EW}} = &-\frac{1}{4}\Big(\partial_\mu\mathbf{W}_\nu - \partial_\nu\mathbf{W}_\mu - g\mathbf{W}_\mu\times\mathbf{W}_\nu\Big)\cdot\Big(\partial^\mu\mathbf{W}^\nu - \partial^\nu\mathbf{W}^\mu - g\mathbf{W}^\mu\times\mathbf{W}^\nu\Big)\\ &-\frac{1}{4}\Big(\partial_\mu B_\nu - \partial_\nu B_\mu\Big)\Big(\partial^\mu B^\nu - \partial^\nu B^\mu\Big)\\ &+\overline{L}\gamma^\mu\Big(i\partial_\mu - g\frac{1}{2}\boldsymbol{\tau}\cdot\mathbf{W}_\mu - g'\frac{Y}{2}B_\mu\Big)L\\ &+\overline{R}\gamma^\mu\Big(i\partial_\mu - g'\frac{Y}{2}B_\mu\Big)R.\end{aligned} \tag{2.16}$$

The V-A structure of the weak interactions results in the absence of charged weak interactions involving right-handed fermions and left-handed anti-fermions. This is captured by assigning charges to the SM fermions as listed in Table 2.2 such that they satisfy Eq. (2.14). The charges differ based on the chirality, or “handedness”, of the fermions.

This specification for the charges results in the left-handed fermion fields being treated as isospin doublets, L, which transform under SU(2) for each lepton and quark generation:

$$L = \begin{pmatrix} e_L \\ \nu_{e,L} \end{pmatrix}, \begin{pmatrix} \mu_L \\ \nu_{\mu,L} \end{pmatrix}, \begin{pmatrix} \tau_L \\ \nu_{\tau,L} \end{pmatrix}, \begin{pmatrix} u_L \\ d_L \end{pmatrix}, \begin{pmatrix} c_L \\ s_L \end{pmatrix}, \begin{pmatrix} t_L \\ b_L \end{pmatrix}. \tag{2.17}$$

Meanwhile, the right-handed fermion fields are treated as isospin singlets, R, which only transform under U(1):

$$R = e_R,\ \mu_R,\ \tau_R,\ u_R,\ d_R,\ c_R,\ s_R,\ t_R,\ b_R, \tag{2.18}$$

where each object is a Dirac field whose chirality is indicated by its subscript. Note that the right-handed neutrinos are absent. This comes from them having zero charge across the board in Table 2.2. As a result, they do not participate in any of the SM interactions.

Particle			Q	Y	T^3
Quarks	Left-Handed	u_L	2/3	1/3	1/2
		d_L	-1/3	1/3	-1/2
	Right-Handed	u_R	2/3	4/3	0
		d_R	-1/3	-2/3	0
Leptons	Left-Handed	e_L	-1	-1	1/2
		$\nu_{e,L}$	0	-1	-1/2
	Right-Handed	e_R	-1	-2	0
		$\nu_{e,R}$	0	0	0

Table 2.2: The charges of the SM fermions in units of the electric charge, e. The charges are the same for each generation, so only the first generation of quarks and leptons are shown.

Using this specification of the fermion fields we can identify the interactions of the fermions with the charged W boson. Expanding the term

$$-g\frac{1}{2}\overline{L}\gamma^{\mu}\boldsymbol{\tau}\cdot\mathbf{W}_{\mu}L \tag{2.19}$$

from Eq. (2.16) and keeping only those terms where the charged W and lepton fields are present gives

$$
\begin{aligned}
-\frac{g}{\sqrt{2}}\gamma^{\mu}\Big(&\overline{e}_L W_\mu^+ \nu_{e,L} + \overline{\nu}_{e,L} W_\mu^- e_L \\
&+ \overline{\mu}_L W_\mu^+ \nu_{\mu,L} + \overline{\nu}_{\mu,L} W_\mu^- \mu_L \\
&+ \overline{\tau}_L W_\mu^+ \nu_{\tau,L} + \overline{\nu}_{\tau,L} W_\mu^- \tau_L\Big),
\end{aligned}
\tag{2.20}
$$

which corresponds to the Feynman diagrams at the top of Fig. 2.4. It is this type of interaction that is responsible for the W decay to leptons. In the absence of quark flavor mixing, the interaction terms of the quark sector look similar:

$$
\begin{aligned}
-\frac{g}{\sqrt{2}}\gamma^{\mu}\Big(&\overline{u}_L W_\mu^+ d_L + \overline{d}_L W_\mu^- u_L \\
&+ \overline{c}_L W_\mu^+ s_L + \overline{s}_L W_\mu^- c_L \\
&+ \overline{t}_L W_\mu^+ b_L + \overline{b}_L W_\mu^- t_L\Big).
\end{aligned}
\tag{2.21}
$$

These terms correspond to the Feynman diagrams at the bottom of Fig. 2.4 and it is the presence of these interactions that allow the W to be produced directly at a hadron collider. Taking into account quark flavor mixing via the CP violating [48] Cabibbo-Kobayashi-Maskawa matrix [49, 50] modifies this picture so that additional small interaction terms appear between the different quark generations.

The strength of the weak interactions is suppressed at energies much smaller that the masses of the the charged and neutral weak bosons. But the EW theory cannot assign masses directly to the gauge bosons without breaking gauge invariance. This is resolved by the introduction of spontaneous symmetry breaking which generates the masses for the gauge bosons whilst preserving gauge invariance. The simplest implementation of this EWSB process is the Higgs mechanism [26, 27, 28]. The lagrangian for EWSB via the Higgs mechanism is

$$
\begin{aligned}
\mathcal{L}_{\mathrm{EWSB}} =& \Big|D_\mu \phi\Big|^2 - \Big(\mu^2 \phi^\dagger \phi + \lambda(\phi^\dagger \phi)^2\Big) \\
&- \Big(G_1(\overline{L}\phi R + \overline{R}\phi_c L) + G_2(\overline{L}\phi_c R + \overline{R}\phi L)\Big),
\end{aligned}
\tag{2.22}
$$

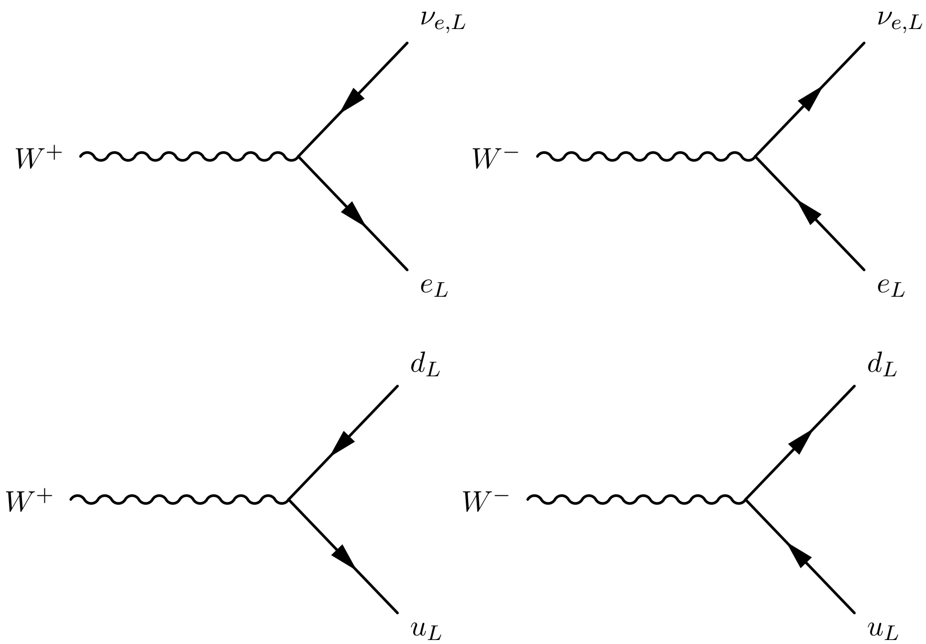

Figure 2.4: Feynman diagrams of the couplings of the W boson to the first generation of leptons (top) and quarks (bottom). The quark generations can mix while the lepton generations do not.

where the first term shows the interactions of the newly introduced scalar Higgs field, ϕ, with the gauge bosons; the second term is the famous "mexican-hat" potential of the Higgs field, with parameters $\mu^2 < 0$ and $\lambda > 0$, that is responsible for the spontaneous symmetry breaking in the Higgs mechanism; and the third term shows the Yukawa interactions of the Higgs field with the fermions, with couplings G_1 and G_2, that give the fermions their masses. Before EWSB, ϕ (and its conjugate ϕ_c) are complex isospin doublets of four scalar fields:

$$\phi = \frac{1}{\sqrt{2}} \begin{pmatrix} \phi_1 + i\phi_2 \\ \phi_3 + i\phi_4 \end{pmatrix}, \qquad \phi_c = \frac{1}{\sqrt{2}} \begin{pmatrix} -\phi_3 + i\phi_4 \\ \phi_1 - i\phi_2 \end{pmatrix}. \tag{2.23}$$

Upon EWSB, we choose $\phi_3 = v + h$ and $\phi_1 = \phi_2 = \phi_4 = 0$ such that the Higgs fields become

$$\phi = \frac{1}{\sqrt{2}} \begin{pmatrix} 0 \\ v + h \end{pmatrix}, \qquad \phi_c = \frac{1}{\sqrt{2}} \begin{pmatrix} v + h \\ 0 \end{pmatrix}, \tag{2.24}$$

where $v = m_h/\sqrt{2\lambda}$ is the stable minimum of the "mexican-hat" potential and is a function of the Higgs boson mass, $m_h = 2\sqrt{-\mu^2}$, and h is the quantum vacuum fluctuation of the Higgs field about this minimum. Plugging this into the first line of Eq. (2.22) results in the mass terms,

$$m_W^2 W_\mu^+ W^{-\mu} + \frac{1}{2} m_Z^2 Z_\mu Z^\mu + \frac{1}{2} m_A^2 A_\mu A^\mu, \tag{2.25}$$

where $m_W = \frac{1}{2} v g$, $m_Z = \frac{1}{2} v \sqrt{g^2 + g'^2}$, and $m_A = 0$. The two neutral gauge boson fields, W_μ^3 and B_μ, now mix according to the weak mixing angle, θ_W, to form two new fields,

$$A_\mu = \cos\theta_W B_\mu + \sin\theta_W W_\mu^3 \tag{2.26}$$

$$Z_\mu = -\sin\theta_W B_\mu + \cos\theta_W W_\mu^3, \tag{2.27}$$

where Z_μ corresponds to the Z boson field and A_μ corresponds to the photon field. Looking at the values for the mass terms, the $W^\pm$ and Z fields receive a mass while A is massless. The $W^\pm$ and Z fields obtain their masses by "eating" the ϕ_1, ϕ_2, and ϕ_4 fields, known as the Goldstone bosons, which give the gauge boson fields their longitudinal polarization, necessary for any massive field. At LO, the masses of the W and Z can be related by the weak mixing angle:

$$\frac{M_W}{M_Z} = \cos\theta_W, \tag{2.28}$$

where θ_w is defined by the ratio of the coupling constants g and g' such that

$$\frac{g'}{g} = \tan\theta_W. \tag{2.29}$$

The Higgs field, h, also has interactions with the W and Z gauge bosons after plugging into the first line of Eq. (2.22). The relevant terms look like

$$\frac{vg^2}{8} h W_\mu^+ W^{-\mu} + \frac{g^2}{4} h^2 W_\mu^+ W^{-\mu} + \frac{vg^2}{4\cos^2\theta_W} h Z_\mu Z^\mu + \frac{g^2}{8\cos^2\theta_W} h^2 Z_\mu Z^\mu, \tag{2.30}$$

which can be identified with the Feynman diagrams in Fig. 2.5.

The non-Abelian character of the EW theory introduces the $-g\mathbf{W}_\mu \times \mathbf{W}_\nu$ term in (2.11)

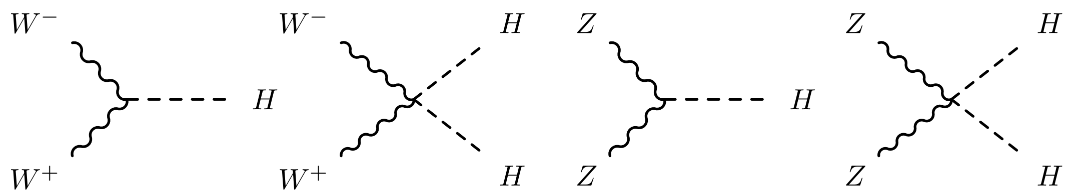

Figure 2.5: Feynman diagrams of the Higgs couplings with the W and Z gauge bosons.

which predicts self-interactions among the EW gauge bosons. In particular, the Lorentz contraction of the field strength in Eq. (2.10) introduces the term

$$-\frac{1}{4}g^2(\mathbf{W}_\mu \times \mathbf{W}_\nu)\cdot(\mathbf{W}^\mu \times \mathbf{W}^\nu), \tag{2.31}$$

which can be expanded to

$$\begin{aligned}
-\frac{1}{2}g^2\Big(&W_\mu^+W^{-\mu}W_\nu^+W^{-\nu} - W_\mu^+W^{+\mu}W_\nu^-W^{-\nu}\\
&+2W_\mu^+W^{-\mu}W_\nu^3W^{3\nu} - 2W_\mu^+W^{3\mu}W_\nu^-W^{3\nu}\Big).
\end{aligned} \tag{2.32}$$

Upon EWSB this becomes

$$\begin{aligned}
&-\frac{1}{2}g^2\Big(W_\mu^+W^{-\mu}W_\nu^+W^{-\nu} - W_\mu^+W^{+\mu}W_\nu^-W^{-\nu}\Big)\\
&-\sin^2\theta_W g^2\Big(W_\mu^+W^{-\mu}A_\nu A^\nu - W_\mu^+A^\mu W_\nu^-A^\nu\Big)\\
&-\cos^2\theta_W g^2\Big(W_\mu^+W^{-\mu}Z_\nu Z^\nu - W_\mu^+Z^\mu W_\nu^-Z^\nu\Big)\\
&-\sin\theta_W\cos\theta_W g^2\Big(W_\mu^+W^{-\mu}A_\nu Z^\nu + W_\mu^+W^{-\mu}Z_\nu A^\nu\\
&\qquad\qquad - W_\mu^+A^\mu W_\nu^-Z^\nu - W_\mu^+Z^\mu W_\nu^-A^\nu\Big),
\end{aligned} \tag{2.33}$$

where each successive term in parentheses can thus be identified as one of the quartic gauge coupling (QGC) interactions $WWWW$, $WW\gamma\gamma$, $WWZZ$, or $WWZ\gamma$ whose coupling strengths are given by the constants in front and whose Feynman diagrams are shown in Fig. 2.6. Neutral interactions that do not include the W, like $ZZ\gamma\gamma$ or $ZZZZ$, do not appear in the SM EW lagrangian.

While the fundamental parameters of the EW theory are connected to each other by

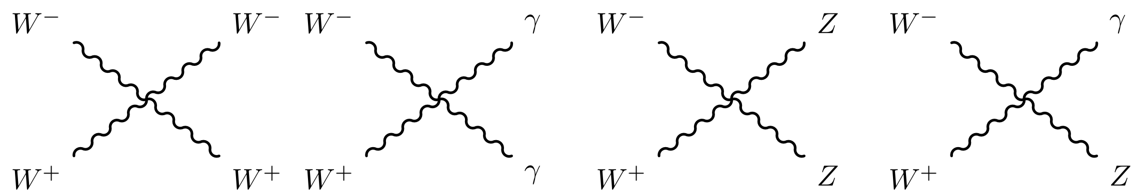

Figure 2.6: Feynman diagrams of EW QGC couplings

relations like those above, they are not all known *a priori* and so must be determined from experiment. Of primary interest to the topic of this thesis are the measured parameters related to the behavior and properties of the W, Z, and Higgs bosons. The W was first discovered in 1983 via $p\overline{p}$ collisions at the SPS by observing its decay to an electron and an electron neutrino [29]. Its mass has been measured to be 80.385 ± 0.015 GeV [1]. The W width, assuming a Breit-Wigner distribution, has also been measured, with an average value of 2.085 ± 0.042 GeV [1]. Roughly 1/3 of of the time the W decays approximately evenly into each of the three lepton generations (ignoring kinematics), as expected from lepton universality, indicated by the shared coupling of Eq. (2.20). The leptonic decays of the W result in a charged lepton with the same charge as the parent W (as dictated by charge conservation) and a neutrino (or anti-neutrino if the parent W has negative charge), as indicated in the top of Fig. 2.4. The W decays into quarks the remaining 2/3 of the time with a positively (negatively) charged W decaying into a up-type quark (anti-quark) and down-type anti-quark (quark), like in the bottom of Fig. 2.4. The measured branching fractions for the W are summarized in Table 2.3.

The Z boson was also discovered at the SPS shortly after the W [30]. It is one of the most important particles for measurements at the LHC as it has a unique decay signature into Same-Flavor Opposite-Sign (SFOS) pairs of fermions (for example, e^+e^-). It is measured to have a mass of 91.1876 ± 0.0021 GeV and a width of 2.4952 ± 0.0023 GeV. The measured branching fractions for the Z are summarized in Table 2.3.

The Higgs boson was discovered in 2012 at the LHC jointly by the ATLAS [31] and CMS [32] collaborations. Combined measurements of the mass between the two experiments show the current measured value of the Higgs mass to be $m_H = 125.09 \pm 0.21(\text{Stat.}) \pm$

Decay Mode		Branching Fraction [%]
W^+ (W^-)	$e^+\nu_e$ $(e^-\overline{\nu}_e)$	10.71 ± 0.16
	$\mu^+\nu_\mu$ $(\mu^-\overline{\nu}_\mu)$	10.63 ± 0.15
	$\tau^+\nu_\tau$ $(\tau^-\overline{\nu}_\tau)$	11.38 ± 0.21
	Quarks	67.41 ± 0.27
Z	e^+e^-	3.363 ± 0.004
	$\mu^+\mu^-$	3.366 ± 0.007
	$\tau^+\tau^-$	3.370 ± 0.008
	Invisible	20.00 ± 0.06
	Quarks	69.91 ± 0.06

Table 2.3: Measured branching fractions of the W and Z bosons as reported by the Particle Data Group [1]. Only the inclusive branching fraction of the W and Z decay to all quark generations is reported. The invisible branching fraction of the Z boson comes from the decay of the Z to neutrinos. The branching fractions sum to 100% separately for the W and Z bosons within their uncertainties.

0.11(Syst.) GeV [51]. Detailed studies of the spin [52, 53], width [54, 55], and couplings [56] are all consistent with the single Higgs boson of the SM. Precision measurements of the Higgs branching fraction have not been performed, though measurements of the Higgs in different decay channels are consistent with the branching fraction to WW being around 20%, as expected for a Higgs boson with the observed mass [1, 57].

2.2 WWW Production

In this thesis, we are interested in the inclusive production of three W bosons from proton-proton collisions: $pp \to W^+W^+W^- + X$ and $pp \to W^+W^-W^- + X$, where X is intended to refer to the fact that no requirements are placed on additional particles produced in the hard interaction. The Feynman diagrams from Fig. 2.6, Fig. 2.4, and Fig. 2.5, along with their associated lagrangian terms, can be used to construct the main contributions to the amplitude for this process. The relevant tree-level Feynman diagrams for this production process are shown in Fig. 2.7. This is sensitive both to the $WWWW$ coupling (non-resonant production) and to associated Higgs production[4] where the Higgs decays to two

[4]Associated Higgs production involves the radiation of a Higgs boson off another particle (in this case a W boson). It is sometimes referred to as "Higgsstrahlung", by analogy with electron Bremsstrahlung where an electron radiates a photon.

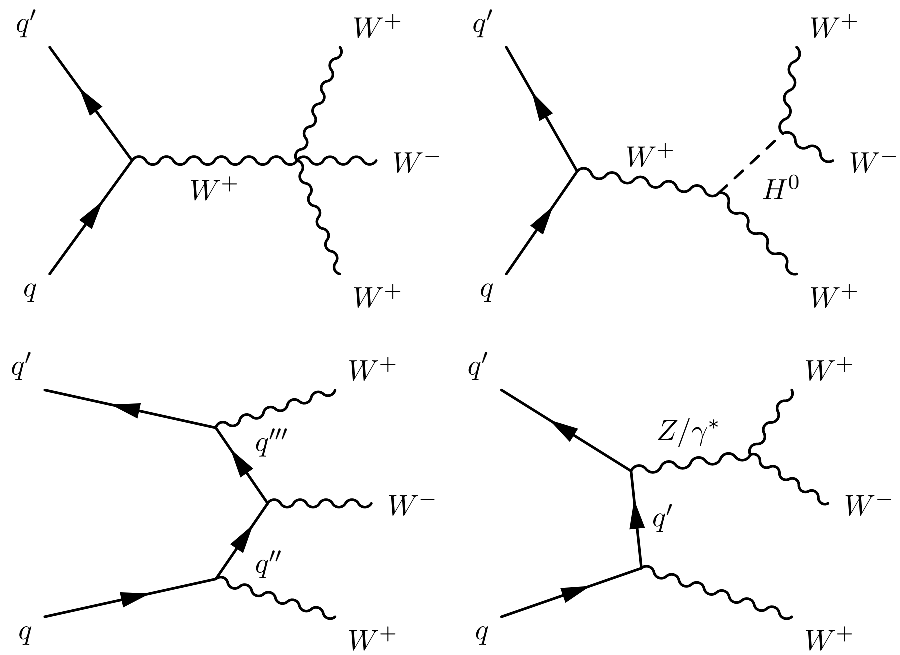

Figure 2.7: The tree level Feynman diagrams for WWW production. The incoming fermion lines in each diagram consist of an up-type quark (anti-quark) and down-type anti-quark (quark). In this case, the charge of the initial state quarks is assumed to sum to +1, leading to the same charge in the final state. It is also possible for the initial and final states to sum to -1 via charge conjugation.

W bosons (resonant production). The Higgs decay results in one W boson being produced off-shell, $H \rightarrow WW^*$, making this the leading contribution to off-shell production. The resonance from the Higgs can clearly be seen from the distribution of $m_{W^+W^-}$ taken from the simulation of WWW events in Fig. 2.8.

In principle, the LO partonic cross-section for the exclusive processes, $pp \rightarrow W^+W^+W^-$ and $pp \rightarrow W^+W^-W^-$, can be computed by constructing the amplitude from the tree-level Feynman diagrams in Fig. 2.7. The LO total cross-section could then be computed from this using Eq. (2.9), to account for the quarks originating from the incoming protons. This could then be continued to higher orders. In reality, however, it is much more complicated. Other effects like initial and final state photon radiation off of the incoming and outgoing fermions end up modifying the kinematic behavior and must be considered. At a hadron collider, QCD effects like initial and final state gluon radiation using the diagrams in

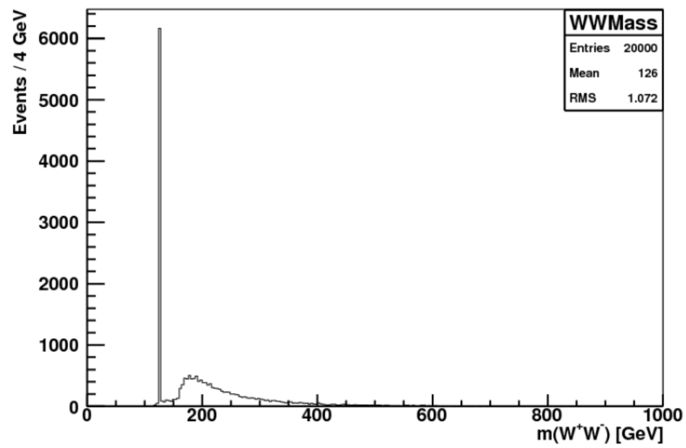

Figure 2.8: Invariant mass distribution of two opposite-sign W bosons in WWW events at truth level. The Higgs mass peak is clearly visible around 125 GeV.

Fig. 2.1 occur as well. The effects of asymptotic freedom and color confinement described in Sec. 2.1.1 lead to cascades of hadronization from the radiated gluons that are referred to as parton showers. This results in an abundance of residual jets and other hadronic activity occurring along with the original hard scattering process. This cannot be calculated by hand and is instead simulated using Monte Carlo (MC).

The inclusive cross-section for this process is computed at NLO in QCD, after accounting for initial and final state radiation, parton showering, and other effects, using the MadGraph generator. It finds an inclusive cross-section of

$$\sigma(pp \to WWW + X) = 241.47 \pm 0.13 \text{ fb}, \tag{2.34}$$

where the uncertainty is purely statistical. Additional uncertainties on the PDF and scale choices increase the uncertainty by only a few percent. The contribution from resonant production is computed separately and found to make up about 64% of the total inclusive cross-section. More details on the determination of the signal cross-section, uncertainties, and kinematics are presented in Sec. 5.1.2.1.

Due to the short lifetime of the W boson, each of the W bosons in the WWW process will decay before reaching the detector. This results in a measurable final state for the

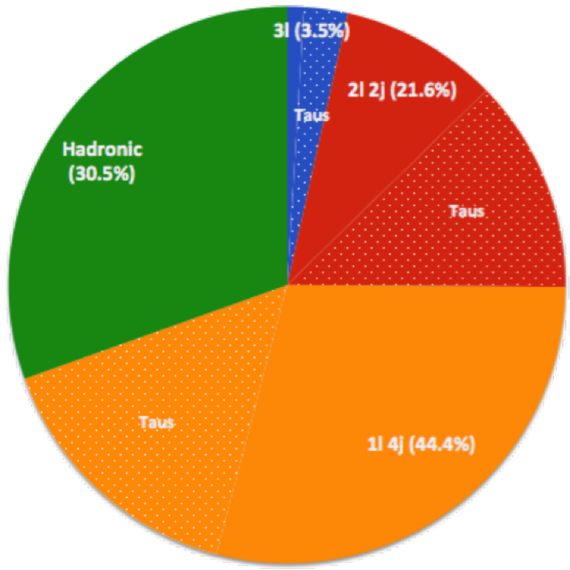

Figure 2.9: Pie chart showing the different decay modes contributing to the total cross-section for the WWW process. The dotted areas indicate the portion of each decay mode which is due to the production of tau leptons.

WWW production process that includes some combination of leptons and quarks (manifested as jets). The branching fractions for the WWW process can be determined from the individual W branching fractions listed in Table 2.3. The expected WWW branching fractions are summarized in the pie chart in Fig. 2.9. For this thesis, we are primarily interested in the final state where each W boson decays leptonically (the fully-leptonic final state) which has the smallest overall branching fraction at roughly 3.5%. In fact, since the τ leptons have a short lifetime, we choose to omit W decays to τ leptons from our fully-leptonic definition as well. This further reduces the fully-leptonic branching fraction to 0.97%. While small, this fully-leptonic final state should have smaller backgrounds than the other decay channels, making it one of the most sensitive channels for studying this process. The branching fraction when one W boson is allowed to decay hadronically is considerably larger, at 21.6% (or 9.2% when excluding decays to τ leptons). This is referred to as the "semi-leptonic" decay channel. The presence of the two leptons from the other two W decays still allows for background discrimination, though not as much as in the fully-leptonic channel. As a result, this channel has also been studied, though it is not the focus of this thesis. The remaining channels have not been studied. The combination of the fully-leptonic and semi-leptonic channels is presented in Chapter 6.

2.3 Effective Field Theory

The lagrangian of the SM, summarized by Eq. (2.1), (2.2), (2.10), and (2.22) has so far been very successful. But, as we continue to probe higher energy scales, there is reason to believe that the SM's luck will run out. If history is any guide, the SM is simply an approximation of a larger theory whose details are not relevant at current energies. Indeed, the SM leaves important questions unanswered (for example, a description of dark matter) that could be explained by the observation of some new high energy phenomena.

This idea of the SM as an approximate theory can be made explicit using an Effective Field Theory (EFT) [58] approach which includes new terms in the lagrangian, in addition to the SM. As a function of the energy, these terms start small but become increasingly important at higher and higher energies. In general, the new EFT terms might look like this:

$$\mathcal{L}_{\mathrm{EFT}} = \mathcal{L}_{\mathrm{SM}} + \sum_{n=5}^{\infty} \sum_{i} \frac{c_{n,i}}{\Lambda^{n-4}} \mathcal{O}_{n,i}, \tag{2.35}$$

where Λ is some new energy scale relevant to the new physics we seek to describe and the $c_{n,i}$ are dimensionless couplings. While the operators of the SM have mass dimension 4, the EFT operators, $\mathcal{O}_{n,i}$, have a mass dimension $n > 4$ which describe the new interactions between the SM fields at low energy due to the new physics model. The sum over i is simply to indicate that there are in general multiple possible new operators for a given mass dimension. These EFT operators come from "integrating out" the high energy interactions between the SM fields and the fields in the new physics model, leaving behind contact interactions between the SM fields and factors of Λ^{n-4} in the denominator. These factors of Λ suppress the new terms with respect to the SM, with the suppression becoming stronger as n grows. Thus, typically, only the first terms in the summation over n are important at low energy.

The list of possible gauge-invariant EFT operators to consider is long [59, 60, 61]. One way to shorten the list is to impose certain symmetries. Enforcing the conservation of baryon and lepton number restricts us to only even values of n:

$$\mathcal{L}_{\mathrm{EFT}} = \mathcal{L}_{\mathrm{SM}} + \sum_i \frac{c_{6,i}}{\Lambda^2}\mathcal{O}_{6,i} + \sum_j \frac{c_{8,j}}{\Lambda^4}\mathcal{O}_{8,j} + \ldots, \tag{2.36}$$

where we have truncated the series at $n = 8$ since these higher order terms are small. The leading $n = 6$ terms predict new anomalous triple gauge coupling (aTGC) and anomalous quartic gauge coupling (aQGC) interactions, while the sub-leading $n = 8$ terms predict only new aQGC interactions. Predictions of aTGC interactions have been studied in detail at LEP, the Tevatron, and the LHC, though none have been observed [1]. But there is still hope! It could be that new physics is suppressed in aTGC interactions but not in aQGC interactions[5]. Then the new physics might first appear at $n = 8$, where only aQGC interactions occur.

In a linear EFT model where the Higgs field is indeed the mechanism for EWSB, the possible $n = 8$ operators in Eq. (2.36) can be split into three categories: those containing covariant derivatives, as in Eq. (2.15), of the Higgs field, ϕ; those containing covariant derivatives of the Higgs field and the field strength tensors, as in Eq. (2.11) and (2.12); or those containing only field strength tensors [61, 62]. All of these operators preserve CP symmetry. In this thesis, we are interested only in the first category, which is limited to just two operators,

$$\mathcal{O}_{S,0} = \left[(D_\mu\phi)^\dagger D_\nu\phi\right] \times \left[(D^\mu\phi)^\dagger D^\nu\phi\right] \tag{2.37}$$

$$\mathcal{O}_{S,1} = \left[(D_\mu\phi)^\dagger D^\mu\phi\right] \times \left[(D_\nu\phi)^\dagger D^\nu\phi\right], \tag{2.38}$$

which could come from integrating out some new vector gauge boson resonance coupling

[5]For instance, the aTGC interactions could first appear at the one loop level while the aQGC interactions appear at tree level.

to the EW gauge bosons [63]. Plugging these into Eq. (2.36) and dropping all other terms besides the SM, we get

$$\begin{aligned}\mathcal{L}_{\mathrm{EFT}} = \mathcal{L}_{\mathrm{SM}} &+ \frac{f_{S,0}}{\Lambda^4}\Big[(D_\mu\phi)^\dagger D_\nu\phi\Big] \times \Big[(D^\mu\phi)^\dagger D^\nu\phi\Big] \\ &+ \frac{f_{S,1}}{\Lambda^4}\Big[(D_\mu\phi)^\dagger D^\mu\phi\Big] \times \Big[(D_\nu\phi)^\dagger D^\nu\phi\Big],\end{aligned} \tag{2.39}$$

where we have introduced the new arbitrary couplings $f_{S,0}$ and $f_{S,1}$[6]. Note that the subscript notation for these operators is different from the one used in Eq. (2.35) and Eq. (2.36). Expanding these new terms gives additional quartic interactions between the EW gauge bosons. If we just keep those with interactions between the charged EW gauge bosons we get the new interaction terms

$$\frac{1}{16}g^4v^4\Big(\frac{f_{S,0}}{\Lambda^4}\ W^+_\mu W^{+\mu} W^-_\nu W^{-\nu} + \frac{f_{S,1}}{\Lambda^4}\ W^+_\mu W^{-\mu} W^+_\nu W^{-\nu}\Big), \tag{2.41}$$

where $v = 246$ GeV is the Higgs vacuum expectation value [1]. These modify the couplings of the charged SM QGC interaction in Eq. (2.33) and Fig. 2.6 to obtain the new charged interaction term

$$\begin{aligned}\frac{g^2}{2}\Bigg[&\Big(1 + \frac{1}{8}g^2v^4\ \frac{f_{S,0}}{\Lambda^4}\Big)\ W^+_\mu W^{+\mu} W^-_\nu W^{-\nu} \\ &- \Big(1 - \frac{1}{8}g^2v^4\ \frac{f_{S,1}}{\Lambda^4}\Big)\ W^+_\mu W^{-\mu} W^+_\nu W^{-\nu}\Bigg].\end{aligned} \tag{2.42}$$

Such a modification enhances the predicted cross-section in Eq. (2.34). This is described in more detail later in Sec. 5.1.2.2.

In principle, the EFT is only valid below the energy scale, Λ, though we cannot know this scale directly as we are only able to probe them in the ratio with the couplings:

[6] An alternative set of couplings, α_4 and α_5, are sometimes also used which can be related to $f_{S,0}$ and $f_{S,1}$ via a simple linear transformation [63]. For the charged interaction vertex this is

$$\begin{aligned}\alpha_4 &= \frac{f_{S,0}}{\Lambda^4}\frac{v^4}{8} \\ \alpha_4 + 2\ \alpha_5 &= \frac{f_{S,1}}{\Lambda^4}\frac{v^4}{8},\end{aligned} \tag{2.40}$$

where $v = 246$ GeV is the Higgs vacuum expectation value [1].

$f_{S,0}/\Lambda^4$ and $f_{S,1}/\Lambda^4$. Above Λ the EFT breaks down and can lead to unitarity violation. In particular, for the operators with dimension $n = 8$, the strength of the couplings rises so rapidly with energy that unitarity violation can occur at energies well within the accessible range of the LHC. As is, this limits the applicability of the EFT framework. Currently, an effort to reconcile EFT with unitarity is ongoing in the theoretical community. One promising method is k-matrix unitarization, which introduces minimal model dependence, though it is only available for quasi-elastic $VV \to VV$ processes [64]. It is not currently understood how this applies to $V \to VVV$ processes relevant for aQGCs in the context of WWW production. Thus, if we are to employ a unitarized EFT framework an alternative method must be used.

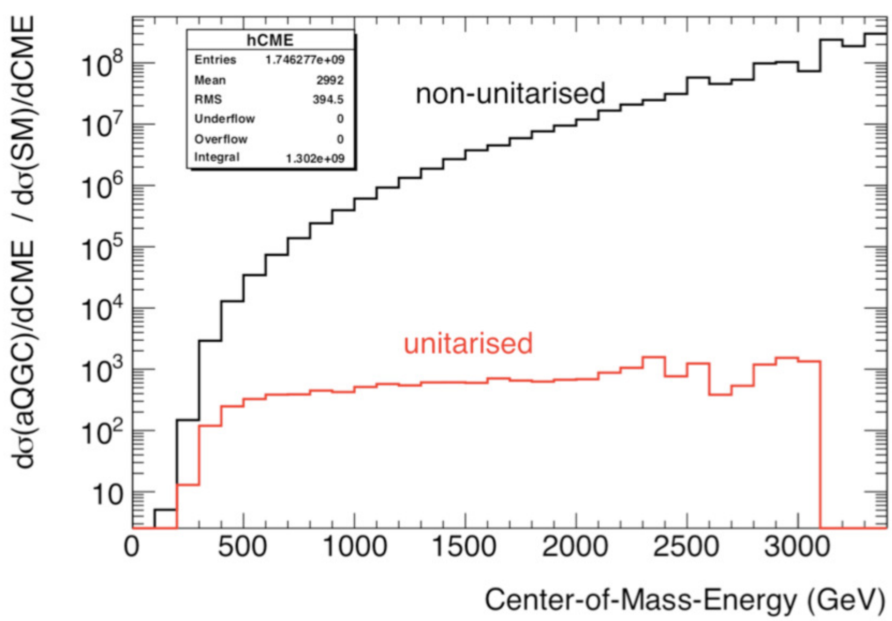

Figure 2.10: The unitarized and non-unitarized differential cross sections as a function of $\sqrt{s}$ for the EFT prediction with $f_{S,0}/\Lambda^4 = 6 \times 10^{-7}$ GeV^{-4} divided by the SM values. The form-factor function from Eq. (2.43) with $n = 1$ and $\Lambda_U = 180$ GeV is used for unitarization. The choice of parameters here serves merely as a demonstration.

In order to unitarize the EFT predictions we choose to apply an energy dependent form-factor to the aQGC parameters according to the approach from [62]. The form-factor, $f(s)$, looks like

$$f(s) = \frac{1}{\left(1 + \frac{s}{\Lambda_U^2}\right)^n}, \tag{2.43}$$

where s is the center-of-mass energy squared, n is an arbitrary exponent, and Λ_U is a new arbitrary energy scale. These two new arbitrary parameters, n and Λ_U, introduce a model dependence into the EFT. The effect of the form-factor is to reduce the differential cross-section as a function of the center of mass energy, which becomes more severe for increasing n and decreasing Λ_U. This can be seen as applied to one particular choice of aQGC and unitarization parameters in Fig. 2.10. The unitarization scheme has been employed recently by ATLAS in [65]. The choice of unitarization parameters and their impact on the aQGC cross-sections for the WWW process are discussed in more detail in Sec. 5.1.2.2.

2.4 Status of QGC Measurements and aQGC Limits

A variety of measurements sensitive to SM QGC interactions have been performed at colliders. In particular, measurements sensitive to $WW\gamma\gamma$ have been performed at LEP [66, 67], the Tevatron [68], and the LHC [65, 69, 70]; to $WWZ\gamma$ at LEP [71, 72, 73] and at the LHC [69]; to $ZZ\gamma\gamma$ at LEP [74, 67]; and to $WWWW$ at the LHC [75, 76]. No measurements, however, have been performed looking at the WWW production process directly.

Non-unitarized limits on the $f_{S,0}$ vs $f_{S,1}$ aQGC parameters have been performed by CMS in [77]. Limits on α_4 vs α_5, using the k-matrix unitarization scheme, have been performed by ATLAS in [75] and [78].

Chapter 3

Collider Physics and The Large Hadron Collider

The Large Hadron Collider (LHC) [79] is a 27 km circumference collider ring located at CERN approximately 100 m underground on the French-Swiss border near Geneva, Switzerland. Its primary goal is to collide protons at energies on the TeV scale, energies that are so large they can replicate conditions just moments after the big bang. The products of these collisions can be observed by several independent but complementary detectors placed at different points around the ring. Since the dynamics of the collisions are governed by quantum effects, the types of processes of interest cannot be produced on demand, but instead occur at random with some probability. The probabilities for these physics processes are typically very small and are thus quite rare[1]. Also, these physics processes do not last long enough to reach the detector and are instead observed indirectly through their decays. Since multiple physics processes can have the same decay signature, it is not possible to say with certainty that a given collision comes from a specific physics process. Instead, we must count the number of observed collisions for a given signature and compare this to the number expected from the quantum mechanical probabilities provided by cross-section calculations. If the observed number differs from the expected, then it could simply suggest that the theoretical expectation is not well understood. Or, it could suggest the presence of some new physics process beyond the SM. In order to make an adequate statement, we must be able to count enough collisions of the desired signature such that the statistical uncertainty is low (say 10 to 1000 depending on the signature

[1]ATLAS has been able to measure cross-sections as low as about 1 fb [75], which is roughly 14 orders of magnitude below the measured inclusive cross-section at the LHC [80].

and its backgrounds). This places a demand on the LHC to produce as many collisions as possible, even of these rare processes. To accomplish this, the LHC is designed to collide protons at a maximum frequency of 40 MHz, or 40 million times per second! More details about the LHC and collider physics in general are presented below.

3.1 Collider Physics

From the perspective of a particle physicist studying the products of particle collisions, we are interested in collisions produced at the highest possible energies, measured by the collision center-of-mass energy, and at the highest possible rates, measured by the luminosity. The center-of-mass energy, E_{CM}, is the collision energy in the rest frame of the collision. For head-on collisions with both beams at the same energy, E, like at the LHC, this is simply the sum of the energies, or $E_{CM} = 2E$. So, E_{CM} grows linearly as a function of the beam energy. This is in contrast with fixed target experiments where $E_{\mathrm{CM}} \propto \sqrt{E}$ and thus grows much more slowly. Frequently this is related to the Mandelstam variable, s, which is the squared magnitude of the Lorentz four-vectors of the incoming collision particles p_1 and p_2, such that $s = (p_1 + p_2)^2 = E_{\mathrm{CM}}^2$. The high beam energies required prefer a circular collider (as opposed to a linear collider) so that the particles may be repeatedly accelerated at each cycle using the same hardware. In order to accelerate the particles, they must be both stable (if they are to hang around long enough to collide) and charged (so that they may respond to electromagnetic steering and acceleration). This leaves just protons and electrons (and their anti-particles)[2]. To get the particles to very high energies, the particles are ultimately accelerated using electromagnetic waves in radio-frequency cavities. The beam is chopped up into “bunches” separated at regular intervals to synchronize with and “surf” the wave amplitude. The frequency of the radio-waves thus determines the bunch spacing. To bend the particles around the ring at high beam energies requires tremendously strong dipole magnets. Thus, the limiting factor for the energy is

[2]It is also possible to collide heavy ions, such as lead. In fact, the LHC does collide heavy ions when it is not colliding protons, though that is not the focus of this thesis.

ultimately the requirements on the dipole magnets, which must be superconducting and at the cutting-edge of current technology.

Upon acceleration, these particles emit synchrotron radiation. Too much synchrotron radiation and the beam could lose more energy than is practical. Electrons and positrons are fundamental particles and thus provide very clean collisions, but their small mass means that they suffer from high energy losses due to synchrotron radiation. This decides the overall radius and size of the collider ring, since a smaller ring means tighter turns and thus more acceleration[3]. Protons and anti-protons, with their larger mass, are much less affected by synchrotron radiation and thus can be accelerated to higher energies for a fixed radius circular collider. As a result, these are the particles used in modern high energy colliders, with proton-antiproton collisions at the Tevatron and Sp$\overline{\text{p}}$S, and proton-proton collisions at the LHC.

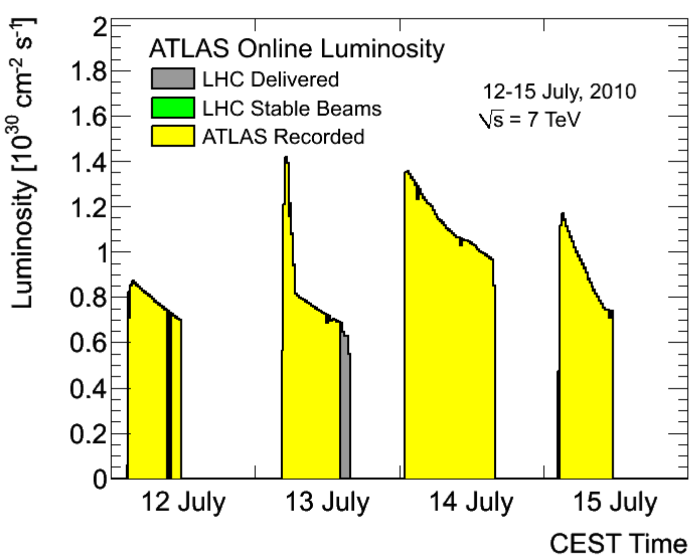

Figure 3.1: Instantaneous luminosity as a function of time as recorded by ATLAS for several runs in 2010.

The luminosity, L, can be thought of as the overall intensity of the beam. For a colliding

[3] In fact, the LHC uses the same tunnel (which was the same size) as the Large Electron-Positron (LEP) Collider and which operated from 1989 to 2000 but only up to energies of 209 GeV for the reasons described.

beam it may be simply defined as

$$L = f\frac{N_b^2}{4\pi\sigma^2}R, \tag{3.1}$$

where f is the collision frequency (related to the bunch spacing and thus in the MHz radio-frequency range), N_b is the number of particles in a bunch (usually 10-100 billion), R is a geometrical factor taking into account details like the crossing angle of the collision (on the order of unity), and σ is the transverse size of the bunch[4] (which is usually on the order of tens of microns). Thus, modern colliders typically have luminosities on the order of 10^{30} to 10^{34} cm^{-2}s^{-1} [1]. The transverse size of the beam is governed by the relativistic energy of the beam and is carefully tuned in the LHC using arrays of focusing magnets. The luminosity of the beam is not constant, but instead steadily decreases exponentially as a function of time, t:

$$L(t) = L_0 e^{-t/\tau_L}, \tag{3.2}$$

where L_0 is the initial luminosity and τ_L is the lifetime of the beam. The finite lifetime (on the order of hours) comes from gradual degradation of the beam quality, mainly due to the beam collisions themselves. As the beam reaches the end of its life (usually 1/4 to 1/2 of the peak luminosity), the beam is dumped and a new run is started. This process is repeated as many times as possible. An example of the instantaneous luminosity in ATLAS can be seen for several runs in 2010 in Fig. 3.1. The luminosity is then integrated over time as a measure of how many collisions were performed (and also how much data was collected). This can then be related to the cross-section for a given process, σ, to estimate how many events from that process, N, would have been produced on average:

$$N = \sigma \int L \; \mathrm{d}t. \tag{3.3}$$

While it is true that the we desire to increase the luminosity as much as possible, there

[4] Not to be confused with the cross-section in particle physics.

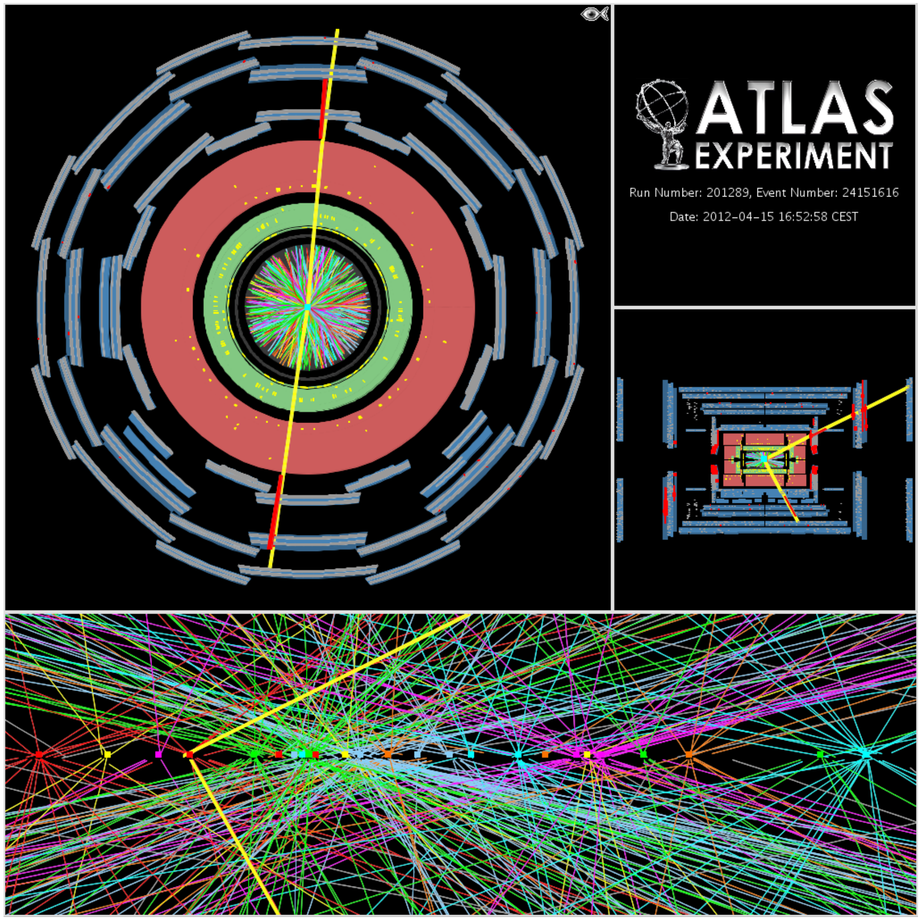

Figure 3.2: An event display of 20 pileup interactions in a single bunch crossing. The resulting tracks are shown, along with two high energy muons extrapolated back to a single primary vertex. The upper left shows a cross-section of the whole detector in the transverse plane, the upper right shows the detector viewed along the $r - z$ plane, and the bottom portion is zoomed in to the length of the bunch crossing. The average bunch crossing length at the LHC is around 10 cm [1].

is one important subtlety. Limitations on the size of the luminosity do not just come from the collider but also come from the detectors' ability to handle "pileup". Pileup is the phenomena of multiple collisions occurring during a single bunch crossing. Since we are trying to make statements about the physics of collisions, and not bunch crossings, we must be able to identify the individual collisions themselves. The typical length of a bunch is usually on the order of tens of centimeters while the number of pileup collisions per bunch crossing is on the order of ten or more. Furthermore, the collisions do not occur inside the detector. Instead, the decay products are measured a few centimeters away, where the detector volume starts. Thus, to distinguish individual collisions the detector must be able to extrapolate the tracks of the decay products back to the collision point with a resolution much less than a centimeter. This process is called vertexing and places strict requirements on the precision of the tracking systems for any detector built at a modern collider. An example of the vertexing challenges for a typical bunch crossing in ATLAS is shown in Fig. 3.2. Another issue of pileup is that each collision produces thousands of tracks which all contribute to the occupancy of the detector. If the occupancy is saturated, the detector may not be able to resolve individual tracks and would thus be useless. This is a serious concern for detectors at future colliders where problems of pileup will continue to grow.

3.2 The LHC Accelerator Complex

The LHC was designed to provide proton-proton collisions at an energy of 14 TeV (7 TeV per beam) and a peak luminosity of 10^{34} cm^{-2}s^{-1} with a 25 ns collision bunch spacing (40 MHz). Protons are collected from hydrogen gas by first stripping away the electron in an electric field[5]. The protons are injected into a series of lower energy accelerators before ultimately reaching the LHC to be accelerated to the full energy and begin collisions. The various stages of the LHC accelerator complex are shown in Fig. 3.3. The protons are accelerated initially using the LINAC2 linear accelerator. Next, the protons accelerate through the circular Proton Synchrotron Booster (PSB), Proton Synchrotron (PS), and Super Proton Synchrotron (SPS). Finally, they are split into two beams and injected into the LHC traveling in opposite directions. Once in the LHC ring they are accelerated to their full energy and then made to collide at four points along the ring where detectors are positioned to examine the products of the collisions. The two general purpose detectors,

[5]Anti-protons can be produced from the products of particle collisions with a fixed target and then trapping them using a process called stochastic cooling. This process is much slower than the process for collecting protons. While colliding both protons and antiprotons increases the cross-section for many physics processes, the high luminosity requirements on the LHC, coupled with the relatively short luminosity lifetime, make it challenging to do and still provide adequate integrated luminosity.

ATLAS [81] and CMS [82], are positioned at opposite sides of the ring. Meanwhile, the two specialized detectors, ALICE [83] and LHC-b [84], are situated at equal points along the ring nearest ATLAS. The total injection process takes about 4 minutes.

3.3 Data Collection

In 2010 and 2011 the LHC operated at a center-of-mass energy of 7 TeV, while in 2012 the LHC operated at a center-of-mass energy of 8 TeV[6]. The peak luminosity and peak pileup versus time during these runs are shown in the the top and bottom of Fig. 3.4, respectively. This thesis focuses on the 8 TeV data collected in 2012. This run had a bunch spacing of 50 ns, 1.6 to 1.7 $\times 10^{11}$ protons per bunch, a beam radius of 18.8 μm, and an average peak luminosity of 7.7×10^{33} cm^{-2}s^{-1} [85]. The luminosity lifetime, τ_L, corresponding to Eq. (3.2), ranged from 7 hours to 14 hours during a single run [86]. The total integrated luminosity in 2012 is shown on the left of Fig. 3.5. The overall delivered integrated luminosity from the LHC in 2012 was 23.3 fb^{-1}, while that recorded was 21.7 fb^{-1}. The amount of data recorded that is relevant for this thesis and described in Sec. 5 is slightly less at 20.3 fb^{-1}. The pileup conditions during 2012 were such that an average of 20.7 collisions occurred per bunch crossing. The distribution of the average interactions per crossing in 2011 and 2012 are shown on the right of Fig. 3.5. The increase in the average pileup in 2012 is due to the increased peak luminosity.

[6]This was reduced from the initial design energy of 14 TeV due to a quenching incident in the superconducting dipole magnets in 2008 when running at full energy.

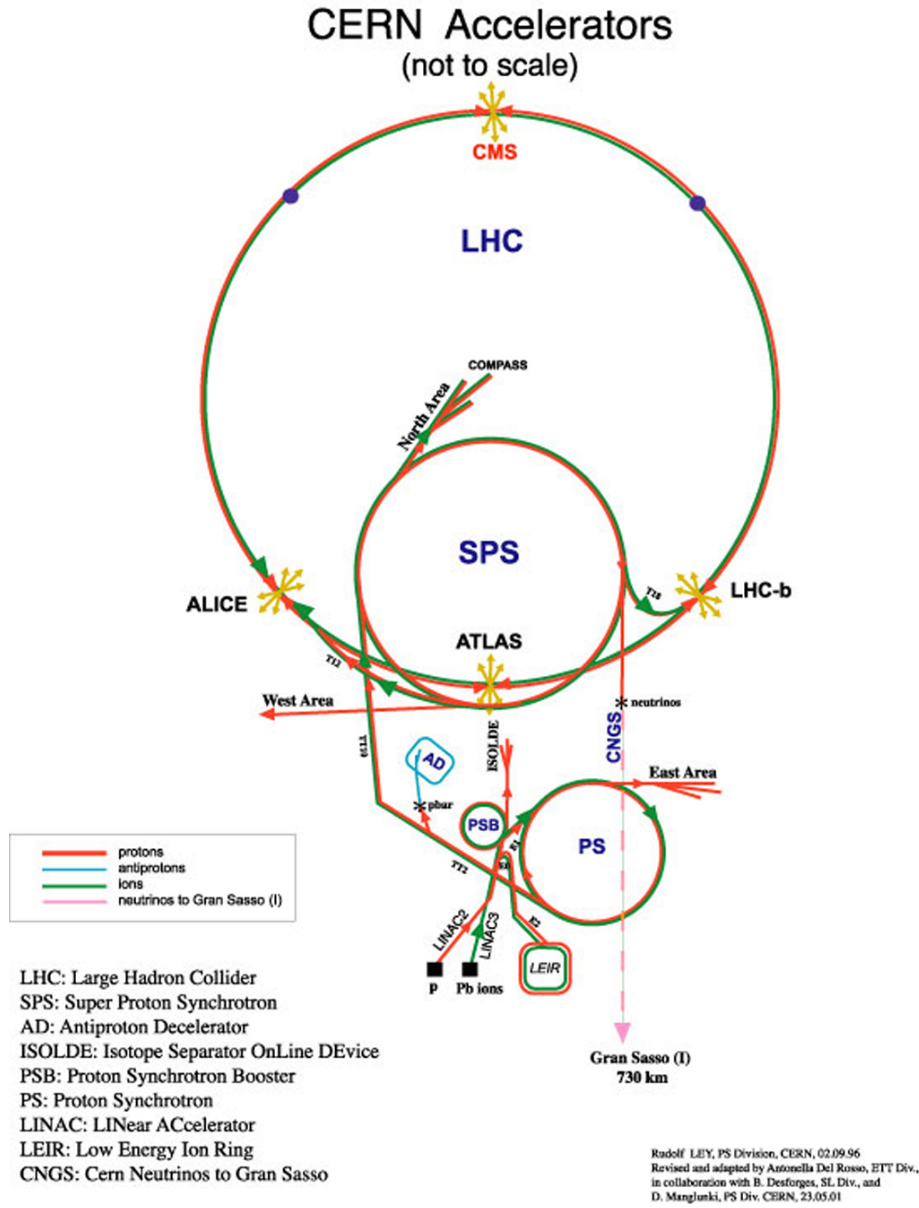

Figure 3.3: Diagram of the different accelerators in the CERN accelerator complex [9]. Those relevant for the LHC are the LINAC2, PSB, PS, SPS, and the LHC itself. The ATLAS detector is labeled at the bottom of the LHC ring.

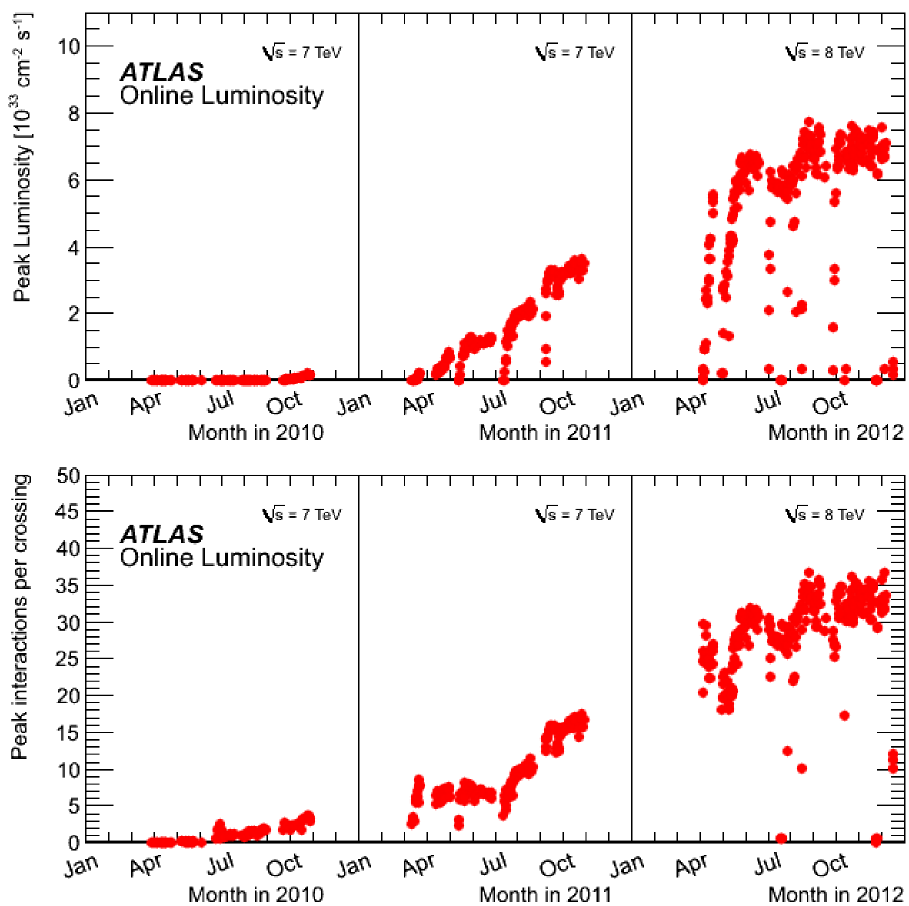

Figure 3.4: (Top) The peak luminosity from the LHC as a function of time for 2010, 2011, and 2012 data-taking periods and (Bottom) the peak number of pileup interactions as a function of time as recorded by ATLAS. The peak luminosity and pileup interactions have both increased since the LHC began operation in 2010. The gaps in recorded values are due to technical stops and long shutdowns for maintenance and upgrade work.

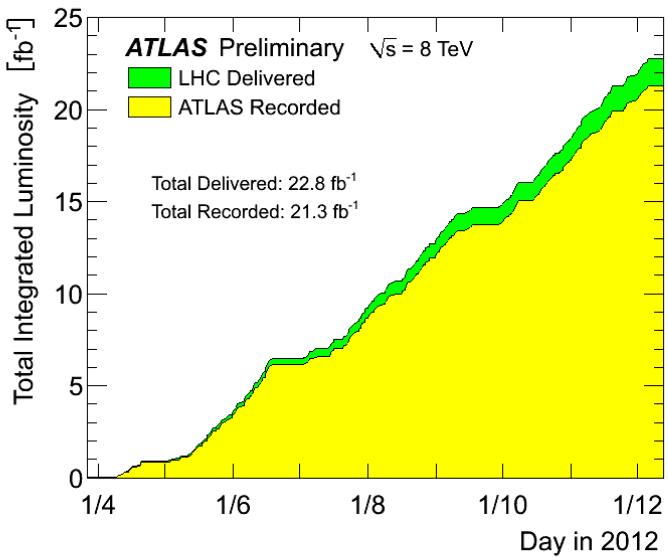

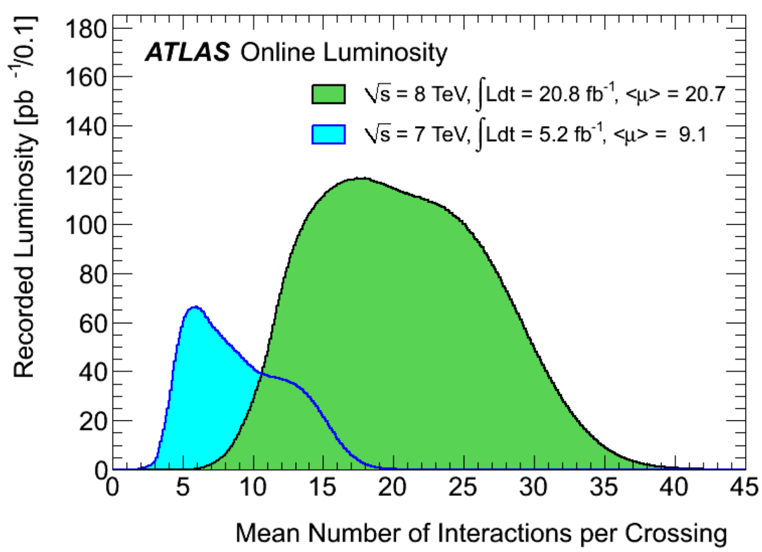

Figure 3.5: (Top) The integrated luminosity as a function of time in 2012. The amount delivered by the LHC is shown in green while the amount recorded by ATLAS is overlayed in yellow. More than 93 % of the integrated luminosity delivered by the LHC in 2012 was recorded by ATLAS. (Bottom) The distribution of pileup interactions, parameterized as the mean number of interactions per crossing, $<\mu>$, recorded by ATLAS in 2011 and 2012.

Chapter 4

The ATLAS Detector

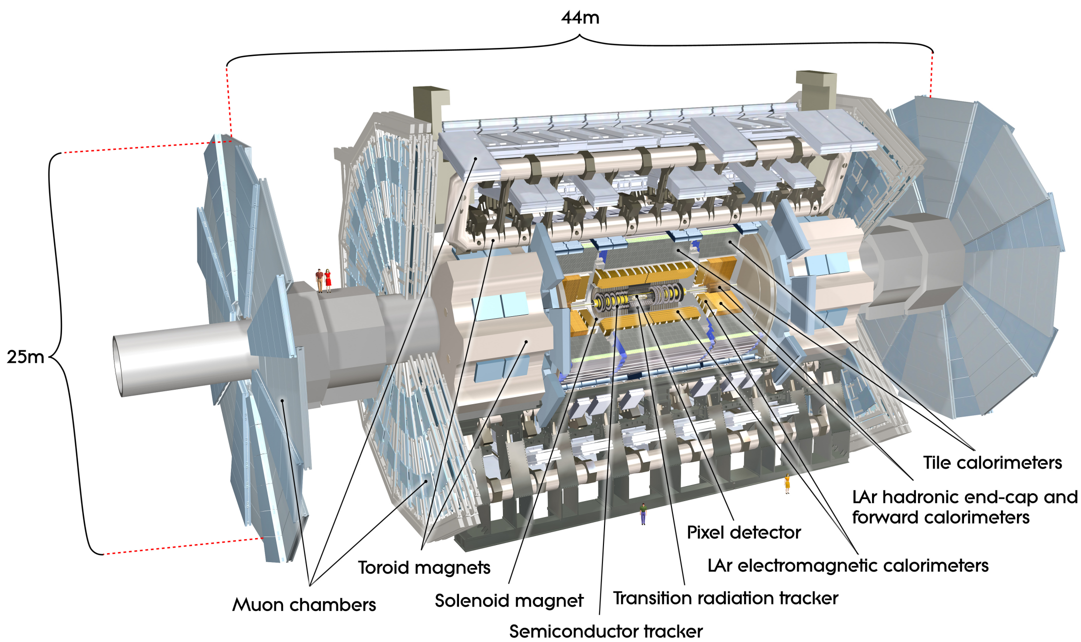

Figure 4.1: A diagram of the ATLAS detector where the detector has been artificially opened up to reveal the LHC beam line and the various sub-detector components within. The sub-detector components are labeled as such.

The ATLAS detector [81] is designed to measure the products of the particle collisions produced by the LHC. In particular, the detector seeks to measure those stable (or meta-stable) particles whose decay lifetime is sufficiently long enough to interact with the detector. This includes a variety of fundamental particles (like muons) as well as composite particles (like neutrons). The wide variety of particles to be measured requires the implementation of several sub-detector systems that work in tandem to identify and measure their properties. A cylindrical geometry for the detector is chosen which builds up around the beam line and surrounds the collision point so that most of the collision products will pass through it. A diagram of the ATLAS detector can be seen in Fig. 4.1. Its cylindrical shape is evident, with a diameter of 25 meters and length of 44 meters. The detector is massive, weighing in at roughly 7000 tonnes; but it is also highly granular, with over 100 million detection elements that are arranged very precisely, in many cases on the order of tens of microns. In the "opened" view of Fig. 4.1, the proton-proton collisions from the LHC occur at the core of the detector and the sub-detector components build up around this point.

The detectable products of the collision pass outward from the collision point through the different components where their energy and momentum are measured. The way in which the particles interact with the various sub-detector systems helps to identify the types of particles produced. This can be more clearly seen in the diagram of Fig. 4.2, which shows how the most typical products of the LHC collisions interact with the different components of the ATLAS detector. Nearest the collision point is the inner detector (ID), designed to measure the paths of charged particles passing through using several different subsystems. This is surrounded by a 2 Tesla solenoidal magnet. The field from the magnet bends the trajectory of charged particles in order to measure their momentum. Beyond that is the calorimeter system which measures the energy deposits of all particles passing through (except for neutrinos). The calorimeter system itself is divided up into components which fall into two main categories: the electromagnetic (ECAL) and hadronic calorimeter (HCAL) systems. The ECAL is situated in front of the HCAL and is designed primarily to absorb and measure the energy and position of electrons and photons. The HCAL is designed to do the same for composite particles like protons and neutrons. Surrounding the calorimeter system is the muon spectrometer (MS), which is the largest component of the ATLAS detector and the one that determines its size. It is designed to quickly identify and measure the trajectory of muons as they pass through and leave the detector using precision and triggering components. The MS is also composed of three large superconducting air-core toroid magnets which allow for a measurement of the muon momentum. The neutrinos pass through without interacting.

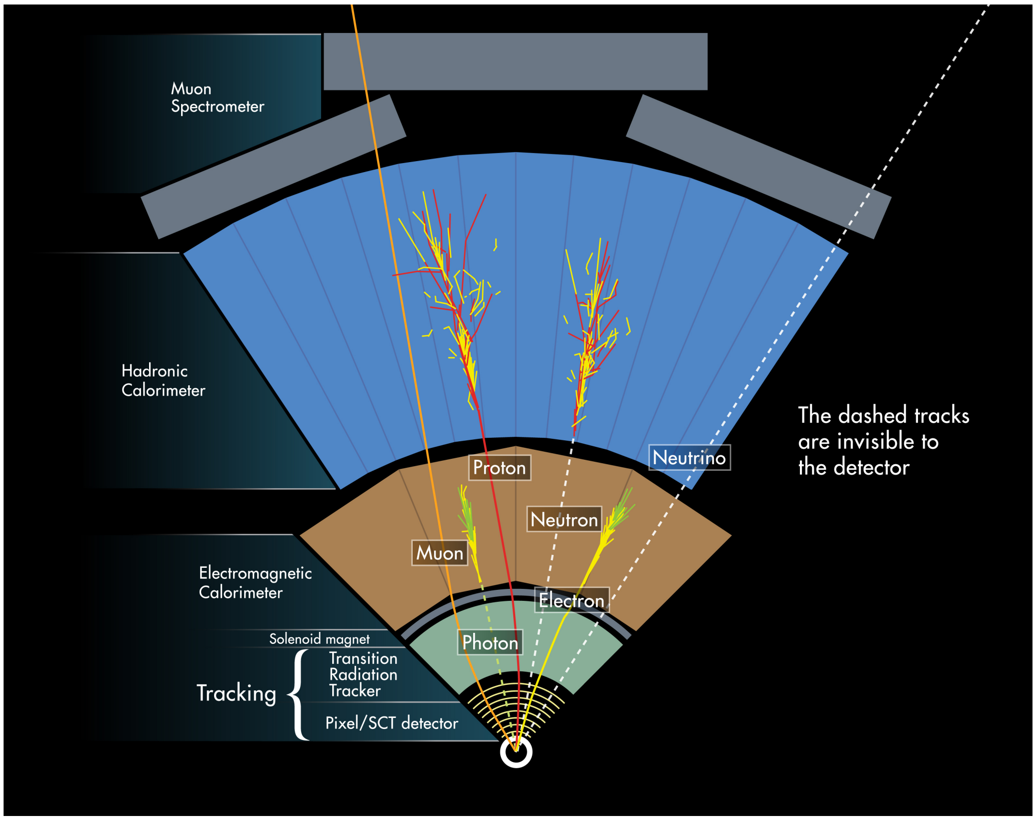

Figure 4.2: A diagram of one wedge of the ATLAS detector as viewed from looking down the LHC beam line. The sub-detector components are shown along with the particles that typically come from the collision. The paths of the particles are shown to indicate how each particle interacts with the detector.

The geometry of the ATLAS detector is defined using a right-handed cylindrical coordinate system with the x-axis pointing inwards towards the center of the LHC ring, the y-axis pointing up, and the z-axis pointing along the beam-line, sometimes referred to as the longitudinal or axial direction. The $x-y$ plane, which is perpendicular to the beam-line, is referred to as the transverse plane. In this plane, positions are defined using cylindrical coordinates with r being the distance from the beam-line and ϕ being the azimuthal angle.

The ATLAS detector has nearly uniform 2π coverage in ϕ[1]. For describing the direction of the particle with respect to the z-axis, a quantity called the rapidity, y, can be related to the particle energy, E, and longitudinal momentum, p_z, by

$$y = \frac{1}{2} \ln \left(\frac{E + p_z}{E - p_z} \right), \tag{4.1}$$

whose distribution is invariant under Lorentz boosts in the longitudinal direction. This is a useful characteristic as the longitudinal momentum of the partons within the proton are not known on an event-by-event basis, as discussed in Sec. 2.1.2. At the LHC, most stable particles are produced with energies much larger than their mass. In this limit, the rapidity can be simplified to a quantity called the pseudo-rapidity, η, where

$$\eta = -\ln \tan(\theta/2), \tag{4.2}$$

which is only a function of the polar angle, θ, the direction of the particle with respect to the positive z-axis. The distribution of rapidity for the inclusive cross-section at the LHC falls mostly within the ATLAS ID and MS detector volumes of $|\eta| < 2.5$ and $|\eta| < 2.7$, respectively, though the calorimeter system is extended out to $|\eta| < 4.9$ in order to ensure good coverage.

The transverse momentum of charged tracks can be determined by measuring how they bend in a magnetic field. The deviation of the trajectory from a straight line path is referred to as the sagitta, s[2]. The sagitta is proportional to the magnetic field strength and inversely proportional to the magnitude of the particle's momentum in the transverse plane, known as the transverse momentum or p_{T}. Thus, a straight-line trajectory resembles an infinite-momentum charged particle (or a neutral particle of any momentum), while a

[1] While the ID and calorimeter systems are designed to have minimal cracks in ϕ, the spatial extent of the MS makes this challenging due to service and support structures. Thus, there are (somtimes large) cracks in the ϕ coverage in the MS.

[2] Technically, the sagitta, s, is defined in terms of an arc as the distance from the center of the arc to the center of its base. It can be related to the radius of the arc, r, and half the length of the line connecting the two ends of the arc, l, by $s = r - \sqrt{r^2 - l^2}$.

bent trajectory corresponds to a charged particle with a finite momentum. As a result, the transverse momentum resolution, Δp_T, is related to the precision on the measurement of the sagitta, Δs by

$$\frac{\Delta p_T}{p_T} = \frac{\Delta s}{s}. \tag{4.3}$$

This has the effect that the relative uncertainty on the momentum measurement grows linearly as a function of the momentum.

The total momentum of the proton-proton collision in the transverse plane is nearly zero. Since the detector has nearly full azimuthal coverage in the transverse plane, we can test this constraint by measuring the total transverse momentum from the particles measured in the detector such that

$$\left| \sum_{i \in \text{All Particles}} \vec{p}_{\mathrm{T},i} \right| = 0, \tag{4.4}$$

where the transverse momentum is added vectorialy and then the magnitude is taken. After adding up the p_{T} of all of the particles to obtain the total transverse momentum, any imbalance with respect to this constraint is referred to as the missing transverse energy, $E_{\mathrm{T}}^{\mathrm{miss}}$, and is attributed to the neutrinos produced in the collision. There is no such constraint on the longitudinal momentum of the partons on an event-by-event basis as discussed in Sec. 2.1.2. This is the case even though the momentum of the protons along the z-direction is, in fact, known. Thus, there is no direct way of determining with certainty the momentum of the neutrinos in the z-direction.

4.1 Inner Detector

The inner detector (ID) is the detector system that is closest to the beam pipe and thus the first system that the products of the LHC collisions encounter on their way from the collision point. Its primary role is to measure the trajectory and momentum of charged particles via ionization as they pass through the detector. It must be capable of measuring these tracks

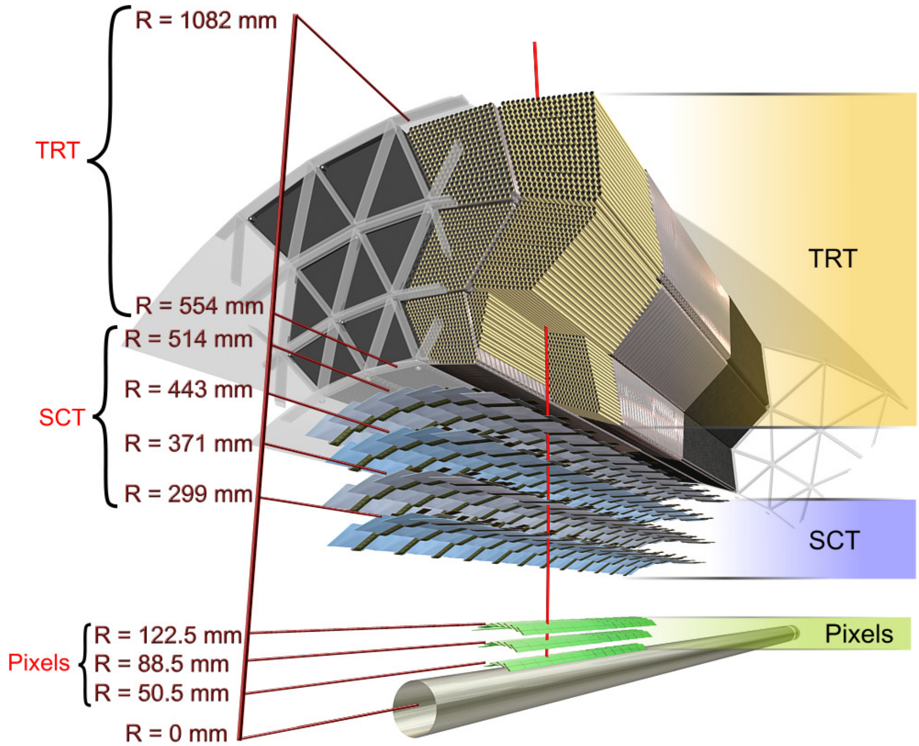

Figure 4.3: Diagram of the ATLAS Inner Detector (ID) showing a wedge of the barrel system. The three detector systems are clearly labeled. The LHC beam pipe is axial to the system and is shown at the bottom of the diagram.

with high precision in order to obtain precise momentum measurements. It must also be able to accurately extrapolate the tracks back to the collision point. This allows one to obtain primary and secondary interaction vertices with adequate resolution for overcoming pileup conditions (see Sec. 3.1). In addition, since the system is so close to the LHC beam line, it must be able to handle high particle fluxes. This requires that the ID must have a very high granularity and fast electronics readouts such that the occupancy of the detector is small enough to distinguish between individual tracks. The detector materials and electronics must also be sufficiently radiation hard that they can withstand years of LHC exposure time[3]. These tough requirements push the limits of available technology

[3]The layer of the pixel detector that is closest the beam line is subjected to so much radiation that it is expected to be replaced every three years. Meanwhile, the radiation exposure of the other ID components drops off rapidly (already by a factor of 6 for the third pixel layer and by over a factor of 200 for the outer TRT) and is expected to survive for the planned lifetime of the detector.

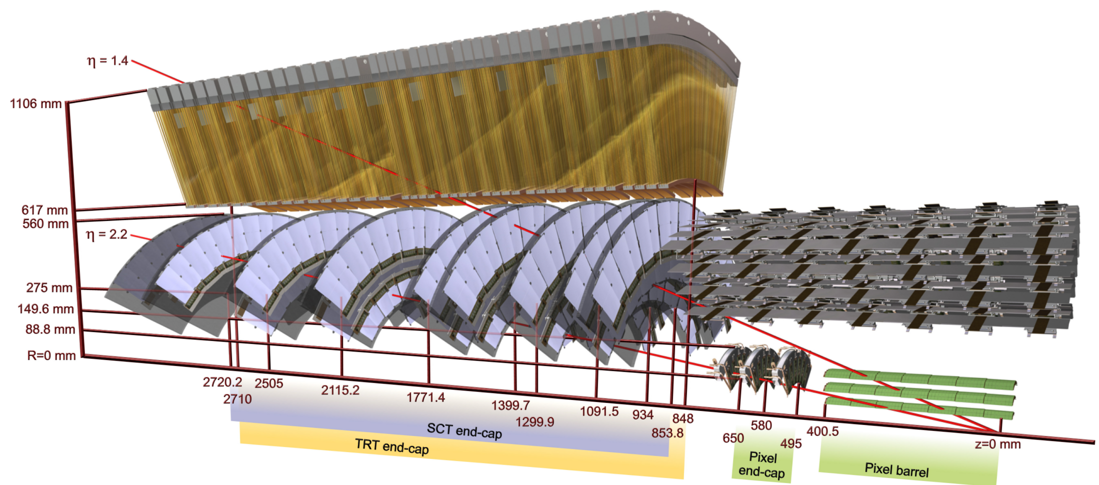

Figure 4.4: Diagram of the ATLAS Inner Detector (ID) showing a wedge of the end-cap system as well as a part of the SCT and Pixel barrel systems. The detector systems are clearly labeled. The LHC beam pipe is axial to the system but is not shown. Trajectories of two charged tracks with a $p_{\mathrm{T}} = 10$ GeV are shown along $\eta = 1.4$ and $\eta = 2.2$ as indicated by the solid bright red lines.

and thus make the ID the most sophisticated detector system in ATLAS.

There are three different detector subsystems within the ID, together immersed in a uniform 2 Tesla axial magnetic field: the pixel detector, the silicon microstrip tracker (SCT), and the transition radiation tracker (TRT). These three detector systems can be seen in the barrel in Fig. 4.3 and from an alternate view also showing one of the end-caps in Fig. 4.4. The pixel detector is composed of more than seventeen hundred thin doped silicon sensors with dimension 19 mm $\times$ 64 mm. Each sensor has more than forty-six thousand readout elements (with a nominal size of 50 μm $\times$ 400 μm), corresponding to the "pixels" which give the detector its name. A charged particle passing through an individual pixel produces a signal which identifies its location. The combination of several layers can thus be used to form the trajectory of the particle. Each sensor is attached to a single readout electronic board, which comprises one module. The modules are arranged into three cylindrical barrel layers (at $r = 51$ mm, 89 mm, and 120 mm) and two end-caps each with three disk-shaped layers (at $|z| = 500$ mm, 580 mm, and 650 mm) such that there is uniform azimuthal coverage. A cut-out diagram of the pixel detector structure with

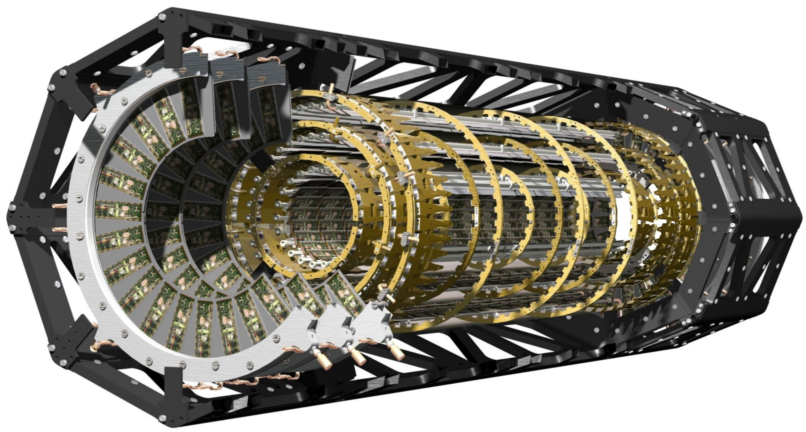

Figure 4.5: A cut-out diagram of the ATLAS pixel detector showing the arrangement of the pixel modules (green) in three layers of the barrel and three layers of one end-cap system. Some of the support structure is also shown.

modules in place in both the barrel and end-caps is shown in Fig. 4.5. The barrel covers roughly $|\eta| < 1.7$ and the two end-caps roughly $1.7 < |\eta| < 2.5$. The spatial resolution of the pixel detector is around 10 μm in the $R-\phi$ plane and 115 μm orthogonal to this plane [87].

The SCT uses almost sixteen thousand thin silicon strip sensors, though not of the same type as in the pixel detector. A barrel silicon strip sensor has dimension 6.36 cm $\times$ 6.40 cm with 768 readout strips running along the longer dimension. The barrel strips are placed in four concentric cylindrical layers, uniformly in azimuth (at r =300 mm, 370 mm, 440 mm, and 510 mm). They are aligned axially with a strip pitch of 80 μm, and covering roughly $|\eta| < 1.4$, as can be seen in Fig. 4.3. In each of the two end-caps the sensors are made to form nine disks spaced apart along the axial direction (at $|z|$ =0.85 m, 0.93 m, 1.1 m, 1.3 m, 1.4 m, 1.8 m, 2.1 m, 2.5 m, and 2.7 m) covering roughly $1.4 < |\eta| < 2.5$, as seen in Fig. 4.4. The strips are similar to those in the barrel except that they are tapered along the strip direction. The sensors are then oriented such that the taper expands radially outward with a strip pitch ranging from 60 μm to 90 μm as $|z|$ increases. The spatial resolution is about 17 μm in the $R - \phi$ plane [87]. Due to the length of the strips, the precision is considerably worse in the axial direction for the barrel and the radial direction for the end-caps, with a precision of roughly 580 μm.

The TRT uses a fundamentally different technology than the pixel and SCT. Drift tubes are used of 4 mm in diameter which are filled with a Xenon-based gas mixture and with an anode wire running through the center. The tubes can be placed in close proximity such that many measurements, around 36, can be made on a single charged track. An important feature of the TRT is its ability to identify electrons using transition radiation. The tubes are surrounded in polypropylene material which induce transition radiation from incident highly relativistic charged particles. The transition radiation photons are absorbed by the Xenon in the gas which amplifies the signal. The effect is strongest for electrons, which allows for excellent discrimination between electrons and other charged particles, like pions. The barrel TRT runs from roughly $|\eta| < 0.7$ and is constructed from 144 cm long straws aligned axially. Over fifty-two thousand straws are interleaved with polypropylene fibers to form 73 layers of straws spaced roughly 7 mm apart and surrounding the beam-pipe with a cylindrical symmetry and uniform coverage in azimuth, as seen in Fig. 4.3. In each of the two end-caps, two wheels are formed from over seventy-three thousand straw tubes, 37 cm in length, oriented and distributed uniformly in azimuth. The inner wheel is formed from twelve layers and the outer wheel from eight layers of straws spaced 8 mm and 15 mm apart, respectively, with 768 straws per layer, seen in Fig. 4.4. The end-caps cover roughly $0.7 < |\eta| < 2.2$. An individual straw has a precision of about 130 μm along its diameter [87].

4.2 Calorimeters

The ATLAS calorimeter is designed to measure the energy deposits of the products of the LHC collisions which pass through it except for the neutrinos. A diagram of the calorimeter system can be seen in Fig. 4.6. The calorimeter system is split into four main systems: the electromagnetic calorimeter (ECAL), the tile hadronic calorimeter (HCAL), the hadronic end-cap calorimeter (HEC), and the Forward Calorimeter (FCAL). Each

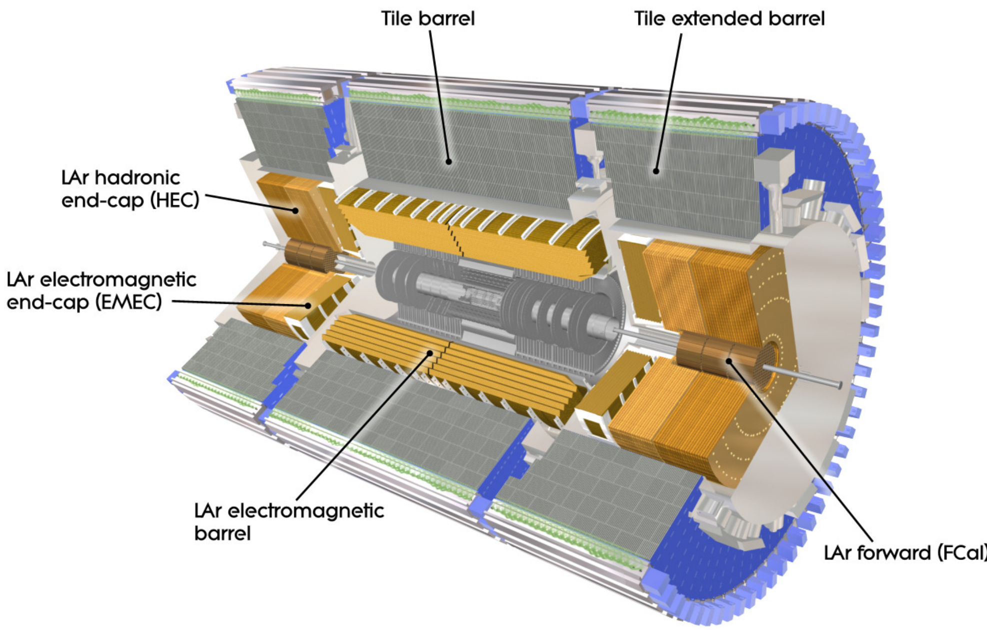

Figure 4.6: Diagram of ATLAS calorimeter system with cut-out portion to allow a view of the nested sub-components.

system is optimized to measure either electromagnetic or hadronic calorimeter deposits, though there is no way to make this exclusive; in general, electromagnetic and hadronic particles will interact with both. The amount of energy incident particles will lose due to electromagnetic interactions in a material can be quantified by measuring the material thickness in units of radiation length, X_0. Similarly, the amount of energy loss due to hadronic interactions can be quantified by measuring the material thickness in units of interaction length, λ. Those calorimeter systems optimized for measuring electromagnetic energy deposits generally have high radiation length and low interaction length. They are then placed in front of the calorimeter systems optimized for measuring hadronic energy deposits which have high interaction lengths, though the radiation length is usually also large.

The ECAL is a sampling calorimeter that uses lead as the sampling medium and liquid Argon (LAr) as the active medium from which the charge of the electromagnetic shower

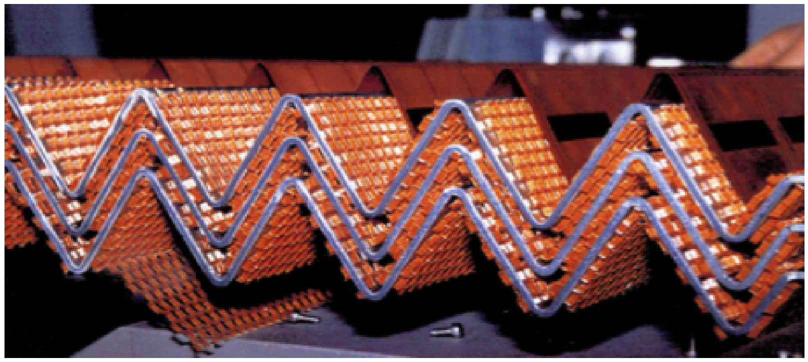

Figure 4.7: Photo of three ECAL sampling layers showing its accordion-like structure. In the picture, the horizontal directions corresponds to the radial direction when the detector is in position, which is the direction the LHC products would follow.

produced by incident particles on the sampling medium can be collected. LAr is used as the active medium because of its radiation hardness and its linear response. The lead sampling medium alternates with the active LAr medium using lead sheets 1 to 2 mm thick with an approximately 4 mm wide LAr gap between each sheet and electrodes placed in the middle of the gaps. The lead sheets are constructed using a unique "accordion"-like structure, as seen in Fig. 4.7. This is to provide a uniform resolution with no gaps in the azimuthal direction. The ECAL itself can be split up into a barrel region ranging from $0 < |\eta| < 1.3$ and two end-cap regions ranging from $1.5 < |\eta| < 3.2$. The thickness of the barrel region ranges from 22 X_0 to 30 X_0 for $|\eta| < 0.8$ and from 24 X_0 to 33 X_0 for $0.8 < |\eta| < 1.3$. The barrel region is divided into individual modules which together surround the beam-line in a cylindrical shape. A diagram of one such module can be seen in Fig. 4.8. From this one can see that each module is segmented in η and ϕ, as well as into three layers in depth. Segmentation is applied to obtain pointing information, which aids in the identification and measurement of electromagnetic objects in conjunction with measurements from the ID, and also shape information about the shower, which is useful for particle identification[4]. The very fine segmentation in η of the first layer in depth is important for precision tracking and shape measurements. The second layer has a larger

[4]For instance, the fine segmentation can be used to resolve the two separate showers separated by a small opening angle in $\pi^0 \to \gamma\gamma$ decay.

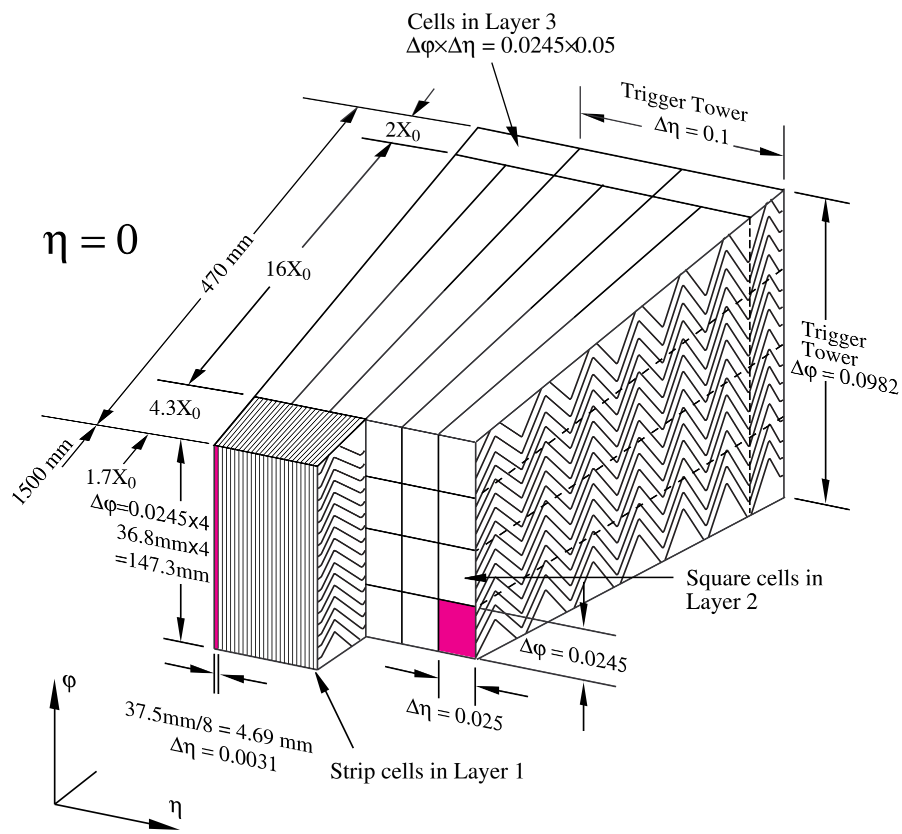

Figure 4.8: A diagram of one ECAL barrel module covering 22.5° in azimuth. When inside the detector, it is oriented as indicated by the axes.

depth and thus collects most of the energy. There are two identical end-cap regions, one on each side of the collision point. Each end-cap region consists of two wheels: the outer wheel from $1.4756 < |\eta| < 2.5$, with a thickness ranging from 24 X_0 to 38 X_0, and the inner wheel from $2.5 < |\eta| < 3.2$, with a thickness ranging from 26 X_0 to 36 X_0. The regions from $1.5 < |\eta| < 2.5$ in the inner and outer wheels both have three layers, with the first being a finely segmented precision layer similar to the barrel regions. Outside this region there are only two layers with a coarser segmentation. The ECAL also consists of a pre-sampler detector with a single layer of LAr in front of the full barrel ECAL and in front of the end-cap ECAL from $1.5 < |\eta| < 1.8$. This aids in the measurement of the energy deposits prior to reaching the ECAL and allows for a better understanding of the energy deposited in the transition region between the barrel and end-caps.

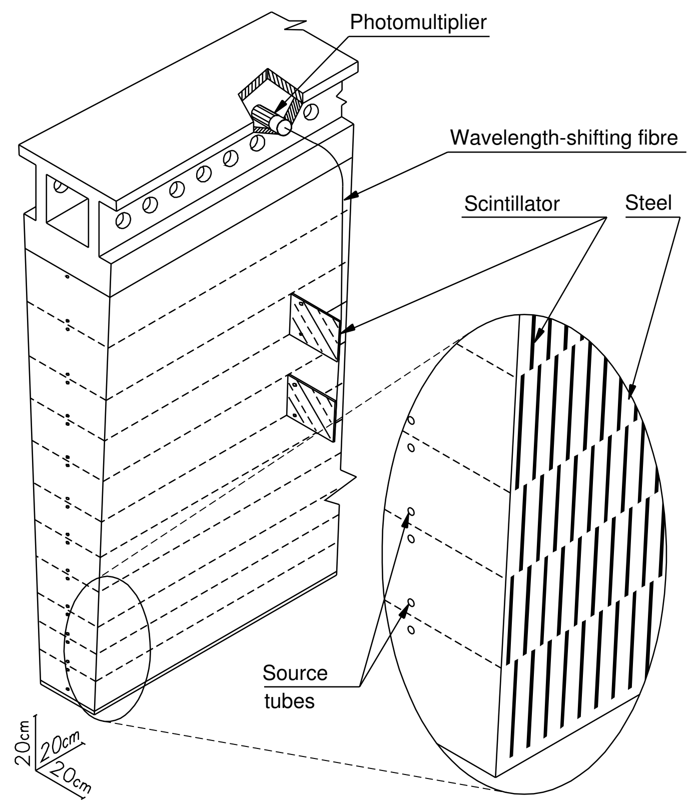

Figure 4.9: A diagram of one tile HCAL module covering 5.625° in azimuth. The radial direction when positioned in the detector corresponds to the vertical direction in the image.

The tile HCAL is a steel sampling calorimeter with scintillating tiles used as the active material. Steel is chosen as the sampling material since it gives a good depth in interaction lengths with a maximum depth of 7.4 λ, while also having a low cost. It is split into a central barrel and two extended barrels which together cover a region from $|\eta| < 1.7$, as can be seen in Fig. 4.6. As in the ECAL barrel, the tile HCAL is divided into individual modules that surround the collision point in azimuth. A diagram of one such module is shown in Fig. 4.9. The scintillating tiles alternate periodically with the self-supporting steel body and are oriented radially. The scintillation light is routed through wavelength-shifting fibers and collected at photo-multiplier tubes placed at the back of the module. This configuration allows for a near uniform coverage in azimuth. In the crack region from $1.2 < |\eta| < 1.6$ between the central barrel and extended barrels, special modules are placed

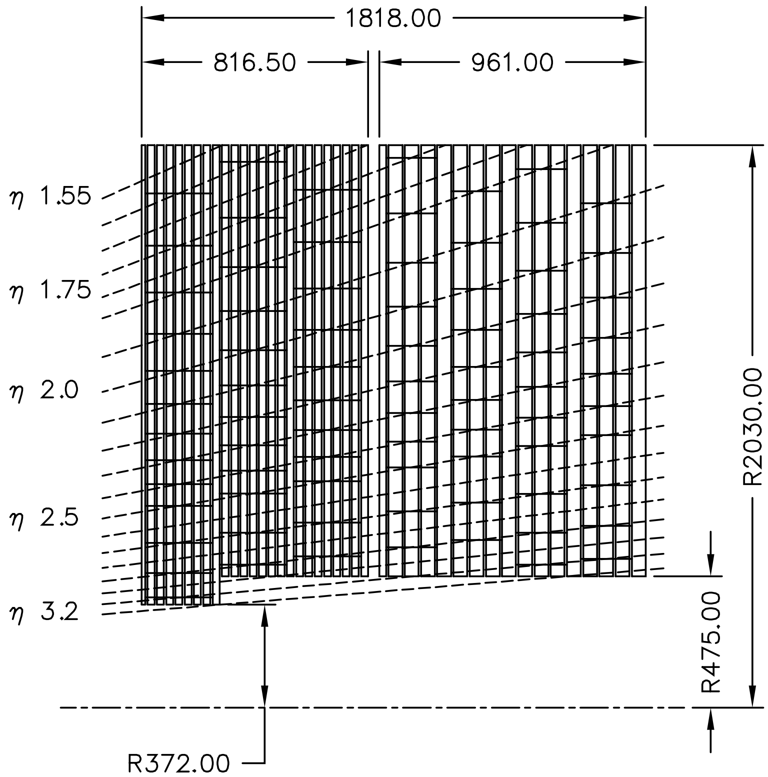

Figure 4.10: A schematic showing one quadrant of the HEC system in the R-z plane. The dashed lines indicate the pointing direction achieved by the segmentation of the readouts. Dimensions are in mm.

to recover and correct for energy losses in this region.

The HEC is designed to measure hadronic energy deposits in the end-cap regions from $1.5 < |\eta| < 3.2$. It uses copper plates as the sampling material with LAr gaps for the active material. Two separate wheels are formed from flat plates of copper alternating with LAr gaps further divided by electrodes for collecting the ionization charge from the hadronic shower in the LAr. The rear wheel is more coarse than the front wheel, as can be seen in the schematic of Fig. 4.10. The electronics readout is segmented such that pointing information can be obtained, as indicated by the dashed lines. The maximum radial depth of the HEC is roughly 10 λ.

The FCAL is in the region of the detector nearest to the beam-line, where the radiation flux is highest, covering the range from $3.1 < |\eta| < 4.9$. It is split into three cylindrical mod-

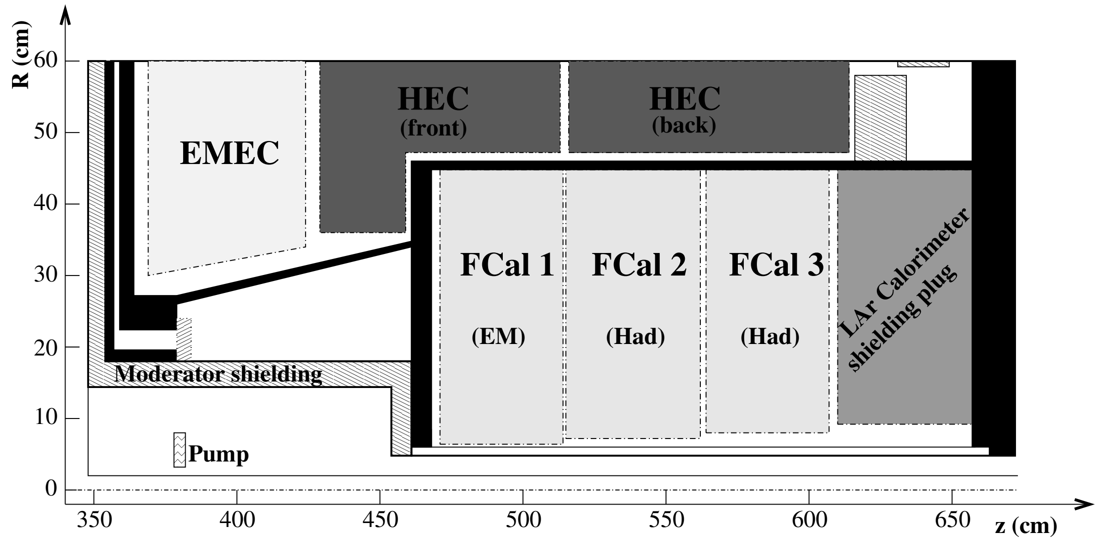

Figure 4.11: A schematic showing the end-cap of the ECAL, the two HEC modules, and the three FCAL modules, as well as additional shielding, in one quadrant of the ATLAS detector, as viewed in the R-z plane. The R-direction is shown with a larger scale than in the Z-direction.

ules, oriented as in Fig. 4.11, with the first being designed for measuring electromagnetic deposits and the other two for hadronic deposits. Each FCAL module is constructed from copper plates with roughly ten thousand uniformly spaced holes drilled in the direction parallel to the beam-line. The holes are filled with rods serving as the primary sampling material, with a thin LAr gap surrounding the rods serving as the active material. The first FCAL uses copper rods to optimize for electromagnetic deposits while the second and third FCAL modules use tungsten rods to optimize for hadronic deposits. The first FCAL has a radiation length of 27.6 X_0 and an interaction length of 2.66 λ. Meanwhile, the interaction length of the second and third modules is around 3.6 λ.

4.3 Muon Spectrometer

The Muon Spectrometer (MS) is the largest component of the ATLAS detector and the component that determines its overall size. It is designed to measure and identify muons as they pass through the MS and leave the detector. It surrounds the beam pipe, as

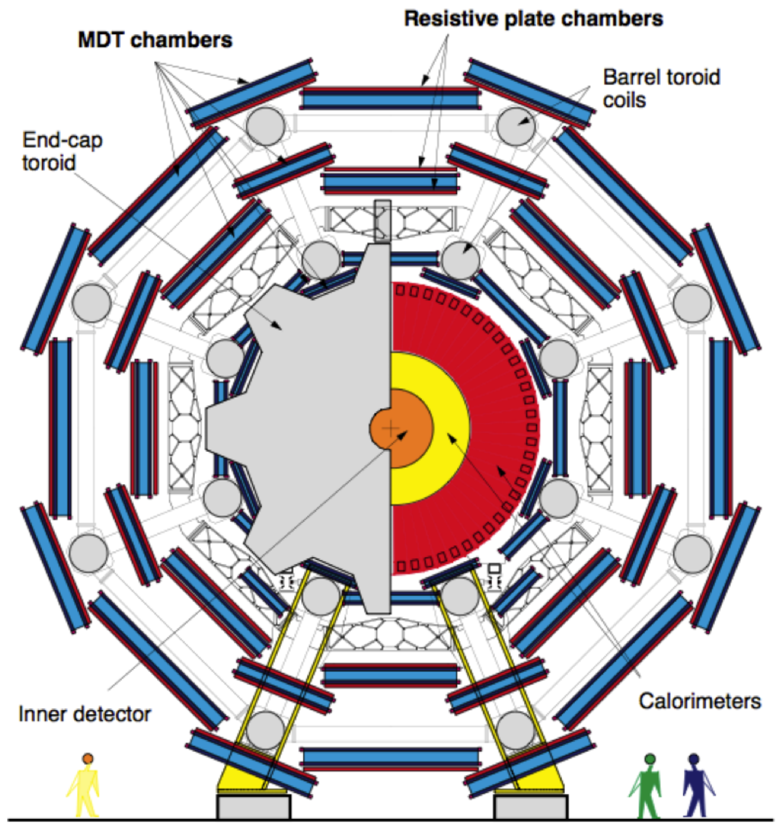

Figure 4.12: A cross-section of the MS in the transverse $(r - \phi)$ plane viewed from one end of the detector. The MDT chambers, RPCs, and barrel and end-cap toroids of the MS system are clearly labeled. The barrel toroid coils extend in to and out of the page while only half of the end-cap toroid is shown to reveal the ID and calorimeter systems. The LHC beam pipe runs through the center.

well as the ID and calorimeter systems, using a cylindrical geometry with a barrel and two end-caps. The MS is comprised of several different technologies: Muon Drift Tubes (MDT) and Cathode Strip Chambers (CSC) are used as precision tracking components for measurements of the muon trajectory, Resistive Plate Chambers (RPC) and Thin Gap Chambers (TGC) are used as triggering components with good timing resolution, and a toroidal magnet system is used for bending the muon trajectory in order to extract a momentum measurement. A diagram of the MS in the transverse plane is shown in Fig. 4.12 where the MDT chambers and RPCs of the barrel are clearly shown along with

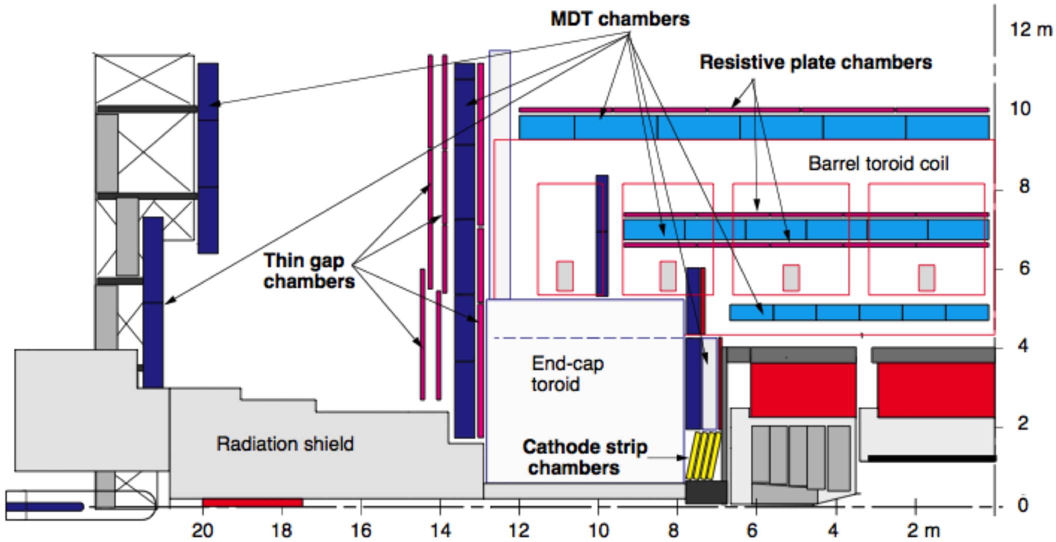

Figure 4.13: One quadrant of the MS as viewed in the $R - z$ plane. The MDT chambers, RPCs, TGCs, CSCs are clearly indicated, as are the the end-cap and barrel toroids. Support structures, shielding and the calorimeter and ID systems are also drawn. The LHC beam pipe runs from left to right along the bottom.

the barrel and end-cap toroids. Another view of the MS in Fig. 4.13 is displayed in one quadrant along the axial direction which shows the barrel and end-cap toroids, along with the MDT chambers in the barrel and end-cap, the RPCs in the barrel, and the CSCs and TGCs in the end-cap.

The MS magnet system is composed of several large air-core toroids built from superconducting coils which produce a magnetic field of roughly 0.5 Tesla in the barrel and 1 Tesla in the end-cap. The geometry of the MS magnet system is shown on the left of Fig. 4.14. In the barrel, eight 25 m long toroidal coils inside stainless-steel vacuum enclosures are placed uniformly in azimuth around the barrel. In the two end-caps, each end-cap toroid is composed of eight square coils (rotated with respect to the barrel toroids) separated by supporting wedges and then surrounded in a single cryostat. The resulting field is non-uniform as can be seen on the right of Fig. 4.14. The field strength in the transverse plane is roughly zero and so is referred to as the non-bending plane, while the η direction is referred to as the bending plane. To achieve adequate momentum resolution,

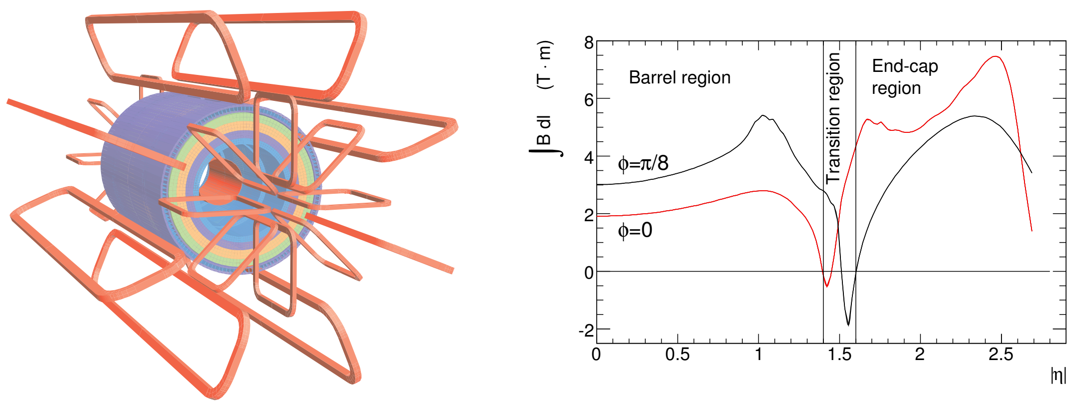

Figure 4.14: (Left) Diagram of MS toroid magnet geometry shown in red. The tile calorimeter is also shown. (Right) Predicted field strength of the MS magnet system as a function of $|\eta|$ for $\phi = 0$ in red and $\phi = \pi/8$ in black.

the resulting field must be known precisely. The field is measured in all directions using sensors placed throughout the MS and shown to usually agree with predictions within a few milli-Tesla. The field is especially non-uniform in the region from $1.3 < |\eta| < 1.65$, referred to as the transition region, where the bending power of the field actually becomes zero for certain values of η and ϕ. This results in degraded momentum resolution and poor trigger efficiencies in this region.

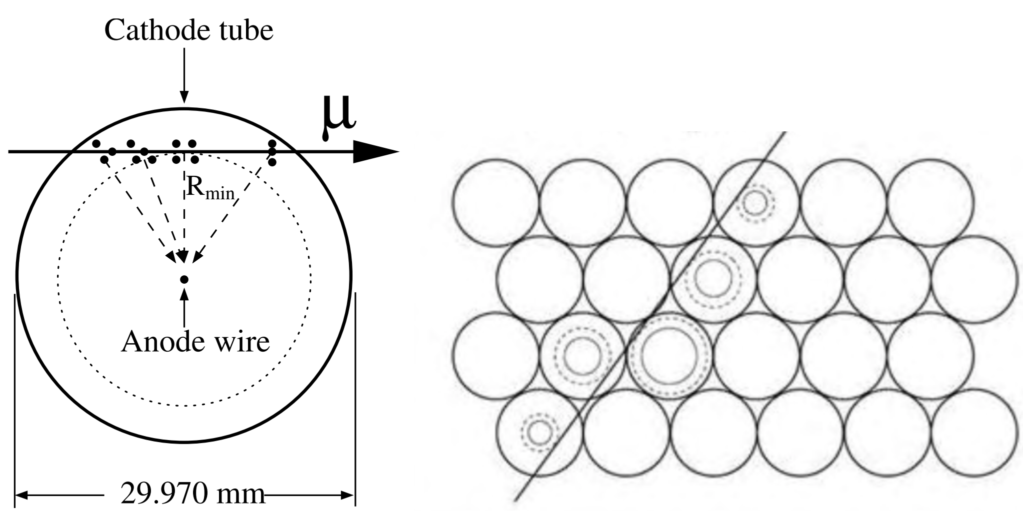

Figure 4.15: (Left) Cross-section of single MDT tube with muon track passing through. Ionized electrons (black dots) collect on the anode wire due to the applied electric field. (Right) Muon track reconstructed from array of MDT tubes.

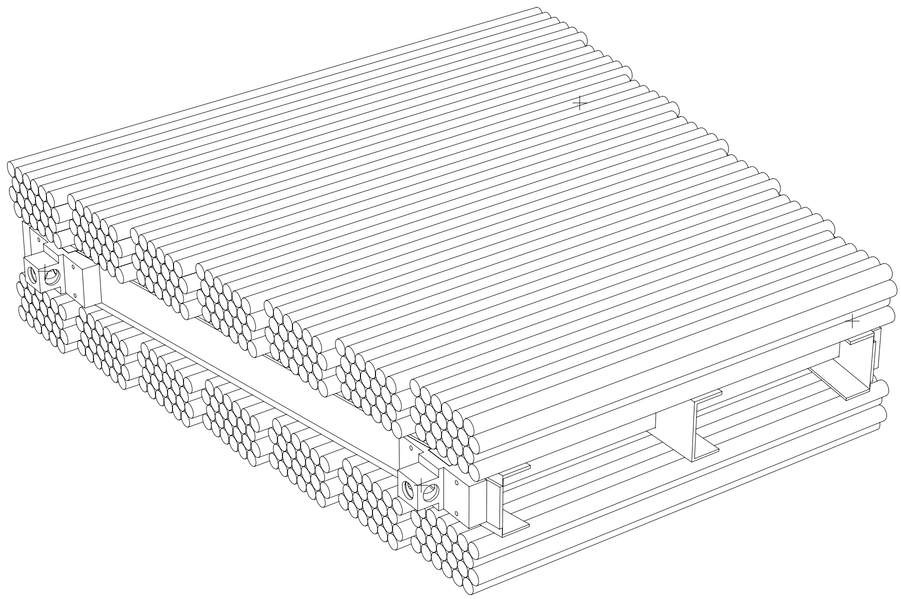

Figure 4.16: Schematic of a single MDT chamber.

The precision tracking system has stringent requirements on the precision of the muon trajectory measurement, which come from design goals on the resolution of the muon transverse momentum measurement to be about 10% at 1 TeV. Given the magnetic field strength in the MS, a muon with this momentum is expected to have a sagitta of about 500 μm in the bending plane. According to Eq. (4.3), this then translates into a precision requirement of no more than 50 μm on the sagitta. In order to achieve this, MDT chambers are used everywhere in the MS from $|\eta| < 2.7$ except in the inner layer of the end-cap from $2 < |\eta| < 2.7$ where the rates are too high. Here, CSCs are used instead. The MDT system is an arrangement of roughly 1000 MDT chambers composed of aluminum drift tubes roughly 30 mm in diameter and a couple meters in length filled with a gas mixture (Ar/CO2) and a high voltage wire (3000 V) running through the center. It was chosen as the main muon tracking system because of its precision, simplicity, and reliability. When a muon passes through an MDT it ionizes the gas and electrons are collected at the wire. The drift-time for the electron signal to collect on the wire can be used to determine the radial distance away from the wire at which the muon passed, like on the left of Fig. 4.15. The cylindrical symmetry of the tube is useful as the resolution is roughly flat, at around 80 μm in the bending plane, as a function of the angle of incidence of the muon hitting the tube. It is not possible, however, to determine the direction of the muon in the bending plane from just one tube. For that reason, tubes are arranged together in multi-layers of 3 to 8 tubes such that the trajectory can be reconstructed from matching the pattern of hits in multiple layers to form track segments, such as on the right of Fig. 4.15. A chamber is built from 2 multi-layers separated by a spacer ranging from 6 mm to 300 mm wide depending on the chamber, as in Fig. 4.16. The precision per chamber is roughly 35 μm. The long length of the MDTs means that they cannot provide a useful measurement in the non-bending plane. Chambers are arranged in three concentric shells in the barrel at r =5 m, 7.5 m, and 10 m as in Fig. 4.12 and in several rings in the end-cap at $|z|$ =7.4 m, 10.8 m, 14 m, and 21.5 m as in Fig. 4.13. In each shell or ring the chambers are made to overlap in order to avoid gaps in azimuth. Tracks are then reconstructed by interpolating between the track segments of the individual chambers. Still, there are gaps, in particular around $|\eta| = 0$ due to a hole for services and due to the feet holding up the detector, seen in Fig. 4.12. An optical alignment system is used to monitor the MDT chambers for deformations. The tension of the wires can also be adjusted to account for sag where needed. Despite having very good precision, the maximum drift time can be as high as 700 ns, which is far too slow for LHC bunch identification.

The CSC are used in the region of the MS closest to the interaction point where the crossing rate of tracks is greater than 150 Hz/cm^2, too high for successful operation of the MDT chambers. The CSCs can handle up to 1000 Hz/cm^2 while maintaining adequate precision in the bending plane. A CSC is a multi-wire proportional chamber composed of planes of cathode strips sandwiching a row of parallel anode wires and filled with a non-circulating gas (Ar/CO2) in the gap. The two planes of cathode strips are separated by 5mm with the anode wires running directly between the two planes. A signal is induced on the cathode strips due to an avalanche of electrons from the ionizing muon collecting on

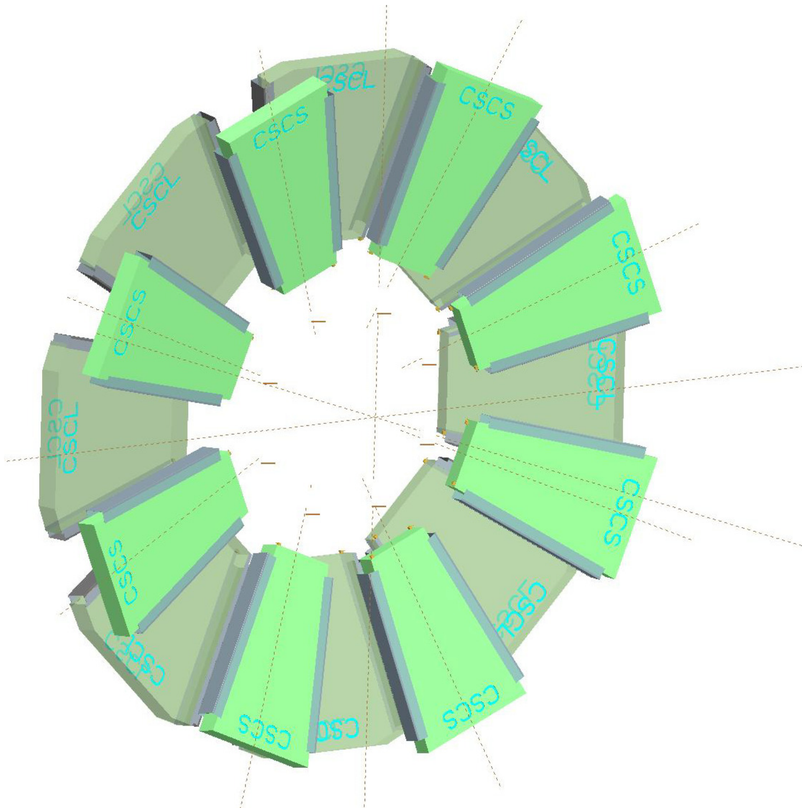

Figure 4.17: Diagram showing the arrangement of the CSCs in the end-cap.

the anode wire. The two planes of cathode strips are segmented in orthogonal directions providing measurements in both the bending and non-bending planes of the detector. A CSC is composed of four of these layers, each giving separate η and ϕ measurements. The resolution in the bending plane is roughly 60 μm while the coarser segmentation in the non-bending plane results in a resolution of roughly 5 mm. Two rings are formed from the chambers such that the anode wires point radially and there are no gaps in ϕ, as can be seen in Fig. 4.17. The rings are positioned at roughly $|z| = 7.5$ m. The rectangular symmetry of the individual channels results in a degradation of the resolution based on the angle of incidence. This is resolved by titling the chambers slightly toward the interaction point. The signal pulse height can be used to match the tracks if multiple tracks are present in a CSC in a given event. This is useful in the high occupancy environment near the beam-line. The small separation between cathode strips results in a short electron drift time allowing

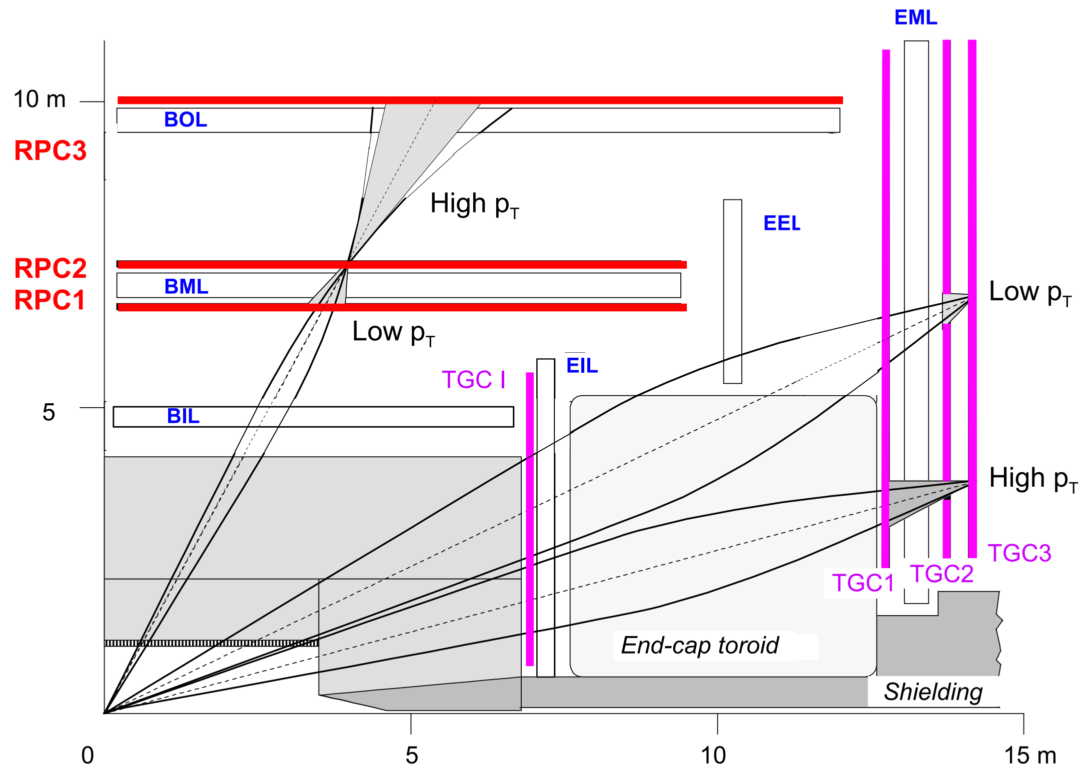

Figure 4.18: Layout of the trigger components for one quadrant in the $r - z$ plane. RPC and TGC chambers are clearly labeled. Possible muon trajectories are seen for low and high p_{T} roads formed by the trigger algorithm (see Sec. 4.4).

for a good timing resolution of about 7 ns per layer.

The triggering system in the MS is designed to be able to identify muons coming from individual bunch crossings of the LHC and to discriminate them based on their position and p_{T} in the region $|\eta| < 2.4$. This information is then used to trigger on high p_{T} muons, as described in Sec. 4.4. The individual bunch crossings of the LHC are designed to be separated by only 25 ns, as described in Chapter 3. Thus, the system must be able to resolve individual tracks with a time resolution of this size. To distinguish high p_{T} muons from straight-track neutral particles or from curved-track low-momentum charged particles, the system must be able to measure the sagitta of the trajectory in the toroidal magnetic field, though not necessarily with the same precision as in the precision tracking system. Furthermore, to distinguish individual tracks, position measurements must be performed in both the bending and non-bending planes. The measurement in the non-bending plane is also used to complement the measurements of the bending plane from the MDT chambers. RPCs are used in the barrel region from $|\eta| < 1.05$ and TGCs in the end-cap from $1.05 < |\eta| < 2.4$. The layout of the MC triggering system can be seen in the diagram in Fig. 4.18. The RPCs are parallel electrode-plate detectors which use no wires. A single RPC layer consists of resistive plates aligned in parallel and separated by 2 mm with a gas mixture (primarily $C_2H_2F_4$) in the gap. An electric field of 4.9 kV/mm is applied between the plates which results in electron avalanches forming in the gas along the track. This gives a signal pulse time resolution of about 5 ns. The pitch of the individual plates is 23 mm in η and 35 mm in ϕ. A single RPC consists of two such layers. Three concentric shells are formed from the RPCs around the beam line at about $r = 6.5$ m, 7.5 m, and 10 m as in Fig. 4.18. The separation between the inner and outer layers allows for a discrimination of muons with $9 < p_{\mathrm{T}} < 35$ GeV while the separation between the inner and middle layers allows for discrimination of low-p_{T} muons with $6 < p_{\mathrm{T}} < 9$ GeV.

The TGCs are multi-wire proportional chambers, similar to the CSCs. In a single TGC layer, the cathodes are separated by 2.8 mm and the wire-to-wire pitch is 1.8 mm. A high voltage of 2900 V is applied to the anode wires resulting in a quasi-saturated electron avalanche in the gas mixture (CO2/n-pentane) due to incident tracks. The small wire-to-wire pitch and high voltage result in a good timing resolution for the signal pulse. The resulting signal pulse resolution is dependent on the angle-of-incidence of the incoming track, but still results in a signal width within 25 ns for about 99% of tracks. TGC chambers are built from either two or three layers. The TGC chambers are then arranged in rings such that they overlap in azimuth to eliminate gaps. The TGC rings are arranged as in Fig. 4.18 with a ring of two-layer TGCs placed in front of the end-cap MDT inner layer at about $|z| = 7$ m, a ring of three-layer TGCs placed in front of the end-cap MDT middle layer at around $|z| = 13$m, and two rings of two-layer TGCs placed just behind the end-cap MDT middle layer at around $|z| = 14$ m.

4.4 Trigger

The very small design bunch spacing of 25 ns (40.08 MHz) at the LHC, combined with the average raw digitized event size of around 1 Megabyte, means that to record every collision would require a bandwidth of around 40 Terabytes per second, far surpassing the capabilities of modern hard-disks. Thus, recording every collision is clearly untenable. Fortunately, the type of collisions of interest at the LHC (high p_{T} leptons and jets, high $E_{\mathrm{T}}^{\mathrm{miss}}$) are sufficiently rare that most collisions can be filtered out before recording. This is accomplished by using a so-called "triggering" system, that quickly analyzes coarse information about the collision and only records those collisions deemed to be of interest. The trigger is implemented in stages. The 40.08 MHz collisions are first passed to a custom electronics Level-1 (L1) trigger, designed to reduce the rate to below 75 kHz; it is then passed to the relatively simple software-based selection in the Level-2 (L2) trigger, designed to reduce the rate to no more than 3.5 kHz; finally, it is passed to the third stage, called the Event Filter (EF), which uses a more complex software-based selection similar to the offline selection, reducing the rate to below 200 Hz. The L2 and EF triggers are referred to together as the High-Level Trigger (HLT). This results in a much more reasonable bandwidth for writing the data of about 0.2 Gigabytes per second. To achieve these goals requires careful design and also (sometimes difficult) choices about what types of collisions to keep. This is discussed in more detail below.

The L1 trigger system is designed to use reduced granularity information from the calorimeter and muon systems with custom electronics to make on-the-fly decisions about interesting physics objects. The inner detector is not used at L1. Information about muons is taken from the muon track measurements of the RPC and TGC components of the MS as described in Sec. 4.3. This information is used to build coarse trajectories called roads. The width of the road is used to make one of a few possible p_{T} cuts on the trajectory in the range of roughly $6 < p_{\mathrm{T}} < 35$ GeV. Meanwhile, information from the calorimeters is limited to coarse trigger "towers" mostly of dimension 0.1×0.1 in $\Delta\eta \times \Delta\phi$. Look-up-tables are used to quickly identify the transverse energy from the road. This is then summed using several sliding window algorithms to identify high p_{T} electrons and photons, hadronically decaying taus, jets, large $E_{\mathrm{T}}^{\mathrm{miss}}$, or large E_{T}. In both the L1 muon and calorimeter triggers, special care is taken to account for object multiplicities and to not double count physics objects. One important challenge is that the calorimeter signals and muon time of flight are slow enough[5] that the signals from multiple bunch crossings occur in the detector simultaneously. Thus, each signal must be carefully synchronized with the bunch crossing from which it came. This must also account for the latency of the trigger itself, which is around 2 μs. The information from the L1 muon and calorimeter triggers are passed to the Central Trigger Processor which makes a decision about whether or not to pass the event to the L2 trigger. It does this by testing a number of possible conditions (for example, is there at least one muon with $p_{\mathrm{T}} > 15$ GeV?) and then taking the logical OR of all of these conditions.

The L2 trigger takes as input so-called "Regions-of-Interest" (RoI) which are provided by the L1 trigger (for example, a cluster of trigger towers or a muon road). By restricting to RoIs, the L2 trigger need only consider about 1-2% of the total event[6]. The L2 trigger runs simplified reconstruction algorithms in the RoIs on a computer processing farm. A number of more detailed conditions are tested to investigate if an interesting physics object really is present in the RoI. If so, those conditions which returned a positive result are passed to the EF.

The EF is also run on a processor farm, but runs reconstruction algorithms which are very similar to those run during offline reconstruction. In many cases the EF will run on the full event. The conditions that were satisfied in L1 and L2 determine which algorithms and conditions are run in the EF. The list of conditions tested at the EF (and how they are connected to the L1 and L2) is referred to as the trigger menu. The trigger menu can have hundreds of items. Given the finite bandwidth of the trigger, the trigger menu

[5] One of the rare instances where the speed of light can be considered slow!

[6] There are some instances of the L2 trigger using the full event, but this is used sparingly.

must be carefully chosen as not all are created equal. Some trigger items can take up a lot of bandwidth, some not. Some might be considered essential, some obscure. To mitigate this problem, some trigger items might be "pre-scaled", meaning they are only kept some random fraction of the time. In the end, the trigger menu is an important statement about the physics priorities of the collaboration. If any of the trigger menu items are satisfied they are finally written to disk.

Chapter 5

Search for $WWW \to \ell\nu\ \ell\nu\ \ell\nu$

A measurement of the WWW production process is sought by using a dataset containing 20.3 fb^{-1} of integrated luminosity collected from the LHC at an energy of $\sqrt{s} = 8$ TeV in 2012. In addition to being the first study of this particular process, it is also the first study to search for a final state with more than two massive gauge bosons, and one of the first studies to search for aQGCs. The total cross-section for this process is expected to be roughly 224 femtobarns, as determined using MadGraph [88]. If measured, it would be one of the smallest cross-section measurements within ATLAS. For this thesis, we focus on the WWW process studied in the so-called "fully leptonic" decay channel where each W boson decays leptonically (excluding τ lepton decays). As can be seen in Fig. 2.9, this decay channel occurs only about 1% of the time; the rest of the time at least one of the W bosons decays hadronically. While the branching fraction is small, this channel has a smaller background than those that include hadronic W decays. As a result, the fully leptonic channel is one of the most sensitive channels for studying this process.

The data is studied in a "signal region" where the signal is most prominent with respect to the background. This region is primarily characterized by having three high p_{T} leptons (e or μ), with additional requirements determined using an optimization procedure. To understand the data in this region we must model both the signal and the backgrounds that fall into it. The signal is modeled using Monte Carlo (MC) simulation while the backgrounds are modeled using a combination of MC simulation and data-driven techniques. Prior to the measurement, each important background is studied in a "control region", where there is little to no signal contamination, to ensure that the backgrounds are described accurately. In the signal region, the agreement of the data with the signal plus background prediction is determined using a "cut-and-count" approach where the total number of data events observed in the signal region is compared to the expected number of events from the model. A fit to the data is performed using a profile likelihood with the relative normalization of the signal as the parameter of interest and with statistical and systematic uncertainties treated as nuisance parameters. From this fit, the measured signal cross-section and uncertainty, the sensitivity of the data to the signal under the background only hypothesis, and limits on new physics in an effective field theory are extracted. The details are described below.

5.1 Data and Simulation Samples

5.1.1 Data

This analysis is based on the study of the full proton-proton collision data from the LHC in 2012. The amount of data used in this analysis corresponds to an integrated luminosity of 20.3 fb^{-1}. The uncertainty on the integrated luminosity is 1.9% following the same methodology as in [89]. The data are selected after requiring that at least one of four single lepton triggers passed during data taking, specifically:

Either at least one isolated electron with $p_{\mathrm{T}} > 24$ GeV

or at least one electron with $p_{\mathrm{T}} > 60$ GeV

or at least one isolated muon with $p_{\mathrm{T}} > 24$ GeV

or at least one muon with $p_{\mathrm{T}} > 36$ GeV

For the isolated lepton triggers, the isolation requirement is evaluated using the scalar sum of the p_{T} of all tracks surrounding the lepton (excluding the lepton track itself) in a cone of $\Delta R < 0.2$ such the sum does not exceed 12% (10%) of the muon (electron) p_{T}.

5.1.2 Simulation samples

An important tool for the modeling of physics processes at the LHC is Monte Carlo simulation (MC). MC relies on random sampling to connect the matrix element formulations derived from quantum mechanical perturbation theory into actual predictions for the results of proton-proton collisions at the LHC. The prediction of a single collision from the MC represents one possible outcome of the proton-proton collision, with all of the products of the hard-scattering and their four-momenta. This result can be passed through additional MC simulation to describe hadronization and the soft products of the collision e.g. photon radiation. Finally, these products are passed through a detailed simulation of the response of the ATLAS detector built in GEANT4 [90] so that the same reconstruction algorithms can be applied as in the data. This sampling is repeated many times to populate the distribution of possible outcomes. Dedicated MC programs are provided by theorists for different processes to different orders in perturbation theory, and then interfaced to different PDFs. Details of the different processes simulated from MC and their treatment are presented below.

5.1.2.1 Signal Processes

The SM WWW signal processes are implemented in the Monte Carlo generator VBFNLO, described in [91] and [92], which can generate partonic events at LO in QCD with NLO cross-sections, and in MadGraph [88], which can generate partonic events at NLO with NLO cross-sections. The partonic events are further processed by Pythia8 [93] and Photos [94] to add the effects of beam remnant interactions and initial and final state radiation. SM parameters, such as the Higgs mass, must be provided to the MC generators as input. The underlying event parameters are set in Pythia8 using the ATLAS tune of AU2 [95]. The MC generators must also be provided an appropriate PDF. The PDF used in the LO VBFNLO generation is the LO CTEQ6L1 PDF set [96]; CT10 NLO [5] is used in the NLO VBFNLO cross-section calculation. The PDF used in the NLO MadGraph generation and cross-section calculation is CTEQ6L1 but this is re-weighted to CT10 NLO using a k-factor ranging from 1.08 to 1.10. For the reasons described in Sec. 2.1.2, renormalization and factorization scales must be chosen. The renormalization and factorization scales are dynamically set to the WWW invariant mass in the VBFNLO samples; they are set to a fixed scale equal to the Z mass in MadGraph. The VBFNLO samples are restricted to leptonic decays of the W bosons where each lepton has a p_{T} of at least 5 GeV. The MadGraph samples include all decays of the W boson, with a requirement that jets have a a p_{T} of at least 10 GeV but with no requirement on the p_{T} of the leptons. They are compared in a common fiducial phase space, described in more detail in Sec. 5.3.3. The VBFNLO and MadGraph samples handle interference between off-shell $WH \to WWW(*)$ and on-shell WWW production at LO, but MadGraph is not able to do this at NLO. As a result, the NLO MadGraph samples are split into separate samples for the two different production mechanisms. Both sets are further split by the WWW charge mode. For each sample, the cross-sections are summarized in Table 5.1 in their full phase space and in the common fiducial phase space. The fiducial cross-sections are observed to be nearly the same between the two generators. This serves as a good check of the understanding of the signal process. The MadGraph cross-sections are used throughout the remainder of the analysis.

Sample		Cross-section [fb]	
		Inclusive	Fiducial
VBFNLO	$W^+W^+W^- \to l\nu l\nu l\nu$	4.95 ± 0.007	0.2050 ± 0.0070
	$W^-W^+W^- \to l\nu l\nu l\nu$	2.65 ± 0.004	0.0987 ± 0.0037
	Sum	7.60 ± 0.008	0.3037 ± 0.0072
MadGraph	$W^+W^-W^+ \to$ Anything	59.47 ± 0.11	0.0900 ± 0.0048
	$W^-W^+W^- \to$ Anything	28.069 ± 0.076	0.0476 ± 0.0043
	$W^+H \to W^+W^+W^-(*) \to$ Anything	99.106 ± 0.019	0.1114 ± 0.0029
	$W^-H \to W^-W^+W^-(*) \to$ Anything	54.804 ± 0.010	0.0603 ± 0.0015
	Sum	241.47 ± 0.13	0.3092 ± 0.0072

Table 5.1: Inclusive and fiducial cross-sections at NLO for VBFNLO and MadGraph samples. The sum of the inclusive cross-sections are different because of the different branching fractions in the two cases. The sum of the fiducial cross-sections, however, are expected to be similar because they are computed for the same phase space, as described in Sec. 5.3.3. Only statistical uncertainties are shown.

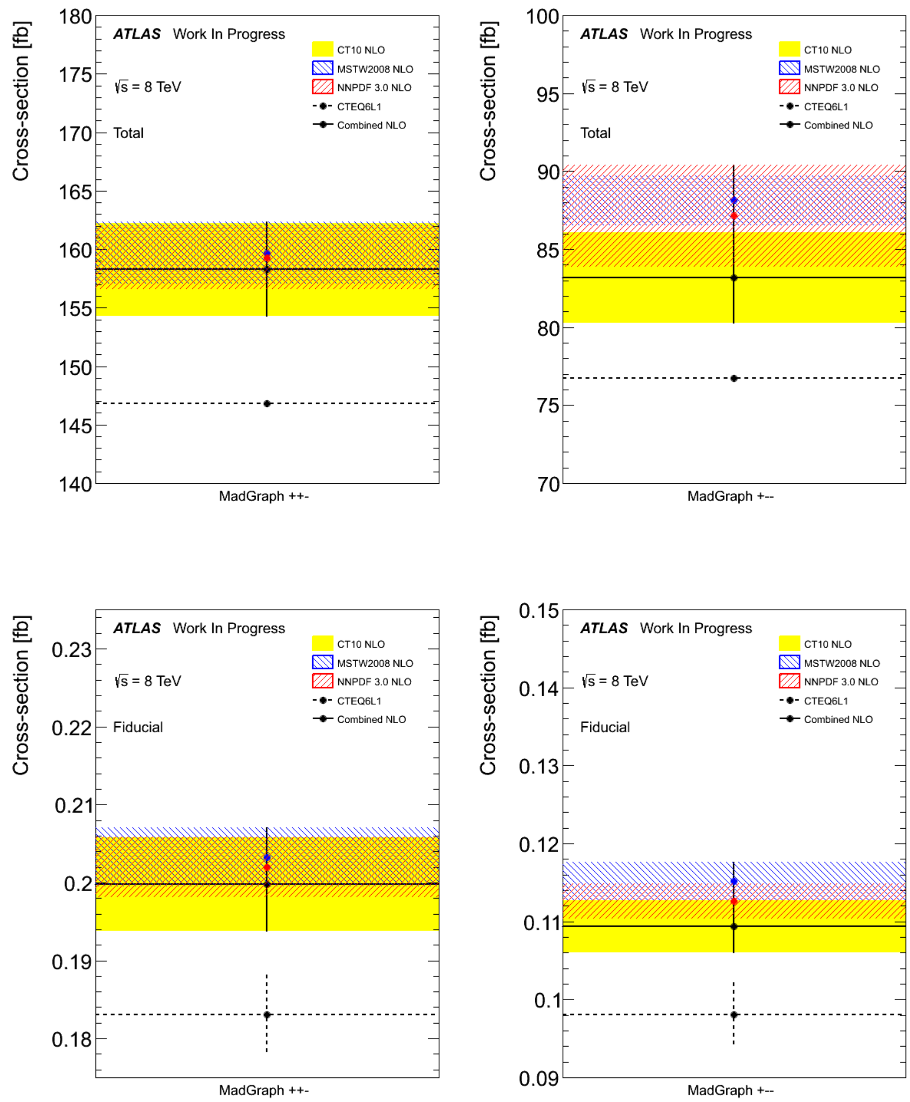

Figure 5.1: The signal cross-sections for different PDFs along with their uncertainties are shown on the MadGraph WWW signal samples for the total WWW phase space and branching fraction for the $W^+W^+W^-$ (top left) and $W^+W^-W^-$ (top right) charge modes and in the fiducial region for $W^+W^+W^-$ (bottom left) and $W^+W^-W^-$ (bottom right). The bands show the PDF uncertainty for CT10 NLO (solid yellow), MSTW 2008 NLO (hashed blue), and NNPDF 3.0 NLO (hashed red). The solid line shows the envelope of all uncertainty bands used as the final PDF uncertainty estimate. The central value of CT10 NLO is taken as the central value of the estimate. The dashed-line shows the cross-section and statistical uncertainty for the CTEQ6L1 pdf sets used in the original generation step.

	PDF Uncertainty	
	$W^+W^+W^-$	$W^+W^-W^-$
Total	$+2.58\%$ -2.51%	$+8.69\%$ -3.47%
Fiducial	$+3.64\%$ -3.00%	$+7.57\%$ -3.08%

Table 5.2: Summary of PDF uncertainties estimated on NLO MadGraph cross-sections in both the fiducial and total phase space.

Uncertainties on the signal prediction mainly come from the choice of PDF, the inherent PDF uncertainty, and the renormalization and factorization scales, as described in Sec. 2.1.2. The uncertainty due to the choice of PDF is derived for the MadGraph cross-sections following a modified version of the pdf4lhc [41] recommendations. The resulting uncertainty is shown separately for the two different charge modes in both the fiducial and the inclusive phase space in Table 5.2. The uncertainty is determined by comparing three different PDFs: CT10 NLO [97], MSTW2008 NLO [2], and NNPDF 3.0 NLO [42]. This comparison is presented in Fig. 5.1. Symmetric 68% CL uncertainties are determined for CT10 NLO and MSTW 2008 NLO using the 68% CL set provided for MSTW directly and the 90%CL set for CT10 after scaling down by a factor of 1.645 in order to approximate a 68 % CL uncertainty. The uncertainty of the NNPDF 3.0 NLO PDF set is determined by using the standard deviation of the distribution of 101 MC PDFs provided in the PDF set; the nominal value is taken from the mean of the same PDFs. The CT10 NLO PDF central value is used as the nominal value of the final estimate. The final PDF uncertainty on that estimate is taken as the envelope of the uncertainty bands for all three PDF sets.

The uncertainty on the factorization and renormalization scales are determined by varying each of them independently up or down by a factor of two. The effect of these variations on the cross-sections as compared to the nominal are shown separately for the two different charge modes in Table 5.3. The symmetric uncertainty is then determined by taking the maximum variation for each charge mode; namely, 2.62% for $W^+W^+W^-$ and 2.53% for $W^-W^+W^-$.

	$\mu_F \backslash \mu_R$	$\frac{1}{2}M_{WWW}$	M_{WWW}	$2M_{WWW}$
	$\frac{1}{2}M_{WWW}$	2.62%	-0.14%	-2.11%
$W^+W^+W^-$	M_{WWW}	2.13%	0	-2.41%
	$2M_{WWW}$	1.56%	0.24%	-2.42%
	$\mu_F \backslash \mu_R$	$\frac{1}{2}M_{WWW}$	M_{WWW}	$2M_{WWW}$
	$\frac{1}{2}M_{WWW}$	1.91%	1.38%	-2.00%
$W^-W^+W^-$	M_{WWW}	1.61%	0	-2.53%
	$2M_{WWW}$	1.25%	-1.05%	-2.12%

Table 5.3: The relative variation of the NLO cross sections corresponding to different choices of factorization, μ_F, and renormalization, μ_R, scales for the $W^+W^+W^-$and $W^-W^+W^-$processes.

The signal cross-sections and uncertainties are thus determined to be

$$\sigma^{\text{Total}}_{\text{Theory}} = 241.47 \pm 0.13 \text{ (Stat.) } {}^{+10.33}_{-6.08} \text{ (PDF) } \pm 6.3 \text{ (Scale) fb} \tag{5.1}$$

for the inclusive cross-section and

$$\sigma^{\text{Fiducial}}_{\text{Theory}} = 309.2 \pm 7.2 \text{ (Stat.) } {}^{+15.05}_{-8.36} \text{ (PDF) } \pm 8.0 \text{ (Scale) ab} \tag{5.2}$$

for the fiducial cross-section.

5.1.2.2 aQGC signal

MC samples of the aQGC signal processes described in Sec. 2.3 have been generated using VBFNLO at NLO in QCD. The cross-sections for the aQGC signal depend on the values of the couplings $f_{s,0}$ and $f_{s,1}$. MC samples have been generated for a grid of points in the $f_{s,0}$ vs $f_{s,1}$ space and their cross-sections are shown in Fig. 5.2.

The issues of unitarity violation Sec. 2.3 are taken into account using a form factor like in Eq. (2.43). The choices of the exponent, n, and form factor scale, Λ, are somewhat ad-hoc. Furthermore, a complete study of the unitarity behavior of this process has never been performed, so there are not currently detailed prescriptions on what to choose. However,

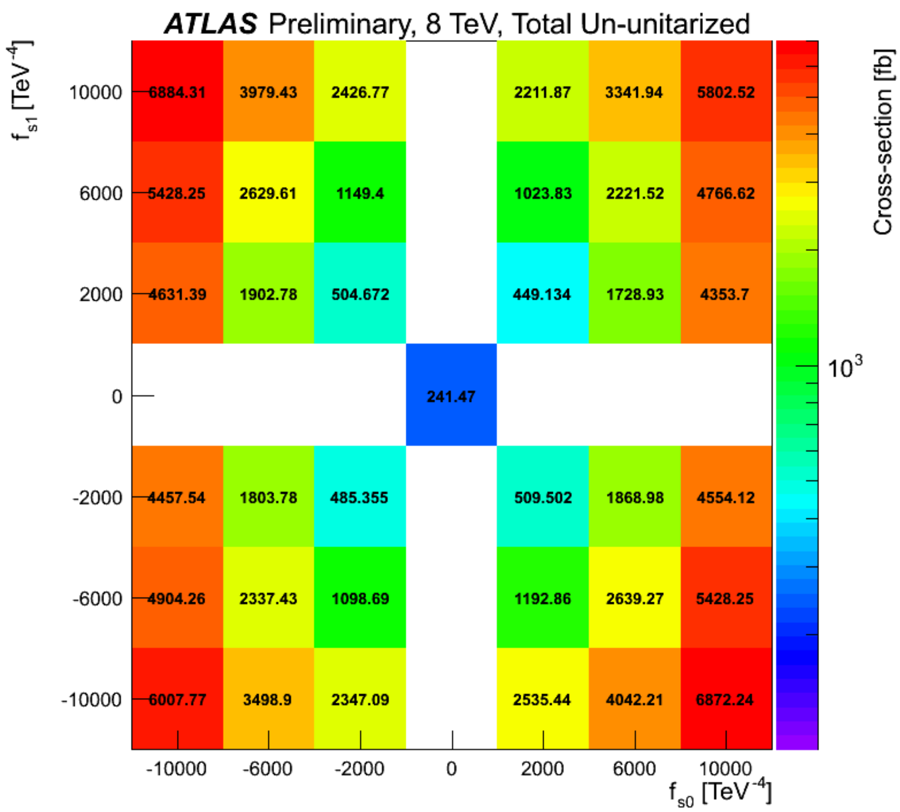

Figure 5.2: Total cross-section for non-unitarized aQGC signal samples as a function of $f_{s,0}$ vs $f_{s,1}$. The total SM cross-section is shown at $f_{s,0} = f_{s,1} = 0$ for comparison.

based on discussions with the authors of VBFNLO, who are at the moment trying to perform these studies, an exponent of $n = 1$ is expected to be sufficient to achieve unitarity for this process. As for the choice of Λ, we have chosen to look at a few different values, which cover a wide range but which should follow a smooth interpolation. This has the advantage of providing information about the sensitivity to the form factor that can be interpreted by theorists as they see fit. Dedicated MC samples are generated with the unitarization applied for values of $\Lambda = 500$ GeV, 1000 GeV, 2000 GeV, and 3000 GeV. The cross-sections for each of these unitarization cases are shown in Fig. 5.3.

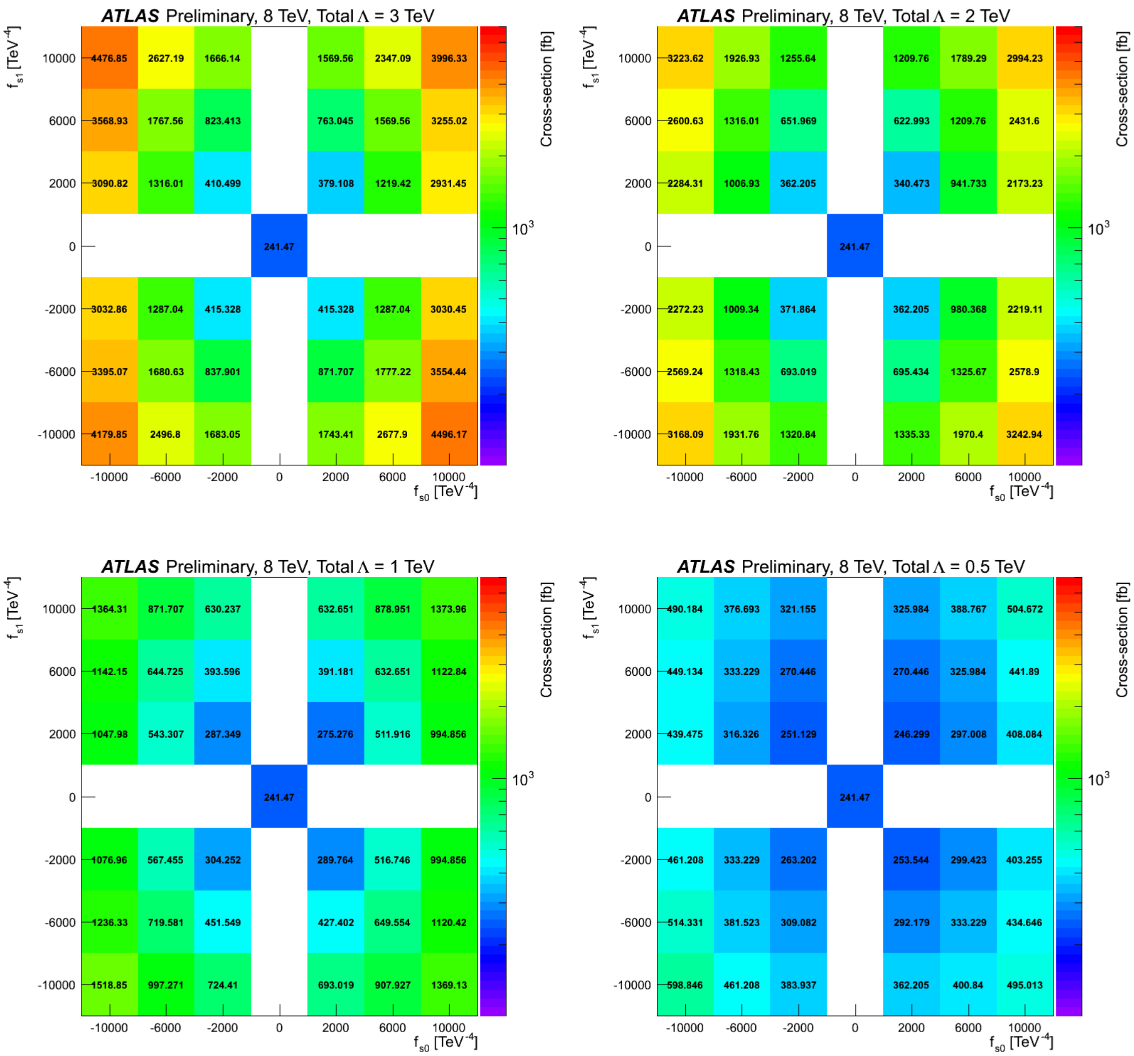

Figure 5.3: Total cross-section for unitarized aQGC signal samples as a function of $f_{s,0}$ vs $f_{s,1}$. Four different values of the unitarization scale, Λ, are chosen: 3 TeV (Top Left), 2 TeV (Top Right), 1 TeV (Bottom Left), and 0.5 TeV (Bottom Right). The total SM cross-section is shown at $f_{s,0} = f_{s,1} = 0$ for comparison.

5.1.2.3 Background samples

There are other processes produced in proton-proton collisions at the LHC which can mimic the signal processes. These are referred to as background processes. In many cases, the background processes are either more abundant than or of a similar abundance to the signal. As a result, they must be well understood if there is any hope of distinguishing between the two. The background processes to the signal fall into two general categories: irreducible and reducible. The irreducible backgrounds are those that have the exact same final state as the signal. Thus, they are characterized by having either exactly three prompt leptons, meaning they come directly from the hard scattering process. The reducible backgrounds are those which do not have the exact same final state as the signal, but can mimic the signal in some circumstances. For our signal, this includes backgrounds with four or more prompt leptons, where only three leptons are measured; two prompt leptons and an isolated photon, which can mimic an electron, referred to as the photon backgrounds; or two prompt leptons and a jet that mimics a lepton, referred to as the fake backgrounds. We treat similarly those backgrounds with three or more prompt leptons, hereby referred to as the prompt background. The prompt and photon backgrounds are estimated primarily using MC simulation while the fake background is estimated using the data itself. This will be described in more detail in Sec. 5.4.3. For now, we will focus only on the processes estimated using MC simulation.

Of the prompt backgrounds, the WZ process is the most important contribution since it has a large cross-section (compared to the signal) and results in a final state with exactly three leptons. Another important prompt background is the ZZ process, which has a similar cross-section to the WZ process, but is typically selected when four leptons are produced but one escapes detection. Thus, this process is suppressed by the efficiency for not measuring the presence of a lepton. These are collectively referred to as the di-boson processes, sometimes indicated as VV where $V = W$ or Z[1]. The di-boson processes are produced using the POWHEG [98, 99, 100, 101] generator with the CT10 NLO PDF set and hadronized through PYTHIA8 using the AU2 tune, same as the signal. Other prompt backgrounds include tri-boson processes like ZWW and ZZZ (referred to collectively as VVV) and $t\bar{t} + V$ production. Tri-boson processes have cross-sections of a similar size to

[1]The WW process is also considered but can only produce at most two prompt leptons, making it negligible.

the signal but are suppressed for a similar reason as the ZZ, since these can produce either four or six lepton final states. The $t\bar{t}+V$ production process occurs when a vector boson is produced in association with a $t\bar{t}$ pair. Since the top quark almost always decays into a W-boson and a b-quark, $t\bar{t}+V$ production also results in three vector bosons which decay into a three or four lepton final state. The VVV and $t\bar{t}+V$ processes were generated using MadGraph with the CTEQ6L1 PDF set and hadronized using Pythia6 [102] with the AUET2B [95] tune.

The photon backgrounds occur entirely from the di-boson process $Z\gamma$ where the Z boson decays to two leptons and the photon mimics an electron. A photon is measured by observing an energy deposit in the electromagnetic calorimeter without any associated track in the inner detector. A photon can mimic an electron if it converts into an electron-positron pair while still inside the inner detector. This leaves a track in the inner detector plus an energy deposit in the calorimeter, which is the tell-tale sign of an electron. The $Z\gamma$ samples were generated with the Sherpa [103] generator and the CT10 PDF set. In addition to this process, the $W\gamma$ process behaves similarly but only has one prompt lepton in addition to the photon, so it is negligible. Still, we generate it by using the AlpGen [104] generator with the CTEQ6L1 PDF set and hadronize it using JIMMY [105] with the AUET2C [95] tune.

Some of the di-boson and tri-boson processes just discussed can also be produced through double parton scattering (DPS). DPS is where two independent scatterings occur in a single proton-proton collision. The cross-sections for these processes are approximately proportional to the product of the two individual scattering cross-sections but are suppressed by the joint probability that both should occur simultaneously. Such collisions are rare The WW and ZZ loop induced processes are generated using the gg2ZZ [106] and gg2WW [107] generators with the CT10 PDF set and hadronized using JIMMY with the AU2 tunes. The DPS processes are generated using Pythia8 with the AU2 tunes and the CTEQ6L1 PDF set.

The fake background is nominally estimated using the data as described in Sec. 5.4.3.

Some of the contributions to this background, however, can be simulated using MC for cross-checks of the estimate from data. The main contributions to the fake background are the single boson processes (V+jets) and $t\bar{t}$ production. The probability for a jet to mimic a lepton is actually quite small and thus difficult to capture with adequate statistics using MC. However, these processes also have very large cross-sections. Combining the two means that in fact the occurrence of a jet mimicking a lepton is not rare and thus non-negligible. The single boson Z+jets processes are generated using SHERPA with the CT10 PDF set; the W+jets processes are generated using ALPGEN with the CTEQ6L1 PDF set and hadronized using JIMMY with the AUET2C tunes. For the Z+jets samples, special care must be taken to remove any overlap between with the $Z\gamma$ simulated samples described earlier. The $t\bar{t}$ processes are generated using the MC@NLO [108] generator with the CT10 PDF set and hadronized in JIMMY. Finally, the fake background also has contributions from single top production, though it is less important. Single top production is simulated separately for three different production mechanisms, differing in their initial and final states, known as s-channel ($qb \to q't$), t-channel ($q'\bar{q} \to \bar{b}t$), and Wt-channel ($bg \to Wt$). The s-channel and Wt-channel are generated using MC@NLO with the CT10 PDF set and hadronized through JIMMY ; the t-channel is generated using MADGRAPH with the CTEQ6L1 PDF set and hadronized using PYTHIA6 with the AUET2B tunes.

5.2 Physics Object Definition and Selection

We attempt to identify and measure the particles coming from the proton-proton collisions of the LHC by using the ATLAS detector. The most interesting physics objects for this analysis are the electrons and muons that come from the WWW decay. We also pay attention to the presence of hadronic activity and neutrinos, however, since these can help discriminate the signal from the backgrounds. Each type of particle has a unique signature in the detector that allows us to identify the particle and reconstruct its properties, such as its charge and four-momentum. This reconstruction process does not guarantee 100%

accuracy either in identifying the particle or measuring its properties. This process results in reconstructed "physics objects" which are selected using specific criteria optimized for good identification efficiency and measurement resolution. The selections used for the physics objects of interest are described below.

Muon objects are identified by the presence of tracks in both the ID and the MS that are shown to match using a statistical combination [109]. After tight quality requirements, the performance of muon reconstruction and identification is like in [110]. To ensure that the track in the inner detector indeed comes from a muon, requirements are placed on the number of hits in the different sub-components of the inner detector. The track is required to extrapolate back to the primary vertex to point within the boundaries of the MS and ID within $|\eta| < 2.5$. The muon p_{T} at the primary vertex is chosen to be limited to $p_{\mathrm{T}} > 10$ GeV. We are not interested in muons coming from jets or other hadronic activity, therefore we ask that they be isolated. The isolation of the muon is evaluated in two ways: using tracks and using energy deposits in the calorimeter. The isolation determined using tracks is calculated by adding up the scalar sum of the p_{T} of all of the tracks (excluding the muon track) in a cone of $\Delta R < 0.2$ from the muon track. We ask that the isolation from tracks be less than 4% of the muon p_{T}. The isolation determined using the calorimeter is calculated in a similar way except that energy deposits are used instead of tracks. We then ask that the isolation from the energy deposits be less than 7% of the muon p_{T} when $p_{\mathrm{T}} < 20$ GeV and less than 10% of the muon p_{T} otherwise.

The signature for electron objects are that they have a track in the inner detector that points to an energy deposit in the EM calorimeter. Tight quality requirements are placed on the electrons to achieve reconstruction and identification performance like in [111]. Similar to the muon objects, the electron track is required to extrapolate back to the primary vertex and have a $p_{\mathrm{T}} > 10$ GeV. The direction of the electron energy deposits are also asked to fall within $|\eta| < 2.47$ and outside the transition region between the EM calorimeter barrel and endcap, $1.37 < |\eta| < 1.52$. The electron objects are required to be isolated and have additional requirements on the track extrapolation, similar to the muon objects.

Jet objects are associated with energy deposits in multiple neighboring cells of the electromagnetic and hadronic calorimeter systems. They are reconstructed by grouping these cells as topological clusters [112] using the anti-k_t algorithm [113] with $\Delta R < 0.4$. The performance of jet identification in ATLAS is described in [114]. The reconstructed jet objects are required to have $p_{\mathrm{T}} > 25$ GeV and $|\eta| < 4.5$ so that they are within the boundaries of the calorimeter systems. The reconstructed jets are furthermore selected to suppress contamination from pileup events. This selection is performed by requiring that the majority of the scalar sum of the p_{T} of the tracks associated with the jet are also matched to the primary vertex. This is referred to as the “Jet Vertex Fraction” [115, 116] and is only used for jets having $p_{\mathrm{T}} < 50$ GeV and $|\eta| < 2.4$, where the algorithm is shown to perform well. Jets without any associated tracks are always kept.

It is also possible to identify jets that come from heavy flavor decays, namely through the decays of b-hadron. We refer to these as b-jets. A b-jet can frequently be identified because of the relatively long lifetime of the b quark, which can result in a decay vertex that is displaced far enough from the original primary vertex to be detected. This can be used to “tag” jets as likely coming from b quarks. A multivariate b-tagging algorithm [117] is used with a working point determined to be 85% efficient at identifying b-jets. Often, b-jets are associated with physics processes other than the signal and are helpful in identifying background processes. As a result, we choose to veto events where b-jets are present when looking in the signal regions.

The presence of neutrinos is inferred by a momentum imbalance in the transverse plane, referred to as the missing transverse energy or $E_{\mathrm{T}}^{\mathrm{miss}}$. The $E_{\mathrm{T}}^{\mathrm{miss}}$ is calculated by adding up all of the energy deposits from calorimeters cells within $|\eta| < 4.9$ and then calibrating them based on the the reconstructed physics object they are associated with. If the association is ambiguous then they are chosen based on the following preference (from most preferred to least): electrons, photons, hadronically decaying τ-leptons, jets, and muons. If the calorimeter deposit is not associated with any physics object they are still considered using their own calibration. The sum is modified to take into account the momentum of muons, which typically leave minimum ionizing energy deposits in the calorimeter without being completely stopped.

It is possible that the reconstructed high p_T electrons, muons, and jets may overlap with each other inside the detector. This can occur because because of the same physics object being reconstructed as different objects in the ATLAS detector. We handle these occurrences using the following scheme in order of precedence:

1. Electron-Muon Overlap: If $|\Delta R(e, \mu)| < 0.1$, then keep the muon and throw away the electron.

2. Electron-Jet Overlap: If $|\Delta R(e, j)| < 0.2$, then keep the electron and throw away the jet.

3. Muon-Jet Overlap: If $|\Delta R(\mu, j)| < 0.2$, then keep the muon and throw away the jet.

The direction is taken from the calorimeter information for electrons, from the combined track information for muons, and from the anti-k_T algorithm for jets. No momentum smearing or calibration corrections are applied to the reconstructed object directions. Using this scheme means that a precedence is set when reconstructed objects overlap such that $\mu > e > j$ where ">" should be interpreted to mean "is kept instead of". Note that this is different from the isolation requirements, which typically remove lower p_T objects which are closer to the reconstructed track.

5.3 Event Selection

The expected number of signal events in the total 2012 LHC dataset is expected to be very small compared to the background. Fortunately, the three lepton signature of the signal allows us to quickly throw out many events which do not look like the signal. Still, this signature is not so unique that it removes enough background to reveal the signal. Thus, we must devise a clever way to discriminate between the signal and these backgrounds.

We select events in two stages: first we start by selecting events which have the general signature of the signal, this is referred to as the pre-selection stage; we then use more stringent cuts to discriminate between the signal and backgrounds, referred to as our signal region selection. The signal region selection is determined by performing an optimization procedure starting from the pre-selection stage that minimizes the uncertainty on the final measurement. This is described in Sec. 5.5.2. The signal region selection is further divided into different categories that are each used in the final measurement and which allows us to specially treat the different backgrounds in each category. The selections used are described in more detail below.

5.3.1 Pre-selection

The pre-selection is a broad selection which throws away backgrounds that do not at all resemble the signal process. It is mainly characterized by requiring the presence of exactly three leptons (electron or muon) following the requirements listed in Sec. 5.2, each with a p_{T} of at least 20 GeV. In addition, the events are required to be of good quality. This means that the events were collected under good conditions during data taking, both from the LHC and ATLAS detector operation[2]. The event is also required to have a primary vertex with at least three associated tracks. Finally, the event is required to pass the single lepton trigger requirements listed in Sec. 5.1.1 where at least one of the three leptons selected must have caused the trigger to fire.

5.3.2 Signal Region Selection

The signal regions used in this analysis are separated based on the number of Same-Flavor Opposite-Sign (SFOS) lepton pairs selected in the event. That is to say, the number of lepton pair combinations in the event which could feasibly come from the leptonic decay of a Z-boson. This results in three separate signal regions listed below with the lepton charge

[2] For instance, during the 2012 data collection, the LAr component of the EM calorimeter was known to occasionally produce artificial bursts of noise. These instances were tracked and events where this occurred were thrown away.

combinations that fall in each category:

- **0 SFOS**: $e^{\pm}e^{\pm}\mu^{\mp}$, $\mu^{\pm}\mu^{\pm}e^{\mp}$
- **1 SFOS**: $e^{\pm}e^{\mp}\mu^{\pm}$, $e^{\pm}e^{\mp}\mu^{\mp}$, $\mu^{\pm}\mu^{\mp}e^{\pm}$, $\mu^{\pm}\mu^{\mp}e^{\mp}$
- **2 SFOS**: $e^{\pm}e^{\pm}e^{\mp}$, $\mu^{\pm}\mu^{\pm}\mu^{\mp}$

Note that in the 2 SFOS region, one lepton is allowed to belong to both pair combinations. Only charge combinations summing to ± 1 are allowed based on charge conservation (neglecting charge mis-identification). The amount of the $W^{\pm}W^{\mp}W^{\pm}$ signal which falls into each category is purely combinatoric. From the above list one can thus see that there are twice as many ways for the signal combinations to fall in the 1 SFOS regions as there are to fall in either the 0 SFOS or 2 SFOS regions. Absent possible differences in signal efficiencies based on the leptons in each signal region, one should expect branching fractions of 25%, 50% and 25% for the 0, 1, and 2 SFOS signal regions, respectively.

	0 SFOS	1 SFOS	2 SFOS
Pre-selection	Exactly 3 leptons with $P_T > 20$ GeV where at least one is trigger matched. (See Section 5.3.1)		
b-tagged Jet Veto	$N_{b-jet} = 0$ (85 % b-tagging efficiency)		
Same-Flavor Mass	$m_{\mathrm{SF}} > 20$ GeV		
Z-Veto ($m_Z = 91.1876$ GeV)	$\lvert m_{ee} - m_Z \rvert > 15$ GeV	$m_{\mathrm{SFOS}} < m_Z - 35$ GeV OR $m_{\mathrm{SFOS}} > m_Z + 20$ GeV	$\lvert m_{\mathrm{SFOS}} - m_Z \rvert > 20$ GeV
Missing E_T		$E_{\mathrm{T}}^{\mathrm{miss}} > 45$ GeV	$E_{\mathrm{T}}^{\mathrm{miss}} > 55$ GeV
Lepton-Missing E_T Angle	$\lvert \phi(3l) - \phi(E_T^{Miss}) \rvert > 2.5$		
Inclusive Jet veto	$N_{\mathrm{Jet}} \leq 1$		

Table 5.4: Optimized signal selection split by number of Same-Flavor Opposite-Sign (SFOS) lepton pairs.

In each signal region, a unique selection is determined by an optimization procedure that minimizes the uncertainty on the expected SM cross-section measurement. The optimization procedure is described in detail in Sec. 5.5.2. The optimization considers many different physical quantities with which to perform a possible selection, comparing different thresholds for a given quantity and for different combinations of quantities. After optimization a few different quantities are determined to be useful for selection. The final selection determined from the optimization is presented in Table 5.4. All cuts are decided from the optimization, and are motivated below.

Since the WWW process is a purely EW process, and since we are looking only at the fully leptonic channel, the signal is expected to have very little hadronic activity. Any observed hadronic activity should come exclusively from the momentum recoil with the WWW system. Thus, the multi-jet contribution to the signal should be small and is safe to apply a selection of $N_{\mathrm{Jet}} \leq 1$ in all signal regions. Further, the signal is expected to have negligible contributions from heavy flavor jets. As a result, vetoing events with jets tagged to come from b-hadron decays also has little effect on the signal expectation. This is true even with the rate for heavy flavor jet mis-identification for the b-tagging algorithms. For the 85% b-tagging efficiency operating point described in Sec. 5.2, the heavy flavor mis-identification rate is measured to be about 1%.

Some of the backgrounds include the production of Z bosons. The invariant mass of the Z-boson can be reconstructed from the SFOS pair coming from the Z-boson decay. This will result in a peak from these backgrounds in the invariant mass distribution around the Z-mass ($m_Z = 91.1876$ GeV [1]). The signal, which does not include Z-bosons, will not have the same peak, but instead will be relatively flat around the region of the Z-peak. As a result, removing events within a window around the peak can do a good job of removing these backgrounds without having a large effect on the signal. For the 1 and 2 SFOS regions, the mass windows chosen for the veto are $(m_Z - 35\text{ GeV}) < m_{\mathrm{SFOS}} < (m_Z + 20\text{ GeV})$ and $(m_Z - 20\text{ GeV}) < m_{\mathrm{SFOS}} < (m_Z + 20\text{ GeV})$, respectively. The windows are chosen differently based on the optimization, described in more detail in Sec. 5.5.2. In the 0 SFOS region, by definition, there are no SFOS pairs that could come from the decay of a Z-boson. The effect of electron charge mis-identification, discussed in Sec. 5.4.2, however, means that a peak can show up in the background of the m_{ee} distribution for same-sign electron/positron pairs. Thus, a veto is performed in this distribution as well, with a mass window of $(m_Z - 15\text{ GeV}) < m_{ee} < (m_Z + 15\text{ GeV})$.

The presence of neutrinos in the signal mean that the signal should have a relatively large $E_{\mathrm{T}}^{\mathrm{miss}}$ compared to most of the backgrounds. Thus, cutting on the $E_{\mathrm{T}}^{\mathrm{miss}}$ distribution such that it is large can remove backgrounds expected to have small $E_{\mathrm{T}}^{\mathrm{miss}}$, like $Z\gamma$ production. Still, there are some large backgrounds with neutrinos, like WZ, and also backgrounds that have contributions to the $E_{\mathrm{T}}^{\mathrm{miss}}$ from objects that have missed reconstruction, like ZZ, which can also have a moderate to large $E_{\mathrm{T}}^{\mathrm{miss}}$. Thus, some care must be taken to choose a threshold to cut on the $E_{\mathrm{T}}^{\mathrm{miss}}$ and different thresholds are chosen for each signal region. In the 1 SFOS region the selection is $E_{\mathrm{T}}^{\mathrm{miss}} > 45$ GeV and in the 2 SFOS region the selection is $E_{\mathrm{T}}^{\mathrm{miss}} > 55$ GeV; in the 0 SFOS region, there is no requirement on $E_{\mathrm{T}}^{\mathrm{miss}}$.

The magnitude and direction of the $E_{\mathrm{T}}^{\mathrm{miss}}$may be interpreted as coming from the vector sum of the neutrinos. By arguments of When comparing the azimuthal direction of the missing E_T to the azimuthal direction of the vector sum of the three charged leptons we find that the direction of the three charged leptons tends to be back-to-back with the direction of the missing E_T. The backgrounds also show this behavior, but it is less pronounced than it is for the signal. As a result, there is some discriminating power when cutting on the difference in the two angles:

$$\Delta\varphi(lll, E_T^{\mathrm{Miss}}) = \phi(lll) - \phi(E_{\mathrm{T}}^{\mathrm{miss}}) = \cos^{-1} \frac{\overrightarrow{p_T^{lll}} \cdot \overrightarrow{E_{\mathrm{T}}^{\mathrm{miss}}}}{p_T^{lll} E_{\mathrm{T}}^{\mathrm{miss}}} \tag{5.3}$$

The behavior of this quantity for signal and background is similar in all three signal regions. As a result, based on the optimization it was chosen to apply the cut $|\Delta\varphi(lll, E_T^{\mathrm{Miss}})| > 2.5$ everywhere.

5.3.3 Fiducial Region Selection

Imposing the reconstruction level selection in Table 5.4 implies a reduction in available the phase space with respect to the used to compute the total cross-section in Eq. (2.34). This is made explicit by re-computing the cross-section in a reduced phase space defined at truth level and modeled after the reconstruction level selection. This is referred to as the "fiducial" phase space and the resulting cross-section as the "fiducial" cross-section.

	0 SFOS	1 SFOS	2 SFOS
Tau Veto	$N_\tau < 1$		
Fiducial Leptons	Exactly 3 leptons with $p_T > 20$ GeV and $\|\eta\| < 2.5$		
Lepton Overlap Removal	$\Delta R(\ell\ell) > 0.1$		
Same-Flavor Mass	$m_{\mathrm{SF}} > 20$ GeV		
Z-Veto ($m_Z = 91.1876$ GeV)	$\|m_{ee} - m_Z\| > 15$ GeV	$m_{\mathrm{SFOS}} < m_Z - 35$ GeV OR $m_{\mathrm{SFOS}} > m_Z + 20$ GeV	$\|m_{\mathrm{SFOS}} - m_Z\| > 20$ GeV
Missing E_T		$E_{\mathrm{T}}^{\mathrm{miss}} > 45$ GeV	$E_{\mathrm{T}}^{\mathrm{miss}} > 55$ GeV
Lepton-Missing E_T Angle	$\|\phi(3l) - \phi(E_T^{Miss})\| > 2.5$		
Inclusive Jet veto	$N_{\mathrm{Jet}} \leq 1$ with fiducial jets of $p_T > 25$ GeV and $\|\eta\| < 4.5$		

Table 5.5: Fiducial regions based on optimized selection.

The chosen fiducial region selection is listed in Table 5.5. The fiducial selections are determined at truth level using Rivet [118], which allows for comparisons between different generators. Only prompt leptons (those not originating from hadron decays) are used for lepton selections, and these the momentum from nearby prompt photons within a cone with $\Delta R = 0.1$ from the lepton are added back to the lepton momentum in order to remove the effects of final state radiation. Generator-level jets are reconstructed by running the anti-k_T algorithm with radius parameter $\Delta R = 0.4$ on all final-state particles after the parton showering and hadronization with the exception of prompt leptons, prompt photons, and neutrinos. The $E_{\mathrm{T}}^{\mathrm{miss}}$ variable is calculated using all generator-level neutrinos. As can be seen, the selection in Table 5.5 looks very similar to that in Table 5.4 except for the object definitions using truth information and that events are removed if τ leptons are present from the W decays. Thus, the fiducial selection does not include the branching fraction for $W \to \tau\nu$ decay where the τ decays leptonically. This allows for a simple definition of the lepton kinematics coming from the hard scatter, which should be easily reproducible by theorists, as opposed to one which would place detailed requirements on the τ decay products as well. This is done even though there will be some contamination from this process in the final reconstruction level selection, as discussed in Sec. 5.5.4.

5.4 Background Estimates

In Sec. 5.1.2.3, three categories of backgrounds were listed based on the source of final state leptons: prompt, photon, and fake backgrounds. In this section, we will elaborate on how each of these backgrounds are determined as well as provide validation for each of these estimates using control regions. Control regions are regions of phase space that are selected to be enriched in a specific background or collection of backgrounds while at the same time being orthogonal to the signal regions of Sec. 5.3.2, or at least far enough removed so as not to bias the signal region estimate.

The prompt and photon backgrounds are estimated using the MC simulation samples listed earlier in Sec. 5.1.2.3. The most important of these backgrounds are the WZ, ZZ, and $Z\gamma$ backgrounds. The predictions for these backgrounds are studied in Sec. 5.4.1. Where appropriate, corrections to the normalization of these samples are applied to take into account higher order corrections; uncertainties on these corrections are also evaluated. In the 1 and 2 SFOS regions, the predictions for the WZ and ZZ backgrounds are straightforward. However, Even though these backgrounds predict at least one SFOS pair from Z-boson decay, they contaminate the 0 SFOS signal region, explained in Sec. 5.3.2, in part because of electron charge mis-identification. The effect of electron charge mis-identification is evaluated in the data and applied as a correction to the WZ and ZZ MC backgrounds in the 0 SFOS region. This is covered in Sec. 5.4.2.

The fake backgrounds are determined using the data as a model. The details of the fake background estimate and validation are presented in Sec. 5.4.3.

5.4.1 Monte Carlo Backgrounds

Several backgrounds to the signal are simulated purely using MC simulation. The details of these processes, like why they function as backgrounds to the signal and which MC generators are used in the simulation, have already been described in Sec. 5.1.2.3. Those simulated backgrounds which are most important have been checked in control regions and are also described below. In some cases, corrections and/or uncertainties on the normalization of these simulated samples are applied. These are also described below.

5.4.1.1 $WZ \to ll l\nu$

The $WZ \to lll\nu$ background is the most important prompt background to the WWW signal process. The most recent measurements of the WZ process at the LHC [119, 120, 121] show some tension with the current NLO MC predictions for this process, with differences of about 10 to 15%. Studies of other di-boson processes [122, 123] suggest that this could be resolved by moving to a NNLO calculation. For the WZ process, however, this type of calculation is not yet available. As a result, we instead use the so-called "2D Sideband" method (also known as the "ABCD" method) [124] to derive a correction using the data itself.

The 2D sideband method is able to determine an estimate for the process of interest using the data while also correcting for background contamination. To do this, first a signal region is chosen which is enriched in the process of interest. This signal region should have at least two independent selection requirements which when inverted suppress the signal and enhance the backgrounds to that signal. Next, by inverting one, the other, or both selection requirements, three different control regions can be formed where the signal is suppressed and the backgrounds are enhanced with respect to the signal region. These control regions are referred to as "sidebands". The three sidebands and the signal region may be related to each other assuming independence of the two different selection requirements. If this assumption holds, then the relative change in the backgrounds should be the same when inverting one cut while keeping the other fixed, and vice-versa. In this way, one may solve algebraically for the background contamination in the signal region and subtract it out, resulting in a pure estimate of the signal from the data.

In this case, the signal region is chosen to be enhanced in the WZ process. The backgrounds to this process are from electroweak contributions (like ZZ, $t\bar{t} + V$, and VVV) and from backgrounds with fake leptons. The contributions to the signal region are thus parameterized as

$$N^{\text{Data}} = N^{WZ} + N^{\text{Fake}} + N^{\text{Electroweak}} \tag{5.4}$$

These backgrounds include processes without Z-bosons. Thus, the presence of the Z-boson in the signal means that applying a Zrequirement of $|m_{\text{SFOS}} - m_Z| < 15$ GeV will suppress these contributions to the background. Also, requiring that the leptons be isolated does a good job of suppressing the fake background. Thus, the same track and calorimeter isolation requirements are applied to electrons and muons as in the WWW signal regions described in Sec. 5.2.

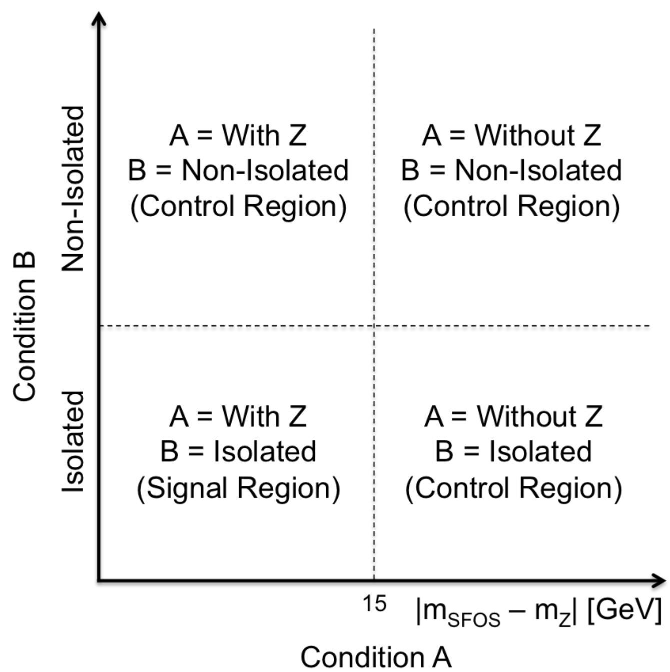

Figure 5.4: Diagram of the four different regions used in the ABCD method as defined from cuts on the 2D plane of isolation versus the Z boson SFOS mass parameter.

The Z and isolation requirements are independently inverted[3] to form the three sidebands. The expectation in each sideband can be parameterized in the same way as Eq. (5.4),

[3]The thresholds are also slightly shifted so that there is a "dead" region between the signal regions and sidebands which is not used by either. This ensures separation between all regions.

resulting in one equation for each region. By specifying the Zboson condition as A and the isolation condition as B, Eq. (5.4) can be rewritten as:

$$N_{A,B}^{\text{Data}} = N_{A,B}^{WZ} + N_{A,B}^{\text{Fake}} + N_{A,B}^{\text{Electroweak}} \tag{5.5}$$

representing the four different equations after varying A and B independently. For example, the signal region is when $A =$ With Z and $B =$ Isolated. The control regions are shown diagrammatically in Fig. 5.4.1.1. One more equation can be found by assuming that the effect of the isolation cut on the fake background is independent of the Zrequirement. That is to say:

$$\frac{R_{\text{With } Z}^{\text{Fake}}}{R_{\text{Without } Z}^{\text{Fake}}} = K \tag{5.6}$$

where

$$R_{A}^{\text{Fake}} = \frac{N_{A,\text{Isolated}}^{\text{Fake}}}{N_{A,\text{Non-Isolated}}^{\text{Fake}}} \tag{5.7}$$

and it is assumed that $K = 1$. This results in five equations: the expectations, Eq. (5.5), from varying the conditions A and B independently, and Eq. (5.6).

If we can solve the equations above for $N_{A,B}^{WZ}$ in the signal region, when $A =$ With Z and $B =$ Isolated, then we have our estimate. There are 5 equations and 16 unknowns. The four unknowns, $N_{A,B}^{\text{Data}}$, are determined using the data directly while the electroweak backgrounds, $N_{A,B}^{\text{Electroweak}}$, and the WZ contributions in the sidebands, $N_{A,B}^{WZ}$ (when $A =$ With Z and $B =$ Isolated are not both true) are determined using WZ MC. This reduces the problem to 5 equations and 5 unknowns. Thus, we can solve algebraically for the remaining unknowns including the desired value for the WZ estimate in the signal region.

The inputs to the system of equations are summarized in Table 5.6[4]. The derived values after solving the system of equations are summarized in Table 5.7. The derived estimate for the WZ contribution to the signal region is 537 ± 35 events, where the uncertainty is purely statistical. Compare this to the estimate from MC of 498 ± 1 events. The ratio of

[4]Note that the WZ MC prediction in the signal region is not used except as a comparison.

	A \ B	Isolated	Non-Isolated
$N_{A,B}^{\text{Data}}$	With Z	724 ± 27	272 ± 16
	Without Z	67 ± 8	118 ± 11
$N_{A,B}^{\text{Electroweak}}$	With Z	172 ± 3	7.7 ± 0.9
	Without Z	29 ± 2	1.9 ± 0.6
$N_{A,B}^{WZ}$	With Z	—	0.896 ± 0.050
	Without Z	31.82 ± 0.35	0.095 ± 0.015

Table 5.6: All of the inputs used to constrain the system of five equations from Eq. (5.4) and Eq. (5.6). The values are derived in the signal region and three sideband regions described in the text. $N_{A,B}^{\text{Data}}$ are determined directly from the data; $N_{A,B}^{\text{Electroweak}}$ and $N_{A,B}^{WZ}$ are determined in MC. The value for $N_{\text{With } Z,\text{Isolated}}^{WZ}$ is not used as an input and is instead solved for as the the main parameter of interest. Still, the value is determined in MC to be 498 ± 1. Only statistical uncertainties are shown.

	A \ B	Isolated	Non-Isolated
$N_{A,B}^{\text{Fake}}$	With Z	14 ± 43	263 ± 16
	Without Z	6.2 ± 8.3	116 ± 11
$N_{A,B}^{WZ}$	With Z	537 ± 35	—
	Without Z	—	—

Table 5.7: Outputs from the system of five equations from Eq. (5.4) and Eq. (5.6) after including the numbers from Table 5.6 as input. The value for $N_{\text{With } Z,\text{ Isolated}}^{WZ}$ is the value of primary interest. Only statistical uncertainties are shown.

the two can be used to derive a k-factor of 1.08 ± 0.07 (stat.).

Systematic uncertainties are also derived on the method by varying the thresholds used to define the sideband regions, varying the normalization of the MC estimates in Table 5.6, and by varying K in Eq. (5.6) to match that observed in MC. The effect of each uncertainty is propagated to the estimate of the WZ normalization in the signal region and are combined in quadrature. The total systematic uncertainty is found to be 5.9%. The final k-factor is thus 1.08 ± 0.07 (stat.) ± 0.07 (syst.). The two uncertainties are added in quadrature to give an overall uncertainty of $\pm 10\%$.

The derived k-factor is applied to the MC estimate in another control region enhanced in the WZ process. This control region is determined using the pre-selection region as described in Sec. 5.3.1 plus an additional requirement that there be 2 SFOS lepton pairs. This gives a good test of the WZ normalization in a control region which is closer to the WWW signal regions, but where the signal is still suppressed since most of the signal region cuts are not applied. The comparison is shown in Fig. 5.5 where the data is shown to be in good agreement with the corrected WZ MC estimate, as desired.

As a further test of the method, a MC estimate which includes the WZ signal as well as the electroweak and fake backgrounds is used as input in place of $N_{A,B}^{\mathrm{Data}}$ to see if the MC estimate for the WZ contribution in the signal region can be recovered. This is referred to as a closure test. The measured value for the WZ normalization from the closure test is found to be 495 ± 39, which is indeed consistent with the estimate from pure MC of 498 ± 1. The closure test also shows consistent results when varying the normalizations of the different components in the MC independently.

5.4.1.2 $ZZ \rightarrow llll$

The $ZZ \rightarrow llll$ process has a similar cross-section as the $WZ \rightarrow lll\nu$ process but is suppressed by the probability that exactly one lepton is not reconstructed. Still, this probability is large enough that the ZZ background is one of the largest in the 1 and 2 SFOS signal regions. Unlike the WZ process, NNLO predictions are available from [123, 125, 126] that

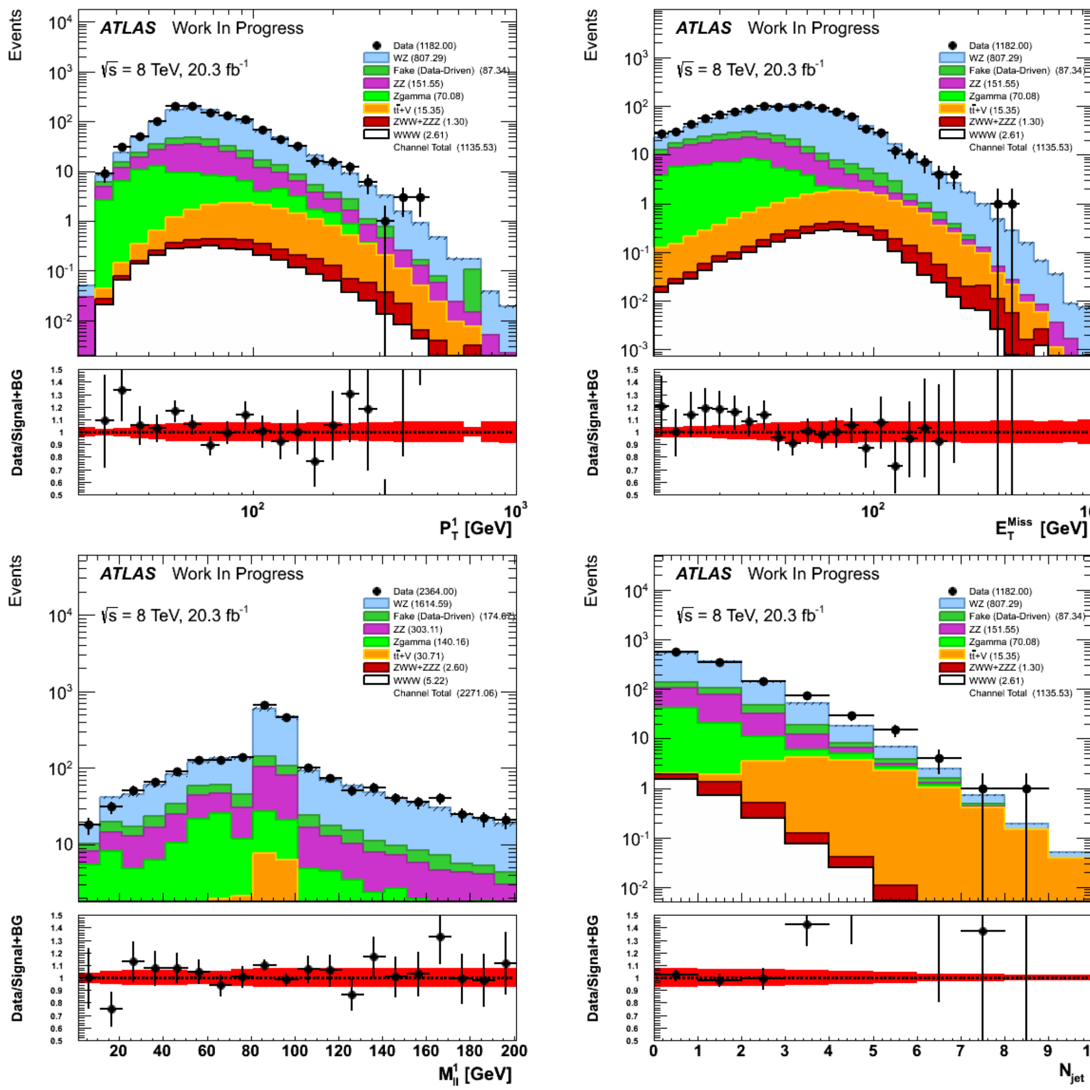

Figure 5.5: WZ control region with 3 lepton pre-selection plus 2 SFOS requirement. Distributions show leading lepton p_T, $E_{\mathrm{T}}^{\mathrm{miss}}$, m_{12}, and jet multiplicity. The systematic band shows the uncertainty on the WZ k-factor.

suggest a k-factor of 1.05 on the overall ZZ prediction. The uncertainty on the prediction is determined to be 15% [123, 125, 126]. This correction is used instead of determining a correction in the data like in Sec. 5.4.1.1.

We may check how well the NLO $ZZ \to llll$ MC prediction and NNLO normalization correction describe the process in the data by looking in a four lepton control region. The reconstructed leptons are required to have the same quality requirements as in Sec. 5.2. The leptons are sorted by p_{T} with the highest p_{T} lepton required to have $p_{\mathrm{T}} > 25$ GeV, the next two to have $p_{\mathrm{T}} > 15$ GeV, and the lowest p_{T} lepton to have $p_{\mathrm{T}} > 10$ GeV. From these leptons, two separate SFOS pairs are formed. If there is any ambiguity, first an SFOS pair is formed which gives the greatest possible di-lepton invariant mass and the remaining leptons form the other pair. This is a similar procedure to [127]. Finally, to suppress background contamination in the control region, the invariant mass of both SFOS pairs are required to be near the Z-mass, with 60 GeV $< m_{\mathrm{SFOS}} <$ 120 GeV for both. The results of the comparison are summarized for a few different distributions in Fig. 5.6 and on the total yield in Table 5.8. The expectation is shown to agree well with the observed data within the stated systematic uncertainty on the k-factor of 15%.

	Event Yield
WZ	0.05 ± 0.01
ZZ	156.2 ± 0.3(stat) ± 22.3(syst)
$Z\gamma$	0.0 ± 0.0
Fake (MC)	3.6 ± 0.2
tri-boson and $t\bar{t} + V$	4.1 ± 0.2
Expected Signal + Background	164.0 ± 0.3 (stat) ± 22.3(syst)
Observed Data	155

Table 5.8: Number of data and predicted events in the ZZ control region. The error quoted on the MC samples, except for ZZ, represents only the statistical error. The systematic error due to the k-factor on the ZZ sample is also shown.

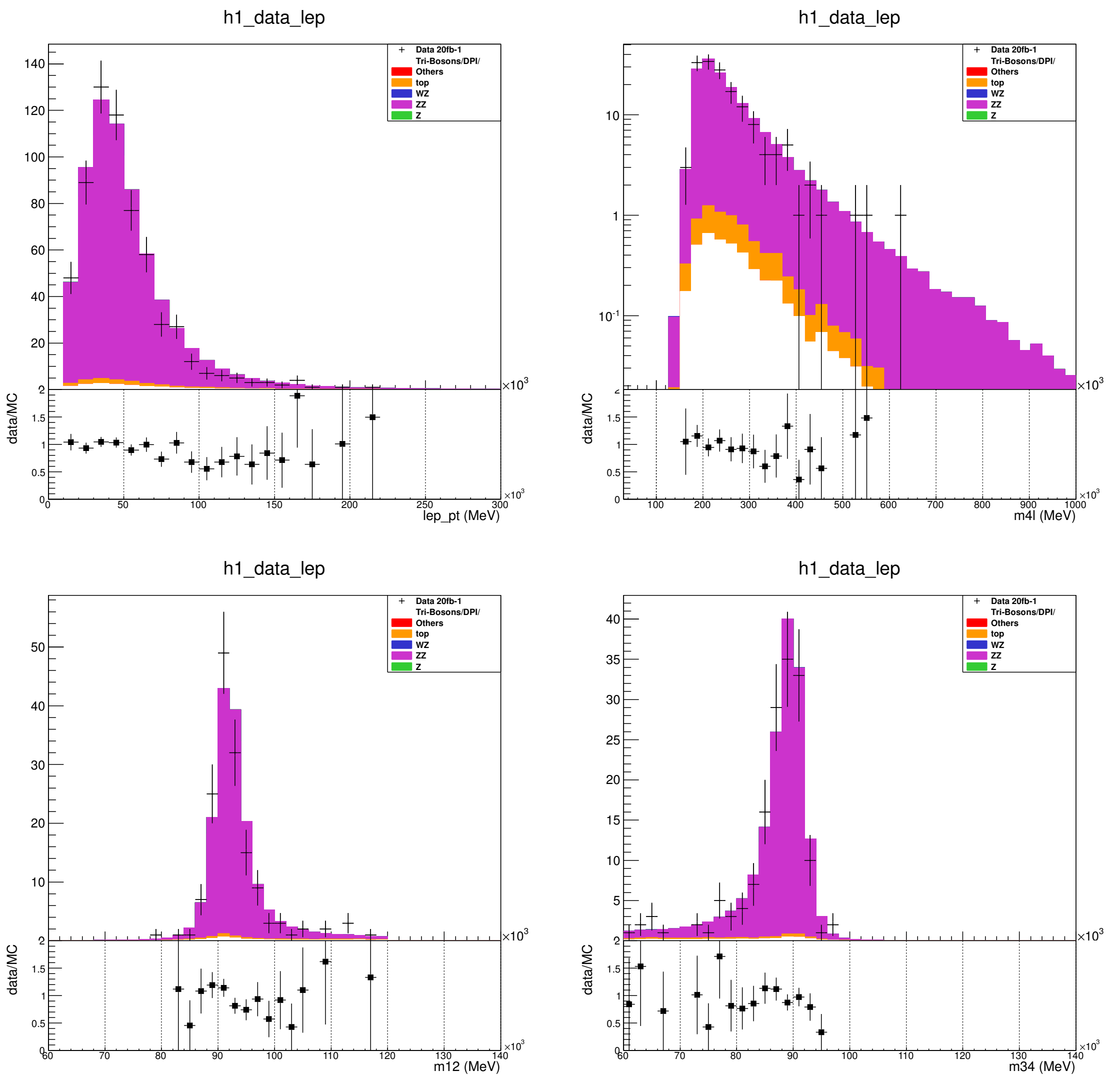

Figure 5.6: $ZZ \to llll$ control region with two separate SFOS pairs. Distributions are shown for the lepton p_{T}, the leading di-lepton mass (m_{12}), the minimum di-lepton mass (m_{34}), and the four lepton mass (m_{4l}).

5.4.1.3 $Z\gamma$

The $Z\gamma$ process can produce three leptons and thus falls into the signal regions. Measurements of this process within ATLAS have shown that this process is well described by MC simulation using the SHERPA generator at both 7 and 8 TeV [124, 128]. Thus, no further correction or uncertainty on the normalization is applied.

The description of the $Z\gamma$ process is tested in a three lepton control region starting from the pre-selection (described in Sec. 5.3.1) and with the same lepton quality requirements as in Sec. 5.2. One of the three leptons should be an electron while the remaining two are required to form a di-muon SFOS pair. For this final state to be produced by the $Z\gamma$ process, the electron should always come from pair production off of the photon, γ, which itself radiates off of the initial state Z boson. As a result, the invariant mass of the di-muon pair coming from the Z-decay will typically be shifted slightly below the Z-mass. However, the invariant mass of the three lepton system should restore this shift such that the mass peak is again centered on the Z-mass. Thus, in order to further suppress backgrounds to the $Z\gamma$ process, we also require that the three-lepton invariant mass, $m_{\mu\mu e}$, be within 15 GeVof the Z-mass. The prediction after this selection is compared to data for a few different distributions in Fig. 5.7 and for the total yield in Table 5.9. The control region is clearly enhanced in the $Z\gamma$ process, and furthermore shows very good agreement. This is even true for distributions of the electron kinematics, such as η and p_{T}, which suggests that the photon conversion mechanism is being well modeled.

5.4.1.4 Other Monte Carlo Backgrounds

Backgrounds due to DPS are generated using MC as described in Sec. 5.1.2.3. The cross-section of the DPS process is calculated assuming that the cross-sections of the two incoming processes can be factorized as in [129] using an effective proton cross-section measured in ATLAS at 7 TeV [130]. An overall 50% uncertainty is placed on the normalization of these cross-sections. This is a conservative estimate of the uncertainty. However, the

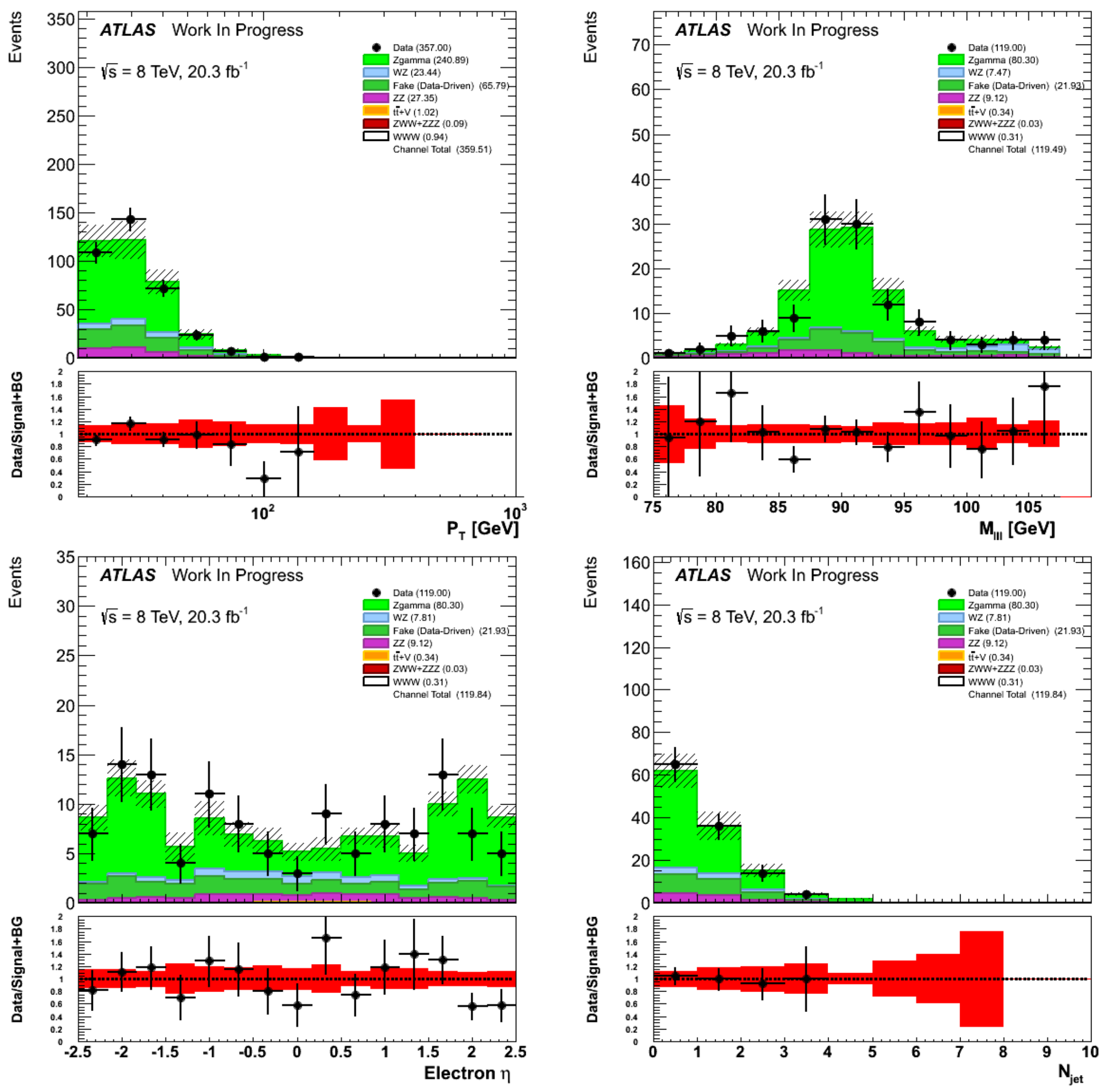

Figure 5.7: Three lepton $Z\gamma$ control region. Distribution are shown for the lepton p_T, three lepton invariant mass ($m_{\mu\mu e}$), electron η, and jet multiplicity.

	Event Yield
WZ	7.47 ± 0.11
ZZ	9.116 ± 0.075
$Z\gamma$	80.3 ± 2.8
$ZWW + ZZZ$	0.0285 ± 0.0046
$t\bar{t} + V$	0.338 ± 0.012
Fake (data-driven)	21.9 ± 1.2
WWW	0.3142 ± 0.0072
Expected Background	119.2 ± 3.1
Expected Signal + Background	119.5 ± 3.1
Observed Data	119

Table 5.9: Expected and observed event yields for the Zγ control region. Only statistical uncertainties are shown.

contributions of these processes are found to be negligible.

The remaining backgrounds evaluated using MC are those containing at least three real leptons but whose cross-sections are small or on the order of the signal process, namely $t\bar{t}+V$ and VVV processes. The theory uncertainties on the $t\bar{t}+V$ normalization have been chosen to be 30% to be consistent with measurements from ATLAS [131]. An uncertainty of 30% is also assigned to the normalization of the VVV samples.

5.4.2 Electron Charge Mis-identification

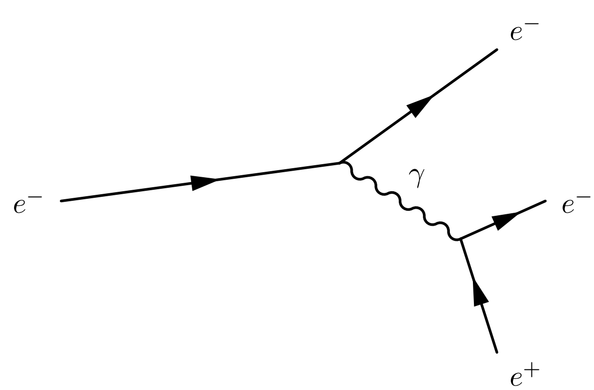

Figure 5.8: Feynman diagram showing combination of bremsstrahlung and pair-production processes that lead to electron charge mis-identification. In this case, we start with an electron and end with two electrons and a positron. For electron charge mis-identification to occur, the positron would have to be the only final state particle that is reconstructed.

High energy electrons produced from the hard scatter of the proton-proton collisions of the LHC will frequently radiate photons in the presence of the ATLAS detector material via bremsstrahlung. Furthermore, it is also common for high energy photons to convert into electron-positron pairs. Chaining these two processes together will cause an electron to radiate a photon which then produces an electron-positron pair, resulting in a three body final state with two electrons and a positron, such as in the Feynman diagram of Fig. 5.8. For muons, their larger mass suppresses these phenomena such that the similar effect for muons is completely negligible.

Often, the energy difference between the products in the final state will be large, such that most of the energy is carried away in only one product. It is thus possible that a majority of the energy of the initial electron is carried away in the positron, which has an opposite charge. If the energy imbalance is large enough, the other two final state electrons may not have enough energy to be reconstructed. As a result, the initial electron will instead be measured as a positron, and the charge of the initial state electron will have effectively been mis-identified. The situation is reversed if starting with a positron. Throughout the rest of this section we use electrons to collectively refer to both electrons and positrons unless otherwise specified.

The strong dependence of charge mis-identification upon the ATLAS material means that care must be taken when describing this process. In particular, the material description in MC, while sophisticated, is not perfect. Thus, it would be better to use the data itself to determine a model for these rates where it does not rely on a model of the detector. Thus, we extract the rates of electron charge mis-identification using the data and only use the rates determined in MC as a cross-check.

The background due to electron charge mis-identification is most important for this analysis in the 0 SFOS signal region, described in Sec. 5.3.2, where it is one of the only mechanisms by which the WZ and ZZ processes enter this region[5]. Without electron

[5]The WZ and ZZ processes can also enter in the 0 SFOS region if the Z bosons decay to τ leptons which then subsequently decay into either electrons or muons with the proper charge and flavor combination. See Sec. 5.4.2.3

charge mis-identification, these events would fall equally in the 1 and 2 SFOS regions. As will be seen shortly, the overall rate of electron charge mis-identification is quite small. Furthermore, it will be seen that the total background in the 0 SFOS region is a good deal smaller than the 1 and 2 SFOS regions. Thus, the migration of events from the 1 and 2 SFOS regions to the 0 SFOS region, resulting from electron charge mis-identification, has a larger relative impact on the background in the 0 SFOS region[6]. As a result, we focus only on modeling the background due to electron charge mis-identification in the 0 SFOS region and assume that an out of the box estimate of this background from MC is adequate for the 1 and 2 SFOS regions.

The electron charge mis-identification background is determined for the 0 SFOS signal region by first extracting the electron charge mis-identification rates using the data as a model, described below. The extracted rates are compared to an alternative method using only MC. The difference between the two is used as a systematic on the rates. The rates are then used to re-weight the WZ and ZZ MC samples on an event-by-event basis according to the probability that electron charge mis-identification could cause the event to migrate into the 0 SFOS region. In this way, the full statistics of the MC samples can be utilized to get a model of the behavior of these processes in the 0 SFOS region, while also taking into account a more accurate material description. Other backgrounds due to electron charge mis-identification are assumed to be negligible. More details on the methods used to extract the rates and the re-weighting method are provided below.

5.4.2.1 Charge Mis-identification Rate Extraction

The rate of electron charge mis-identification is defined as the probability that an electron has its charge mis-identified. These rates depend highly on the kinematics of the individual electrons. In particular, the sensitivity to material dependence described above means that the rate depends on where in the detector the electrons pass through. In general, the

[6] There is also a migration from the 0 SFOS to the 1 and 2 SFOS regions, but the relative number of 0 SFOS events to 1 and 2 SFOS events before electron mis-identification is so small as to make this effect completely negligible.

material density of the ATLAS detector increases for high η (i.e. as the electron gets closer to the beam pipe), as seen in Sec. 4.1. The rate also increases as a function of the electron energy, or p_{T}. These are the two most important kinematic variables for determining the rate[7], and so the rate extraction is binned as a function of both with nine η bins ranging from 0 to 2.5 and six p_{T} bins ranging from 15 to 120 GeV plus an additional overflow bin for $p_{\mathrm{T}} > 120$ GeV.

The rates are studied in a region with two electrons passing the object selection from Sec. 5.2 and that have a di-lepton mass within 10 GeV of the Z mass. No requirements are placed on their charge. Two different methods are used: one using purely MC and one using the data. The method using MC takes $Z \to ee$ MC simulation and relies on being able to determine the charge of each electron from the Z decay by looking directly at the hard scattering process as provided by the generator. This is called "truth" information, at which point the processes of radiation and pair-production have not occurred. It then compares these truth electrons to the "reconstructed" electrons measured after all processes, including those of radiation and pair-production, have been simulated and reconstructed in the detector. The truth and reconstructed electrons are matched by asking that they are nearby each other in η and ϕ. The charge of the matched truth and reconstruction electrons are then compared to see if the charges agree and tallying this for the appropriate p_{T} and η bin. Once all MC events have been recorded, the rate per bin may be determined simply by taking the ratio of the number of electrons where the truth and reconstructed electron charge disagreed per bin to the total number of electrons per bin.

The method using the data instead is the nominal method used for extracting the electron charge mis-identification rates. It uses the same selection as in the MC method, with the events categorized based on whether the electrons from the Z decay are of the same-sign or of opposite-sign. However, in this case there is no truth information to tell which electron's charge has been mis-identified. Instead, we assume that those events in

[7] The material also varies as a function of the azimuthal angle, ϕ, in the detector. However, this is a sub-dominant effect. Furthermore, increasing the dimensionality further significantly harms the statistical power of the method. Thus it is ignored.

the same-sign category are due purely to charge mis-identification and attempt to extract the rates by minimizing a likelihood. Refer to the rate for an electron in a particular p_{T} and η bin i as ε_i. Also, refer to the total number of di-electron events observed in data with one electron in bin i and the other in bin j as $N_{i,j}$. Given the rates, the expected number of same-sign events should be approximately $N_{i,j}(\varepsilon_i+\varepsilon_j)$, where we have ignored higher order terms, which account for the probability for both electrons to have their charges flipped, since they should be small. We do not know the rates *a priori*, but they should follow a Poisson likelihood given the observed total number of events, $N_{i,j}$, and the the observed number of same sign events, $N_{i,j}^{\mathrm{SS}}$, with the following form:

$$\mathcal{L}(\varepsilon_i, \varepsilon_j | N_{i,j}^{\mathrm{SS}}, N_{i,j}) = \frac{(N_{i,j}(\varepsilon_i + \varepsilon_j))^{N_{i,j}^{\mathrm{SS}}} e^{-N_{i,j}(\varepsilon_i+\varepsilon_j)}}{N_{i,j}^{\mathrm{SS}}!} \tag{5.8}$$

From this, we may construct a log likelihood which can be minimized as a function of ε_i and ε_j:

$$-\ln \mathcal{L}(\varepsilon_i, \varepsilon_j | N_{i,j}^{\mathrm{SS}}, N_{i,j}) = N_{i,j}(\varepsilon_i + \varepsilon_j) - N_{i,j}^{\mathrm{SS}} \ln(N_{i,j}(\varepsilon_i + \varepsilon_j)) \tag{5.9}$$

where the terms that are not dependent on ε_i and ε_j have been dropped. Thus, given the data, the values of ε_i and ε_j at the minimum value of the log likelihood are taken as the estimate of the rates. Backgrounds to the $Z \to ee$ process are subtracted using MC.

The rates for the two different methods are shown in Fig. 5.9. For low values of p_{T} and η, where most electrons fall, the rate is small enough to be negligible. The rate increases gradually along both dimensions, reaching as much as 6.7% in the region $p_{\mathrm{T}} > 120$ GeV and $2.4 < |\eta| < 2.5$ as measured in the data, which corresponds to the highest bin in both dimensions. Still, the average rate is only around 0.01 % to 0.1 %. The rates measured using MC truth information are systematically higher than those measured in data, almost by a factor of two, discussed later.

Some variations on the method are also performed in order to better assess its performance and to determine systematic uncertainties. One variation is to perform the same

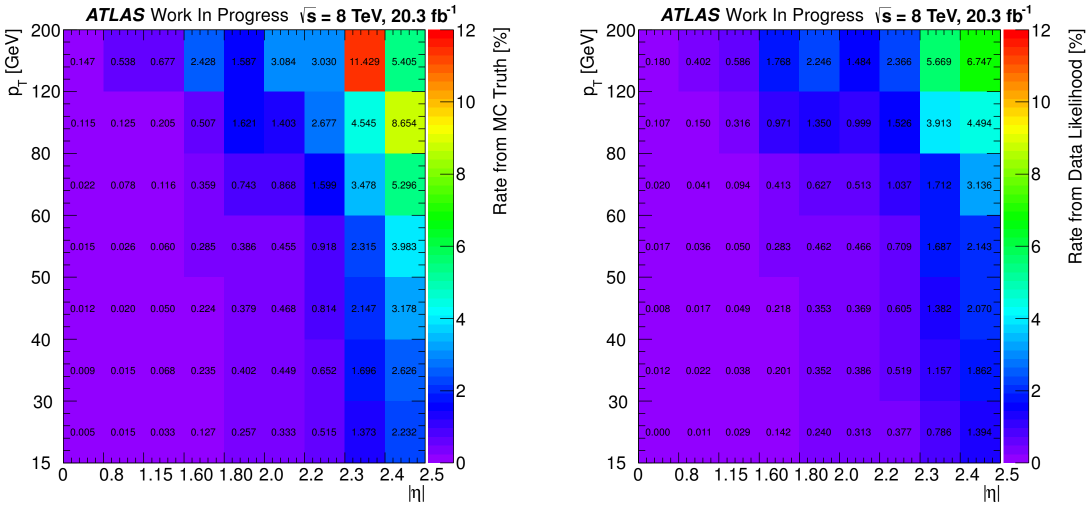

Figure 5.9: Electron charge mis-identification rates as a function of the electron p_{T} and η extracted using the MC truth method (left) and the likelihood method in data (right).

likelihood extraction as in the data, but using only reconstructed MC. This produces similar rates to the truth MC method, suggesting that the differences seen between the data likelihood method and the truth MC method are not due to the method itself. Another variation is to extract the rates from the data with the likelihood method but without performing the background subtraction.

The different variations on rate estimation are compared to the nominal estimate to extract a final systematic. In Fig. 5.10, the two-dimensional rates are unfolded into one-dimension with the bins numbered counting from low values of η and p_{T} to high values. The rates with and without background subtraction are seen to agree quite well, only differing by about 5-6% throughout. The red curve shows the rates evaluated using the same likelihood method applied to the data, but using only reconstructed MC. This variation on the likelihood method using just MC is seen to follow the MC truth method closely, except in a few bins where the statistics are low. The relative difference between the MC truth and MC likelihood methods is transported to the nominal estimate in data and used as another systematic. There is a factor of two difference in the rates evaluated using MC and those using data, with the difference persisting regardless of the methods used. This suggests that the difference is coming from the MC itself, motivating the use of the data-driven rate evaluation in the first place. As such, the difference between the methods using data and those using MC is not used as a systematic. The systematic uncertainties are combined in quadrature with the statistical uncertainty on the nominal estimate to arrive at a final uncertainty on the rates, shown as a hashed band.

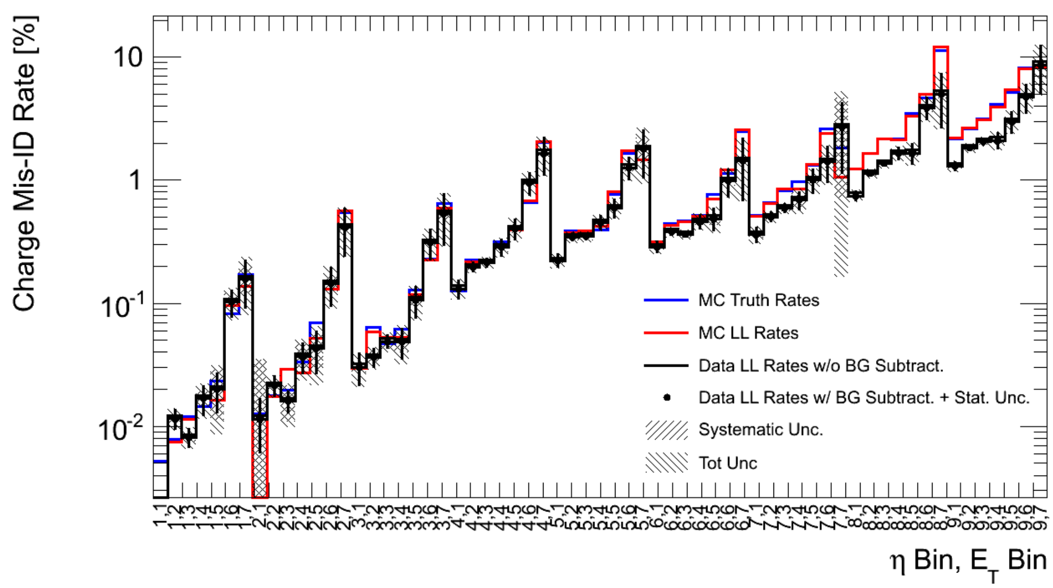

Figure 5.10: Summary of electron charge mis-identification rates using the likelihood method in data with background subtraction (black points) and without background subtraction (black line), the MC truth method (blue line), and the likelihood method in MC (red). Systematic uncertainties are extracted as described in the text and are shown in the gray hashed band pointing from bottom left to top right. The systematic uncertainties are combined with the statistical uncertainties on the black points to arrive at a total uncertainty on the rates, shown in the hashed band pointing from bottom right to top left.

5.4.2.2 Di-boson MC Re-weighting

The electron charge mis-identification rates are primarily important for the determination of the WZ and ZZ background contamination in the 0 SFOS region, as mentioned already. Once derived, the rates are applied to WZ and ZZ MC samples based on whether or not a charge flip could cause the event to appear in the 0 SFOS region. In particular, the following di-boson decays are considered:

- $WZ \to e^{\pm}\nu\ e^{+}e^{-}$
- $WZ \to \mu^{\pm}\nu\ e^{+}e^{-}$
- $WZ \to \tau^{\pm}\nu\ e^{+}e^{-}$
- $ZZ \to e^{+}e^{-}\ e^{+}e^{-}$
- $ZZ \to \mu^{+}\mu^{-}\ e^{+}e^{-}$

No other decay channels are considered. These all share in common that they have at least one electron-positron pair. Except for the $WZ \to \tau^{\pm}\nu\ e^{+}e^{-}$ decay channel, decay channels with tau leptons are not considered because they are suppressed by the tau branching fraction and are thus negligible.

The charge mis-identification rates are then applied to these channels on an event-by-event basis as follows. For each event that is processed, its decay channel is identified at truth level. Each reconstructed lepton is examined and assigned a rate, i.e. a probability to charge flip, based on its reconstructed p_{T} and η values. The probability for a charge flip to occur in an event is then approximately the sum of rates for the individual electrons:

$$p(\text{Charge Mis-Identification in Event}) \approx \sum_{i \in \text{Electrons}} \text{Rate}(p_{\mathrm{T}}^{i}, \eta^{i}) \tag{5.10}$$

Higher order terms where multiple electrons are charge mis-identified is negligible. We are only concerned with the probability that a charge flip results in the event falling into the 0 SFOS region. Consider a step function, $\Theta(e)$, defined for an individual event:

$$\Theta(e) = \begin{cases} 1 & \text{if flipping charge of } e \text{ classifies event as 0 SFOS} \\ 0 & \text{if flipping charge of } e \text{ does NOT classify event as 0 SFOS} \end{cases}$$

Then the probability that a charge mis-identification occurs and results in the event falling in the 0 SFOS region is:

$$p(\text{Event is classified as 0 SFOS}) \approx \sum_{i \in \text{Electrons}} \text{Rate}(p_{\text{T}}^{i}, \eta^{i})\Theta(i) \tag{5.11}$$

Again, we ignore the case where multiple electrons have their charge mis-identified. This probability is then used as an event-by-event weight.

Once the weight has been determined, we then artificially flip the charge of one of the electrons/positrons in the event. If there is only one electron in the event that will lead the event to fall in the 0 SFOS region, its charge is flipped and one proceeds to the next event. However, if there are multiple electrons in the event, there is an ambiguity that must be resolved about which electron's charge should be flipped. One must then be careful in this case to not introduce any bias. We decided to choose a procedure where we pick a single electron from the event at random based on the charge flip rates of the individual electrons. Thus, for an individual electron in an event, the probability that it is chosen to have its charge flipped is:

$$p(e \text{ has been charge flipped}) = \text{Rate}(p_{\text{T}}^{e}, \eta^{e})\Theta(e) \ / \sum_{i \in \text{Electrons}} \text{Rate}(p_{\text{T}}^{i}, \eta^{i})\Theta(i) \tag{5.12}$$

Consider an example where the event under consideration comes from the decay $WZ \to e^{+}\nu e^{+}e^{-}$. Assume all three charged leptons pass reconstruction and are selected then label them as: $e_1^{+}\ e_2^{+}e_3^{-}$. In this case, the only way that this event could be classified as 0 SFOS when flipping the charge of only one electron/positron is to flip the charge of the electron. Thus, $\Theta(e_1^{+}) = \Theta(e_2^{+}) = 0$ and $\Theta(e_3^{-}) = 1$. The event weight will then be equal to the rate of charge mis-identification for e_3^{-} and it will have it's charge flipped to be positive[8].

Now consider an example of an event with the decay of $ZZ \to \mu^{+}\mu^{-}\ e^{+}e^{-}$. If all four leptons are reconstructed and selected, the event will not be considered at all in the

[8]This results in a final state which does not fall into our signal region, since the sum of the charge of the three electrons is +3. Thus, it is just for illustration purposes

three lepton selection of this analysis, so consider the case where the μ^+ is not selected leaving three leptons labeled as: $\mu_1^- e_2^+ e_3^-$. The probability for the muon to charge flip is negligible which leaves the electron and the positron. Flipping the charge of either one at a time will result in the event being classified as 0 SFOS. Thus, in this case $\Theta(\mu_1^-) = 0$ and $\Theta(e_2^+) = \Theta(e_3^-) = 1$. The event weight will then be the sum of the rates for e_2^+ and e_3^-. The probability that the electron has its charge flipped is then $\frac{\text{Rate}(e_3^-)}{\text{Rate}(e_2^+)+\text{Rate}(e_3^-)}$ and similarly for the positron.

5.4.2.3 Validation

This procedure has been validated on the WZ and ZZ samples by comparing the predictions taken directly from MC to the predictions re-weighted in the 0 SFOS signal region using the procedure just described. This is done in Fig. 5.12 for the WZ samples and on Fig. 5.13 for the ZZ samples. It can be seen the agreement in the shape looks good for all the distributions. An offset between the two distributions is observed. This difference is covered partially by the systematic uncertainties of the method. Any remaining difference could be expected from the difference in rates observed at high η and high E_T as seen in Fig. 5.10 and serves as justification for using the data-driven method.

The proportion of contributions to the WZ background coming from charge mis-identification in the 0 SFOS region is demonstrated in Fig. 5.11. Here we can see that the large contribution from WZ decaying to electrons and muons (but not taus) at pre-selection (see Sec. 5.3.1) survives and is non-negligible, even after applying the 0 SFOS cut. This can only come from the electron charge being mis-identified. It is worth noting, however, that there is also a sizable contribution to the 0 SFOS region when the Z decays to taus since it is possible to have two leptonically decaying taus that satisfy the 0 SFOS requirements while correctly identifying the charge. A similar behavior occurs also for the ZZ contribution.

There is no special treatment of the charge mis-identification contribution to other background contributions in the 0 SFOS region or to any contributions to the 1 and 2

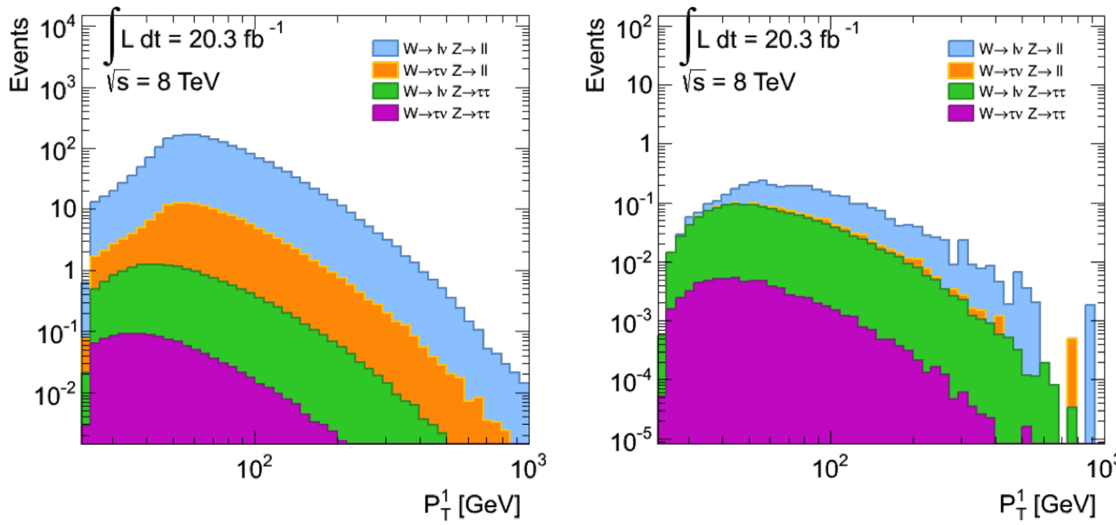

Figure 5.11: Plots of the different branching fractions of the WZ process as a function of the leading lepton p_{T} at pre-selection (left) and after also applying a requirement that events have 0 SFOS lepton pairs (right). The individual decays of W and Z are split up into whether they decay into taus (τ) or into electrons and muons (denoted l). The taus also subsequently decay. The contributions from $WZ \to l\nu ll$ and $WZ \to \tau\nu ll$ after applying the 0 SFOS selection are due purely to charge mis-identification.

SFOS signal regions, including di-boson processes, as the effect is expected to be very small. Any charge mis-identification events are thus taken directly from MC in this case.

5.4.3 Fake lepton background

As discussed in Sec. 5.2, the leptons reconstructed by the ATLAS detector are selected to optimize the measurement resolution and identification efficiency. But this identification is not perfect. A jet, for instance, perhaps from a charged pion, could leave a single track in the inner detector along with a narrow energy deposit in the EM calorimeter; a very similar signature to an electron. Or, a b-hadron could decay into a final state with a high energy muon, making it difficult to distinguish from a muon produced in the hard interaction. We call these mis-reconstructed leptons, “fake” leptons. By contrast, those leptons that have been correctly identified are referred to as “real”.

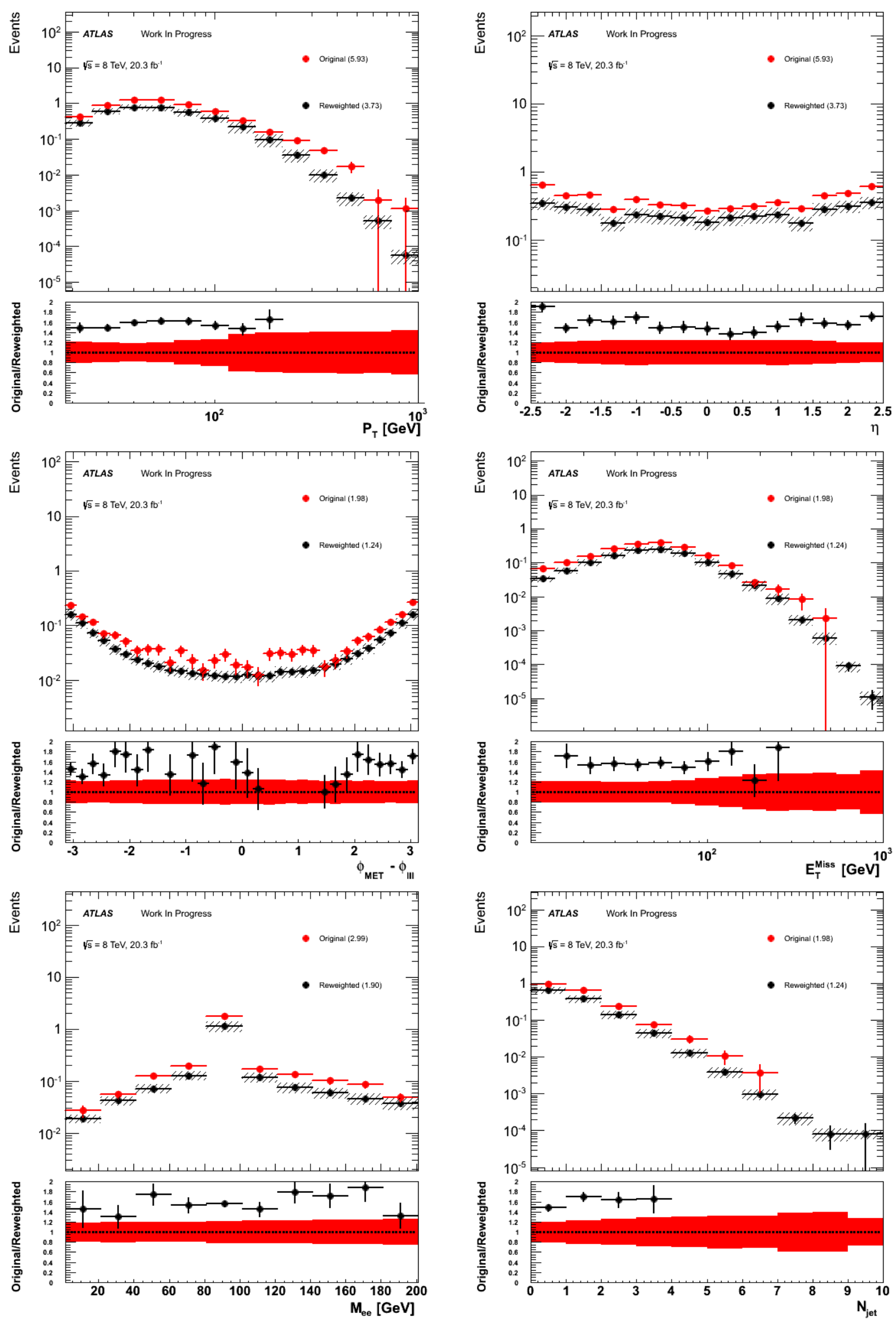

Figure 5.12: Validation of the charge mis-ID rates comparing MC $WZ \to \ell ee$ ($\ell = e, \mu$) samples re-weighted with the charge mis-ID rates measured in the MC $Z \to ee$ sample to the original MC predictions. Distribution of lepton p_T, η, $\Delta\phi(3l, E_T^{Miss})$,$E_{\mathrm{T}}^{\mathrm{miss}}$, Same-sign di-electron invariant mass, and jet multiplicity.

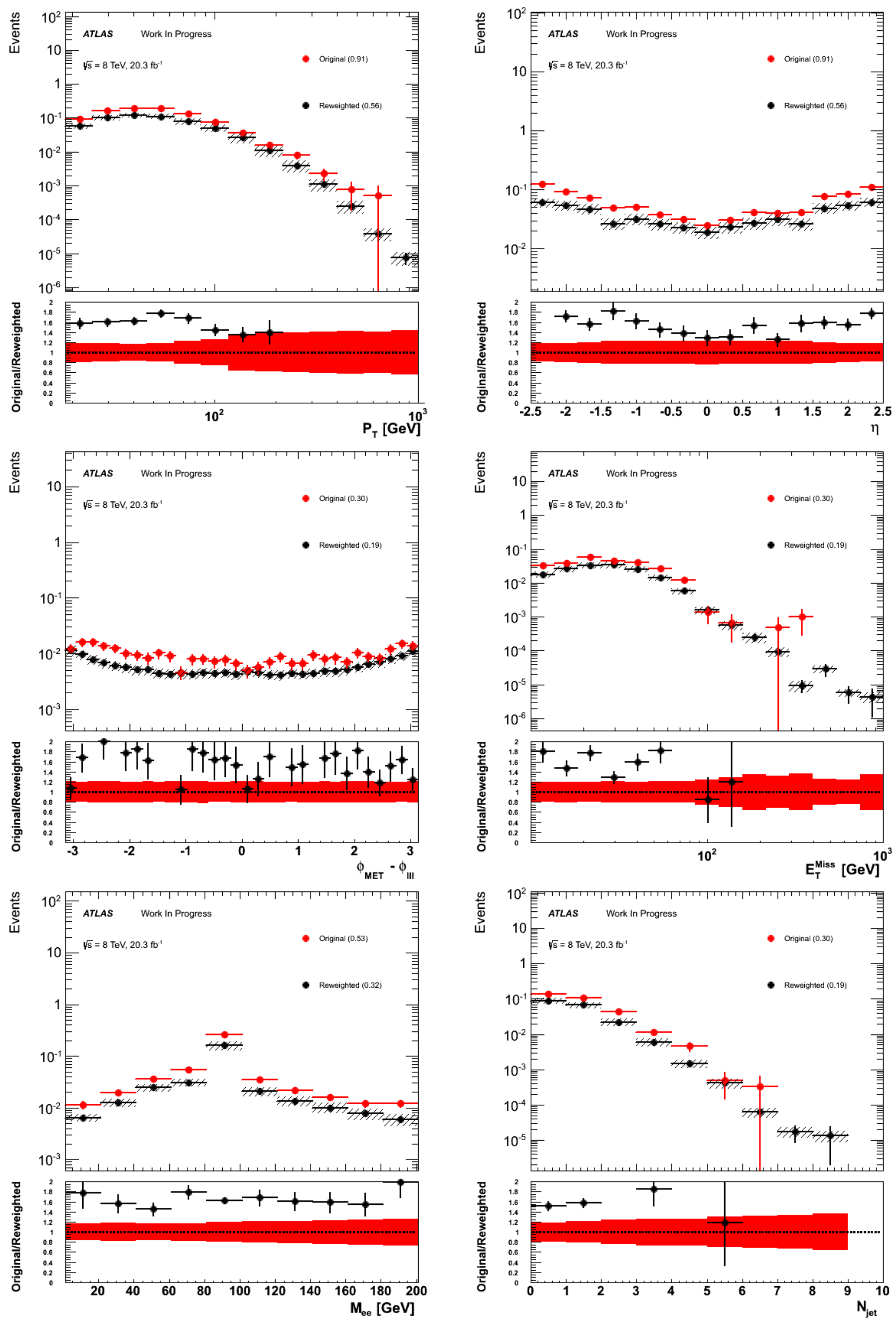

Figure 5.13: Validation of the charge mis-ID rates comparing MC $ZZ \to \ell\ell ee$ ($\ell = e, \mu$) samples re-weighted with the charge mis-ID rates measured in the MC $Z \to ee$ sample to the original MC predictions. Distribution of lepton p_T, η, $\Delta\phi(3l, E_T^{Miss})$,$E_{\mathrm{T}}^{\mathrm{miss}}$, Same-sign di-electron invariant mass, and jet multiplicity.

In particle physics it is never the case that the features describing a given particle are completely separable from another, even hypothetically. Instead, the characteristic features for a type of particle will overlap with that of other particles. For example, both electrons and jets are characterized in part by the presence of calorimeter deposits in the EM calorimeter. The calorimeter deposits form a cone pointing back to the collision point, and the radius of this cone will follow some distribution. On average, the deposit from an electron will have a smaller radius than that of a jet. So, on average the radius of calorimeter deposits can be used to distinguish between the two physics processes. But the overlap of these two distributions is significant enough that using this radius alone will give an unsatisfactorily high error rate for identification. The error rate can be improved by adding information from the inner detector, and so on, further reducing the error rate but never reaching zero. So, while rare, the large number of collisions produced by the LHC means that the measurement of fake leptons will inevitably occur. Thus, we must take them into account.

The modeling of these fake leptons are in general heavily dependent upon the conditions of the detector. The detector is described in MC simulation using GEANT4, thus it is possible and relatively straightforward to model these processes using MC directly. However, in practice, this usually proves to be inadequate because some of the effects which produce fake leptons are so rare that it may be difficult to generate enough MC collisions to obtain adequate statistics. The dataset from the LHC, however, has an extremely large sample size. The trick is then how to extract from the data the information we need for the signal regions of interest in an accurate and unbiased way.

We choose to use the Generalized Matrix Method [132], which may estimate from data the contribution of any combination fake and real leptons. It has been implemented previously in [133]. Versions of the matrix method have been implemented in previous experiments prior to the LHC. The first version to be implemented within ATLAS [134] was restricted to the estimation of events with exactly one fake lepton. Variations of the method have been implemented in numerous publications by ATLAS and CMS ever since.

In essence, the method relies on the definition of two different selections, referred to as "tight" and "loose", defined such that "real" leptons are more likely to pass the "tight" selection than "fake" leptons. If the probability of the "real" and "fake" leptons to pass these selections can be determined (typically in control regions), then in principle the easily defined "tight" and "loose" selections may be used as a proxy to extract an estimate of the "real" and "fake" lepton contributions in a region of one's choosing. The method is described in more detail below.

5.4.3.1 Generalized Matrix Method

The Generalized Matrix Method allows one to extract from data the expected number of events with any combination of fake and real leptons. For any given selection, some fraction of the events will have real leptons, fake leptons, or some combination of the two. For a selection with exactly one lepton, the lepton can simply be either real or fake. Suppose one then defines two orthogonal single lepton selections with in general different combinations of real and fake leptons. Furthermore, design one of the selections to be much more likely to have real leptons than fake leptons, usually taken to be the signal region selection. We will call this the "tight" selection. We can measure directly the number of events in the data that pass this "tight" selection and call it n_T. Choose the other selection to have a different composition of real and fake leptons. Since the "tight" selection is enriched in real leptons, this can be achieved if this other selection has a larger proportion of fake leptons. We will call this the "loose" selection and designate the number of events measured in this selection as n_L.

The total number of real leptons that fall in both regions can be called n_R. The probability that one of these real leptons passes the tight selection is called the real efficiency, or sometimes the real rate, and is denoted by ε_r. Similarly, the total number of fake leptons that fall in both regions is denoted n_F and the probability that one of these fake leptons passes the tight selection is called the fake efficiency, or fake rate, and is denoted by ε_f. The condition that more real leptons pass the tight selection can thus be summarized by saying that $\varepsilon_r >> \varepsilon_f$ be true.

The expected values of n_T and n_L, denoted $\langle n_T \rangle$ and $\langle n_L \rangle$, can be related to n_R and n_F using these rates via a system of equations:

$$\begin{pmatrix} \langle n_T \rangle \\ \langle n_L \rangle \end{pmatrix} = \begin{pmatrix} \varepsilon_r & \varepsilon_f \\ \overline{\varepsilon}_r & \overline{\varepsilon}_f \end{pmatrix} \begin{pmatrix} n_R \\ n_F \end{pmatrix} \tag{5.13}$$

where I have introduced the notation $\overline{\varepsilon}_r = 1 - \varepsilon_r$ and $\overline{\varepsilon}_f = 1 - \varepsilon_f$. Note that this equation is a function of the measured values of n_R and n_F which we are actually seeking to find in terms of the expectations of n_T and n_L. Thus, it is in fact more useful to solve for n_R and n_F by taking the inverse:

$$\begin{pmatrix} n_R \\ n_F \end{pmatrix} = \frac{1}{\varepsilon_r - \varepsilon_f} \begin{pmatrix} \overline{\varepsilon}_f & -\varepsilon_f \\ -\overline{\varepsilon}_r & \varepsilon_r \end{pmatrix} \begin{pmatrix} \langle n_T \rangle \\ \langle n_L \rangle \end{pmatrix} \tag{5.14}$$

So far everything is exact and as long as the condition that $\varepsilon_r >> \varepsilon_f$ is true, as it should be by construction, then there is no risk of encountering the singular condition when $\varepsilon_r = \varepsilon_f$. But in the matrix method, we wish to use the *measured* values of n_T and n_T to derive an *estimate* of the expectation for n_R and n_F, denoted $\hat{n}_R$ and $\hat{n}_F$. Thus, in a rather *ad hoc* way we interpret Eq. (5.14) as follows:

$$\begin{pmatrix} \langle n_R \rangle \\ \langle n_F \rangle \end{pmatrix} \approx \begin{pmatrix} \hat{n}_R \\ \hat{n}_F \end{pmatrix} = \frac{1}{\varepsilon_r - \varepsilon_f} \begin{pmatrix} \overline{\varepsilon}_f & -\varepsilon_f \\ -\overline{\varepsilon}_r & \varepsilon_r \end{pmatrix} \begin{pmatrix} n_T \\ n_L \end{pmatrix} \tag{5.15}$$

This equation solves for the estimators, $\hat{n}_R$ and $\hat{n}_F$, as a function of the measured values n_T and n_L, as well as the rates. The estimators are in general only approximately equal to the expected values, as discussed in [132]. This approximation can break down, sometimes even giving negative values for the estimate. Though it should be adequate if the number of events falling in the "tight" and "loose" selections are not too small. We will assume that the method holds, but these concerns are important to keep in mind whenever using this method.

We now have a way to approximately solve for the estimate of the real and fake lepton contributions to a single lepton selection in our data sample. But, ultimately we are interested in an estimate of the number of fake leptons that fall into our tight selection, call it estimate $\hat{f}_T$. And in principle we can also solve for the number of fake leptons that are loose, $\hat{f}_L$, though this is not our focus. These estimates can be solved for then in a straightforward way, by selecting only the estimated component of fakes.

$$\begin{pmatrix} \hat{f}_T \\ \hat{f}_L \end{pmatrix} = \begin{pmatrix} \varepsilon_r & \varepsilon_f \\ \overline{\varepsilon}_r & \overline{\varepsilon}_f \end{pmatrix} \begin{pmatrix} 0 \\ \hat{n}_F \end{pmatrix} = \begin{pmatrix} \varepsilon_r & \varepsilon_f \\ \overline{\varepsilon}_r & \overline{\varepsilon}_f \end{pmatrix} \begin{pmatrix} 0 & 0 \\ 0 & 1 \end{pmatrix} \begin{pmatrix} \hat{n}_R \\ \hat{n}_F \end{pmatrix} \tag{5.16}$$

Solving for $\hat{n}_R$ and $\hat{n}_F$ and then Substituting in for equation Eq. (5.15) gives an expression for the expected number of tight and loose selected fake leptons as determined from the rates and the measured value of tight and loose leptons:

$$\begin{pmatrix} \hat{f}_T \\ \hat{f}_L \end{pmatrix} = \begin{pmatrix} \varepsilon_r & \varepsilon_f \\ \overline{\varepsilon}_r & \overline{\varepsilon}_f \end{pmatrix} \begin{pmatrix} 0 & 0 \\ 0 & 1 \end{pmatrix} \frac{1}{\varepsilon_r - \varepsilon_f} \begin{pmatrix} \overline{\varepsilon}_f & -\varepsilon_f \\ -\overline{\varepsilon}_r & \varepsilon_r \end{pmatrix} \begin{pmatrix} n_T \\ n_L \end{pmatrix} \tag{5.17}$$

Then, since we are only interested in $\hat{f}_T$, we may simply pluck out the estimated number of tight leptons from fakes:

$$\begin{pmatrix} \hat{f}_T \\ 0 \end{pmatrix} = \begin{pmatrix} 1 & 0 \\ 0 & 0 \end{pmatrix} \begin{pmatrix} \varepsilon_r & \varepsilon_f \\ \overline{\varepsilon}_r & \overline{\varepsilon}_f \end{pmatrix} \begin{pmatrix} 0 & 0 \\ 0 & 1 \end{pmatrix} \frac{1}{\varepsilon_r - \varepsilon_f} \begin{pmatrix} \overline{\varepsilon}_f & -\varepsilon_f \\ -\overline{\varepsilon}_r & \varepsilon_r \end{pmatrix} \begin{pmatrix} n_T \\ n_L \end{pmatrix} \tag{5.18}$$

Evaluating the expression for $\hat{f}_T$ gives:

$$\begin{aligned} \hat{f}_T &= \frac{\varepsilon_f}{\varepsilon_r - \varepsilon_f}\Big(\varepsilon_r(n_T + n_L) - n_T\Big) && (5.19) \\ &= \Big(\frac{\varepsilon_f}{\varepsilon_r - \varepsilon_f} - \varepsilon_r\Big) n_T + \Big(\frac{\varepsilon_f}{\varepsilon_r - \varepsilon_f}\varepsilon_r\Big) n_L && (5.20) \\ &= w_T \; n_T + w_L \; n_L && (5.21) \end{aligned}$$

where in the last line we have reorganized the coefficients in front of n_T and n_L into parameters w_T and w_L which are dependent upon the rates.

Practically, the final estimate of $\hat{f}_T$ can be determined by looping over each event in data, weighting each event using either w_T for those passing the tight selection and w_L for those passing the loose selection, and then summing up all of the weighted events. This is a very useful strategy since it allows one to compute the estimate on the fly using a setup similar to the one already used to process the data itself. Note that since $\varepsilon_r >> \varepsilon_f$ and $0 < \varepsilon_r < 1$, w_T will always be negative. Thus the method will produce negative weights. This is not a concern as long as we keep in mind that the sum is the only thing that is ultimately of interest. However, it is worth noticing that the total estimate can itself be negative when $\varepsilon_r/\overline{\varepsilon}_r < n_T/n_L$. Though this can in general be avoided as long as ε_r is close to unity and if n_L is as large as or larger than n_T, which should usually be the case anyway. In any case, it shows that it is possible to get negative results if the proper conditions are not met.

It will prove useful to rewrite Eq. (5.17) in a more general form:

$$\hat{F} = \mathbf{\Phi} \mathbf{W} \mathbf{\Phi}^{-1} N \tag{5.22}$$

where for the single lepton case

$$N = \begin{pmatrix} n_T \\ n_L \end{pmatrix} \tag{5.23}$$

and

$$\hat{F} = \begin{pmatrix} \hat{f}_T \\ \hat{f}_L \end{pmatrix} . \tag{5.24}$$

The quantity $\mathbf{\Phi}$ is the matrix from Eq. (5.13)

$$\mathbf{\Phi} = \begin{pmatrix} \varepsilon_r & \varepsilon_f \\ \overline{\varepsilon}_r & \overline{\varepsilon}_f \end{pmatrix} \tag{5.25}$$

and $\mathbf{\Phi}^{-1}$ is its inverse. Finally, $\mathbf{W}$ is the fake selection matrix which in this case is identified with

$$\mathbf{W} = \begin{pmatrix} 0 & 0 \\ 0 & 1 \end{pmatrix} \tag{5.26}$$

And if we want only the estimate of the remaining tight leptons like in Eq. (5.18) then we can do

$$\hat{T} = \mathbf{M\Phi W\Phi}^{-1}N \tag{5.27}$$

where

$$\hat{T} = \begin{pmatrix} \hat{f}_T \\ 0 \end{pmatrix} \tag{5.28}$$

and $\mathbf{M}$ is the tight selection matrix:

$$\mathbf{M} = \begin{pmatrix} 1 & 0 \\ 0 & 0 \end{pmatrix} \tag{5.29}$$

So far we have considered only the rates in a single category or bin and for a single lepton. But this process can be extended easily for different bins with in general different rates, (using the lepton p_{T}, for instance) by simply keeping track of each bin using an index. For example, in bin i, one would measure the rates ε_r^i and ε_f^i as well as the values n_T^i and n_L^i to arrive at the expectations for $\hat{f}_T^i$ and $\hat{f}_L^i$ in bin i. Equation (5.22) then becomes $\hat{F}^i = \mathbf{\Phi}^i\mathbf{W}(\mathbf{\Phi}^{-1})^i N^i$. One may then sum over all the of the bins to get a total estimate if desired.

The matrix method can be also extended to multiple leptons, resulting in the generalized matrix method. Consider the three lepton case, which is most relevant to this analysis. Equation (5.27) becomes

$$\hat{T}^{ijk} = \mathbf{M\Phi}^{ijk}\mathbf{W}(\mathbf{\Phi}^{-1})^{ijk}N^{ijk} \tag{5.30}$$

where each of the three leptons can be in separate bins i, j, and k. The matrix $\mathbf{\Phi}^{ijk}$ can by constructed by taking the Kronecker product, denoted by $\otimes$, of the individual single lepton matrices of rates for each lepton:

$$\mathbf{\Phi}^{ijk} = \begin{pmatrix} \varepsilon_r^i & \varepsilon_f^i \\ \bar{\varepsilon}_r^i & \bar{\varepsilon}_f^i \end{pmatrix} \otimes \begin{pmatrix} \varepsilon_r^j & \varepsilon_f^j \\ \bar{\varepsilon}_r^j & \bar{\varepsilon}_f^j \end{pmatrix} \otimes \begin{pmatrix} \varepsilon_r^k & \varepsilon_f^k \\ \bar{\varepsilon}_r^k & \bar{\varepsilon}_f^k \end{pmatrix} \tag{5.31}$$

$$= \begin{pmatrix}
\varepsilon_r^i\varepsilon_r^j\varepsilon_r^k & \varepsilon_r^i\varepsilon_r^j\varepsilon_f^k & \varepsilon_r^i\varepsilon_f^j\varepsilon_r^k & \varepsilon_r^i\varepsilon_f^j\varepsilon_f^k & \varepsilon_f^i\varepsilon_r^j\varepsilon_r^k & \varepsilon_f^i\varepsilon_r^j\varepsilon_f^k & \varepsilon_f^i\varepsilon_f^j\varepsilon_r^k & \varepsilon_f^i\varepsilon_f^j\varepsilon_f^k \\
\varepsilon_r^i\varepsilon_r^j\bar{\varepsilon}_r^k & \varepsilon_r^i\varepsilon_r^j\bar{\varepsilon}_f^k & \varepsilon_r^i\varepsilon_f^j\bar{\varepsilon}_r^k & \varepsilon_r^i\varepsilon_f^j\bar{\varepsilon}_f^k & \varepsilon_f^i\varepsilon_r^j\bar{\varepsilon}_r^k & \varepsilon_f^i\varepsilon_r^j\bar{\varepsilon}_f^k & \varepsilon_f^i\varepsilon_f^j\bar{\varepsilon}_r^k & \varepsilon_f^i\varepsilon_f^j\bar{\varepsilon}_f^k \\
\varepsilon_r^i\bar{\varepsilon}_r^j\varepsilon_r^k & \varepsilon_r^i\bar{\varepsilon}_r^j\varepsilon_f^k & \varepsilon_r^i\bar{\varepsilon}_f^j\varepsilon_r^k & \varepsilon_r^i\bar{\varepsilon}_f^j\varepsilon_f^k & \varepsilon_f^i\bar{\varepsilon}_r^j\varepsilon_r^k & \varepsilon_f^i\bar{\varepsilon}_r^j\varepsilon_f^k & \varepsilon_f^i\bar{\varepsilon}_f^j\varepsilon_r^k & \varepsilon_f^i\bar{\varepsilon}_f^j\varepsilon_f^k \\
\varepsilon_r^i\bar{\varepsilon}_r^j\bar{\varepsilon}_r^k & \varepsilon_r^i\bar{\varepsilon}_r^j\bar{\varepsilon}_f^k & \varepsilon_r^i\bar{\varepsilon}_f^j\bar{\varepsilon}_r^k & \varepsilon_r^i\bar{\varepsilon}_f^j\bar{\varepsilon}_f^k & \varepsilon_f^i\bar{\varepsilon}_r^j\bar{\varepsilon}_r^k & \varepsilon_f^i\bar{\varepsilon}_r^j\bar{\varepsilon}_f^k & \varepsilon_f^i\bar{\varepsilon}_f^j\bar{\varepsilon}_r^k & \varepsilon_f^i\bar{\varepsilon}_f^j\bar{\varepsilon}_f^k \\
\bar{\varepsilon}_r^i\varepsilon_r^j\varepsilon_r^k & \bar{\varepsilon}_r^i\varepsilon_r^j\varepsilon_f^k & \bar{\varepsilon}_r^i\varepsilon_f^j\varepsilon_r^k & \bar{\varepsilon}_r^i\varepsilon_f^j\varepsilon_f^k & \bar{\varepsilon}_f^i\varepsilon_r^j\varepsilon_r^k & \bar{\varepsilon}_f^i\varepsilon_r^j\varepsilon_f^k & \bar{\varepsilon}_f^i\varepsilon_f^j\varepsilon_r^k & \bar{\varepsilon}_f^i\varepsilon_f^j\varepsilon_f^k \\
\bar{\varepsilon}_r^i\varepsilon_r^j\bar{\varepsilon}_r^k & \bar{\varepsilon}_r^i\varepsilon_r^j\bar{\varepsilon}_f^k & \bar{\varepsilon}_r^i\varepsilon_f^j\bar{\varepsilon}_r^k & \bar{\varepsilon}_r^i\varepsilon_f^j\bar{\varepsilon}_f^k & \bar{\varepsilon}_f^i\varepsilon_r^j\bar{\varepsilon}_r^k & \bar{\varepsilon}_f^i\varepsilon_r^j\bar{\varepsilon}_f^k & \bar{\varepsilon}_f^i\varepsilon_f^j\bar{\varepsilon}_r^k & \bar{\varepsilon}_f^i\varepsilon_f^j\bar{\varepsilon}_f^k \\
\bar{\varepsilon}_r^i\bar{\varepsilon}_r^j\varepsilon_r^k & \bar{\varepsilon}_r^i\bar{\varepsilon}_r^j\varepsilon_f^k & \bar{\varepsilon}_r^i\bar{\varepsilon}_f^j\varepsilon_r^k & \bar{\varepsilon}_r^i\bar{\varepsilon}_f^j\varepsilon_f^k & \bar{\varepsilon}_f^i\bar{\varepsilon}_r^j\varepsilon_r^k & \bar{\varepsilon}_f^i\bar{\varepsilon}_r^j\varepsilon_f^k & \bar{\varepsilon}_f^i\bar{\varepsilon}_f^j\varepsilon_r^k & \bar{\varepsilon}_f^i\bar{\varepsilon}_f^j\varepsilon_f^k \\
\bar{\varepsilon}_r^i\bar{\varepsilon}_r^j\bar{\varepsilon}_r^k & \bar{\varepsilon}_r^i\bar{\varepsilon}_r^j\bar{\varepsilon}_f^k & \bar{\varepsilon}_r^i\bar{\varepsilon}_f^j\bar{\varepsilon}_r^k & \bar{\varepsilon}_r^i\bar{\varepsilon}_f^j\bar{\varepsilon}_f^k & \bar{\varepsilon}_f^i\bar{\varepsilon}_r^j\bar{\varepsilon}_r^k & \bar{\varepsilon}_f^i\bar{\varepsilon}_r^j\bar{\varepsilon}_f^k & \bar{\varepsilon}_f^i\bar{\varepsilon}_f^j\bar{\varepsilon}_r^k & \bar{\varepsilon}_f^i\bar{\varepsilon}_f^j\bar{\varepsilon}_f^k
\end{pmatrix} \tag{5.32}$$

and we can solve for the inverse. We are only interested in the components with at least one fake lepton, thus we construct the matrix $\mathbf{W}$ such that:

$$\mathbf{W} = \begin{pmatrix}
0 & 0 & 0 & 0 & 0 & 0 & 0 & 0 \\
0 & 1 & 0 & 0 & 0 & 0 & 0 & 0 \\
0 & 0 & 1 & 0 & 0 & 0 & 0 & 0 \\
0 & 0 & 0 & 1 & 0 & 0 & 0 & 0 \\
0 & 0 & 0 & 0 & 1 & 0 & 0 & 0 \\
0 & 0 & 0 & 0 & 0 & 1 & 0 & 0 \\
0 & 0 & 0 & 0 & 0 & 0 & 1 & 0 \\
0 & 0 & 0 & 0 & 0 & 0 & 0 & 1
\end{pmatrix} \tag{5.33}$$

Furthermore, we have the vector

$$N^{ijk} = \begin{pmatrix} n^{ijk}_{TTT} \\ n^{ijk}_{TTL} \\ n^{ijk}_{TLT} \\ n^{ijk}_{TLL} \\ n^{ijk}_{LTT} \\ n^{ijk}_{LTL} \\ n^{ijk}_{LLT} \\ n^{ijk}_{LLL} \end{pmatrix}. \tag{5.34}$$

In this case, there is only one configuration that gives three tight leptons. Thus, the matrix **M** is constructed to be an 8×8 matrix with 1 in the first element and all other elements equal to 0. This results in the vector T^{ijk} having all elements equal to 0 except for the first, denoted $\hat{f}^{ijk}_{TTT}$, which is the estimate of the number of three lepton events with three tight leptons in bins i, j, and k, where at least one lepton is fake. Putting everything together, we can solve for $\hat{f}^{ijk}_{TTT}$:

$$\begin{aligned} \hat{f}^{ijk}_{TTT} = \; & w_{TTT}(i,j,k)\; n^{ijk}_{TTT} \\ & + (w_{TTL}(i,j,k)\; n^{ijk}_{TTL} + j \leftrightarrow k + i \leftrightarrow k) \\ & + (w_{LLT}(i,j,k)\; n^{ijk}_{LLT} + j \leftrightarrow k + i \leftrightarrow k) \\ & + w_{LLL}(i,k,j)\; n^{ijk}_{LLL} \end{aligned} \tag{5.35}$$

where the terms like $j \leftrightarrow k$ are intended to indicate a copy of the first term in parentheses but with the indices switched as shown. Each term has a w function that is a function of the three lepton indices. These are the weights extracted by the method and they end up taking a simple form:

$$w_{TTT}(i,j,k) = -\frac{\varepsilon^i_r \overline{\varepsilon}^i_f}{\varepsilon^i_r - \varepsilon^i_f} \frac{\varepsilon^j_r \overline{\varepsilon}^j_f}{\varepsilon^j_r - \varepsilon^j_f} \frac{\varepsilon^k_r \overline{\varepsilon}^k_f}{\varepsilon^k_r - \varepsilon^k_f} \tag{5.36}$$

$$w_{TTL}(i,j,k) = \frac{\varepsilon_r^i \bar{\varepsilon}_f^i}{\varepsilon_r^i - \varepsilon_f^i} \frac{\varepsilon_r^j \bar{\varepsilon}_f^j}{\varepsilon_r^j - \varepsilon_f^j} \frac{\varepsilon_r^k \varepsilon_f^k}{\varepsilon_r^k - \varepsilon_f^k} \tag{5.37}$$

$$w_{LLT}(i,j,k) = -\frac{\varepsilon_r^i \varepsilon_f^i}{\varepsilon_r^i - \varepsilon_f^i} \frac{\varepsilon_r^j \varepsilon_f^j}{\varepsilon_r^j - \varepsilon_f^j} \frac{\varepsilon_r^k \bar{\varepsilon}_f^k}{\varepsilon_r^k - \varepsilon_f^k} \tag{5.38}$$

$$w_{LLL}(i,j,k) = \frac{\varepsilon_r^i \varepsilon_f^i}{\varepsilon_r^i - \varepsilon_f^i} \frac{\varepsilon_r^j \varepsilon_f^j}{\varepsilon_r^j - \varepsilon_f^j} \frac{\varepsilon_r^k \varepsilon_f^k}{\varepsilon_r^k - \varepsilon_f^k} \tag{5.39}$$

One can see that for the case of zero or two loose leptons present, the magnitude of the weights are always negative (as long as $\varepsilon_r > \varepsilon_f$), while for those with one or three loose leptons present the magnitude is positive. As with the single lepton case, this is not a concern as the sum should remain positive. However, it might cause some concern to see that the magnitude of these weights decrease the more loose leptons are present, thus the highest magnitude weight will in general be $w(i,j,k)_{TTT}$, which is negative! Fortunately, in the sum this is balanced by the number of leptons observed, which tends to have the opposite trend. As a result, it is those terms with exactly one loose lepton observed that end up dominating the entire calculation, which has a positive weight.

Matrix Method Term	Contribution
TTT	-217.6
TTL	3074.8
TLL	-1.2
LLL	2.7
Other	0.2
Sum	2858.9

Table 5.10: Contribution of individual terms to the overall fake lepton prediction in the fake three lepton pre-selection region. The term called "Other" includes events with more than three leptons.

The generalized matrix method has been evaluated using the rates described later in Sec. 5.4.3.2 at the pre-selection stage described in Sec. 5.3.1. This is shown in Table 5.4.3.1 after summing over all bins i, j, and k. The prediction is shown separately for each term in Eq. (5.35), where for example TTL means the sum over the second line using the weights $w_{TTL}(i,j,k)$. It also includes all other possible contributions from events with more than three leptons, labeled as “Other”. From this it is clear that the TTL term (which also includes the TLT and LTT terms) dominates the calculation, though the effects of the negative weights, in particular from the TTT term, can clearly be seen in the sum. The contributions from events with more than three leptons is observed to be small. Thus, one could arrive at a good approximation to this full method by just using Eq. (5.35) along with just the weights in Eq. (5.36) and (5.37).

In the analysis, a specialized code is used to evaluate the Generalized Matrix Method on all possible combinations of input and output leptons and checks to see which leptons pass the final selection. It uses the on-the-fly weighting method described above and uses a tensor formulation that improves the computational efficiency of the method. This is also used as described in [132]. Uncertainties are calculated by propagating through the uncertainties on the rates. Using the standard propagation of uncertainty, this relies on the derivative of the expectation with respect to the rates. Fortunately, this can be calculated in a straightforward way, though it will not be described here. Correlations between different bins are assumed to be negligible and are ignored. However, since the method relies on calculating multiple weights from the same event, there is a correlation in the uncertainty if these weights end up falling in the same bin. To handle this correlation the uncertainty for these weights are added linearly as opposed to in quadrature when extracting the final uncertainty on the method. The effect of treating the correlation on the uncertainty is observed to be mostly negligible.

5.4.3.2 Rate Determination

The Generalized Matrix Method relies on being able to determine the real and fake rates to be used as inputs to the method. This is usually done by looking into control regions which are designed to be enhanced in sources of real and fake leptons. It is important to note that we can never know with certainty whether a lepton is real or fake. Instead we must be clever enough to find leptons that we are confident are of the appropriate type. One clever trick is to use a method called the tag-and-probe method to better identify real or fake leptons in the control regions; it will be described shortly. Once we have obtained our two separate collections of leptons, one we believe to be rich in real leptons and the other in fake leptons, we can use these leptons to extract the real and fake rates, respectively. The real rate, ε_r^i, in category (or bin) i, is simply defined as the ratio of tight candidate real leptons over the number of tight plus loose candidate real leptons:

$$\varepsilon_r^i = \frac{r_T^i}{r_T^i + r_L^i} \tag{5.40}$$

where r_T^i and r_L^i are the number of tight and loose candidate real leptons in category i, to be distinguished from the n_T^i and n_L^i which are the number of candidate and loose real leptons in the signal regions and whose origin is unknown. Similarly, the fake rate, ε_f^i, in category i, is defined as the ratio of tight candidate fake leptons over the number of tight plus loose candidate fake leptons:

$$\varepsilon_f^i = \frac{f_T^i}{f_T^i + f_L^i} \tag{5.41}$$

where f_T^i and f_L^i are the number of tight and loose candidate fake leptons in category i.

The real and fake rates are not universally the same for all leptons, and in fact can vary strongly. Thus, the choice of categories, i, is an important one. The rates are usually split by lepton flavor and also in bins of at least one kinematic quantity. The splitting of the categories by flavor is very important as the rates are typically very different for electrons and muons. This is in part because the loose and tight selections are usually chosen to be different by necessity. The tight selections are the same as in Sec. 5.2 for both electrons and muons. The loose selections, however, are similar to the tight selection except that the isolation requirements are removed and the object quality classification is loosened for electrons. Another reason for categories by lepton flavor is that the control regions which are enhanced in real and fake sources of leptons are typically different for electrons and muons. Thus, we choose to evaluate the rates separately for both.

The rates also tend to vary as a function of the lepton kinematics. Thus, we further divide the electron and muon categories into sub-categories of mutually exclusive bins of p_{T}.

The number of bins and the bin edges are determined to best capture the shape while also maintaining adequate statistics in each category. In practice it is usually not possible to subdivide the p_{T} by more than a few bins. For the same reason, while the rates also surely vary according to other kinematic criteria, like η, it is usually not possible to subdivide in more than one kinematic variable and still have good statistics.

The control regions are chosen so as to be dominated by a single physics process. For determining the real rates, the control region is chosen to be enhanced in $Z \rightarrow ll$ while the control region for determining the fake rates is chosen to be enhanced in $W \rightarrow l\nu$ plus jets. The reason for this choice is to allow for the application of the tag-and-probe method, which uses one well defined lepton, the "tag", to identify the process, and another lepton, the "probe", as the lepton under study. Both of these control regions have at least one lepton object.

In the control regions enhanced in $Z \rightarrow ll$, if one well-reconstructed tag lepton passing the tight selection is found then the presence of an additional lepton will almost certainly be the other real lepton from the Z decay. Thus, this second "probe" lepton, which can pass either the loose or tight selection requirement is our candidate real lepton. Note that if the probe lepton also passes the tight selection then it could also be used as a tag. In fact, ignoring this possibility can introduce a bias. Thus, we consider both leptons as either tag or probe candidates. Only events where the tag lepton passes the same single lepton triggers and trigger matching requirements as in Sec. 5.3 are used. We also require the presence of a probe lepton that forms an SFOS pair with the tag whose di-lepton mass is within 10 GeVof the Z-mass. Two control regions are formed: one from e^+e^- tag-probe pairs for determining the electron real rates and another from $\mu^+\mu^-$ tag-probe pairs for determining the muon real rates. Since the rates are also determined as a function of the lepton p_{T}, the lepton p_{T} distributions are shown in Fig. 5.14 for the data as well as the expectation. They are show separately for electrons and muons and based on whether the probe leptons pass just the tight selection (the top row of Fig. 5.14) or both the loose and tight selections (the bottom row of Fig. 5.14). The data clearly agrees well with the

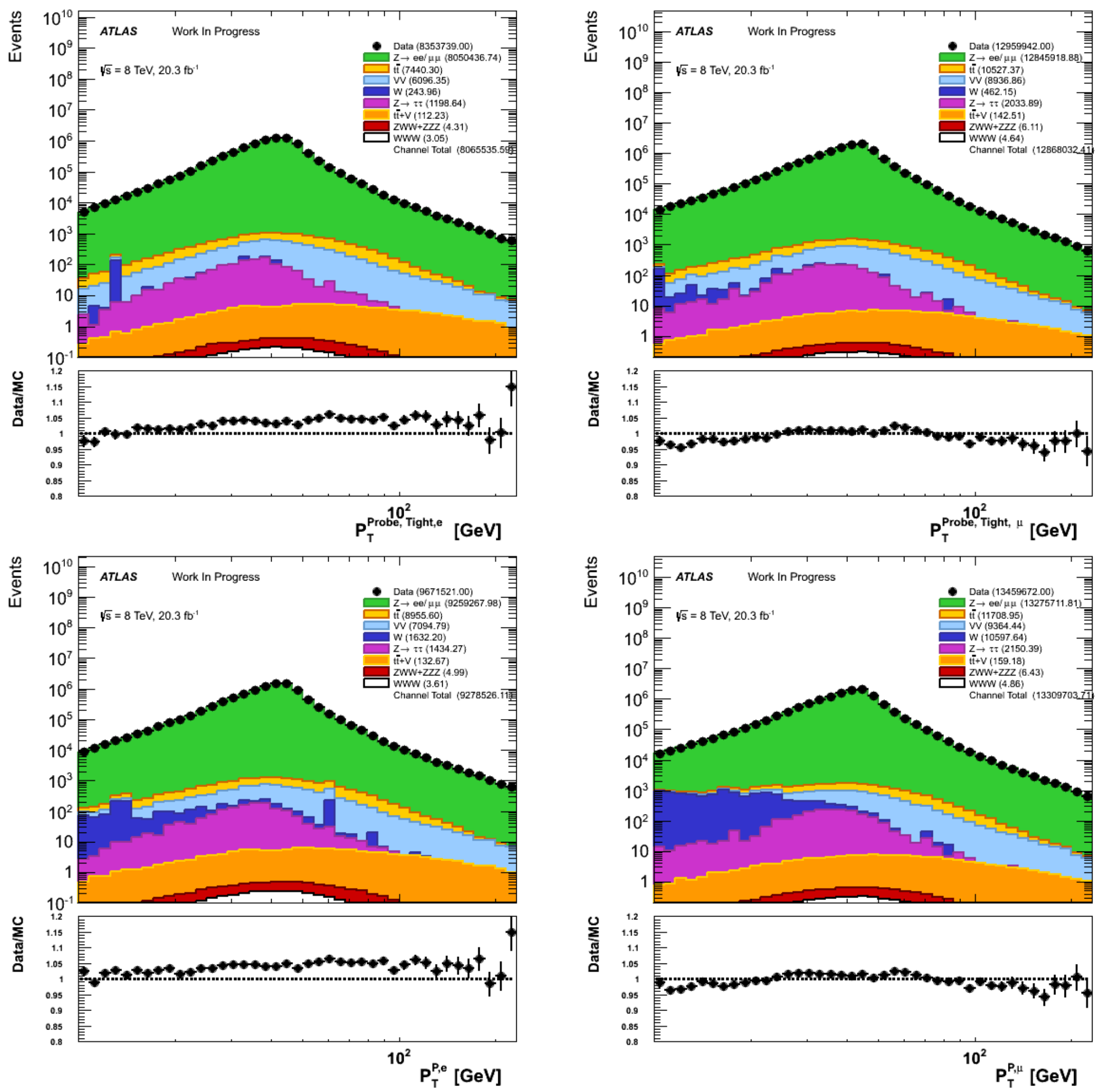

Figure 5.14: Probe lepton p_{T} distributions in SFOS tag and probe control regions used to derive real rates. Electron (left) and muon (right) are shown when the probe lepton is either tight (top) or no additional selection (besides the pre-selection) is required (bottom)

expectation, which is dominated by the $Z \to ll$ process, as expected. The ratio of the candidate real leptons passing just the tight selection over those passing the loose and tight selections determines the real rate according to Eq. (5.40).

The real rates are shown separately for electrons and muons in Fig. 5.15 after adjusting to a coarser binning to improve the statistics. It is interesting to note that the real rates are uniformly lower for electrons than for muons, but both follow the same trend of increasing as a function of the lepton p_{T}, and are relatively high even for the lowest value of 81%. The difference between the rates calculated either the data or the MC exclusively is taken as a systematic uncertainty on the nominal estimate from the data. The rates and the systematic uncertainties are summarized for electrons in Table 5.11 and for muons in Table 5.12.

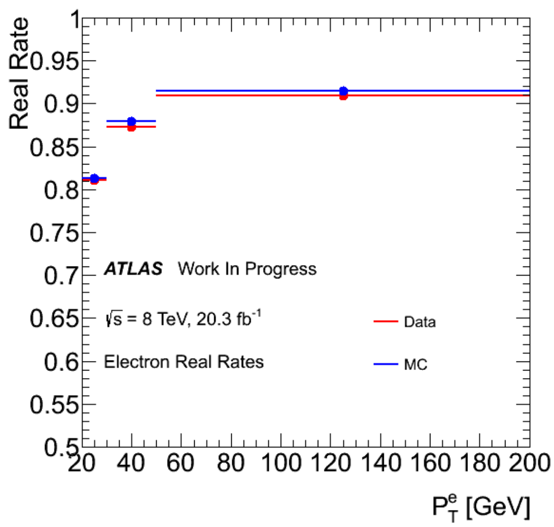

Figure 5.15: Real lepton efficiency as a function of p_{T} and measured in data (red) and MC (blue) for electrons (left) and muons (right).

	Data		MC		
	ε	σ_{stat}	ε	σ_{stat}	σ_{sys}
$p_T \in [20, 30]$ GeV	0.8105	0.0011	0.8134	0.0013	0.0028
$p_T \in [30, 50]$ GeV	0.8732	0.0005	0.8794	0.0006	0.0062
$p_T > 50$ GeV	0.9097	0.0012	0.9150	0.0012	0.0053

Table 5.11: Measured real efficiencies for electrons including statistical and systematic absolute uncertainties. Systematic is calculated by taking the difference between the efficiencies measured in data and MC. The efficiency measured in data is used as the nominal central value.

On the other hand, in the $W \to l\nu$ + Jets control region there is only one real lepton being produced by the process. If a well reconstructed tag lepton passing the tight selection is found in this control region it is most likely coming from the W decay. In this case, if we measure a second "probe" lepton it is most likely a jet faking a lepton. Thus, we have

	Data		MC		
	ε	σ_{stat}	ε	σ_{stat}	σ_{sys}
$p_T \in [20, 30]$ GeV	0.9217	0.0010	0.9291	0.0012	0.0074
$p_T \in [30, 50]$ GeV	0.9700	0.0004	0.9737	0.0006	0.0038
$p_T > 50$ GeV	0.9862	0.0011	0.9878	0.0011	0.0017

Table 5.12: Measured real efficiencies for muons including statistical and systematic absolute uncertainties. Systematic is calculated by taking the difference between the efficiencies measured in data and MC. The efficiency measured in data is used as the nominal central value.

found a candidate fake lepton. The control regions are formed by requiring the presence of one tag lepton passing the tight selection plus trigger requirements of Sec. 5.3 with a $p_{\mathrm{T}} > 40$ GeV and a probe lepton passing either the loose or tight selection. The leptons are required to have the same sign, since on average a fake lepton will have equal probably of a positive or negative charge, while background processes like WW,$t\bar{t}$, and Z production produce opposite-sign lepton pairs. Only muons are used as tag leptons. The reason for this is that the chance of an electron passing tight selection to be a jet fake is higher than that for muons. It is also possible for electrons to come from photon conversion (PC) while for muons this is very unlikely. Thus, using only muons as tag leptons further reduces contamination from backgrounds in this control region. The control region is then split based on whether the probe lepton is an electron or a muon in order to determine the electron and muon fake rates separately. Events with additional leptons are thrown away. To suppress contamination from multi-jet background processes to the $W \to l\nu$ + Jets process, like QCD, a cut of $E_{\mathrm{T}}^{\mathrm{miss}} > 10$ GeV is also applied.

The fake rate that is determined depends upon the source of fake leptons. One way to assess this sensitivity is to consider the number of b-jets present in the event. We consider two different cases regarding the b-jet multiplicity: inclusive and exclusive. The inclusive case makes no requirement on the number of b-jets while the exclusive case asks that at least one b-jet is present. These two different scenarios are ultimately compared in order to assess a final systematic on the fake rate. The exclusive case is used as the nominal estimate.

The processes contributing to the fake rate are known to not be well modeled by MC, as discussed earlier in Sec. 5.4.3. This is the primary reason for attempting to estimate the fake lepton contribution from data in the first place. Thus, we do not seek to describe the data using MC. However, this control region is also not as pure with sources of fake leptons as the real lepton control region is for real leptons, because the neutrino in the $W \to l\nu$ control region cannot be identified directly. In particular, there is a significant contamination from processes with real leptons, like WW, $t\bar{t}$, and Z processes as well as processes from photon conversion sources, even after the attempts at reducing these backgrounds in the control region selection described above. These backgrounds can be modeled using MC and so we attempt to subtract the MC estimates of these backgrounds from the data before extracting the fake rates. In effect, this means that the values of f_T^i and f_L^i in Eq. (5.41) are not taken directly from the data but are instead corrected by the subtraction

$$f_{T/L}^i = N_{T/L}^{\mathrm{Data},i} - N_{T/L}^{\mathrm{Real},i} - N_{T/L}^{\mathrm{PC},i} \tag{5.42}$$

where $N_{T/L}^{\mathrm{Data},i}$ is the number of tight or loose probe leptons selected from data in bin i of the fake lepton control region, while $N_{T/L}^{\mathrm{Real},i}$ and $N_{T/L}^{\mathrm{PC},i}$ are the number of tight or loose probe leptons estimated from MC to fall in bin i of the fake lepton control region for real lepton and photon conversion background sources, respectively. The separate contributions to these terms are shown as a function of the lepton p_{T} for muons in Fig. 5.16 and for electrons in Fig. 5.17. They are split based on whether the lepton passes just the tight selection or both the tight and loose selections and also by the inclusive and exclusive b-jet multiplicity categories. These are then used to calculate the fake rate as in Eq. (5.41). A detailed breakdown of the numbers going into the fake rate calculation are summarized in the exclusive b-jet multiplicity category for electrons in Table 5.13 and for muons in Table 5.14.

		$p_T \in [20, 30]$ GeV	$p_T \in [30, 50]$ GeV	$p_T > 50$ GeV
Tight	Data	44	53	77
	Real	9.52 ± 0.76	17.2 ± 1.1	39.7 ± 2
	PC	6.37 ± 0.95	14.9 ± 4.5	26.6 ± 2
	Data - Real - PC	28.1 ± 6.7	20.9 ± 8.7	10.6 ± 9.2
All	Data	662	450	297
	Real	22.0 ± 1.3	29.8 ± 1.9	57.2 ± 5.5
	PC	128 ± 19	97 ± 14	109 ± 15
	Data - Real - PC	512 ± 32	324 ± 26	130 ± 23
Rate (Tight/All)		0.055 ± 0.014	0.065 ± 0.027	0.082 ± 0.072

Table 5.13: Calculation of fake rate for electrons when $N_{b-\mathrm{Jet}} > 0$.

		$p_T \in [20, 30]$ GeV	$p_T \in [30, 40]$ GeV	$p_T > 40$ GeV
Tight	Data	48	23	63
	Real	8.85 ± 0.68	7.78 ± 0.59	26.4 ± 1.1
	PC	0.0 ± 0	0.0 ± 0	0.0 ± 0
	Data - Real - PC	39.1 ± 7	15.2 ± 4.8	36.6 ± 8
All	Data	1910	750	774
	Real	19.8 ± 2.9	13.5 ± 2	30.5 ± 1.5
	PC	9.3 ± 9.2	0.0 ± 0	0.0 ± 0
	Data - Real - PC	1881 ± 45	737 ± 27	744 ± 28
Rate (Tight/All)		0.0208 ± 0.0037	0.0207 ± 0.0066	0.049 ± 0.011

Table 5.14: Calculation of fake rate for muons when $N_{b-\mathrm{Jet}} > 0$.

5.4.3.3 Fake lepton background validation

The performance of the fake background estimate is tested in a control region designed to be enhanced in this background while being orthogonal to the signal regions described in Sec. 5.3.2. The control region starts by using the event pre-selection region described in Section 5.3.1. To reduce contamination from the WZ process, we require that there are 0 SFOS lepton pairs present in the event. Finally, in order to enforce orthogonality with the signal regions we require that $N_{b-\mathrm{Jet}} \geq 1$. As such it is very close to the 0 SFOS signal region where we are most sensitive.

The total predicted events and observed data in this region are shown in Table 5.15. The control region is clearly dominated by the fake lepton background, with 10.91 ± 0.73 (stat.) fake lepton events predicted out of a total of 14.72 ± 0.73 (stat.). Furthermore, the shapes of the predicted and observed kinematic distributions are also shown along with the fake

	Event Yield
WZ	0.338 ± 0.021
ZZ	0.0747 ± 0.0064
$Z\gamma$	0.0058 ± 0.0058
$ZWW + ZZZ$	0.026 ± 0.005
$t\bar{t} + V$	3.228 ± 0.039
Fake (data-driven)	10.91 ± 0.73
WWW	0.1431 ± 0.0052
Expected Background	14.58 ± 0.73
Expected Signal + Background	14.72 ± 0.73
Observed Data	18

Table 5.15: Expected and observed yields for the fake lepton control region. Only statistical uncertainties are shown.

lepton background systematic uncertainties in Fig. 5.18. From this, we can see that the data is largely consistent with the prediction. This is true not just for the overall normalization, but also for the shapes, though the control region is also limited by the number of statistics available. Since the fake lepton background seems to describe the data well in this control region, we have confidence in the method and choose to use the estimate also in the signal regions.

5.5 Event Yields

5.5.1 Event Pre-selection

The signal plus background model (described in detail in Sec. 5.4) is compared to data at pre-selection, defined in Sec. 5.3.1, for a few different kinematic distributions in Fig. 5.19. In the upper plot of each distribution, the colored histograms represent the different categories contributing to the signal plus background model and are split by color based on the category. Hashed bands are shown on the stacked histograms representing the size of the systematic uncertainties on the model, described in Sec. 5.6. The data is shown in the black points where the bars on the points represent the statistical uncertainty on the data. The lower plot shows the ratio of the data over the model. In this case, the error bars correspond to the statistical uncertainty on the ratio due to both the data and the model.

The red band shows the size of the systematic uncertainties with respect to the model. The model is said to be consistent with the data if the ratio is compatible with unity after considering statistical and systematic uncertainties. The different distributions are chosen primarily because of their potential to discriminate between signal and background. The number of signal events at pre-selection is predicted to be 9.78 while the number of predicted background events is 2388.48. This is consistent with the 2472 events observed in the data.

Upon splitting the pre-selection region based on the number of SFOS pairs, we end up with the signal and background predictions in Fig. 5.20, where we can see differences in the branching fraction for the signal to fall into each of the three signal regions. In the 0 and 2 SFOS regions, roughly 2.5 signal events are predicted whereas closer to 5 signal events are predicted in the 1 SFOS region, totaling about 10 signal events predicted at the pre-selection stage. Shifting to looking at the background, perhaps the most striking feature of this plot is the clear difference in background yield and background composition between the 0 SFOS region and the 1 and 2 SFOS regions. More than 1000 background events are predicted in both the 1 and the 2 SFOS regions, but only about 30 background events are predicted in the 0 SFOS region. Clearly then, the advantage of splitting the signal region based on this classification comes when looking at the background, specifically the electroweak WZ and ZZ backgrounds where SFOS lepton pairs may be produced from the decay of the Z boson(s). Consider only the case where the WZ and ZZ decay to either e or μ. The WZ production process is thus characterized by 3 leptons with at least 1 SFOS lepton pair which comes from the Z. If all three leptons from the WZ decay have been reconstructed, then there is a 50 % chance the third lepton will also be able to form a SFOS pair with one of the leptons from the Z decay. Thus, the WZ background will split evenly between the 1 and 2 SFOS classification. Something similar occurs for the ZZ background except that the fourth lepton in the decay must be lost (usually due to possessing a low p_{T}). The large cross-section for these processes means that they become the dominant backgrounds in the 1 and 2 SFOS regions. The 0 SFOS signal region is mostly spared from contamination by these large processes but still includes both the WZ and ZZ processes as background due to the non-negligible (albeit small) effect of mis-measurement of the electron charge described in Sec. 5.4.2. The 0 SFOS signal region is thus unique in having a small background which is almost entirely reducible and dominated instead by the fake background, described in Sec. 5.4.3, along with the aforementioned sub-dominant effect of electron charge mis-identification.

5.5.2 Optimization

A more stringent selection must be applied on top of the pre-selection in Sec. 5.5.1 in order to obtain any sensitivity to the signal. The best selection, however, is not known *a priori*. We attempted to find the best possible selection by starting from a list of kinematic quantities, chosen based on heuristic arguments. These kinematic quantities, along with the signal plus background model, are passed into an optimization framework that systematically seeks to simultaneously maximize the predicted signal and the precision on the final measurement.

The optimization framework considers several thousand independent permutations of the different kinematic quantities, along with variations of the selection thresholds on these cuts, to form combinations of selection cuts which could become a final selection. For each combination, or operating point, that is considered, the signal plus background model is evaluated to determine the expected yields and systematic uncertainties given that selection. The LHC data is not used in the optimization. The prediction is then plugged into the statistical framework described in Sec. 5.7 to extract a value on the expected precision of the measurement. For each operating point, the value on the precision is plotted against the expected signal yield. With some discretion, we then choose the operating point that maximizes the signal yield and gives the smallest absolute precision on the measurement.

The final selection is presented in Table 5.4. Details of the specific cut thresholds that are chosen can be understood by looking closer at some of the quantities used as input to the optimization. For instance, it is observed that different $E_{\mathrm{T}}^{\mathrm{miss}}$ and Z-veto thresholds are chosen for the 1 and 2 SFOS regions. This can be understood to come from a correlation between these two quantities due to their ability to isolate the $Z\gamma$ background. The $Z\gamma$ background shows up in the low-shoulder of the Z-peak in the m_{SFOS} distribution and at low MET. This can be seen both for the 1 and 2 SFOS regions in Fig. 5.21. As a result, the $Z\gamma$ background can be removed either by tuning the Z-mass window used in the veto above, or by removing events with low $E_{\mathrm{T}}^{\mathrm{miss}}$. Thus, the optimization shows that there is some correlation between the Z-veto window and the $E_{\mathrm{T}}^{\mathrm{miss}}$ selection threshold. In the 1 SFOS region, there is a larger contribution from $Z\gamma$ processes than in the 2 SFOS region. This process mostly shows up in the low shoulder of the Z peak. The optimization prefers removing this $Z\gamma$ contribution by setting an asymmetric Z-window in the 1 SFOS region, with the boundaries being 35 GeV below the Z-pole and 20 GeV above and then keeping the $E_{\mathrm{T}}^{\mathrm{miss}}$ cut a little loose, with a threshold of $E_{\mathrm{T}}^{\mathrm{miss}} > 45$ GeV. In the 2 SFOS region, however, the $Z\gamma$ contribution is not as prominent and the optimization happens to prefer a symmetric window of ± 20 GeV around the Z-pole. The looser Z-veto then allows for a tighter missing E_T cut with a threshold of $E_{\mathrm{T}}^{\mathrm{miss}} > 55$ GeV.

The absence of any cut on the $E_{\mathrm{T}}^{\mathrm{miss}}$ distribution in the 0 SFOS region can be better understood by looking at the the efficiency for selection between the signal and the background as a function of the $E_{\mathrm{T}}^{\mathrm{miss}}$ selection threshold. This is shown in Fig. 5.22 both after pre-selection and in the 0 SFOS region. Clearly, the signal efficiency closely follows the background efficiency in the 0 SFOS region. Thus, there is no change in the signal-to-background ratio when cutting on the $E_{\mathrm{T}}^{\mathrm{miss}}$ distribution in the 0 SFOS region and thus no improvement in the sensitivity. On the other hand, there are large shape differences between the signal and background efficiencies at pre-selection, with the signal efficiency remaining flatter at low values of the $E_{\mathrm{T}}^{\mathrm{miss}}$ threshold. So, from this one would expect a selection on the $E_{\mathrm{T}}^{\mathrm{miss}}$ threshold to be useful in the 1 and 2 SFOS regions which have a similar background composition. Indeed, this is what we observe.

The threshold for the jet multiplicity cut of $N_{\mathrm{Jet}} \leq 1$ applied in all signal regions is also determined from the optimization. One might expect that a different value for the threshold, such as a complete veto on the presence of jets, would perform better. Indeed, looking at the efficiency for selection on the jet multiplicity in Fig. 5.23 does show a much stronger background rejection when applying a veto in both the pre-selection region and especially in the 0 SFOS region where there is a larger contribution from fakes due to hadronic activity. The signal rejection, however, of about 40% observed in both regions, is prohibitive. Loosening the selection to the nominal threshold of $N_{\mathrm{Jet}} \leq 1$ instead preserves 90% of the signal, which is quite precious. We are still able to remove much of the fake background in the 0 SFOS region by vetoing events with b-tagged jets as can be seen in Fig. 5.24. It is possible that using a b-tagging operating point with an even higher b-tagging efficiency would further improve the sensitivity in the 0 SFOS region. The nominal operating point used here, however, is the highest efficiency operating point available. Clearly, there is no advantage gained from using a looser operating point as this would only cut less on the background without having an impact on the signal.

The $\Delta\varphi(lll, E_T^{\mathrm{Miss}})$ distribution for the signal is observed to be more back-to-back (i.e. closer to π) than that for the background. This is especially true in the 0 SFOS region, as can be seen from the efficiencies plotted as a function of the $\Delta\varphi(lll, E_T^{\mathrm{Miss}})$ selection threshold shown in Fig. 5.25. The selection efficiency for the signal is relatively flat for most of the range up to about a threshold of $|\Delta\varphi(lll, E_T^{\mathrm{Miss}})| > 2.5$ in both the pre-selection and 0 SFOS regions. At this threshold the signal selection efficiency is about 80%. The optimization prefers a selection around this range for all signal regions. The optimization also considered selecting on alternative definitions of $\Delta\phi$ that only considered one of the three leptons but this was observed to not offer as strong of a separation between the signal and background.

The efficiencies as a function of the lepton p_{T} threshold are shown in Fig. 5.26. The signal efficiency is observed to be slightly flatter than the background efficiency. The signal efficiency, however, still falls fairly rapidly as a function of the lepton p_{T} threshold. Thus, a tighter selection on the lepton p_{T} is not preferred by the optimization. We also considered applying different p_{T} thresholds to the leptons based on their p_{T} order and other criteria, but this did not show any increased performance.

Finally, we considered other quantities like the transverse mass of the $E_{\mathrm{T}}^{\mathrm{miss}}$ and three lepton system:

$$m_T^{lll} = \sqrt{2p_T^{lll}E_{\mathrm{T}}^{\mathrm{miss}}(1 - \cos(\Delta\varphi(lll, E_{\mathrm{T}}^{\mathrm{miss}})))} \tag{5.43}$$

as well as vetoes on additional leptons with lower p_{T}, and various di-lepton mass selections. None of these, however, were preferred by the optimization.

5.5.3 Signal Region Yields

The optimized signal region selection described in Sec. 5.5.2 and Sec. 5.3.2 and listed in Table 5.4 is applied to the data as well as the signal plus background model. A plot of the predicted yields for the signal plus background, along with systematic uncertainties, is compared to the data for each signal region in Fig. 5.27. A detailed breakdown of the predicted yields and overall uncertainties on each background as well as the signal prediction and observed data are presented in Table 5.16. A breakdown of the systematic uncertainty contributions to the signal and the backgrounds in each signal region are summarized in Table 5.17. More details are presented about each signal region below.

	0 SFOS	1 SFOS	2 SFOS
WZ	$0.6176 \pm 0.0043\ ^{+0.0699}_{-0.0701}$	$11.89 \pm 0.14\ ^{+1.32}_{-1.29}$	$9.05 \pm 0.13\ ^{+0.99}_{-1.00}$
ZZ	$0.0658 \pm 0.0039\ ^{+0.0112}_{-0.0112}$	$0.581 \pm 0.016\ ^{+0.106}_{-0.105}$	$0.477 \pm 0.011\ ^{+0.095}_{-0.086}$
$WWZ + WZZ$	$0.1126 \pm 0.0099\ ^{+0.0146}_{-0.0117}$	$0.140 \pm 0.011\ ^{+0.015}_{-0.013}$	$0.0785 \pm 0.0080\ ^{+0.0097}_{-0.0106}$
$t\bar{t}$+V	$0.0388 \pm 0.0043\ ^{+0.0061}_{-0.0077}$	$0.0503 \pm 0.0048\ ^{+0.0074}_{-0.0089}$	$0.0239 \pm 0.0033\ ^{+0.0074}_{-0.0058}$
DPS	$0.0 \pm 0.0\ ^{+0.0}_{-0.0}$	$0.0088 \pm 0.0080\ ^{+0.0080}_{-0.0084}$	$0.023 \pm 0.016\ ^{+0.019}_{-0.029}$
$Z\gamma$	$0.0 \pm 0.0\ ^{+0.0}_{-0.0}$	$0.20 \pm 0.13\ ^{+0.29}_{-0.13}$	$0.110 \pm 0.096\ ^{+0.163}_{-0.288}$
Fake	$1.51 \pm 0.26\ ^{+1.40}_{-1.29}$	$1.90 \pm 0.34\ ^{+1.90}_{-1.77}$	$0.49 \pm 0.16\ ^{+0.47}_{-0.46}$
Signal	$1.344 \pm 0.015\ ^{+0.073}_{-0.079}$	$1.394 \pm 0.016\ ^{+0.073}_{-0.082}$	$0.611 \pm 0.010\ ^{+0.032}_{-0.036}$
Total Background	$2.35 \pm 0.26\ ^{+1.40}_{-1.30}$	$14.77 \pm 0.39\ ^{+2.36}_{-2.22}$	$10.25 \pm 0.23\ ^{+1.15}_{-1.22}$
Total Predicted	$3.69 \pm 0.26\ ^{+1.41}_{-1.30}$	$16.16 \pm 0.39\ ^{+2.33}_{-2.18}$	$10.86 \pm 0.23\ ^{+1.12}_{-1.19}$
Data	5	13	6

Table 5.16: A summary of the expected yields compared to data for all three signal regions. Statistical uncertainties are shown as a symmetric uncertainty on the central value. Systematic uncertainties are shown as an asymmetric uncertainty and are shown after taking the quadrature sum of all individual uncertainties. In the actual analysis, each systematic uncertainty is treated as an individual nuisance parameter and are NOT added in quadrature. The presentation here serves only as a demonstration of the overall size of the systematic uncertainties for each source in the individual signal regions.

Source of Uncertainty	Signal			Backgound		
	0 SFOS	1 SFOS	2 SFOS	0 SFOS	1 SFOS	2 SFOS
Electron	$^{+1.56}_{-1.47}$	$^{+1.66}_{-1.61}$	$^{+1.02}_{-1.06}$	$^{+0.68}_{-0.69}$	$^{+2.34}_{-1.49}$	$^{+1.05}_{-1.54}$
Muon	$^{+0.56}_{-0.54}$	$^{+0.54}_{-0.54}$	$^{+0.74}_{-0.83}$	$^{+0.19}_{-0.19}$	$^{+1.09}_{-0.48}$	$^{+0.81}_{-0.80}$
MET	$^{+1.38}_{-1.75}$	$^{+0.71}_{-0.89}$	$^{+0.23}_{-0.35}$	$^{+0.79}_{-0.73}$	$^{+1.38}_{-0.11}$	$^{+2.12}_{-2.66}$
Jet	$^{+2.36}_{-2.26}$	$^{+2.06}_{-2.34}$	$^{+1.56}_{-2.22}$	$^{+1.10}_{-1.06}$	$^{+2.74}_{-2.03}$	$^{+2.94}_{-4.41}$
Trigger	$^{+0.09}_{-0.09}$	$^{+0.09}_{-0.09}$	$^{+0.20}_{-0.20}$	$^{+0.06}_{-0.06}$	$^{+0.09}_{-0.09}$	$^{+0.21}_{-0.21}$
Matrix Method	—	—	—	$^{+58.56}_{-53.98}$	$^{+12.64}_{-11.78}$	$^{+4.34}_{-4.23}$
Charge Mis-ID	—	—	—	$^{+0.45}_{-0.44}$	—	—
Pileup	$^{+0.92}_{-0.77}$	$^{+1.10}_{-1.30}$	$^{+1.50}_{-1.24}$	$^{+0.52}_{-0.42}$	$^{+0.22}_{+0.00}$	$^{+1.39}_{-1.40}$
Luminosity	$^{+2.80}_{-2.80}$	$^{+2.80}_{-2.80}$	$^{+2.80}_{-2.80}$	$^{+2.80}_{-2.80}$	$^{+2.80}_{-2.80}$	$^{+2.80}_{-2.80}$
Theory	$^{+5.55}_{-3.75}$	$^{+5.55}_{-3.75}$	$^{+5.55}_{-3.75}$	$^{+2.66}_{-2.66}$	$^{+8.07}_{-8.07}$	$^{+8.85}_{-8.85}$
Statistical	$^{+1.14}_{-1.14}$	$^{+1.12}_{-1.12}$	$^{+1.70}_{-1.70}$	$^{+10.99}_{-10.99}$	$^{+2.67}_{-2.67}$	$^{+2.20}_{-2.20}$

Table 5.17: Categorized systematic uncertainties for signal and background predictions in all three signal regions. All uncertainties are shown as a percentage of the nominal prediction.

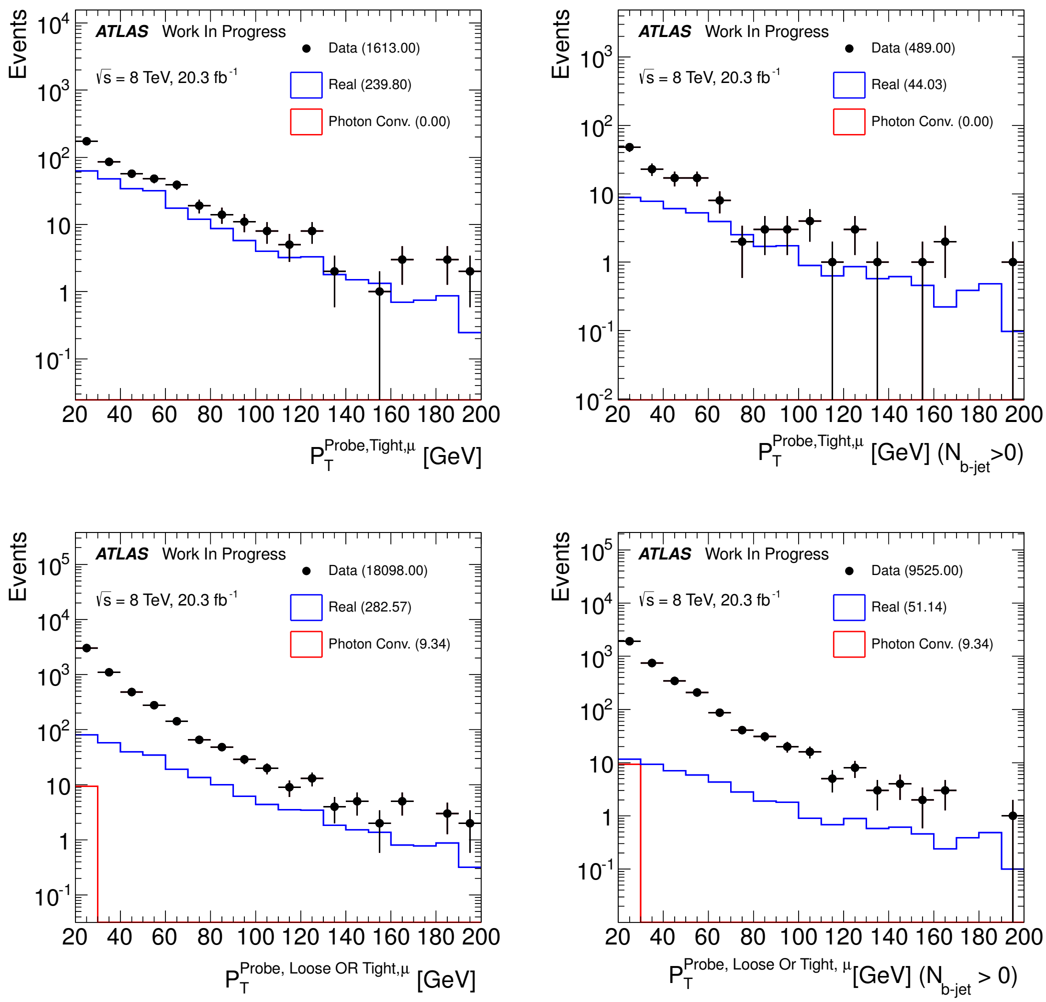

Figure 5.16: Transverse momentum distributions p_{T} of tight probe muons (top) and loose OR tight probe muons (bottom) passing signal selection criteria in the control Same-Sign $\mu - \mu$ control region without any additional requirement on b-jets in the event (left) and at least one b-jet (right). The amount observed in data (black points) corresponds to $N_T^{\mathrm{Data},i} + N_L^{\mathrm{Data},i}$ (bottom) and $N_T^{\mathrm{Data},i}$ (top) following the notation in Eq. 5.42. Meanwhile, the contribution determined in MC to come from real leptons (blue line) and from photon conversion (red line) are shown separately; they are not stacked. The real lepton contribution corresponds to $N_T^{\mathrm{Real},i} + N_L^{\mathrm{Real},i}$ (bottom) and $N_T^{\mathrm{Real},i}$ (top) and the photon conversion contribution corresponds to $N_T^{\mathrm{PC},i} + N_L^{\mathrm{PC},i}$ (bottom) and $N_T^{\mathrm{PC},i}$ (top) again using the notation in Eq. 5.41. The photon conversion is observed to be negligible for muons.

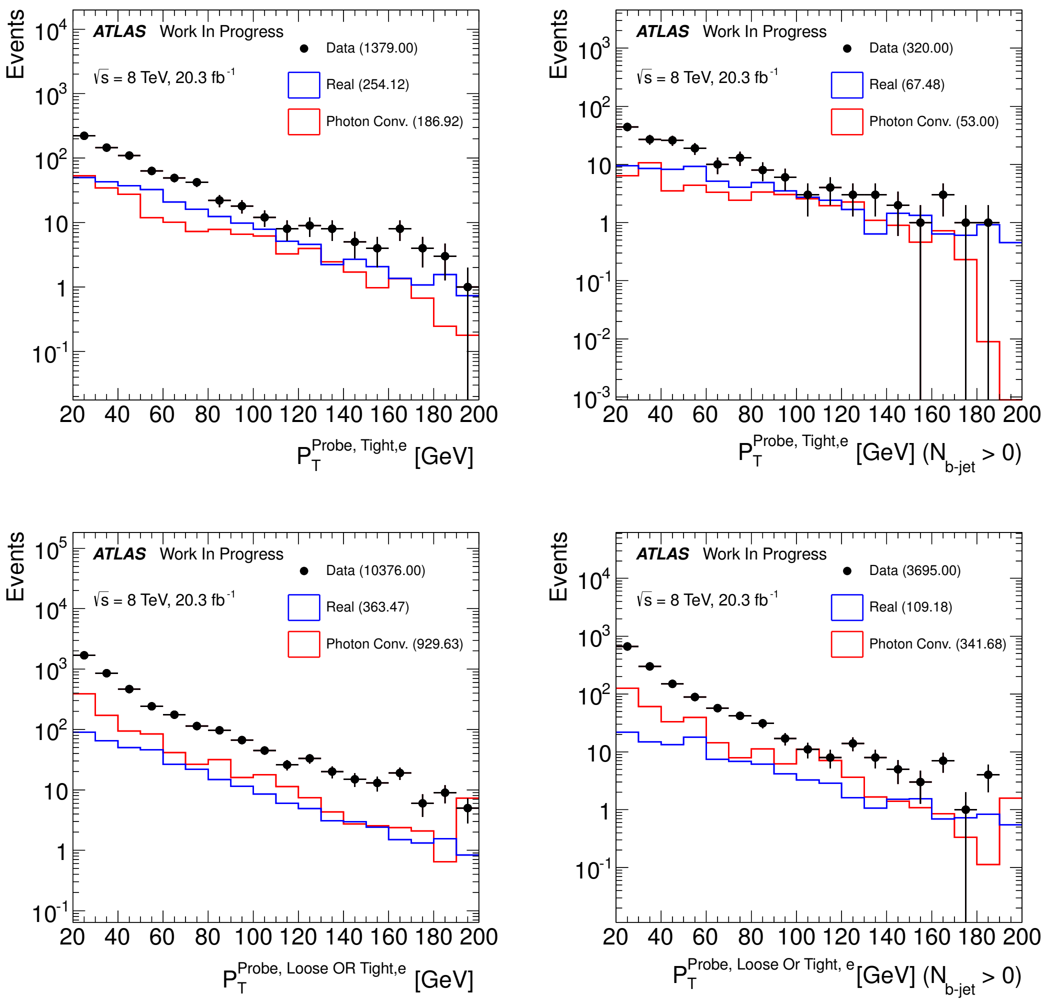

Figure 5.17: Transverse momentum distributions p_{T} of tight probe electrons (top) and loose OR tight probe muons (bottom) passing signal selection criteria in the control Same-Sign $e-\mu$ control region without any additional requirement on b-jets in the event (left) and at least one b-jet (right). The amount observed in data (black points) corresponds to $N_T^{\mathrm{Data},i} + N_L^{\mathrm{Data},i}$ (bottom) and $N_T^{\mathrm{Data},i}$ (top) following the notation in Eq. 5.42. Meanwhile, the contribution determined in MC to come from real leptons (blue line) and from photon conversion (red line) are shown separately; they are not stacked. The real lepton contribution corresponds to $N_T^{\mathrm{Real},i} + N_L^{\mathrm{Real},i}$ (bottom) and $N_T^{\mathrm{Real},i}$ (top) and the photon conversion contribution corresponds to $N_T^{\mathrm{PC},i}+N_L^{\mathrm{PC},i}$ (bottom) and $N_T^{\mathrm{PC},i}$ (top) again using the notation in Eq. 5.41.

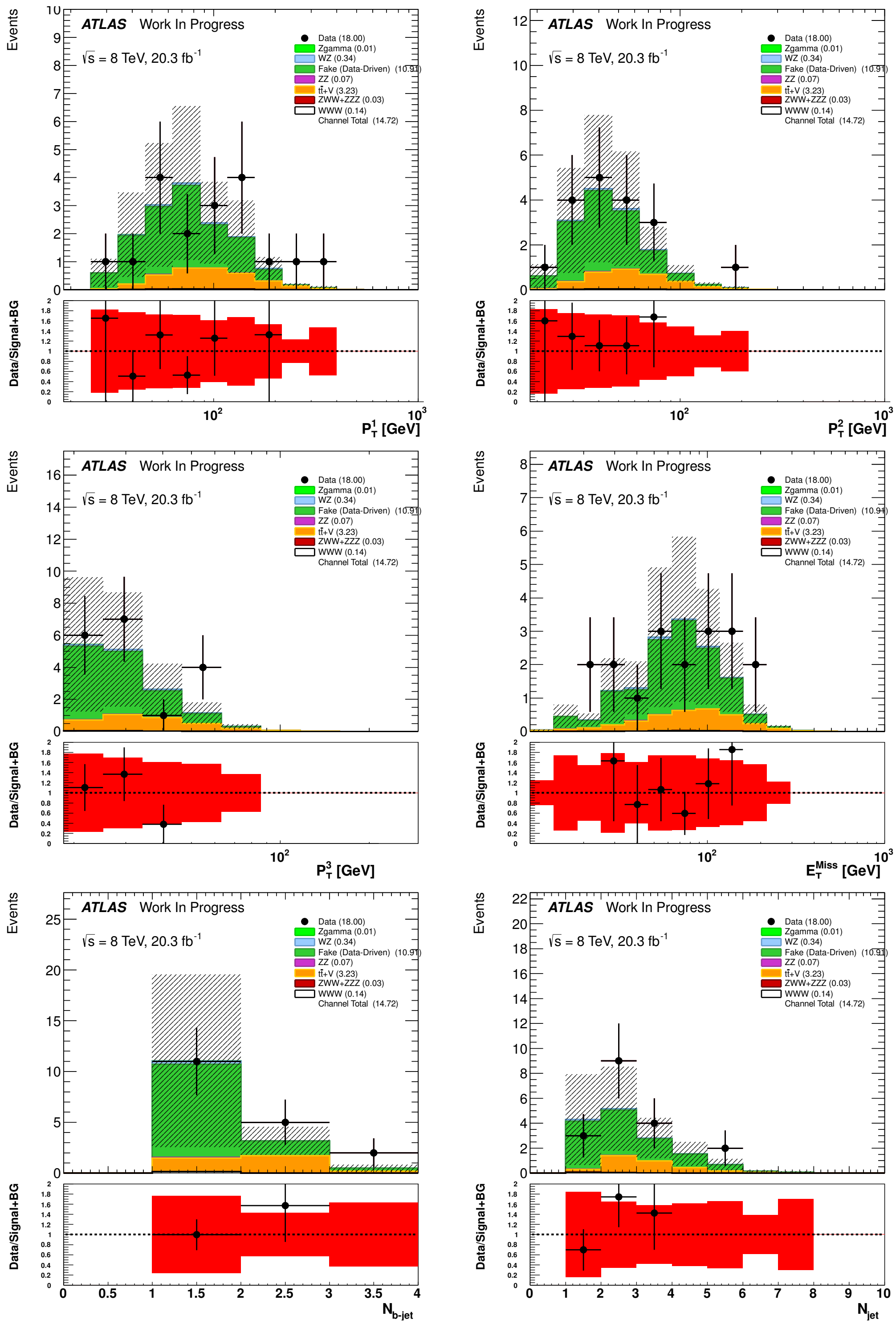

Figure 5.18: Distributions in a control region designed to study the data-driven fake lepton background estimate.

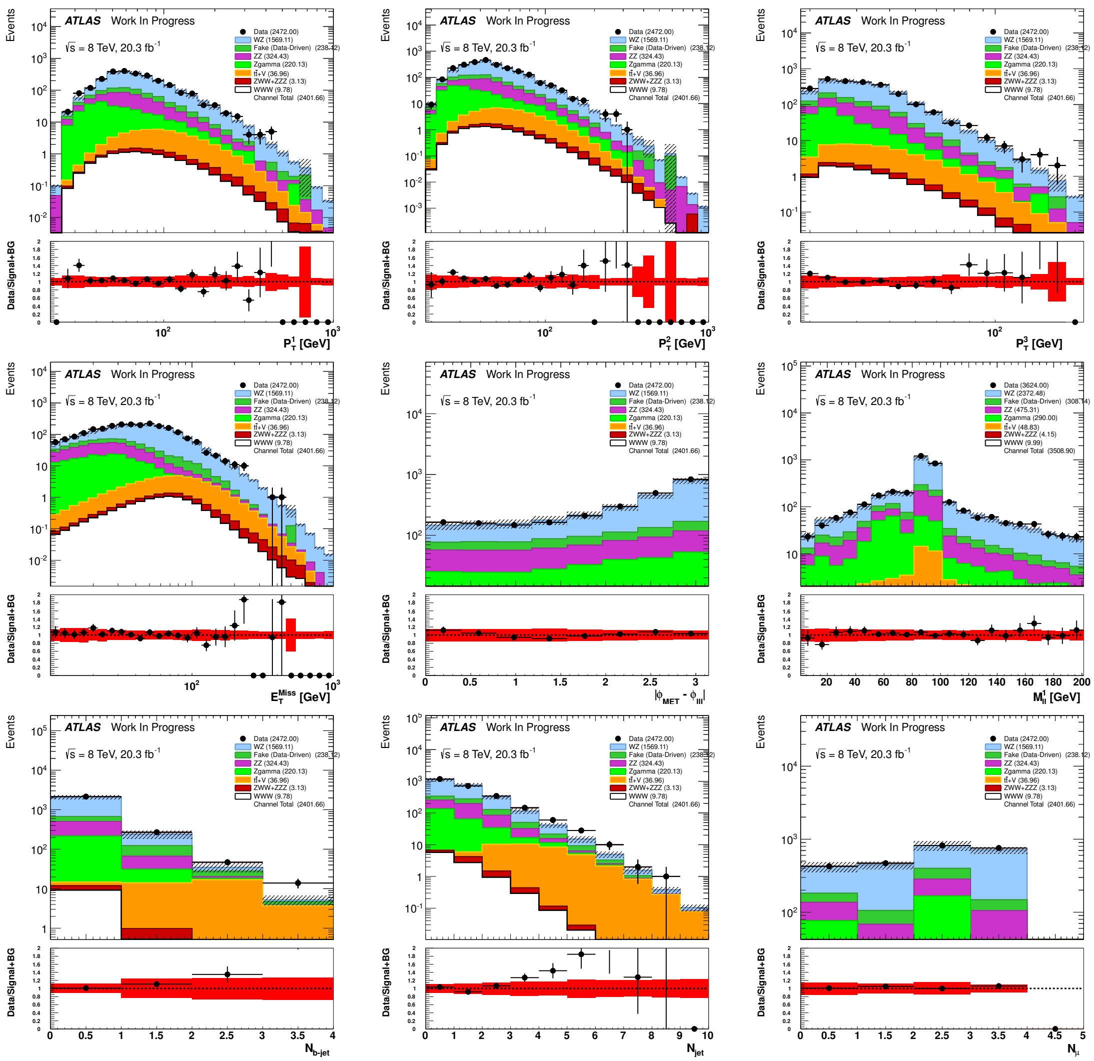

Figure 5.19: Distributions showing the observed data compared to the background estimate at event pre-selection. From top to bottom and left to right, these distributions are: the leading, sub-leading, and minimum lepton p_{T} (ordered by their p_{T}), $E_{\mathrm{T}}^{\mathrm{miss}}$, $\Delta\varphi(lll, E_{T}^{\mathrm{Miss}})$, m_{SFOS}, N_{Jet}, $N_{b-\mathrm{Jet}}$, and N_{μ}.

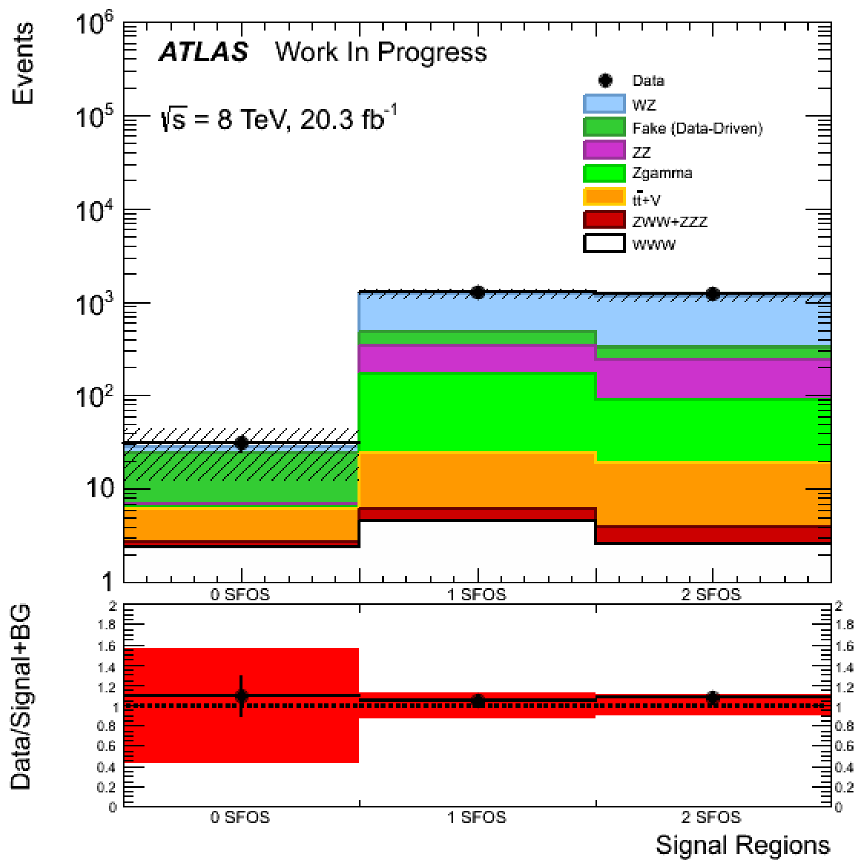

Figure 5.20: Yields at event pre-selection in the 0, 1 and 2 SFOS regions. The most important systematic uncertainties (discussed in section 5.6) are shown, namely from the fake estimates and the uncertainties on the WZ and ZZ k-factors.

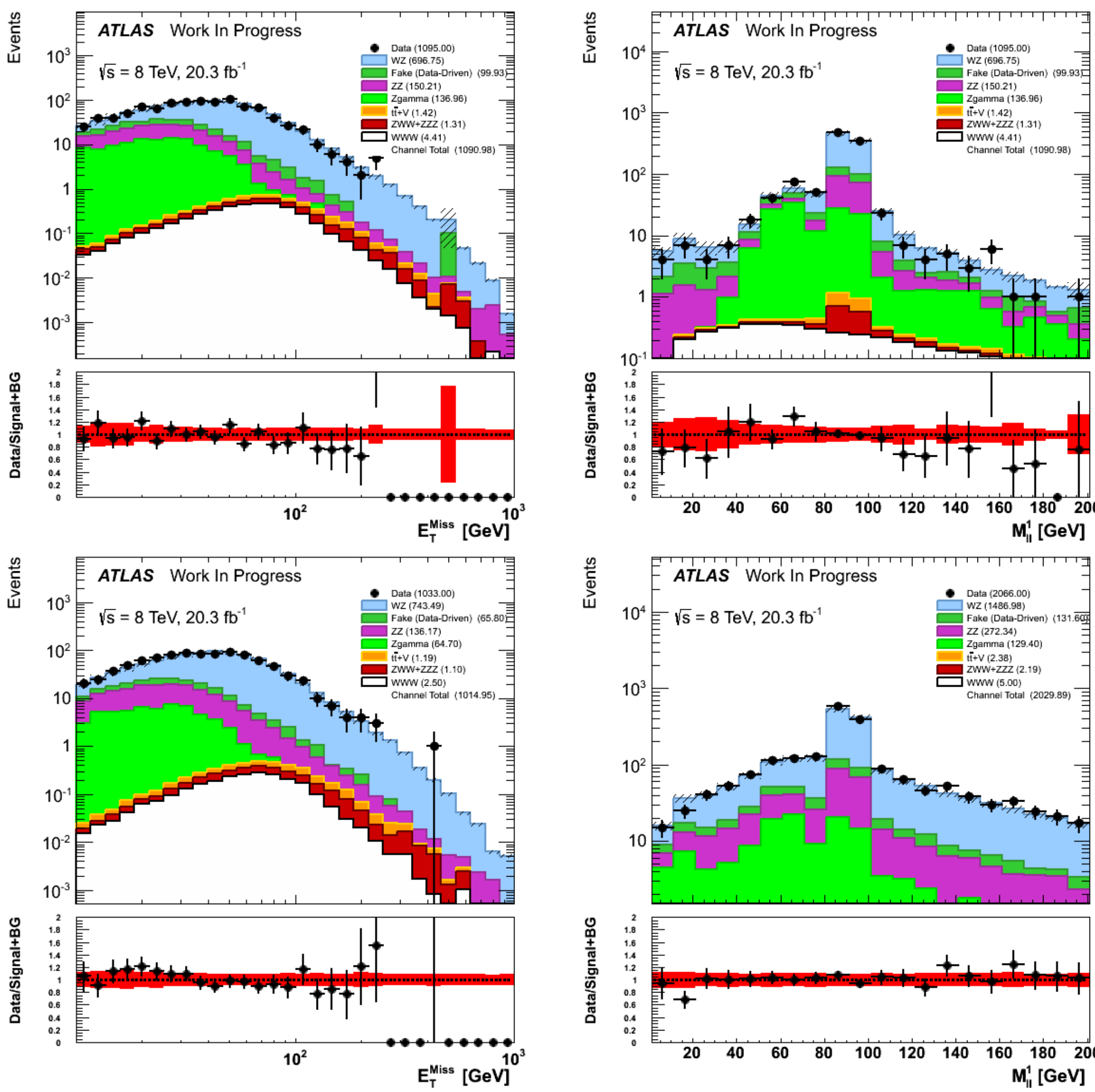

Figure 5.21: Plots of the $E_{\mathrm{T}}^{\mathrm{miss}}$(left) and m_{SFOS} (right) distributions in the 1 SFOS (top) and 2 SFOS (bottom) regions after pre-selection plus the b-veto requirement.

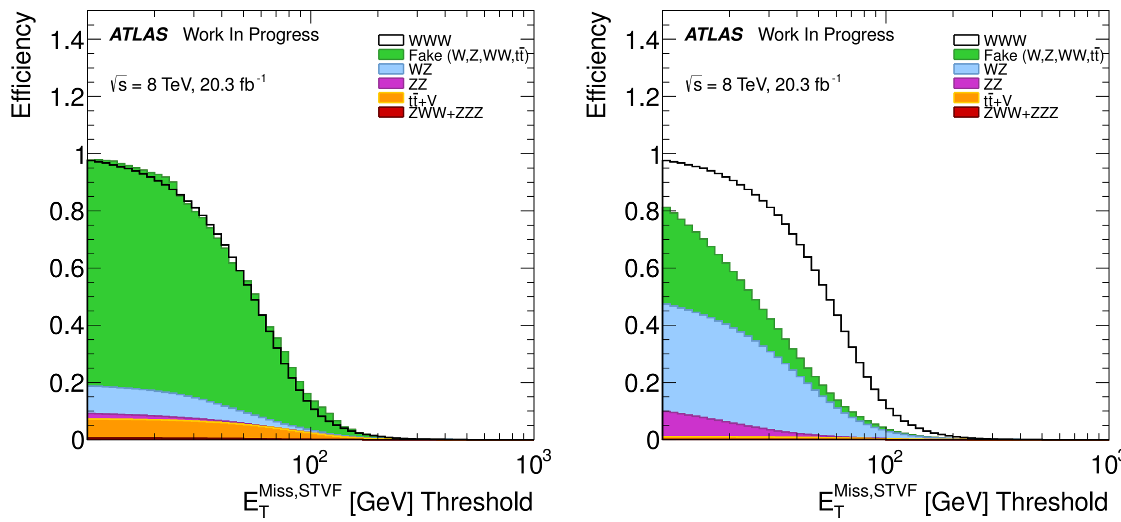

Figure 5.22: Signal and background efficiencies for the selection $E_{\mathrm{T}}^{\mathrm{miss}} > X$ as a function of the $E_{\mathrm{T}}^{\mathrm{miss}}$ selection threshold, X, in both the 0 SFOS (left) and pre-selection (right) regions.

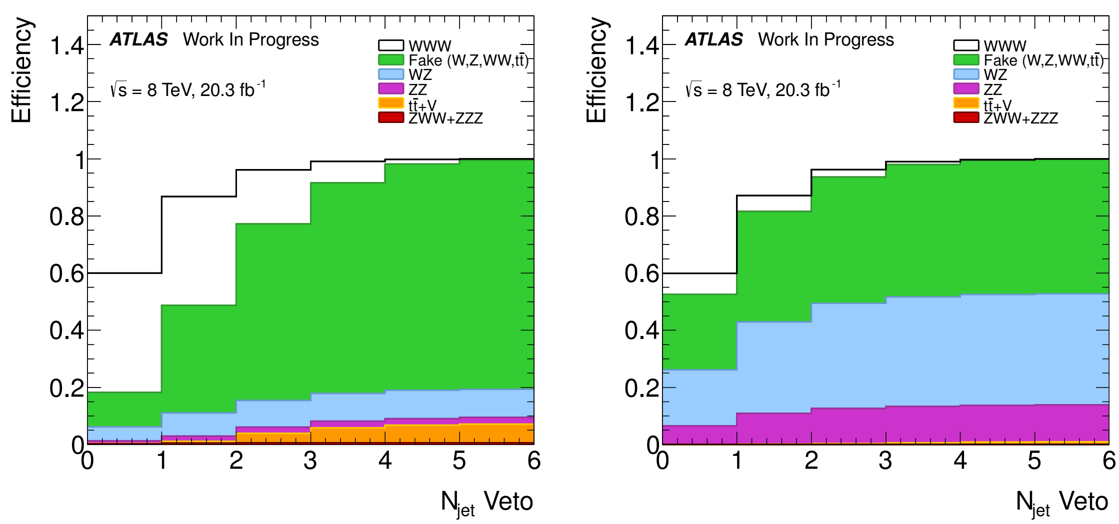

Figure 5.23: Signal and background efficiencies for the selection $N_{\mathrm{Jet}} \leq X$ as a function of the N_{Jet} selection threshold, X, in both the 0 SFOS (left) and pre-selection (right) regions.

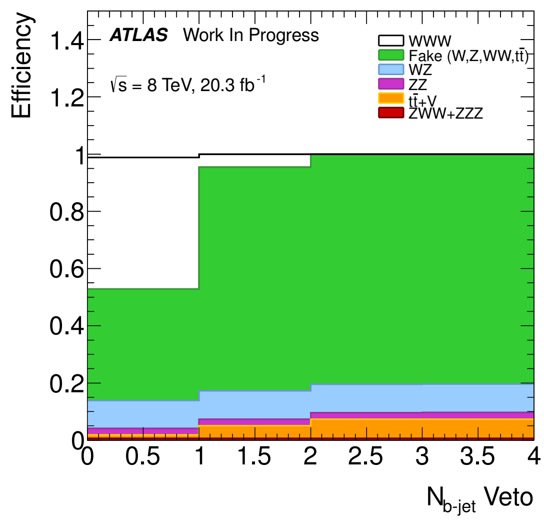

Figure 5.24: Signal and background efficiencies for the selection $N_{b-\mathrm{Jet}} \leq X$ as a function of the $N_{b-\mathrm{Jet}}$ selection threshold, X, in both the 0 SFOS (left) and pre-selection (right) regions.

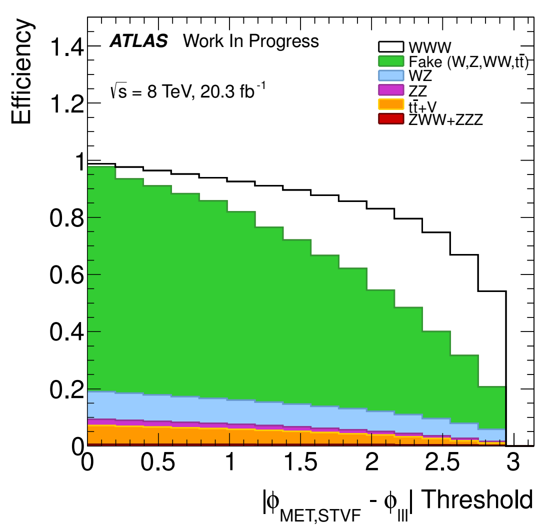

Figure 5.25: Signal and background efficiencies for the selection $|\Delta\varphi(lll, E_T^{\mathrm{Miss}})| > X$ as a function of the $\Delta\varphi(lll, E_T^{\mathrm{Miss}})$ selection threshold, X, in both the 0 SFOS (left) and pre-selection (right) regions.

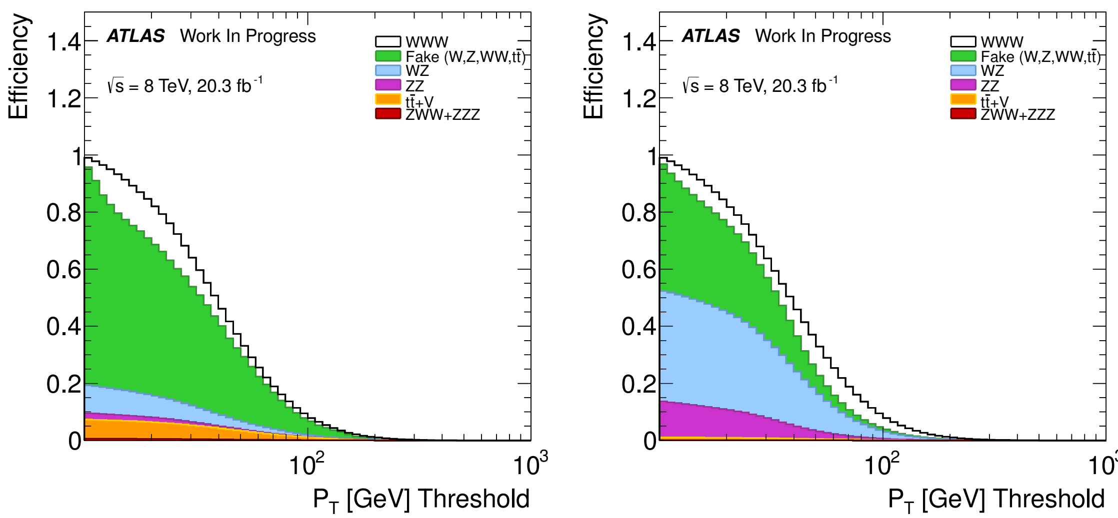

Figure 5.26: Signal and background efficiencies for the selection Lepton $p_{\rm T} > X$ as a function of the $p_{\rm T}$ selection threshold, X, in both the 0 SFOS (left) and pre-selection (right) regions.

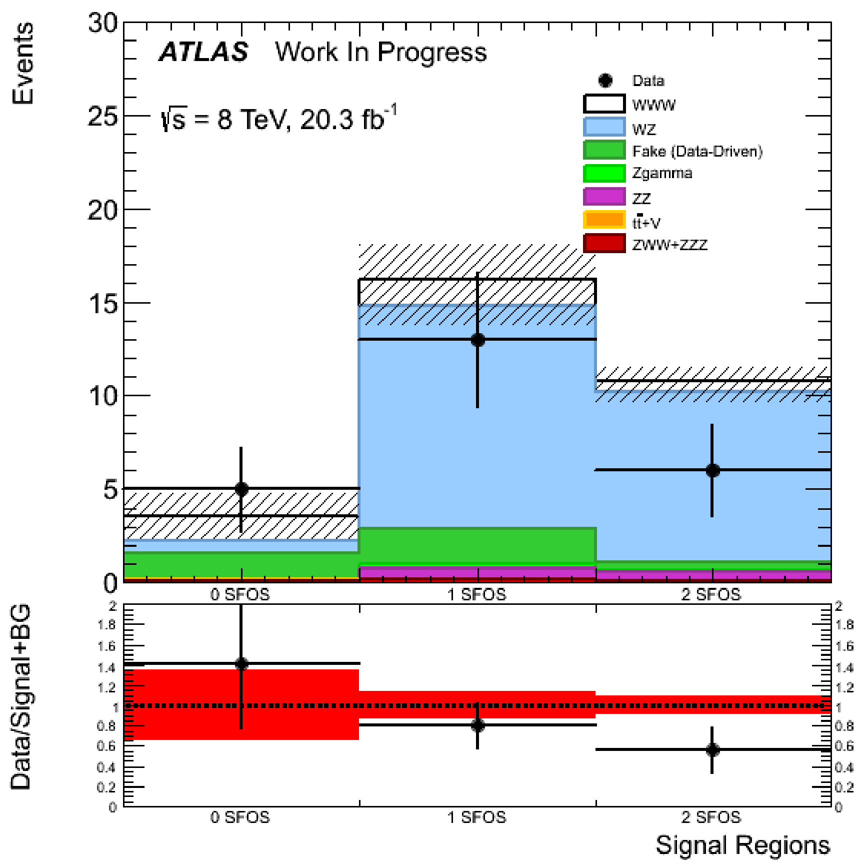

Figure 5.27: Yields after full selection in the 0, 1 and 2 SFOS regions. The most important systematic uncertainties are shown, namely from the fake estimates and the uncertainties on the WZ and ZZ k-factors.

5.5.3.1 0 SFOS Signal Region

	Signal		Background		Data	
	Yield	Eff.	Yield	Eff.	Yield	Eff.
0 SFOS	2.31	—	21.36	—	30	—
Charge Sum $= \pm 1$	2.30	1.00	19.55	0.92	27	0.90
$N_{\mathrm{b-jet}} = 0$	2.29	0.99	8.59	0.44	10	0.37
$m_{SF} > 20$ GeV	2.25	0.98	8.32	0.97	10	1.00
$\lvert m_{ee} - m_Z \rvert > 15$ GeV	2.06	0.91	7.09	0.85	9	0.90
$\lvert \Delta\phi(3l, E_T^{Miss}) \rvert > 2.5$	1.41	0.69	2.51	0.35	6	0.67
$N_{\mathrm{Jet}} \leq 1$	1.34	0.95	2.35	0.94	5	0.83

Table 5.18: Cut-flows showing the event yields and efficiencies for each cut in the 0 SFOS signal region starting from event pre-selection separately for the total signal and total background predictions, along with the observed data. Event yields for MC backgrounds and signal include all weights and are normalized to an integrated luminosity of 20.3 fb^{-1}. The fake lepton background only includes the matrix method weights. The data is unweighted. Efficiencies show the ratio of the yield with respect to the previous cut. The efficiency is first calculated at the first cut after event pre-selection.

The prediction from the 0 SFOS signal region at each stage of the selection is summarized in Table 5.18 for the signal and background predictions, as well as for the data. There is also a more detailed set of predictions at each stage for the different background sources in Table 5.19. From this, we can clearly see the enormous impact of the 0 SFOS cut on removing the backgrounds, for the WZ background in particular. We can also see the strong impact that the $N_{b-\mathrm{Jet}}$ and $\Delta\varphi(lll, E_T^{\mathrm{Miss}})$ cuts have without removing much of the signal. The signal plus background predictions as compared to the data for the distribution just before each cut is applied are shown in Fig. 5.28. From this it is clear that the data seems to be well modeled at each stage of the selection.

After the full selection is applied, the 0 SFOS signal region is found to be the most sensitive of the three channels, as expected, with a predicted signal to background ratio of 56%. This can be seen from Table 5.16, where the expected signal is 1.344 compared to an expected background of 2.35. Together they combine to give a total prediction of 3.69 signal plus background events with 5 events observed in the data. The Poisson probability of observing ≥ 5 events with 3.69 events expected from the signal plus background prediction is 30.7%. Thus, we can see that this is in good agreement with the observed 5 events in

	Background					
	WZ		ZZ		$t\bar{t}+V$	
	Yield	Eff.	Yield	Eff.	Yield	Eff.
Pre-selection	1566.91	—	323.60	—	36.93	—
0 SFOS	2.84	0.002	0.50	0.002	0.26	0.01
Charge Sum $= \pm 1$	1.92	0.68	0.33	0.65	0.26	0.99
$N_{\text{b-jet}} = 0$	1.91	0.99	0.33	0.99	0.25	0.98
$m_{SF} > 20$ GeV	1.88	0.98	0.32	0.98	0.25	0.98
$\lvert m_{ee} - m_Z\rvert > 15$ GeV	1.27	0.68	0.21	0.66	0.22	0.90
$\lvert\Delta\phi(3l, E_T^{Miss})\rvert > 2.5$	0.65	0.51	0.07	0.34	0.09	0.38
$N_{\text{Jet}} \leq 1$	0.62	0.95	0.07	0.91	0.04	0.45
	Background					
	$ZZZ + ZWW$		$Z\gamma$		Fake	
	Yield	Eff.	Yield	Eff.	Yield	Eff.
Pre-selection	3.12	—	219.80	—	238.12	—
0 SFOS	0.25	0.08	0.20	0.001	17.31	0.07
Charge Sum $= \pm 1$	0.25	1.00	0.00	0.00	16.79	0.97
$N_{\text{b-jet}} = 0$	0.25	0.99	0.00	0.00	5.85	0.35
$m_{SF} > 20$ GeV	0.24	0.98	0.00	0.00	5.63	0.96
$\lvert m_{ee} - m_Z\rvert > 15$ GeV	0.22	0.90	0.00	0.00	5.17	0.92
$\lvert\Delta\phi(3l, E_T^{Miss})\rvert > 2.5$	0.13	0.59	0.00	0.00	2.17	0.42
$N_{\text{Jet}} \leq 1$	0.11	0.86	0.00	0.00	1.51	0.70

Table 5.19: Cut-flows showing the event yields and efficiencies for each cut in the 0 SFOS signal region starting from event pre-selection and binned by background category. Event yields for MC backgrounds and signal include all weights and are normalized to an integrated luminosity of 20.3 fb^{-1}. The fake lepton background only includes the matrix method weights. The data is unweighted. Efficiencies show the ratio of the yield with respect to the previous cut. The efficiency is first calculated at the first cut after event pre-selection.

data from the statistical uncertainty alone.

The fake background makes up more than half of the total expected background prediction, with 1.51 background events predicted from fakes compared to 2.35 events expected from the total background. The systematic uncertainty on the fake background is approaching 100% for the reasons described in Sec. 5.4.3.2. As can be seen in Table 5.17, this results in the systematic uncertainty on the total background estimate that is around 60%. This further increases the compatibility of the data with the expectation, and thus reduces the sensitivity.

The other backgrounds are less important. The WZ background is the second largest,

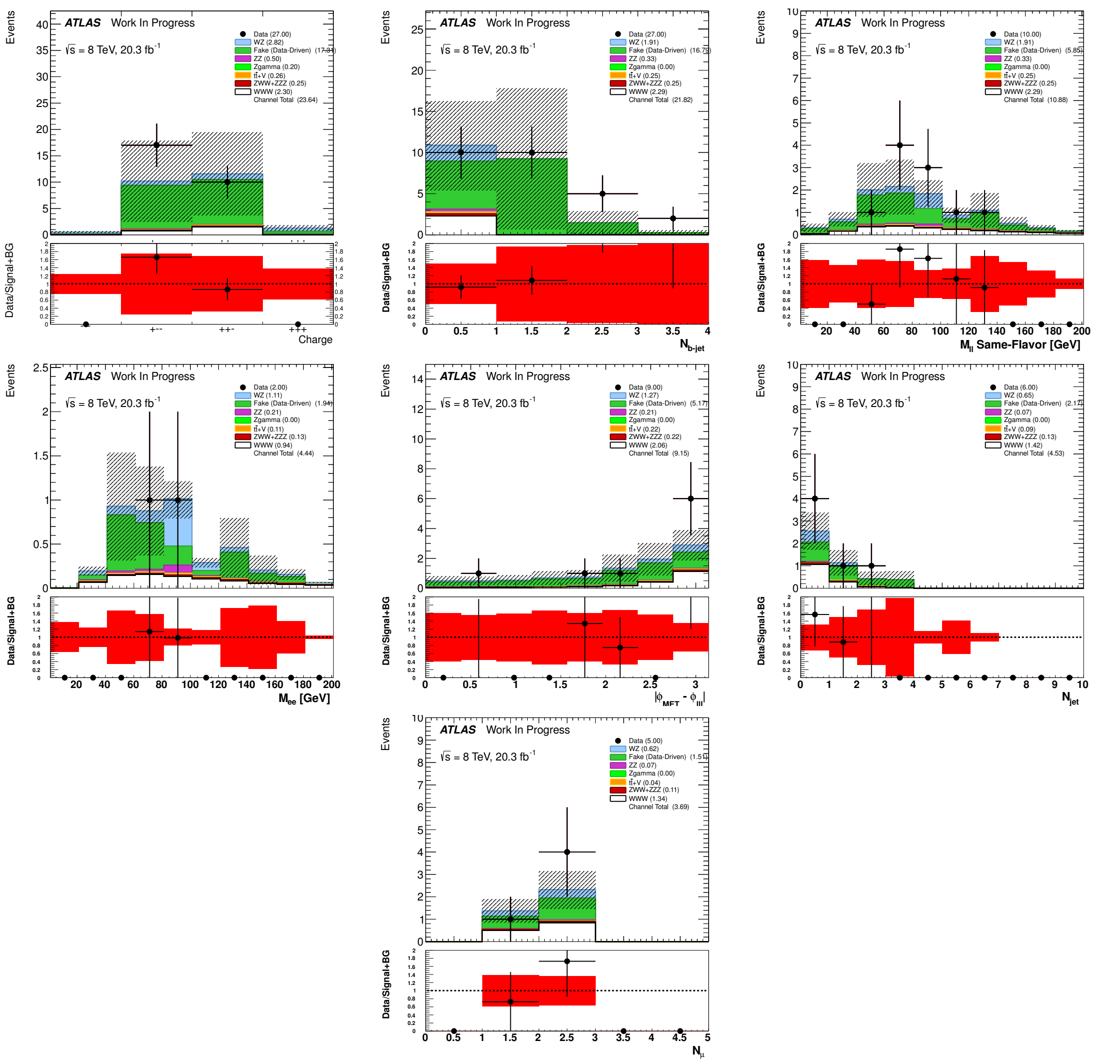

Figure 5.28: Distributions showing data compared to the signal plus background estimate in the 0 SFOS region at each stage of the selection before the cuts are applied to the given distribution. Plots should be read sequentially from left to right and from top to bottom. Referring to Table 5.18, the top left plot is shown before cut #3 is applied, top middle is before cut #5, and so on until the bottom right which is after all cuts are applied.

coming from charge mis-identification, with 0.6176 events predicted. The uncertainty on the WZ background is dominated by that from the WZ normalization uncertainty, which is 10%, and also has a small contribution from the charge mis-identification estimate uncertainty. The VVV contributions is the third largest, predicting 0.1126 with a small uncertainty. The ZZ background has a similar source and uncertainty as the WZ, but is about 10 times smaller in size. The $t\bar{t}+V$ background contributes even less and the DPS and $Z\gamma$ backgrounds have 0 contribution within the statistical uncertainties of the MC.

5.5.3.2 1 SFOS Signal Region

	Signal		Background		Data	
	Yield	Eff.	Yield	Eff.	Yield	Eff.
1 SFOS	4.67	—	1231.49	—	1260	—
$N_{\mathrm{b-jet}} = 0$	4.42	0.94	1086.66	0.88	1095	0.87
NOT $m_Z - 35$ GeV $<$ $m_{\mathrm{SFOS}} < m_Z + 20$ GeV	2.76	0.63	97.96	0.090	93	0.08
$E_T^{Miss} > 45$ GeV	1.91	0.69	29.83	0.30	27	0.29
$\lvert\Delta\phi(3l, E_T^{Miss})\rvert > 2.5$	1.48	0.77	16.73	0.56	16	0.59
$N_{\mathrm{Jet}} \leq 1$	1.39	0.94	14.77	0.88	13	0.81

Table 5.20: Cut-flows showing the event yields and efficiencies for each cut in the 1 SFOS signal region starting from event pre-selection separately for the total signal and total background predictions, along with the observed by data. Event yields for MC backgrounds and signal include all weights and are normalized to an integrated luminosity of 20.3 fb^{-1}. The fake lepton background only includes the matrix method weights. The data is unweighted. Efficiencies show the ratio of the yield with respect to the previous cut. The efficiency is first calculated at the first cut after event pre-selection.

The 1 SFOS signal region is not as sensitive as the 0 SFOS region, with a signal to background ratio of about 9.2%. The background is overwhelmingly dominated by WZ contributions. Similar to the 0 SFOS region, the predictions and data at each stage of the 1 SFOS signal region selection are shown in Table 5.20 and Table 5.21. The 1 SFOS requirement leaves much of the WZ and ZZ backgrounds, but the Z-veto and $E_{\mathrm{T}}^{\mathrm{miss}}$ cuts are very effective at removing most of this while keeping the signal.

Again, we can also see the signal plus background predictions as compared to the data for the distribution just before each cut is applied in the 1 SFOS region by looking at Fig. 5.29. Here, the distributions again appear to be well modeled at each stage of the selection. Looking closer at the N_{Jet} distribution, we can see that there is a deficit of data in the $N_{\mathrm{Jet}} = 1$ bin which is kept in the selection and results in a slight deficit in the prediction. Further, if we look at the N_μ distribution we see that this deficit seems to fall exclusively in the $N_\mu = 1$ bin. A more detailed investigation of the cut-flows in the

	Background					
	WZ		ZZ		$t\bar{t}+V$	
	Yield	Eff.	Yield	Eff.	Yield	Eff.
Pre-selection	1566.91	—	323.60	—	36.93	—
1 SFOS	757.38	0.48	171.39	0.53	18.10	0.49
$N_{\text{b-jet}} = 0$	696.90	0.92	150.14	0.88	1.42	0.08
NOT $m_Z - 35$ GeV $< m_{\text{SFOS}} < m_Z + 20$ GeV	44.30	0.06	13.79	0.09	0.37	0.26
$E_T^{Miss} > 45$ GeV	21.38	0.48	1.46	0.11	0.29	0.78
$\|\Delta\phi(3l, E_T^{Miss})\| > 2.5$	13.07	0.61	0.71	0.49	0.11	0.39
$N_{\text{Jet}} \leq 1$	11.90	0.91	0.58	0.82	0.05	0.45

	Background					
	$ZZZ + ZWW$		$Z\gamma$		Fake	
	Yield	Eff.	Yield	Eff.	Yield	Eff.
Pre-selection	3.12	—	219.80	—	238.12	—
1 SFOS	1.55	0.50	149.60	0.68	133.47	0.56
$N_{\text{b-jet}} = 0$	1.31	0.84	136.96	0.92	99.93	0.75
NOT $m_Z - 35$ GeV $< m_{\text{SFOS}} < m_Z + 20$ GeV	0.34	0.26	22.44	0.16	16.72	0.17
$E_T^{Miss} > 45$ GeV	0.24	0.71	1.36	0.06	5.10	0.31
$\|\Delta\phi(3l, E_T^{Miss})\| > 2.5$	0.17	0.69	0.20	0.15	2.47	0.48
$N_{\text{Jet}} \leq 1$	0.14	0.84	0.20	1.00	1.90	0.77

Table 5.21: Cut-flows showing the event yields and efficiencies for each cut in the 1 SFOS signal region starting from event pre-selection and binned by background category. Event yields for MC backgrounds and signal include all weights and are normalized to an integrated luminosity of 20.3 fb^{-1}. The fake lepton background only includes the matrix method weights. The data is unweighted. Efficiencies show the ratio of the yield with respect to the previous cut. The efficiency is first calculated at the first cut after event pre-selection.

individual $N_\mu = 1$ and $N_\mu = 2$ bins suggests that this is most likely a statistical fluctuation. Overall, the deficit is not very significant, with the Poisson probability of observing 13 or less events with 16.16 expected being 26.2%.

The fake background is only the second largest background in this region, making up about 13% of the total. Still, even with the 10% uncertainty on the normalization of the dominant WZ background, the fake background uncertainty is the largest uncertainty on the background estimation, approaching 13%, as can be seen in Table 5.17. The $t\bar{t}+V$ and VVV backgrounds are of a similar absolute size as in the 0 SFOS region, but the larger overall background makes them even less important. The DPS and $Z\gamma$ uncertainties con-

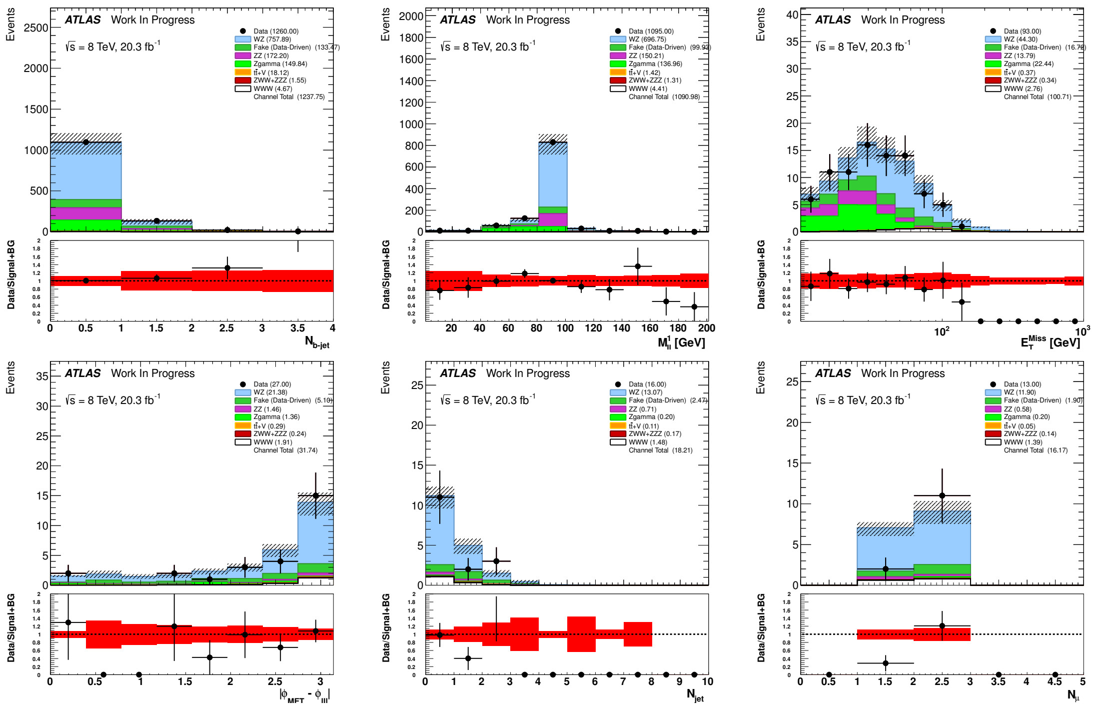

Figure 5.29: Distributions showing data compared to the signal plus background estimate in the 1 SFOS region at each stage of the selection before the cuts are applied to the given distribution. Plots should be read sequentially from left to right and from top to bottom. Referring to Table 5.20, the top left plot is shown before cut #3 is applied, top middle is before cut #4, and so on until the bottom right which is after all cuts are applied.

tribute a finite amount to the background within the statistical uncertainties, but remain negligible.

5.5.3.3 2 SFOS Signal Region

The 2 SFOS signal region has a similar background composition as the 1 SFOS signal regions, since it is also dominated by the WZ background. As a result, the systematic uncertainties on the signal and background are very similar to the 1 SFOS region. As can be seen in Table 5.20 and Table 5.21, however, the overall background prediction is slightly smaller than the 1 SFOS signal region. This is mainly because the tighter $E_{\mathrm{T}}^{\mathrm{miss}}$ cut removes more of the WZ background. The signal and the also contributes slightly less to the total, but this is true immediately after applying the SFOS requirement. The reason

	Signal Yield	Signal Eff.	Background Yield	Background Eff.	Data Yield	Data Eff.
2 SFOS	2.66	—	1132.53	—	1182	—
$N_{\text{b-jet}} = 0$	2.50	0.94	1012.07	0.89	1033	0.87
$\lvert m_{\text{SFOS}} - m_Z \rvert > 20$ GeV	1.46	0.58	108.88	0.11	108	0.10
$E_T^{Miss} > 55$ GeV	0.83	0.57	18.99	0.17	18	0.17
$\lvert\Delta\phi(3l, E_T^{Miss})\rvert > 2.5$	0.65	0.78	11.64	0.61	8	0.44
$N_{\text{Jet}} \leq 1$	0.61	0.94	10.25	0.88	6	0.75

Table 5.22: Cut-flows showing the event yields and efficiencies for each cut in the 2 SFOS signal region starting from event pre-selection separately for the total signal and total background predictions, along with the observed data. Event yields for MC backgrounds and signal include all weights and are normalized to an integrated luminosity of 20.3 fb^{-1}. The fake lepton background only includes the matrix method weights. The data is unweighted. Efficiencies show the ratio of the yield with respect to the previous cut. The efficiency is first calculated at the first cut after event pre-selection.

	Background					
	WZ		ZZ		$t\bar{t}+V$	
	Yield	Eff.	Yield	Eff.	Yield	Eff.
Pre-selection	1566.91	—	323.60	—	36.93	—
2 SFOS	807.27	0.52	151.28	0.47	15.35	0.42
$N_{\text{b-jet}} = 0$	743.12	0.92	136.16	0.90	1.19	0.08
$\lvert m_{\text{SFOS}} - m_Z \rvert > 20$ GeV	44.95	0.06	21.13	0.16	0.22	0.18
$E_T^{Miss} > 55$ GeV	15.86	0.35	0.97	0.05	0.14	0.65
$\lvert\Delta\phi(3l, E_T^{Miss})\rvert > 2.5$	10.09	0.64	0.55	0.57	0.07	0.49
$N_{\text{Jet}} \leq 1$	9.07	0.90	0.48	0.86	0.02	0.35

	Background					
	$ZZZ+ZWW$		$Z\gamma$		Fake	
	Yield	Eff.	Yield	Eff.	Yield	Eff.
Pre-selection	3.12	—	219.80	—	238.12	—
2 SFOS	1.30	0.41	69.99	0.32	87.34	0.37
$N_{\text{b-jet}} = 0$	1.10	0.85	64.70	0.92	65.80	0.75
$\lvert m_{\text{SFOS}} - m_Z \rvert > 20$ GeV	0.19	0.17	29.52	0.46	12.87	0.20
$E_T^{Miss} > 55$ GeV	0.12	0.63	0.43	0.01	1.47	0.11
$\lvert\Delta\phi(3l, E_T^{Miss})\rvert > 2.5$	0.10	0.82	0.11	0.25	0.72	0.49
$N_{\text{Jet}} \leq 1$	0.08	0.82	0.11	1.00	0.49	0.69

Table 5.23: Cut-flows showing the event yields and efficiencies for each cut in the 2 SFOS signal region starting from event pre-selection and binned by background category. Event yields for MC backgrounds and signal include all weights and are normalized to an integrated luminosity of 20.3 fb^{-1}. The fake lepton background only includes the matrix method weights. The data is unweighted. Efficiencies show the ratio of the yield with respect to the previous cut. The efficiency is first calculated at the first cut after event pre-selection.

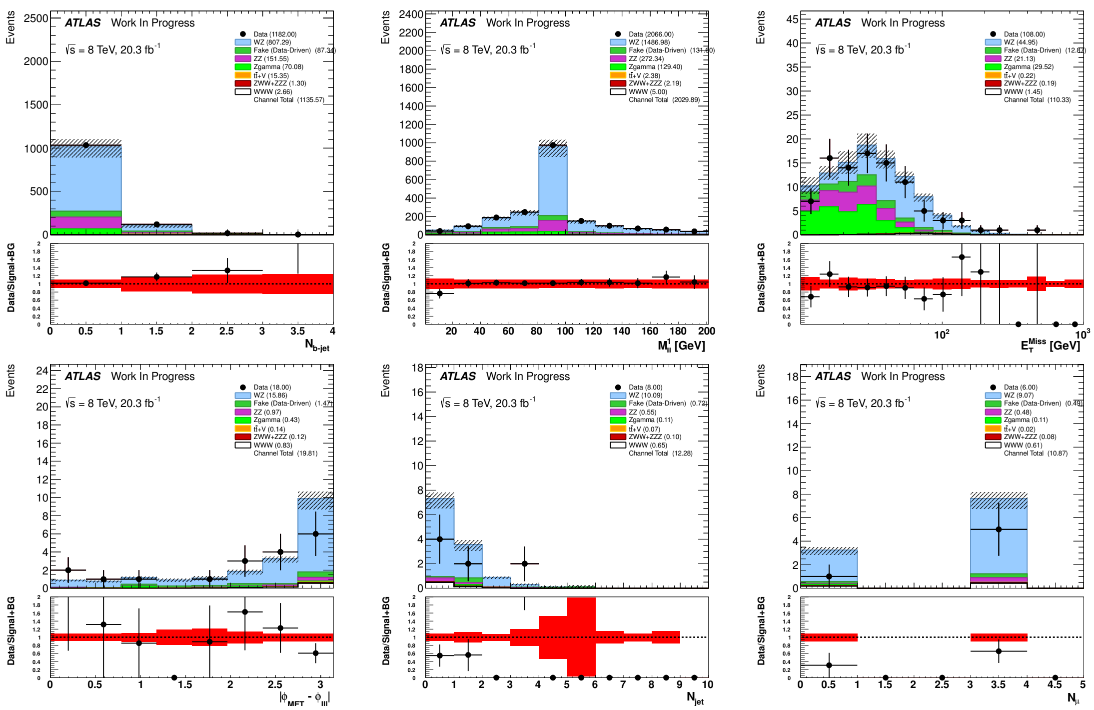

Figure 5.30: Distributions showing data compared to the signal plus background estimate in the 2 SFOS region at each stage of the selection before the cuts are applied to the given distribution. Plots should be read sequentially from left to right and from top to bottom. Referring to Table 5.22, the top left plot is shown before cut #3 is applied, the top middle is before cut #4, and so on until the bottom right which is after all cuts are applied.

can be understood as described in Sec. 5.3.2: there are twice many charge and flavor combinations to produce 1 SFOS pairs as there are 2 SFOS pairs.

From the cut-flow tables we can also see that there is a deficit in the data compared to the prediction which appears after the $\Delta\varphi(lll, E_T^{\text{Miss}})$ selection. Looking at the distributions at each cut for the 2 SFOS region in Fig. 5.30, one can clearly see the deficit occurring in the bin furthest to the right in the $|\Delta\varphi(lll, E_T^{\text{Miss}})|$ distribution. The deficit then propagates through uniformly in the N_{Jet} and N_μ distributions until the final estimate. Note that the bin where the deficit occurs in the $|\Delta\varphi(lll, E_T^{\text{Miss}})|$ distribution is also dominated by the WZ background. Recall from Sec. 5.4.1.1 that We have verified the modeling of the WZ background as a function of this quantity in control regions. Furthermore, the $|\Delta\varphi(lll, E_T^{\text{Miss}})|$ distribution shows good agreement in the 1 SFOS region at this stage where it is also dominated by the WZ background. We have no reason to believe that the modeling of the WZ background should be very different or should break down in the 2 SFOS region as compared to elsewhere. Thus, the deficit is most likely a statistical fluctuation and not due to a problem in the modeling of the background. The Poisson probability of observing ≤ 6 events when 10.86 events are expected is 8.5%. Thus, even though this is the largest deviation observed in the signal regions, it is still within 2 standard deviations (5%).

5.5.4 Fiducial Cross-sections and Correction Factors

The SM signal predictions at reconstruction level are reported above in Sec. 5.5.3. In anticipation of the SM cross-section measurement extraction in Sec. 5.7 and Sec. 6.2, the number of expected signal events at reconstruction level, N_i^{Reco}, in signal region i, are factorized such that

$$N_i^{\mathrm{Reco}} = N_i^{\mathrm{Fid}} \times C_i \tag{5.44}$$

where N_i^{Fid} is the number of events expected from the fiducial level selection of Sec. 5.3.3 and C_i is the "correction factor" which accounts for differences between the fiducial level prediction and the reconstruction level prediction. In practice, N_i^{Reco} and N_i^{Fid} are computed explicitly from the signal MC using the selections in Table 5.4 and Table 5.5, respectively. The correction factor is then derived by the simple rearrangement

$$C_i = \frac{N_i^{\mathrm{Reco}}}{N_i^{\mathrm{Fid}}} \tag{5.45}$$

In this thesis, the numbers in the numerator and denominator are both derived for the SM signal using the VBFNLO generator.

The number of predicted fiducial events, N_i^{Fid}, can be interpreted as a fiducial cross-section, σ_i^{Fid}, using the LHC integrated luminosity and Eq. (3.3). Recall from Sec. 5.1.2.1 and Table 5.1 that the fiducial cross-sections for the SM signal were generated using both MadGraph and VBFNLO and were shown to be in good agreement. The fiducial cross-sections from MadGraph are used in the final estimates.

Channel	C_i	Fiducial Cross-section [ab]
0 SFOS	$0.534 \pm .021$	123.6 ± 4.7
1 SFOS	$0.500 \pm .018$	136.9 ± 4.7
2 SFOS	$0.615 \pm .038$	48.8 ± 2.9

Table 5.24: Correction factors, C_i, and fiducial cross-sections derived separately for each signal region. Correction factors are determined using VBFNLO ; fiducial cross-sections are determined using MadGraph.

The values for the correction factors and fiducial cross-sections in each signal region of Sec. 5.5.3 are reported in Table 5.24. Note that the sum of the fiducial cross-sections in each signal region gives the combined fiducial cross-section which was reported in Eq. 5.2 along with PDF and scale uncertainties.

One important caveat about this framework is that the fiducial selection explicitly vetoes for the presence of leptonically decaying τ leptons coming from the W decay, while for the reconstruction level selection no such veto is applied. This allows for a simple fiducial definition. However, this also means that the correction factor will be inflated by the presence of events with leptonically decaying τ leptons passing the reconstruction level selection. Studies of the WWW signal MC suggest that this could be as high as 20%. Bear in mind this is not corrected for explicitly in the interpretation of Sec. 5.7.

5.6 Corrections and Systematic Uncertainties

The predictions for the signal and background are subject to the choices made in building the model described thus far in Sec. 5. If we are to believe our predictions we must understand how sensitive the predictions are to these choices. To that end, we also compute the prediction for numerous variations on the nominal prediction. Each one of these variations is called a systematic uncertainty. Each systematic uncertainty is designed to assess the sensitivity to a given choice made when building the model. This analysis has almost 50 different systematic uncertainties, each of which is varied independently. The size of each systematic uncertainty is treated as a separate nuisance parameter as input to the statistical model used in the interpretation of the model when compared to data, described later in Sec. 5.7.

The systematic uncertainties can be split up into four categories: theory, methodology, experiment, and luminosity. I will summarize them below, in each case giving the size of the uncertainties in the three signal regions. Some of these variations have been mentioned already in previous sections but will be referred to here again for completeness.

5.6.1 Theoretical Uncertainties

		Background								Signal
		WZ	ZZ	VVV	$t\bar{t}+V$	DPS	$Z\gamma$	Fake (Data)	Total BG	
Signal	PDF	—	—	—	—	—	—	—	—	2.80
	μ_R and μ_F Choice	—	—	—	—	—	—	—	—	2.60
Norm.	WZ	10.00	—	—	—	—	—	—	2.63	—
	ZZ	—	15.00	—	—	—	—	—	0.42	—
	VVV	—	—	30.00	—	—	—	—	1.44	—
	$t\bar{t}+V$	—	—	—	30.00	—	—	—	0.50	—
	DPS	—	—	—	—	50.00	—	—	—	—

Table 5.25: Size of theoretical uncertainties in percent for the 0 SFOS signal region. The background uncertainties are shown for the individual background components as well as the total. The signal uncertainty is shown separately. Those marked — are either not applicable or below 0.02 % and thus considered to be negligible

		Background								Signal
		WZ	ZZ	VVV	$t\bar{t}+V$	DPS	$Z\gamma$	Fake (Data)	Total BG	
Signal	PDF	—	—	—	—	—	—	—	—	2.80
	μ_R and μ_F Choice	—	—	—	—	—	—	—	—	2.60
Norm.	WZ	10.00	—	—	—	—	—	—	8.05	—
	ZZ	—	15.00	—	—	—	—	—	0.59	—
	VVV	—	—	30.00	—	—	—	—	0.28	—
	$t\bar{t}+V$	—	—	—	30.00	—	—	—	0.10	—
	DPS	—	—	—	—	50.00	—	—	—	—

Table 5.26: Size of theoretical uncertainties in percent for the 1 SFOS signal region. The background uncertainties are shown for the individual background components as well as the total. The signal uncertainty is shown separately. Those marked — are either not applicable or below 0.02 % and thus considered to be negligible

The theoretical uncertainties are those on the signal PDF and on the background cross-

		Background								Signal
		WZ	ZZ	VVV	$t\bar{t}+V$	DPS	$Z\gamma$	Fake (Data)	Total BG	
Signal	PDF	—	—	—	—	—	—	—	—	2.80
	μ_R and μ_F Choice	—	—	—	—	—	—	—	—	2.60
Norm.	WZ	10.00	—	—	—	—	—	—	8.83	—
	ZZ	—	15.00	—	—	—	—	—	0.70	—
	VVV	—	—	30.00	—	—	—	—	0.23	—
	$t\bar{t}+V$	—	—	—	30.00	—	—	—	0.07	—
	DPS	—	—	—	—	50.00	—	—	0.11	—

Table 5.27: Size of theoretical uncertainties in percent for the 2 SFOS signal region. The background uncertainties are shown for the individual background components as well as the total. The signal uncertainty is shown separately. Those marked — are either not applicable or below 0.02 % and thus considered to be negligible

section predictions. They are summarized for the 0, 1, and 2 SFOS regions in Table 5.25, Table 5.26, and Table 5.27, respectively. The motivation for the PDF uncertainties has been described already in Sec. 2.1.2. There are several uncertainties evaluated on the signal PDF, all of which are described in more detail in Sec. 5.1.2.1. These are the PDF choice, including uncertainties reported by the individual PDFs, as well as variations in the renormalization and factorization scales. The effect on the signal prediction from these is around 2-3%.

The most important MC backgrounds have uncertainties evaluated on their cross-section. In particular, these are the uncertainties on the normalization of the WZ, ZZ, $Z\gamma$, VVV, $t\bar{t}+V$, and DPS background predictions described in Sec. 5.4. Their impact when propagated to the final background prediction varies by channel. In general, the uncertainty on the WZ prediction is the largest, contributing about 2.6% in the 0 SFOS region and around 8-9% in the 1 and 2 SFOS regions. In the 0 SFOS region, the uncertainty on the VVV prediction contributes about 1.4% and that on the ZZ prediction is about 0.4%; all others fall below that. In the 1 and 2 SFOS regions the ZZ uncertainty is around 0.6-0.7%; the rest are negligible.

		Background								Signal
		WZ	ZZ	VVV	$t\bar{t}+V$	DPS	$Z\gamma$	Fake (Data)	Total BG	
Matrix Method	Electron	—	—	—	—	—	—	9.62	6.20	—
	Muon	—	—	—	—	—	—	5.06	3.26	—
	b-jet selection	—	—	—	—	—	—	90.19	58.14	—
	Charge Mis-ID	1.58	1.31	—	—	—	—	—	0.45	—

Table 5.28: Size of the methodological uncertainties in percent for the 0 SFOS signal region. The background uncertainties are shown for the individual background components as well as the total. The signal uncertainty is shown separately. Those marked — are either not applicable or below 0.02 % and thus considered to be negligible

		Background								Signal
		WZ	ZZ	VVV	$t\bar{t}+V$	DPS	$Z\gamma$	Fake (Data)	Total BG	
Matrix Method	Electron	—	—	—	—	—	—	36.50	4.69	—
	Muon	—	—	—	—	—	—	5.11	0.66	—
	b-jet selection	—	—	—	—	—	—	91.16	11.72	—
	Charge Mis-ID	—	—	—	—	—	—	—	—	—

Table 5.29: Size of the methodological uncertainties in percent for the 1 SFOS signal region. The background uncertainties are shown for the individual background components as well as the total. The signal uncertainty is shown separately. Those marked — are either not applicable or below 0.02 % and thus considered to be negligible

		Background								Signal
		WZ	ZZ	VVV	$t\bar{t}+V$	DPS	$Z\gamma$	Fake (Data)	Total BG	
Matrix Method	Electron	—	—	—	—	—	—	22.21	1.07	—
	Muon	—	—	—	—	—	—	6.80	0.33	—
	b-jet selection	—	—	—	—	—	—	87.19	4.20	—
	Charge Mis-ID	—	—	—	—	—	—	—	—	—

Table 5.30: Size of the methodological uncertainties in percent for the 2 SFOS signal region. The background uncertainties are shown for the individual background components as well as the total. The signal uncertainty is shown separately. Those marked — are either not applicable or below 0.02 % and thus considered to be negligible

5.6.2 Methodological Uncertainties

The methodological uncertainties are those due to the data-driven modeling of the fake and charge mis-identification backgrounds, described in Sec. 5.4.3 and Sec. 5.4.2, respectively. They are summarized for the 0, 1, and 2 SFOS regions in Table 5.28, Table 5.29, and Table 5.30, respectively. The uncertainty on the fake background is the most important systematic uncertainty in the analysis, contributing about 60% on the final background prediction in the 0 SFOS signal region. The smaller contribution of the fake background in the 1 and 2 SFOS regions reduces it in those regions to 5-10%. The uncertainty on the charge mis-identification only impacts the background prediction in the 0 SFOS channel. The small size of this background after the final selection means it only contributes about 0.5% to the uncertainty on the final background prediction in that region.

5.6.3 Experimental Corrections and Uncertainties

		Background								Signal
		WZ	ZZ	VVV	$t\bar{t}+V$	DPS	$Z\gamma$	Fake (Data)	Total BG	
Electron	Efficiency	1.80	1.83	1.52	1.42	—	—	—	0.62	1.45
	Scale	0.96	1.63	1.75	2.00	—	—	—	0.29	0.51
	Resolution	0.18	0.88	1.83	1.23	—	—	—	0.10	0.23
Muon	Efficiency	0.52	0.53	0.54	0.55	—	—	—	0.19	0.54
	Scale	0.12	0.30	—	—	—	—	—	—	—
	Resolution	—	0.48	0.75	—	—	—	—	—	0.10
Jet	Flavor Tagging	0.26	0.42	0.49	4.25	—	—	—	0.12	0.27
	Flavor Composition	1.44	2.25	3.07	3.55	—	—	—	0.60	1.36
	Scale	1.58	2.60	5.66	11.96	—	—	—	0.80	1.45
	Resolution	0.57	0.84	1.55	6.20	—	—	—	0.35	1.06
	Pileup	0.35	0.30	1.80	1.91	—	—	—	0.19	0.24
	Vertex Fraction	0.08	0.06	—	2.27	—	—	—	0.06	0.12
MET	Scale	2.54	2.74	1.33	1.30	—	—	—	0.79	1.74
	Resolution	0.23	0.77	2.42	2.21	—	—	—	0.16	0.13
Trigger	Electron	0.09	0.10	—	—	—	—	—	—	0.06
	Muon	0.18	0.17	—	—	—	—	—	0.05	0.07
	Pileup	1.42	0.31	4.11	2.51	—	—	—	0.52	0.92

Table 5.31: Size of the experimental uncertainties in percent for the 0 SFOS signal region. The background uncertainties are shown for the individual background components as well as the total. The signal uncertainty is shown separately. Those marked — are either not applicable or below 0.02 % and thus considered to be negligible

The experimental uncertainties are those on the event and object reconstruction for MC predictions of the signal and background. Most of the systematic uncertainties evaluated in the analysis fall in this category. There are systematic uncertainties taking into account variations on the identification and reconstruction efficiency of electrons and muons; the momentum/energy resolution and scale of reconstructed electrons, muons, jets, and $E_{\mathrm{T}}^{\mathrm{miss}}$;

		Background								Signal
		WZ	ZZ	VVV	$t\bar{t}+V$	DPS	$Z\gamma$	Fake (Data)	Total BG	
Electron	Efficiency	1.59	1.96	1.51	1.52	0.69	2.10	—	1.41	1.56
	Scale	1.03	1.26	1.01	—	—	75.62	—	1.72	0.59
	Resolution	0.21	0.84	1.29	1.01	—	43.66	—	0.66	0.07
Muon	Efficiency	0.54	0.50	0.52	0.55	0.32	0.87	—	0.47	0.53
	Scale	0.21	—	—	—	—	—	—	0.17	0.10
	Resolution	0.59	0.86	0.22	0.85	—	43.44	—	0.96	0.07
Jet	Flavor Tagging	0.34	0.81	0.77	4.97	1.23	0.61	—	0.31	0.30
	Flavor Composition	1.82	3.57	2.56	6.92	—	2.56	—	1.67	1.20
	Scale	2.15	4.02	3.52	6.78	—	—	—	1.91	1.32
	Resolution	0.32	2.34	0.43	6.44	0.24	2.63	—	0.41	1.31
	Pileup	0.41	1.62	2.10	4.81	—	—	—	0.41	0.34
	Vertex Fraction	0.12	0.34	0.70	1.89	—	—	—	0.12	0.15
MET	Scale	0.33	5.90	1.57	1.65	—	44.87	—	0.98	0.71
	Resolution	0.32	0.25	1.38	2.13	—	51.75	—	0.96	0.47
Trigger	Electron	0.06	0.10	—	0.05	—	—	—	0.05	0.05
	Muon	0.08	0.13	—	—	—	0.26	—	0.07	0.07
	Pileup	0.35	4.30	1.80	2.52	28.56	38.30	—	0.20	1.30

Table 5.32: Size of the experimental uncertainties in percent for the 1 SFOS signal region. The background uncertainties are shown for the individual background components as well as the total. The signal uncertainty is shown separately. Those marked — are either not applicable or below 0.02 % and thus considered to be negligible

the trigger efficiencies evaluated in MC; the effects of pileup; and the jet specific uncertainties, like those related to b-tagging. They are summarized for the 0, 1, and 2 SFOS regions in Table 5.31, Table 5.32, and Table 5.33, respectively.

The efficiencies for reconstructing and identifying electrons and muons are modeled in MC using simulations of the detector. Differences between the observed efficiencies in data and MC are corrected by scaling the efficiency in MC, applied using event-by-event weights. Uncertainties on these "scale factors" are propagated to the event-by-event weights. The impact on the final prediction ends up being relatively small, with sub-percent level contributions coming from both the electron and muon efficiencies for both the signal and background in all channels. Differences in the electron and muon uncertainties between channels are due to differences in the lepton flavor combinatorics described in Sec. 5.3.2.

The momentum and energy measurements for electrons, muons, jets and $E_{\mathrm{T}}^{\mathrm{miss}}$ must

		Background								Signal
		WZ	ZZ	VVV	$t\bar{t}+V$	DPS	$Z\gamma$	Fake (Data)	Total BG	
Electron	Efficiency	1.01	0.64	1.28	0.81	1.65	3.00	—	0.97	0.99
	Scale	0.69	0.51	0.59	2.34	—	0.37	—	0.64	0.33
	Resolution	0.18	0.28	0.22	1.17	—	86.94	—	1.00	0.24
Muon	Efficiency	0.73	0.85	0.67	0.75	0.48	—	—	0.69	0.71
	Scale	0.25	0.26	—	—	—	—	—	0.23	0.13
	Resolution	0.58	0.61	1.03	—	—	—	—	0.51	0.41
Jet	Flavor Tagging	0.36	0.72	0.96	4.87	0.49	2.02	—	0.37	0.30
	Flavor Composition	1.44	2.35	2.44	5.91	—	122.95	—	2.66	1.26
	Scale	1.43	1.85	3.05	16.16	—	91.84	—	2.24	1.41
	Resolution	1.31	2.13	—	16.44	42.30	86.96	—	2.31	0.99
	Pileup	0.34	0.82	—	3.23	—	—	—	0.34	0.19
	Vertex Fraction	0.28	0.44	—	3.47	—	—	—	0.28	0.07
MET	Scale	1.29	8.67	1.08	4.41	55.97	86.94	—	2.46	0.20
	Resolution	—	1.79	1.74	4.70	55.97	86.94	—	1.00	0.26
Trigger	Electron	—	—	—	—	—	—	—	—	—
	Muon	0.22	0.31	0.19	0.24	0.44	—	—	0.21	0.20
	Pileup	1.12	8.04	6.69	0.19	7.67	16.49	—	1.40	1.50

Table 5.33: Size of the experimental uncertainties in percent for the 2 SFOS signal region. The background uncertainties are shown for the individual background components as well as the total. The signal uncertainty is shown separately. Those marked — are either not applicable or below 0.02 % and thus considered to be negligible

be assessed for their accuracy and precision, usually referred to as scale and resolution, respectively. The scale of the momentum and energy for each object is calibrated using the data and corrected if necessary. Uncertainties on these calibrations are propagated separately to each object. The corrections and uncertainties on the scale from the electrons, muons, and jets propagate to the $E_{\mathrm{T}}^{\mathrm{miss}}$ and a separate correction and uncertainty on additional contributions to the $E_{\mathrm{T}}^{\mathrm{miss}}$ not associate with these physics objects (so-called "soft terms") are also evaluated. The momentum and energy resolution has also been evaluated using the data for electrons, muons, jets and $E_{\mathrm{T}}^{\mathrm{miss}}$ soft-terms. Uncertainties due to the resolution are evaluated by randomly varying the momentum and energy measurements using a probability distribution whose width is determined by the resolution and centered about the calibrated value. These uncertainties on the scale and resolution propagate to the final estimate by so-called "bin migration", whereby the uncertainties on the momentum and energy measurement for a given object might move it across the threshold for some selection cut[9]. This can then change the overall event selection efficiency. The size of the uncertainties on the signal and background predictions tend to be around 1-2% for all objects and channels.

The efficiency for the events to pass the trigger is evaluated for both data and MC. The efficiencies in MC are corrected to match the data and an uncertainty is associated with this correction. They are applied depending on the trigger that was fired and the objects in the event. The variations from the uncertainties modify the event weights which ultimately has an impact on the final predictions. The uncertainty on the signal and background predictions from the trigger efficiency end up being only about 0.05-0.07% for each channel.

The MC is corrected on an event-by-event basis to match the pileup distribution observed in data. This correction depends on the MC process. Uncertainties on this correction are varied which again results in a change in the event-by-event weight for the predictions. The size of this uncertainty is around 1% for signal and background in all channels.

Jet specific uncertainties come from variations on the b-jet tagging and b-jet misidentification as well as uncertainties on the jet-vertex fraction calculations, both described in Sec. 5.2. There are also uncertainties related to the construction of jets due to pileup and the flavor composition of the jets. These result in modifications to the observed jet multiplicity leading to bin-migration effects for the b-veto and jet multiplicity cuts when going to the signal regions. The resulting uncertainties for the jet energy resolution and scale, as well as the flavor composition, range from 1-3% on the signal and background predictions. All others fall below 1%.

[9] For example, a muon with $p_{\mathrm{T}} = 22$ GeV might be modified during the systematic uncertainty valuation to have instead $p_{\mathrm{T}} = 19$ GeV. Thus, with a cut of $p_{\mathrm{T}} > 20$ GeV, the muon would pass the cut in the original case but not after variation.

5.6.4 Luminosity Uncertainty

The luminosity delivered by the LHC must be measured in order to determine how to scale the MC cross-section predictions to extract the number of events as in Eq. (3.3). This was described in Sec. 5.1.1. The resulting uncertainty on the integrated luminosity scales the overall predictions for the MC signal and background predictions. Thus, the uncertainty on the signal prediction in each channel is simply 1.9%, while the uncertainty on the background predictions is less since it is not estimate purely from MC. The luminosity uncertainty on the total background is 0.68% in the 0 SFOS region, 1.7% in the 1 SFOS region, and 1.8% in the 2 SFOS region.

5.7 Cross-section Measurement

In this analysis we seek to measure the fiducial cross-section, σ^{Observed}, for the WWW production process in the fully-leptonic channel (e,μ). The observed cross-section is parameterized by looking at the signal strength, μ, which is related to the expected fiducial cross-sections from section 5.5.4 by the relation:

$$\sigma^{\text{Observed}} = \mu \sum_{i \in \text{Channels}} \sigma_i^{\text{Fiducial}} \tag{5.46}$$

Assuming a counting experiment in each bin i, the expected event count is given by:

$$N_i^{\text{exp}}(\mu, \boldsymbol{\theta}) = N_i^{\text{exp}}(\mu, \mathcal{L}_0, \Delta_{\mathcal{L}}, \boldsymbol{\theta}_s, \boldsymbol{\theta}_b) \tag{5.47}$$

$$= \mu \cdot \left(\mathcal{L}(\mathcal{L}_0, \Delta_{\mathcal{L}}) \cdot \sigma_i^{\text{Fiducial}} \cdot C_i(\boldsymbol{\theta}_s) \right) + \sum_{\text{bkg}} N_i^{\text{bkg}}(\boldsymbol{\theta}_b) \tag{5.48}$$

where C_i is the correction factor measured in each bin as discussed in section 5.5.4 and $\sigma_i^{\text{Fiducial}}$ is the fiducial cross-section in each bin. The individual background expectations in a given bin/channel, i, are expressed simply by the number of events for a given background as N_i^{bkg}. The signal efficiencies and background expectations are assumed to follow probability distributions described by shape parameters determined from dedicated measurements of the background normalizations and systematic uncertainties. The set of correction factor shape parameters are referred to as $\boldsymbol{\theta}_s$; the set of normalization and shape parameters on the background expectations are referred to as $\boldsymbol{\theta}_b$. The integrated luminosity, $\mathcal{L}$, is assumed to have an uncertainty that follows a Gaussian distribution with nominal integrated luminosity, $\mathcal{L}_0$, and width, $\Delta_{\mathcal{L}}$. Collectively, we refer to all of these parameters, except for μ as the set of nuisance parameters, $\boldsymbol{\theta} = (\mathcal{L}_0, \Delta_{\mathcal{L}}, \boldsymbol{\theta}_s, \boldsymbol{\theta}_b)$.

The discovery significance is tested using frequentist statistics to estimate the degree of compatibility with the background-only hypothesis [135]. The measurement and uncertainty are evaluated by using the shape of the profile likelihood ratio [1] which is a function of the data and the signal strength.

5.7.1 Profile Likelihood Ratio

The likelihood used is constructed as follows:

$$L(\mu, \boldsymbol{\theta}) = \mathrm{Gaus}(\mathcal{L}; \mathcal{L}_0, \Delta_{\mathcal{L}}) \prod_{i \in \mathrm{Chan}} \mathrm{Pois}(N_i^{obs} | N_i^{exp}(\mu, \boldsymbol{\theta})) \prod_{j \in \mathrm{Sys}} \mathrm{Gaus}(\theta_j; \theta_j^0, 1) \tag{5.49}$$

using the HistFactory tool [136]. Note that the systematic uncertainties are given Gaussian constraints with $\pm 1\sigma$ uncertainties.

The basic form of the test statistic used for comparing hypotheses is called the profile likelihood ratio, $\lambda(\mu)$, and is defined as:

$$-\ln \lambda(\mu) = -\ln \frac{L(\mu, \hat{\hat{\boldsymbol{\theta}}}(\mu))}{L(\hat{\mu}, \hat{\boldsymbol{\theta}})} \tag{5.50}$$

Note that it no longer depends on the nuisance parameters, $\boldsymbol{\theta}$, and instead depends only on μ. The denominator is the unconditional maximum likelihood (ML) evaluated at the ML estimators $\hat{\mu}$ and $\hat{\boldsymbol{\theta}}$. This quantity is a unique constant when specified for a given likelihood and set of nuisance parameters. The numerator is the conditional ML which depends on μ

and evaluated at the conditional ML estimator for the set of nuisance parameters, $\hat{\hat{\boldsymbol{\theta}}}$, which itself depends on μ. The presence of the nuisance parameters are handled in the profiling step when constructing the profile likelihood ratio, which results in a smearing of the profile likelihood ratio contour. During profiling, the systematic uncertainties are interpolated using a piecewise linear function for shape uncertainties and a piecewise exponential function for the normalization uncertainties in order to maintain a normalization that is greater than zero. The negative of the logarithm of the profile likelihood ratio is used because the logarithm is monotonic and typically easier to work with. Clearly, the profile likelihood ratio runs from $0 < \lambda(\mu) < 1$ with values close to 0 showing more agreement with the background only hypothesis and values closer to 1 showing more agreement with the signal hypothesis. When taking the negative log likelihood, the range is mapped to the entire positive axis and inverted. This means that values close to 0 are more background-like and larger values are more signal-like.

The minimum of the negative log of the profile likelihood is taken as the measurement of the signal strength; the uncertainty on the measurement is taken from the shape of the negative log profile likelihood assuming the behavior in the asymptotic limit can be used. The asymptotic behavior of the profile likelihood is used to evaluate the final confidence interval.

5.7.2 Testing for Discovery Significance

The rejection of the background-only hypothesis ($\mu = 0$) is used to estimate the significance of a possible observation of the signal. For the purposes of this test, the following test statistic is used:

$$q_0 = \begin{cases} -2\ln\lambda(0), & \hat{\mu} \geq 0 \\ 0, & \hat{\mu} < 0 \end{cases} \tag{5.51}$$

The test statistic is set to 0 when $\hat{\mu} < 0$ to enforce the notion that an observation which is less than the background expectation should not be treated as signal like. The p-value in this case tells us the degree of incompatibility with the background-only hypothesis and is defined as:

$$p_0 = \int_{q_{0,\mathrm{obs}}}^{\infty} f(q_0|\mu = 0)\,\mathrm{d}q_0 \tag{5.52}$$

where $q_{0,\mathrm{obs}}$ is the observed value of q_0 and $f(q_0|\mu = 0)$ is the probability density of the test statistic q_0 under the background-only hypothesis which is evaluated using MC. By examining the p-value one can say what the probability is that the deviation away from the background-only hypothesis is due to chance. A small probability suggests that such a fluctuation is unlikely. Frequently one refers to the significance:

$$Z = \Phi^{-1}(1 - p_0) \tag{5.53}$$

where Φ^{-1} is the inverse of the Gaussian cumulative distribution function. In this way, one may refer to $Z\sigma$ significance of a measurement where usually 3σ is considered to constitute 'evidence' and 5σ constitutes discovery.

The distribution of q_0 is shown in Fig. 6.3 for the combination. The observed null p-value is found to be 0.24 for the combination which corresponds to a significance of 0.70σ. One may compare to this to an expected p-value of 0.25 corresponding to a significance of 0.66σ.

5.7.3 Measurement and Uncertainty using Profile Likelihood Interval

The measured value of the signal strength is determined by looking at the minimum of the negative log profile likelihood for each channel separately and also for the combination of all channels. The size of the uncertainty on the measurement is taken by looking at the shape of the negative log profile likelihood contour which in general should follow a parabolic shape centered about the minimum in the asymptotic limit. In this limit, Wilk's theorem [137] can be used [1] to determine that the range of the uncertainty for a given number of Gaussian σ can be related directly to the negative profile log likelihood. In particular, for a 1σ uncertainty one expects that $|-\ln\lambda(\mu)| \leq 1/2$. Note that even if

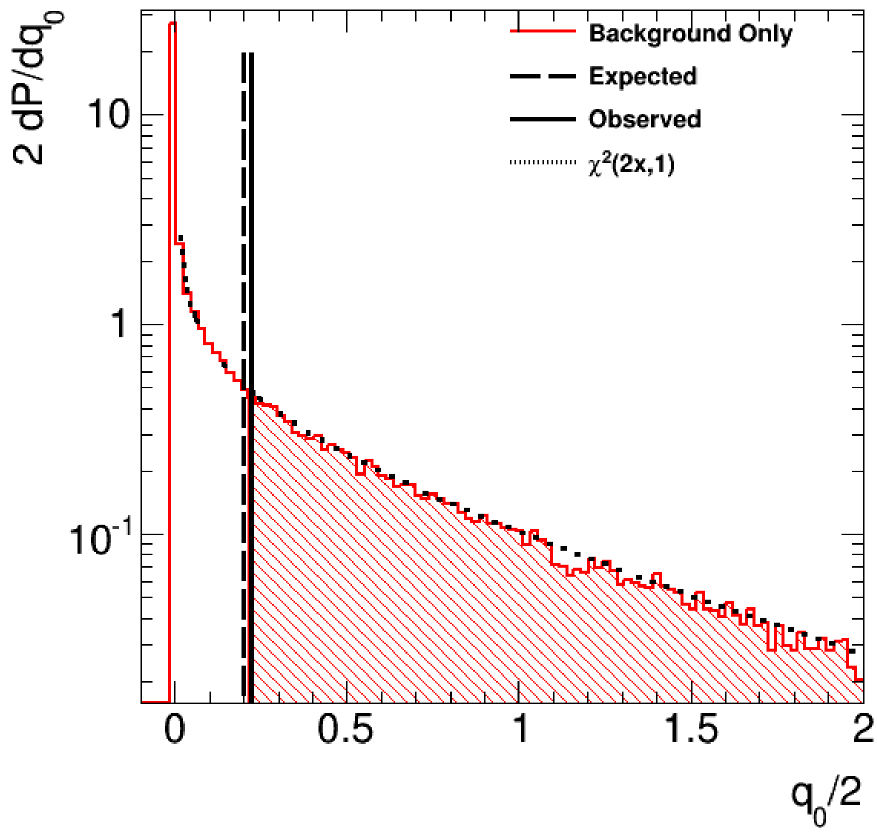

Figure 5.31: Probability distribution of the background-only hypothesis as a function of q_0 for the combination of all three channels. The probability distributions are determined using toy MC. The solid black line represents the observed value of q_0 seen in the data. The shaded area above this line represents the null p-value or the integral of the background hypothesis in the signal-like region. The dotted black curve shows a χ^2 distribution for 1 degree of freedom with which it can be seen is a good approximation of the the background-only PDF.

the contour is not distributed symmetrically about the minimum value, invariance of the likelihood under transformations like $g(\hat{\mu}, \hat{\boldsymbol{\theta}})$ where g is some function, means the same conclusion still holds. The range of the measured value of μ is left unrestricted and thus allowed to become negative.

The profile likelihood contour is evaluated once without systematic uncertainties included as nuisance parameters in order to estimate the size of the measurement uncertainty purely from statistical effects. It is then then evaluated a second time with the systematic uncertainties included as nuisance parameters whose errors are constrained to be Gaussian and then profiled out. The contour with systematic uncertainties included represents the total uncertainty. The systematic uncertainty is determined by assuming that the total uncertainty is formed from the statistical and systematic uncertainties being added in quadrature. The negative log likelihood contour is for the combination of all three channels in Fig. 6.4. The expected value and uncertainties for the fiducial cross-section is:

$$\sigma^{\text{Expected}} = 309.2^{+434}_{-338}(\text{stat})^{+316}_{-342}(\text{sys})\text{ab} \tag{5.54}$$

and the observed fiducial cross-section is:

$$\sigma^{\text{Observed:}} = 315.1^{+347}_{-334}(\text{stat})^{+326}_{-348}(\text{sys})\text{ab} \tag{5.55}$$

5.8 Anomalous Quartic Gauge Couplings

The sensitivity of this analysis to the anomalous quartic gauge coupling (aQGC) signal described in Sec. 2.3 and Sec. 5.1.2.2 has also been assessed. This aQGC signal predicts more events than the SM alone. Since the measurement of the SM signal in Sec. 5.7 was shown to be consistent with the data, this implies that no aQGC signal has been observed. However, we can set a limit on the sensitivity to this signal.

In this section we first describe the prediction of the number of aQGC signal events to fall in each signal region defined in Sec. 5.3 as a function of the parameters $f_{s,0}$ and $f_{s,1}$. That is followed by a determination of the the frequentist 95% confidence level upper limit on the aQGC signal also as a function of these parameters.

5.8.1 aQGC Signal Yields

The total cross-sections for the non-unitarized and unitarized aQGC signal samples as a function of $f_{s,0}$ vs $f_{s,1}$ were presented in Sec. 5.1.2.2. The fiducial cross-sections for

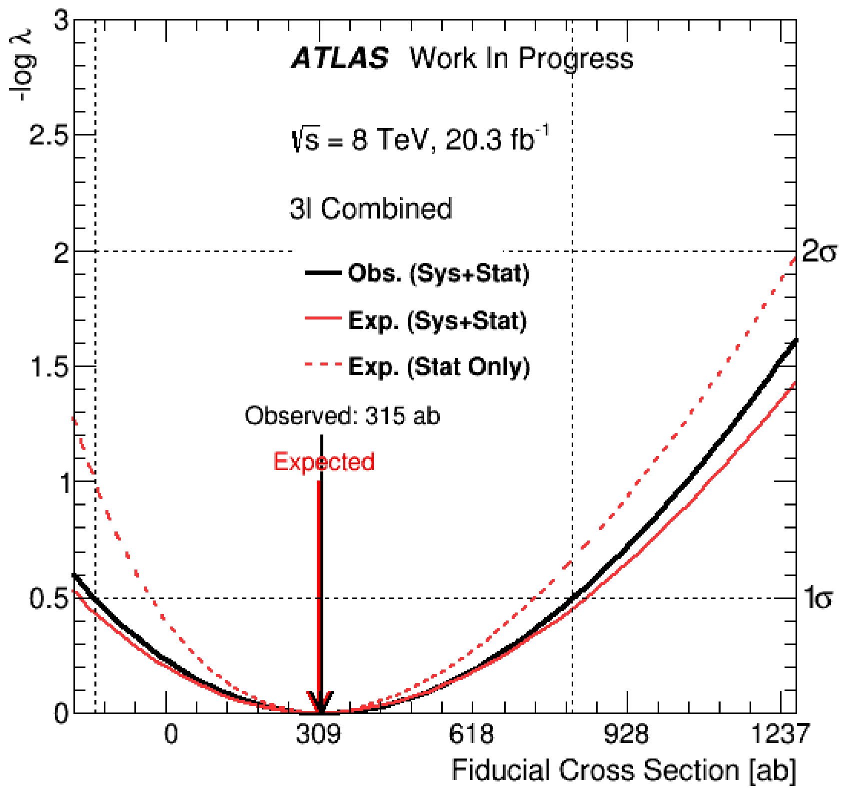

Figure 5.32: The profile likelihood contours evaluated as a function of the signal strength for the combination of all three channels. The observed (black) and expected (red) contours are shown when considering only statistical uncertainty (dashed line) and when considering both statistical and systematic uncertainties (solid line). The dotted black lines pinpoint the location of the 1 σ and 2 σ total Gaussian uncertainties on the measurement of the signal strength which corresponds to the minimum value of the contour.

these samples were determined using the same selection as in Sec. 5.3.3 and are shown in Fig. 5.33.

The reconstructed number of events were evaluated for the non-unitarized aQGC signal samples using the same selection as in Sec. 5.3.2. These values can be used in conjunction with the fiducial cross-sections to calculate a correction factor according to Eq. (5.45) as a function of $f_{s,0}$ and $f_{s,1}$. The correction factors for the non-unitarized signal samples are shown averaged over the three signal regions, along with a comparison to the SM point, in

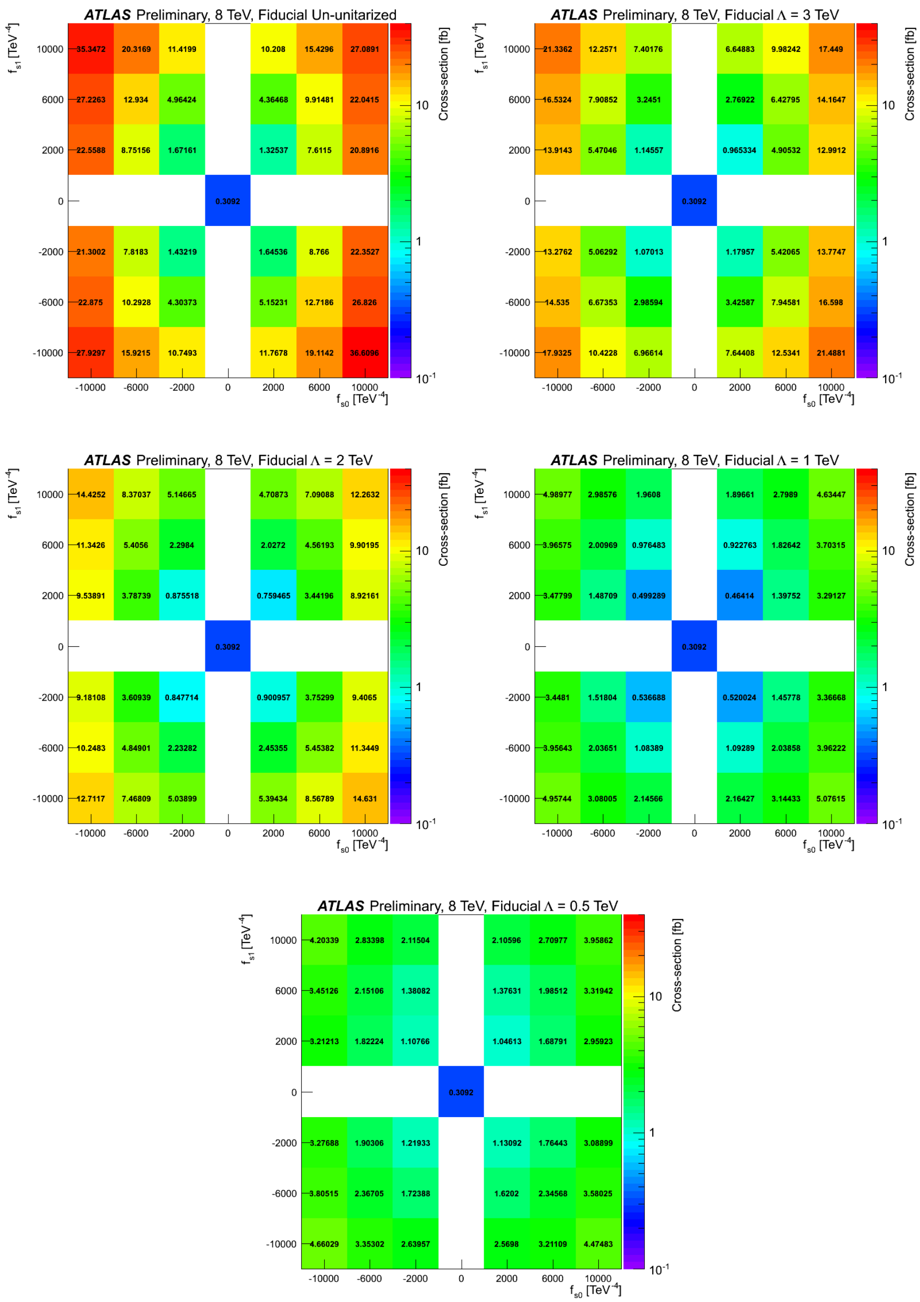

Figure 5.33: Fiducial cross-section for unitarized and non-unitarized aQGC signal samples as a function of $f_{s,0}$ vs $f_{s,1}$. The non-unitarized samples (Top Left) are shown along with the unitarization with four different unitarization scales, Λ: 3 TeV (Top Right), 2 TeV (Middle Left), 1 TeV (Middle Right), and 0.5 TeV (Bottom Center). The total SM cross-section is shown at $f_{s,0} = f_{s,1} = 0$ for comparison.

Fig. 5.34. The correction factor for the SM point is clearly smaller than that for the aQGC points by about 40%. Dedicated studies show that this is a real effect that ultimately comes from the aQGC samples having a harder p_{T} spectrum than the SM points and the following two effects:

- The effect of leptonically decaying τ leptons is not canceled in Eq. (5.45).
- The electron reconstruction efficiency is strongly p_{T} dependent.

Note that the harder p_{T} spectrum for the aQGC signal samples also increases the fiducial cross-sections, but the impact on the correction factors is more subtle. The unitarized samples should have a softer p_{T} spectrum and thus a smaller difference between the SM and aQGC correction factors. However, reconstructed MC samples were not produced for the unitarized samples. Instead, we have chosen to use the correction factor for the non-unitarized averaged over the parameter space for both the non-unitarized and unitarized samples. A systematic uncertainty is used which is the difference between this averaged non-unitarized aQGC correction factor and the SM correction factor. This should cover all possible differences in the un-unitarized and unitarized correction factors.

Once the correction factors and fiducial cross-sections have been determined, they can be used to make a prediction on the aQGC signal yield for all points. To allow for interpolation and extrapolation around the discrete aQGC points evaluated in MC, we also fit the predictions using a two-dimensional second order polynomial of the form:

$$N_{aQGC}\big(f_{s,0}, f_{s,1}\big) = w_0 + w_1 f_{s,0}^2 + w_2 f_{s,1}^2 + w_3 f_{s,0} + w_4 f_{s,1} + w_5 f_{s,0} f_{s,1} \tag{5.56}$$

where w_0 through w_5 are the six function parameters in the fit.

5.8.2 Confidence limits

The fits of the aQGC signal predictions described above plus the background predictions from Sec. 5.5.3 are input into a likelihood function in order to extract frequentist 95%

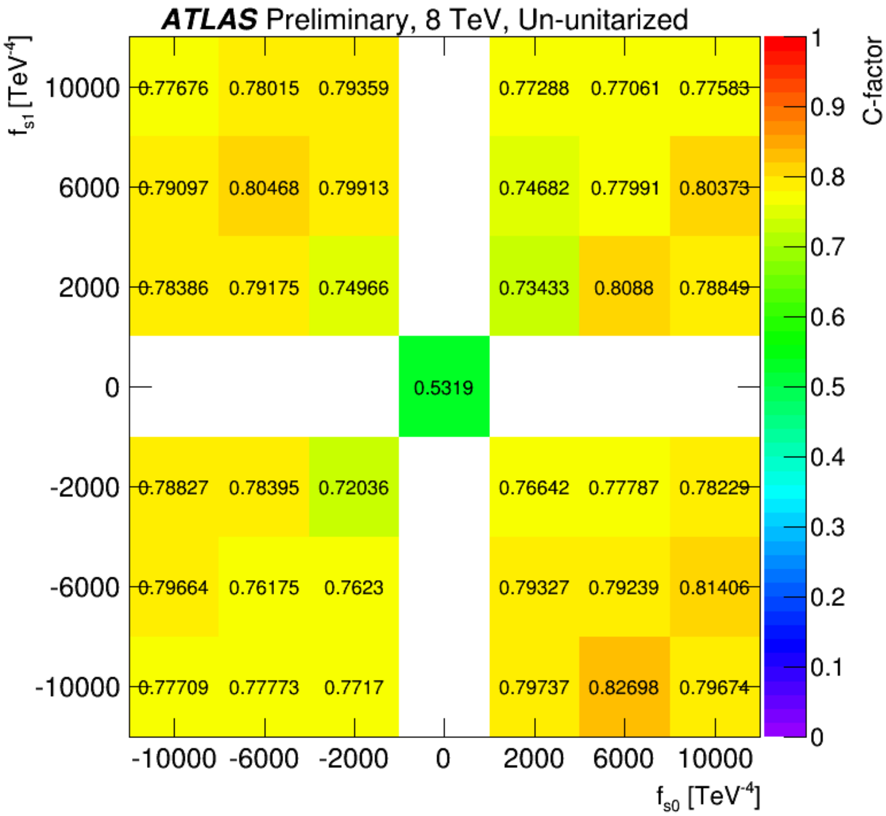

Figure 5.34: Correction factor for non-unitarized aQGC signal samples as a function of $f_{s,0}$ vs $f_{s,1}$. The SM correction factor is shown at $f_{s,0} = f_{s,1} = 0$ for comparison.

confidence level upper limits on the sensitivity to the aQGC signal as observed in the data. The likelihood function used is of a form similar to Eq. (5.49) but are determined using software developed within ATLAS [138] that is different from the one used in Sec. 5.7. The limits are evaluated either by looking at one aQGC parameter at a time, the so-called "one-dimensional" limits, or by looking at both aQGC parameters simultaneously, the "two-dimensional" limits. The one-dimensional limits are presented in Table 5.34 while the two-dimensional limits are presented in Fig. 5.35.

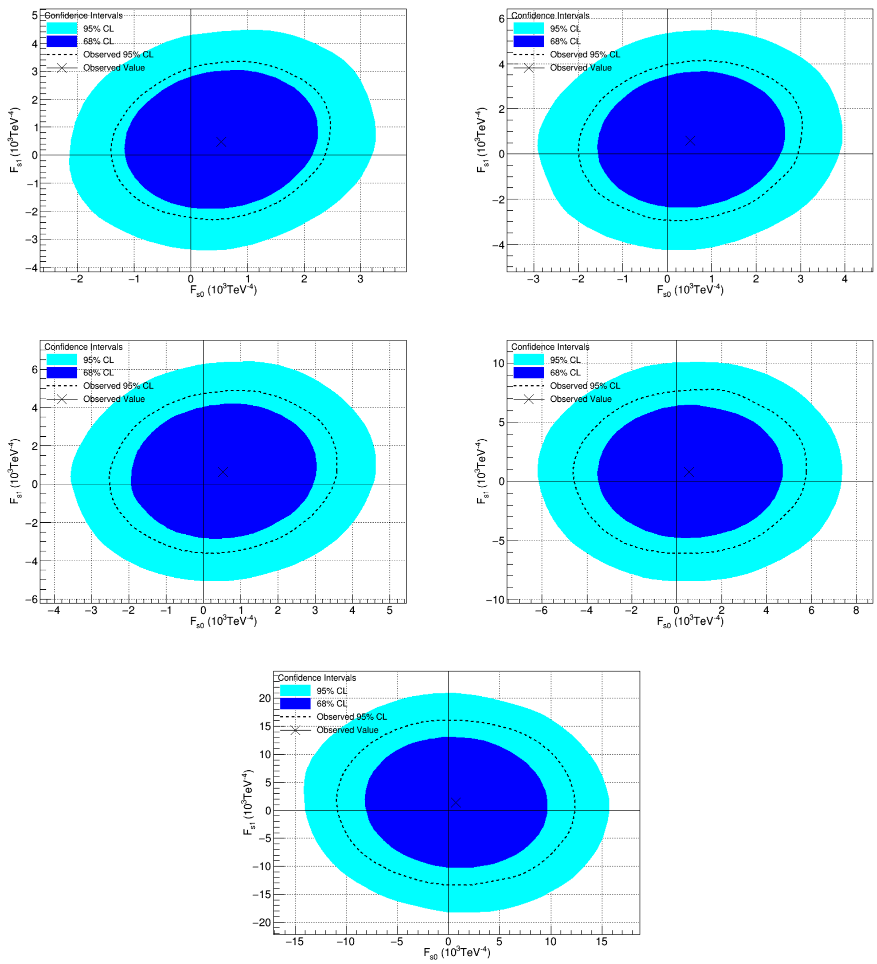

Figure 5.35: Two-dimensional limits at 95% CL for the non-unitarized case (Top Left) and three different choices of the unitarization scale, Λ: 3 TeV (Top Right), 2 TeV (Middle Left), 1 TeV (Middle Right), and 0.5 TeV (Bottom Center).

	Λ [GeV]	Limits on F_{s0} [10^3 TeV^{-4}] Lower	Upper	Measured	Limits on F_{s1} [10^3 TeV^{-4}] Lower	Upper	Measured
Expected	500	-13.61	15.38	—	-17.69	21.02	—
	1000	-6.03	7.31	—	-8.32	10.05	—
	2000	-3.46	4.48	—	-5.04	6.27	—
	3000	-2.82	3.83	—	-4.15	5.34	—
	∞	-2.18	3.14	—	-3.35	4.27	—
Observed	500	-10.75	12.30	0.7 ± 7.5	-13.16	16.07	1.34 ± 8.9
	1000	-4.57	5.63	0.5 ± 3.2	-6.09	7.66	0.7 ± 4.1
	2000	-2.50	3.49	0.5 ± 1.8	-3.56	4.69	0.5 ± 2.5
	3000	-1.98	2.95	0.5 ± 1.5	-2.89	3.96	0.5 ± 2.0
	∞	-1.39	2.38	0.5 ± 1.2	-2.29	3.15	0.4 ± 1.6

Table 5.34: Expected and observed one-dimensional limits on the $f_{s,0}$ vs $f_{s,1}$. The non-unitarized case is when $\Lambda = \infty$.

Chapter 6

Combination of $WWW \to \ell\nu\ \ell\nu\ \ell\nu$ and $WWW \to \ell\nu\ \ell\nu\ jj$

As was discussed in Sec. 2.2, there are other decay channels of the WWW process besides the fully-leptonic decay channel, which was the focus of Chapter 5. In fact, one other decay channel for this process has been studied within ATLAS. This is the semi-leptonic channel where $WWW \to \ell\nu\ \ell\nu\ jj$. The details of this analysis are beyond the scope of this thesis. We can use the results of this channel, however, along with those for the fully-leptonic decay channel, to obtain a stronger measurement on the overall SM WWW total cross-section measurement and better limits on the aQGC signal than those reported for just the fully-leptonic channel in Sec. 5.7 and Sec. 5.8.

In this chapter we will first summarize the results of the semi-leptonic study. This will be followed by a statistical combination of the fully-leptonic and semi-leptonic results leading to an improved measurement on the SM WWW total cross-section and limits on the aQGC signal. The results of this combination are to be published soon [139].

6.1 Search for $WWW \to \ell\nu\ \ell\nu\ jj$

The semi-leptonic analysis uses a selection that is designed to select events from the decay channel $WWW \to \ell\nu\ \ell\nu\ jj$. As such, it requests exactly two leptons and two jets. The selection is similar to the one used the same-sign WW vector boson fusion (VBF) production process of [75] with the main difference being that it requires $|\Delta y(jj)| < 1.5$ and 65 GeV $< m_{jj} <$ 105 GeV to separate the WWW signal from the same-sign WW VBF signal as can be seen in Fig. 6.1. The selection used is listed in Table 6.1. It splits the selection into three separate signal regions based on the final state lepton flavors: ee, $e\mu$, and $e\mu$. The final state leptons are required to have the same sign.

<table>
<tr><th></th><th>$e^{\pm}e^{\pm}$</th><th>$e^{\pm}\mu^{\pm}$</th><th>$\mu^{\pm}\mu^{\pm}$</th></tr>
<tr><td>Lepton</td><td colspan="3">Exactly two same-electric-charge leptons with $p_T > 30$ GeV</td></tr>
<tr><td>Jet</td><td colspan="3">At least two jets with $p_T >$ (20)30 GeV and $|\eta| < 2.5$</td></tr>
<tr><td>$m_{\ell\ell}$</td><td colspan="3">> 40 GeV</td></tr>
<tr><td>$E_{\mathrm{T}}^{\mathrm{miss}}$</td><td colspan="2">$> 55$ GeV</td><td>-</td></tr>
<tr><td>m_{jj}</td><td colspan="3">$65 < m_{jj} < 105$ GeV</td></tr>
<tr><td>$\Delta\eta_{jj}$</td><td colspan="3">$|\Delta\eta_{jj}| < 1.5$</td></tr>
<tr><td>Z veto</td><td>$m_{ee} < 80$ GeV or
$m_{ee} > 110$ GeV</td><td colspan="2">-</td></tr>
<tr><td>Third lepton veto</td><td colspan="3">No third lepton with $p_T > 6$ GeV and $|\eta| < 2.5$</td></tr>
<tr><td>$b-$jet veto</td><td colspan="3">No identified $b-$jets with $p_T > 25$ GeV and $|\eta| < 4.5$</td></tr>
</table>

Table 6.1: Selection criteria for the semi-leptonic channel.

Cut Name	Details
Tau Veto	Remove any events associated with Tau's
Lepton Selection	At least 2 leptons with $P_T > 15$ GeV
Jet Selection	At least 2 jets with $P_T > 15$ GeV
Same-sign Leptons	Leptons must have the same electric charge
Final Lepton Selection	Exactly Two leptons with $P_T > 30$ GeV, $|\eta| < 2.5$
$\Delta R_{\ell\ell}$	$\Delta R_{\ell\ell} > 0.1$ to remove any possible faulty lepton containers
$M_{\ell\ell}$	$M_{\ell\ell} > 40$ GeV
Z Veto	$|M_{ee} - M_Z| < 20$ GeV (only for the ee channel)
Final Jet Selection	Leading(Sub) jet $P_T > 30$ (20) GeV and $|\eta| < 2.5$
$\Delta R_{\ell j}$	min $\Delta R_{\ell j} > 0.3$
MET	MET > 55 GeV (Not applied for the $\mu\mu$ channel)
b-jet Veto	Remove any events that contain any b-tagged jets
ΔR_{jj}	$\Delta R_{jj} < 1.5$ to make sure that the two jets come from the W boson decay
W mass window cut	Two leading jets should have 65 GeV $< M_{jj} <$ 105 GeV
jet-jet rapidity	$|\Delta y(jj)| < 1.5$

Table 6.2: Description of fiducial selection for each of the semi-leptonic channels.

The signal is generated using MadGraph with the same setup as in Sec. 5.1.2.1. Thus, the total cross-section is the same as in Eq. (2.34). The fiducial cross-sections are determined in a similar fashion to that in Sec. 5.3.3 but using the fiducial selection listed in Table 6.2. The fiducial cross-section is

$$\sigma^{\text{Fiducial,Semi-lep}}_{\text{Theory}} = 306 \pm 6.73\ (\text{Stat.})\ ^{+15.3}_{-8.57}\ (\text{PDF})\ \pm 3.05\ (\text{Scale})\ \text{ab} \tag{6.1}$$

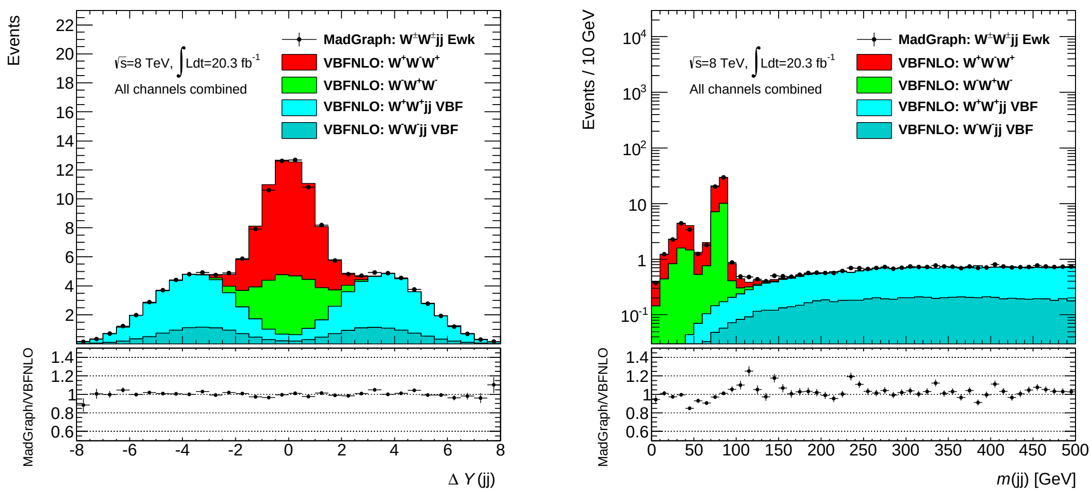

Figure 6.1: Comparison of $\Delta Y(jj)$ and M_{jj} distributions between VBFNLO and MadGraph LO events with two same-sign leptons and two jets in the final state.

The background is estimated in a similar way to Sec. 5.4. The WZ, $V\gamma$, and other same-sign (Z,WW,ZZ, $t\bar{t}+V$, etc) backgrounds are predicted using MC. The charge mis-identification background is evaluated using a data-driven method where the rates are derived in a similar way as in Sec. 5.4.2.1 but are instead applied as weights on the data. The fake lepton background is also evaluated using the data but uses a form factor method instead of the generalized matrix method of Sec. 5.4.3.1.

The resulting signal and background predictions and overall systematic uncertainties, as well as the observed data events, are shown for each semi-leptonic signal region in Table 6.3. Systematics are determined in the same way as in Sec. 5.6 except for the charge mis-identification backgrounds and fake backgrounds which evaluate different systematics due to the different estimation methods used. The systematics for the semi-leptonic channel are summarized in Table 6.4. The fiducial cross-sections and correction factors (like in

	$e^\pm e^\pm$	$e^\pm \mu^\pm$	$\mu^\pm \mu^\pm$
Fake	$0.96 \pm 0.15\ ^{+0.39}_{-0.39}$	$2.04 \pm 0.22\ ^{+0.89}_{-0.89}$	$0.43 \pm 0.06\ ^{+0.25}_{-0.25}$
WZ	$0.74 \pm 0.13\ ^{+0.44}_{-0.44}$	$2.77 \pm 0.27\ ^{+0.66}_{-0.65}$	$3.28 \pm 0.29\ ^{+0.66}_{-0.71}$
$V\gamma$	$0.75 \pm 0.35\ ^{+0.21}_{-0.18}$	$2.48 \pm 0.68\ ^{+0.73}_{-0.74}$	$0.0 \pm 0.0\ ^{+0.0}_{-0.0}$
Charge Mis-identification	$1.13 \pm 0.13\ ^{+0.24}_{-0.24}$	$0.74 \pm 0.08\ ^{+0.16}_{-0.16}$	$0.0 \pm 0.0\ ^{+0.0}_{-0.0}$
Other Same-Sign	$0.46 \pm 0.05\ ^{+0.16}_{-0.15}$	$1.33 \pm 0.1\ ^{+0.37}_{-0.38}$	$1.33 \pm 0.15\ ^{+0.38}_{-0.32}$
Signal	$0.46 \pm 0.03\ ^{+0.07}_{-0.07}$	$1.35 \pm 0.05\ ^{+0.19}_{-0.19}$	$1.65 \pm 0.06\ ^{+0.3}_{-0.3}$
Total background	$4.04 \pm 0.42\ ^{+0.69}_{-0.68}$	$9.36 \pm 0.77\ ^{+1.39}_{-1.39}$	$5.04 \pm 0.34\ ^{+0.8}_{-0.82}$
Total predicted	$4.51 \pm 0.43\ ^{+0.69}_{-0.69}$	$10.72 \pm 0.77\ ^{+1.4}_{-1.4}$	$6.69 \pm 0.34\ ^{+0.85}_{-0.87}$
Data	0	15	6

Table 6.3: A summary of the expected yields compared to data for all three signal regions in the semi-leptonic analysis channel. Statistical uncertainties are shown as a symmetric uncertainty on the central value. Systematic uncertainties are shown as an asymmetric uncertainty and are shown after taking the quadrature sum of all individual uncertainties. In the actual analysis, each systematic uncertainty is treated as an individual nuisance parameter and are NOT added in quadrature. The presentation here serves only as a demonstration of the overall size of the systematic uncertainties for each source in the individual signal regions.

Source of Uncertainty	Signal			Backgound		
	$e^\pm e^\pm$	$e^\pm \mu^\pm$	$\mu^\pm \mu^\pm$	$e^\pm e^\pm$	$e^\pm \mu^\pm$	$\mu^\pm \mu^\pm$
Electron	$^{+3.24}_{-3.47}$	$^{+0.98}_{-1.17}$	$^{+0.0}_{-0.07}$	$^{+0.9}_{-0.93}$	$^{+1.72}_{-0.94}$	$^{+0.09}_{-0.0}$
Muon	$^{+0.0}_{-0.0}$	$^{+1.25}_{-1.18}$	$^{+1.39}_{-1.42}$	$^{+0.39}_{-0.39}$	$^{+1.25}_{-1.22}$	$^{+5.26}_{-6.17}$
MET	$^{+2.44}_{-4.58}$	$^{+0.95}_{-1.67}$	$^{+0.63}_{-0.15}$	$^{+3.47}_{-2.26}$	$^{+3.39}_{-3.39}$	$^{+2.34}_{-1.22}$
Flavor Tagging	$^{+2.15}_{-2.16}$	$^{+2.16}_{-2.17}$	$^{+2.25}_{-2.26}$	$^{+1.27}_{-1.31}$	$^{+2.2}_{-2.34}$	$^{+2.68}_{-2.75}$
Jet Energy Scale	$^{+5.23}_{-5.66}$	$^{+6.58}_{-5.84}$	$^{+6.2}_{-6.08}$	$^{+8.18}_{-8.28}$	$^{+6.42}_{-6.95}$	$^{+6.13}_{-6.33}$
Jet Energy Resolution	$^{+13.13}_{-13.13}$	$^{+12.12}_{-12.12}$	$^{+16.57}_{-16.57}$	$^{+12.34}_{-12.34}$	$^{+8.72}_{-8.72}$	$^{+0.94}_{-0.94}$
Luminosity	$^{+1.9}_{-1.9}$	$^{+1.9}_{-1.9}$	$^{+1.9}_{-1.9}$	$^{+0.92}_{-0.92}$	$^{+1.34}_{-1.34}$	$^{+1.74}_{-1.74}$
Theory	$^{+4.0}_{-7.0}$	$^{+4.0}_{-7.0}$	$^{+4.0}_{-7.0}$	$^{+8.69}_{-8.69}$	$^{+12.44}_{-12.44}$	$^{+15.78}_{-15.78}$

Table 6.4: Categorized systematic uncertainties for signal and background predictions in all three signal regions of the semi-leptonic analysis channel. All uncertainties are shown as a percentage of the nominal prediction.

Channel	C_i	Fiducial Cross-section [ab]
$e^{\pm}e^{\pm}$	$0.450 \pm .036$	50.4 ± 2.5
$e^{\pm}\mu^{\pm}$	$0.531 \pm .026$	125.2 ± 3.8
$\mu^{\pm}\mu^{\pm}$	$0.626 \pm .029$	129.9 ± 3.9

Table 6.5: Correction factors, C_i, and fiducial cross-sections derived separately for each signal region in the semi-leptonic analysis channel. Correction factors and fiducial cross-sections are determined using MadGraph.

Eq. (5.45)) are presented in Table 6.5.

Semi-leptonic aQGC inputs...

More details can be found in [139] once published.

6.2 Combined Cross-section Measurement

The cross-section measurement using the combination of the semi-leptonic and fully-leptonic analysis channels is performed to measure the total cross-section of the WWW process. The same expectation, likelihood, and profile likelihood ratios are used as in Eq. (5.48), Eq. (5.49), and Eq. (5.50), respectively. The same methodology for extracting the measured fiducial cross-section from Sec. 5.7 is used for extracting the combined cross-section measurement except that the semi-leptonic channel inputs are included along with the fully-leptonic channel and that the measurement is extrapolated to the total cross-section. For the fully-leptonic channel, the fiducial cross-section and C-factor inputs are taken from Table 5.24 while the semi-leptonic channel inputs are taken from Table 6.5. The combined measurement on the signal strength, μ, is translated into a measurement on the total cross-section using the relation

$$\sigma^{\text{Total}}_{\text{Observed}} = \frac{\mu}{A} \sum_{i \in \text{Channels}} \sigma_i^{\text{Fiducial}} \tag{6.2}$$

where A is the total acceptance which is the sum of the acceptance in each channel, A_i:

$$A = \sum_i A_i \tag{6.3}$$

and where A_i is computed as

$$A_i = \frac{\sigma_i^{\text{Fiducial}}}{\sigma^{\text{Total}}} \tag{6.4}$$

The $\sigma_i^{\text{Fiducial}}$ are simply the fiducial cross-sections in each channel, i, taken from Table 5.24 and Table 6.5 and σ^{Total} is the expected total cross-section in Eq. (5.1), reprinted here for convenience:

$$\sigma_{\text{Theory}}^{\text{Total}} = 241.47 \pm 0.13 \text{ (Stat.) } {}^{+10.33}_{-6.08} \text{ (PDF) } \pm 6.3 \text{ (Scale) fb} \tag{6.5}$$

The acceptance values for both the semi-leptonic and fully-leptonic channels are summarized here in Table 6.6. The total acceptance is found to be $A = 2.547 \times 10^{-3} \pm 0.039 \times 10^{-3}$.

	Channel	A_i ($\times 10^{-3}$)
Fully-leptonic	0 SFOS	$0.512 \pm .019$
	1 SFOS	$0.567 \pm .020$
	2 SFOS	$0.202 \pm .012$
Semi-leptonic	ee	$0.209 \pm .011$
	$e\mu$	$0.519 \pm .016$
	$\mu\mu$	$0.538 \pm .016$

Table 6.6: Acceptance values, A_i, derived separately for each signal region. The sum of all of the acceptance in each bin is used to compute the overall acceptance, A. Only statistical uncertainties are shown.

The distribution of q_0 is shown in Fig. 6.3 for the combination. The observed null p-value is found to be 0.1657 (0.971 σ) with an expected of 0.152 (1.026 σ).

The negative log likelihood contour is shown for the combination of all six channels in Fig. 6.4. The expected value and uncertainties for the total cross-section is:

$$\sigma_{\text{Expected}}^{\text{Total}} = 241.47 \ {}^{+232}_{-199} \text{ (stat.) } {}^{+152}_{-153} \text{ (syst.) fb} \tag{6.6}$$

while the observed total cross-section is:

$$\sigma_{\text{Observed}}^{\text{Total}} = 227.03 \ {}^{+202}_{-198} \text{ (stat.) } {}^{+154}_{-160} \text{ (syst.) fb} \tag{6.7}$$

6.3 Combined aQGC Limits

	Λ [GeV]	Limits on f_{s0}/Λ^4 [10^3 TeV^{-4}] Lower	Upper	Measured	Limits on f_{s1}/Λ^4 [10^3 TeV^{-4}] Lower	Upper	Measured
Expected	500	-8.12	8.92	—	-10.04	12.91	—
	1000	-3.7	4.16	—	-5.21	6.19	—
	2000	-2.35	2.57	—	-3.33	4.02	—
	3000	-1.87	2.24	—	-2.94	3.58	—
	∞	-1.59	1.91	—	-2.54	3.09	—
Observed	500	-7.66	8.45	0.35	-10.08	12.22	1.11
	1000	-3.11	3.87	0.40	-4.77	5.81	0.85
	2000	-1.92	2.40	0.322	-2.90	3.69	0.49
	3000	-1.6	2.09	0.37	-2.48	3.18	0.47
	∞	-1.27	1.76	0.34	-2.10	2.71	0.40

Table 6.7: Expected and observed one-dimensional limits on $f_{s,0}$ vs $f_{s,1}$.

	Λ [GeV]	Limits on α_4 Lower	Upper	Measured	Limits on α_5 Lower	Upper	Measured
Expected	500	-3.72	4.08	—	-0.439	0.913	—
	1000	-1.69	1.90	—	-0.346	0.465	—
	2000	-1.09	1.18	—	-0.224	0.332	—
	3000	-0.856	1.025	—	-0.245	0.307	—
	∞	-0.728	0.874	—	-0.217	0.270	—
Observed	500	-3.51	3.87	0.160	-0.554	0.863	0.174
	1000	-1.42	1.77	0.183	-0.380	0.444	0.103
	2000	-0.879	1.10	0.147	-0.224	0.295	0.0385
	3000	-0.732	0.957	0.169	-0.201	0.249	0.0229
	∞	-0.581	0.806	0.156	-0.190	0.217	0.0137

Table 6.8: Expected and observed one-dimensional limits on α_4 vs α_5.

Combined limits on the aQGC signal use the same methodology as in Sec. 5.8 except that the inputs from the semi-leptonic channel, described in Sec. 6.1, are included as well. The resulting one-dimensional limits are listed in Table 6.7 while the two-dimensional limits are shown in Fig. 6.5. The combined one-dimensional limits when using the alternative α_4 and α_5 parameters from Eq. (2.40) are shown in Table 6.8.

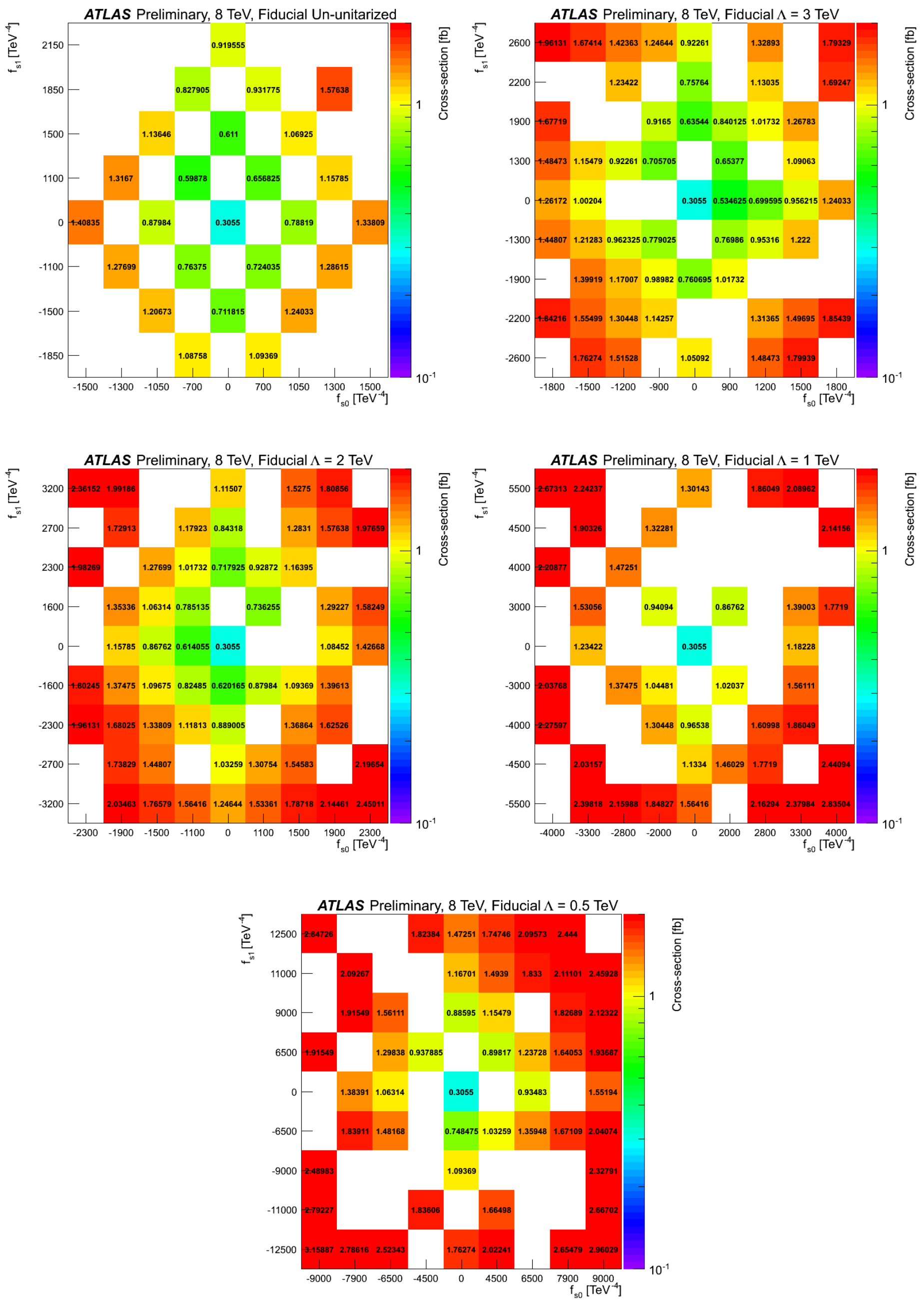

Figure 6.2: Fiducial cross-sections for unitarized and non-unitarized semi-leptonic aQGC signal samples as a function of $f_{s,0}$ vs $f_{s,1}$. The non-unitarized samples (Top Left) are shown along with the unitarization with four different unitarization scales, Λ: 3 TeV (Top Right), 2 TeV (Middle Left), 1 TeV (Middle Right), and 0.5 TeV (Bottom Center). The total SM cross-section is shown at $f_{s,0} = f_{s,1} = 0$ for comparison.

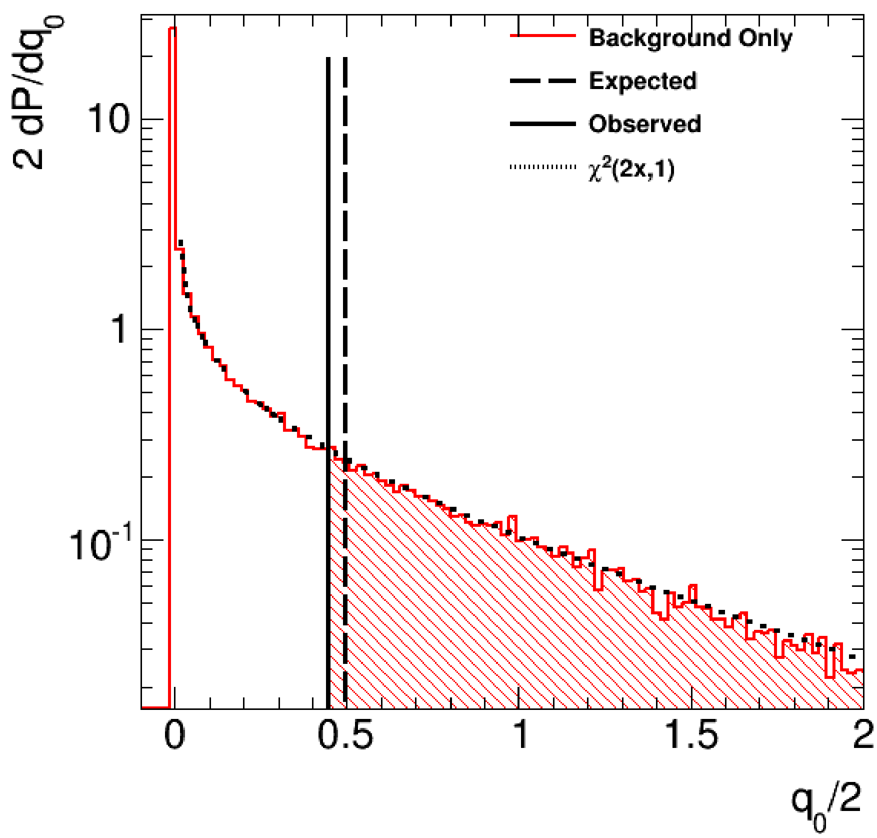

Figure 6.3: PDF of the background only hypothesis as a function of q_0 for the combination of all three channels. PDFs are determined using toy MC. The dashed black line represents the expected value of q_0 while the solid black line represents the observed value of q_0 seen in the data. The shaded area to the right of this line represents the null p-value or the integral of the background hypothesis in the signal-like region. The dotted black curve shows a χ^2 distribution for 1 degree of freedom with which it can be seen is a good approximation of the the background only PDF.

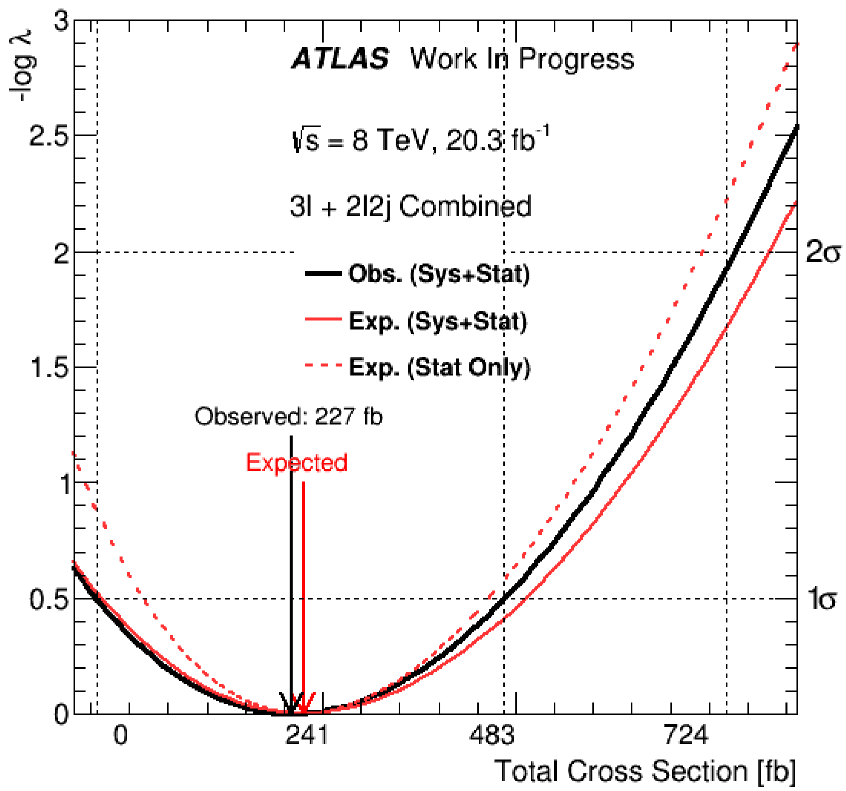

Figure 6.4: The profile likelihood contours evaluated as a function of the signal strength for the combination of all three channels. The observed (black) and expected (red) contours are shown when considering only statistical uncertainty (dashed line) and when considering both statistical and systematic uncertainties (solid line). The dotted black lines pinpoint the location of the 1 σ and 2 σ total Gaussian uncertainties on the measurement of the signal strength which corresponds to the minimum value of the contour.

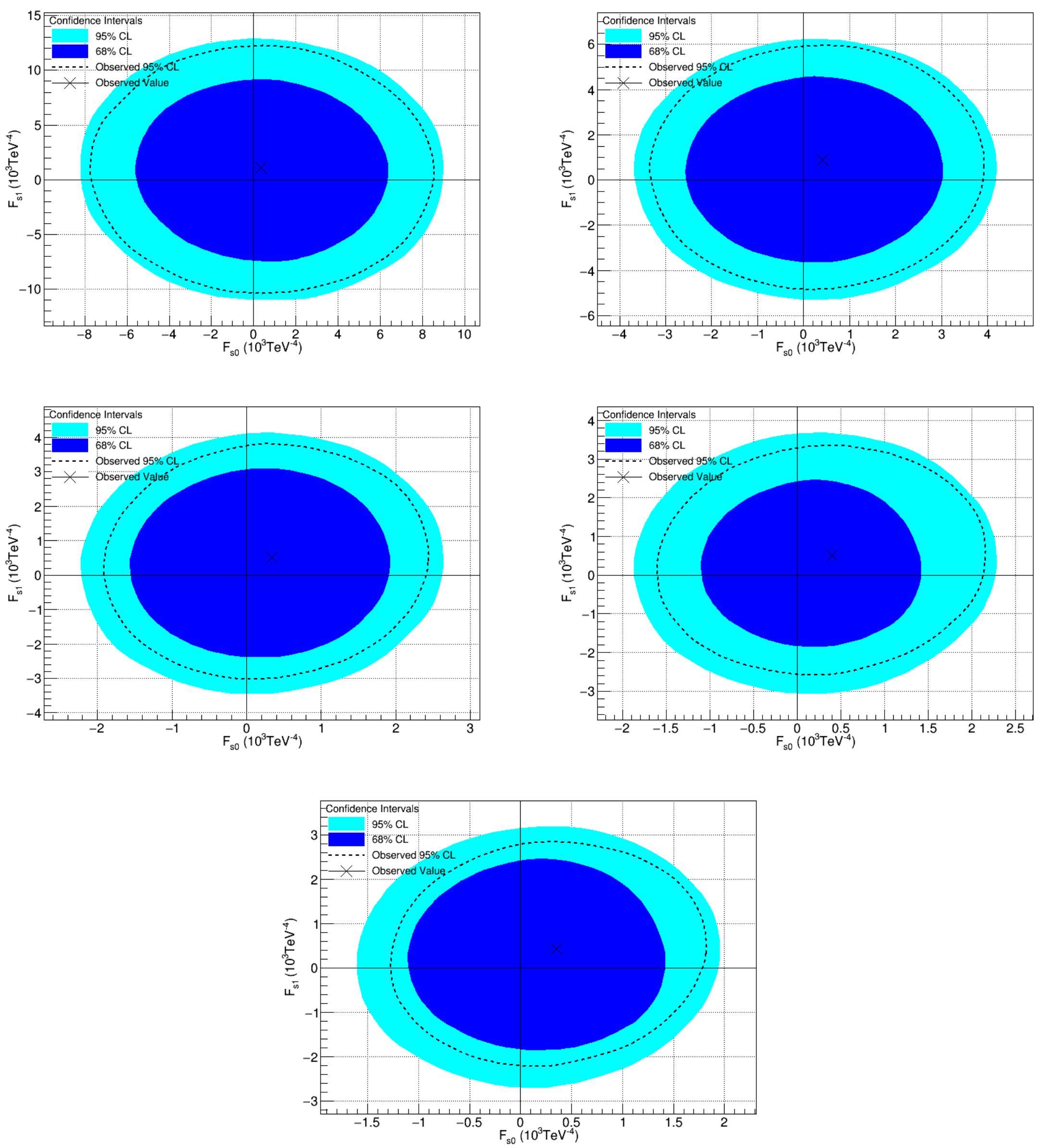

Figure 6.5: Two-dimensional limits at 95% CL on the combination for the non-unitarized case (Top Left) and three different choices of the unitarization scale, Λ: 3 TeV (Top Right), 2 TeV (Middle Left), 1 TeV (Middle Right), and 0.5 TeV (Bottom Center).

Chapter 7

Conclusions

7.1 Summary

The first study searching for the WWW production process was presented using the 2012 dataset from the LHC, with an emphasis on the details of the fully-leptonic decay channel. The search was able to achieve good signal and background discrimination given the very small initial signal to background ratio. The results were interpreted as a measurement on the SM cross-section, though the precision of the measurement is limited by statistics. A study of the semi-leptonic channel was also performed, though it is not the focus of this these. It has a similar sensitivity to the fully-leptonic channel and so slightly improves the precision on the cross-section measurement when combining the two results. The combined observed cross-section is measured to be $227.03\ ^{+202}_{-198}$ (stat.) $^{+154}_{-160}$ (syst.) fb, which is consistent with the expected SM value of 241.47 fb. Though with statistical and systematic uncertainties around 90% and 70%, respectively, it is also largely consistent with a SM signal cross-section of zero. Thus, it is still too early to claim evidence of the SM signal.

Still, we can say with confidence that there is not a strong excess of the SM signal observed in the data. This is made explicit by looking at predictions of new physics manifested as aQGCs in an EFT framework. Limits at 95% CL were set on two aQGC parameters, which were observed to be -1.27×10^3 TeV$^{-4} < f_{S,0}/\Lambda^4 < 1.76 \times 10^3$ TeV^{-4} and -2.10×10^3 TeV$^{-4} < f_{S,1}/\Lambda^4 < 2.71 \times 10^3$ TeV^{-4} for the combined channels when assessing the limits independently. These are the first limits for these parameters performed in the WWW production channel. Additional limits were presented considering the impact of unitarization using a form factor as a function of the unitarization scale. In the most extreme case, when $\Lambda = 500$ GeV, the limits worsen by a factor of 5 to 8.

7.2 Outlook

The LHC is currently operating in Run 2 with a higher center of mass energy of $\sqrt{s} =$ 13 TeV. The cross-sections for the WWW process are expected to improve by roughly a factor of two when moving from 8 TeV to 13 TeV, though this is also true for most of the backgrounds to the process. It is also planned to have significantly more data by the end of Run 2, with possibly as much as 300 fb^{-1} by the end of 2018. This could result in an increase in the amount of signal and background with respect to the 2012 analysis by a factor of around 30, which would be equivalent to more than 100 signal events and the same signal to background ratio if the same signal selection is used. As a result, it should be possible to claim evidence of the WWW process by the end of Run 2 if it does indeed exist.

List of Journal Abbreviations

AIP Conf. Proc.	....	American Institute of Physics Conference Proceedings
Ann. Math. Stat.	....	Annals of Mathematical Statistics
Ann. Phys.	....	Annals of Physics
Chin. Phys.	....	Chinese Physics
Comput. Phys. Commun.	....	Computer Physics Communications
Eur. Phys. J.	....	European Physics Journal
JHEP	....	Journal of High Energy Physics
JINST	....	Journal of Instrumentation
JPCS	....	Journal of Physics: Conference Series
New J. Phys.	....	New Journal of Physics
Nucl. Instrum. Meth.	....	Nuclear Instruments and Methods
Nucl. Phys.	....	Nuclear Physics
Phil. Mag.	....	Philosophical Magazine
Phys. Lett.	....	Physical Letters
Phys. Rev.	....	Physical Review
Phys. Rev. Lett.	....	Physical Review Letters
Prog. Theor. Phys.	....	Progress of Theoretical Physics
Z. Phys.	....	Zeitschrift für Physik

Bibliography

[1] Particle Data Group Collaboration, K. Olive et al., *Review of Particle Physics*, Chin. Phys. **C38** (2014) 090001. `http://cds.cern.ch/record/1753419`.

[2] A. D. Martin, W. J. Stirling, R. S. Thorne, and G. Watt, *Parton distributions for the LHC*, Eur. Phys. J. **C63** (2009) 189–285, `arXiv:0901.0002 [hep-ph]`. `http://cds.cern.ch/record/1153907`.

[3] The ATLAS Collaboration, *Search for new particles in events with one lepton and missing transverse momentum in pp collisions at $\sqrt{s}$ = 8 TeV with the ATLAS detector*, JHEP **09** no. arXiv:1407.7494. CERN-PH-EP-2014-139, (2014) 037. `https://cds.cern.ch/record/1746306`.

[4] D. L. Adams et al., *Search for new heavy gauge bosons in the charged lepton plus missing transverse energy final state using pp collisions at sqrts = 8 TeV in the ATLAS detector*, Tech. Rep. ATL-PHYS-INT-2014-021, CERN, Geneva, Aug, 2014. `https://cds.cern.ch/record/1748664`.

[5] M. Guzzi et al., *CT10 parton distributions and other developments in the global QCD analysis*, `arXiv:1101.0561 [hep-ph]`. `http://cds.cern.ch/record/1318967`.

[6] R. D. Ball et al., *Parton distributions with LHC data*, Nucl. Phys. **B867** (2013) 244–289, `arXiv:1207.1303 [hep-ph]`. `https://cds.cern.ch/record/1460337`.

[7] S. Alekhin, J. Blumlein, and S. Moch, *Parton Distribution Functions and Benchmark Cross Sections at NNLO*, Phys. Rev. **D86** (2012) 054009, `arXiv:1202.2281 [hep-ph]`. `https://cds.cern.ch/record/1423526`.

[8] T. H1 and Z. Collaborations, *Hera Precision Measurements and Impact for LHC Predictions*, in *Proceedings, 46th Rencontres de Moriond on QCD and High Energy Interactions*. 2011. `arXiv:1107.4193 [hep-ex]`. `https://cds.cern.ch/record/1369926`.

[9] R. Ley, *CERN Accelerators*, 2001. `http://www-ekp.physik.uni-karlsruhe.de/~rabbertz/Office/Physics_Talks/QNP06_200606/Images/CERN/AccelComplex-CERN-24072001-photo-di-0107024_01.jpg`.

[10] J. Chadwick, *Possible Existence of a Neutron*, Nature **129** (1932) 312. `https://inspirehep.net/record/28174`.

[11] E. Rutherford, *The scattering of alpha and beta particles by matter and the structure of the atom*, Phil. Mag. **21** (1911) 669–688. https://inspirehep.net/record/45404.

[12] J. Thomson, *Cathode Rays*, Phil. Mag. **90** no. 1, (2010) 25–29. http://dx.doi.org/10.1080/14786431003659214.

[13] A. H. Compton, *A Quantum Theory of the Scattering of X-rays by Light Elements*, Phys. Rev. **21** (1923) 483–502. http://link.aps.org/doi/10.1103/PhysRev.21.483.

[14] C. D. Anderson, *The Positive Electron*, Phys. Rev. **43** (1933) 491–494. http://link.aps.org/doi/10.1103/PhysRev.43.491.

[15] S. H. Neddermeyer and C. D. Anderson, *Note on the Nature of Cosmic-Ray Particles*, Phys. Rev. **51** (1937) 884–886. http://link.aps.org/doi/10.1103/PhysRev.51.884.

[16] C. M. G. Lattes, G. P. S. Occhialini, and C. F. Powell, *Observations on the Tracks of Slow Mesons in Photographic Emulsions*, Nature **160** (1947) 486–492. http://inspirehep.net/record/21950.

[17] G. D. Rochester and C. C. Butler, *Evidence for the Existence of New Unstable Elementary Particles*, Nature **160** (1947) 855–857. http://inspirehep.net/record/28179.

[18] J. J. Aubert et al., *Experimental Observation of a Heavy Particle J*, Phys. Rev. Lett. **33** (1974) 1404–1406. http://link.aps.org/doi/10.1103/PhysRevLett.33.1404.

[19] G. S. Abrams et al., *Discovery of a Second Narrow Resonance in e^+e^- Annihilation*, Phys. Rev. Lett. **33** (1974) 1453–1455. http://link.aps.org/doi/10.1103/PhysRevLett.33.1453.

[20] S. W. Herb et al., *Observation of a Dimuon Resonance at 9.5-GeV in 400-GeV Proton-Nucleus Collisions*, Phys. Rev. Lett. **39** (1977) 252–255. http://inspirehep.net/record/120368.

[21] The D0 Collaboration, *Observation of the Top Quark*, Phys. Rev. Lett. **74** (1995) 2632–2637. http://link.aps.org/doi/10.1103/PhysRevLett.74.2632.

[22] The CDF Collaboration, *Observation of Top Quark Production in $\overline{p}p$ Collisions with the Collider Detector at Fermilab*, Phys. Rev. Lett. **74** (1995) 2626–2631. http://link.aps.org/doi/10.1103/PhysRevLett.74.2626.

[23] S. L. Glashow, *Partial Symmetries of Weak Interactions*, Nucl. Phys. **22** (1961) 579–588. http://inspirehep.net/record/4328.

[24] A. Salam, *Weak and Electromagnetic Interactions*, AIP Conf. Proc. **C680519** (1968). http://inspirehep.net/record/53083.

[25] S. Weinberg, *A Model of Leptons*, Phys. Rev. Lett. **19** (1967) 1264–1266. `http://journals.aps.org/prl/abstract/10.1103/PhysRevLett.19.1264`.

[26] F. Englert and R. Brout, *Broken Symmetry and the Mass of Gauge Vector Mesons*, Phys. Rev. Lett. **13** (1964) 321–323. `http://link.aps.org/doi/10.1103/PhysRevLett.13.321`.

[27] P. W. Higgs, *Broken Symmetries and the Masses of Gauge Bosons*, Phys. Rev. Lett. **13** (1964) 508–509. `http://link.aps.org/doi/10.1103/PhysRevLett.13.508`.

[28] G. S. Guralnik, C. R. Hagen, and T. W. B. Kibble, *Global Conservation Laws and Massless Particles*, Phys. Rev. Lett. **13** (1964) 585–587. `http://link.aps.org/doi/10.1103/PhysRevLett.13.585`.

[29] The UA1 Collaboration, *Experimental observation of isolated large transverse energy electrons with associated missing energy at* $\sqrt{s} = 540$ GeV, Phys. Lett. **B122** (1983) 103 – 116. `http://inspirehep.net/record/188736`.

[30] The UA1 Collaboration, *Experimental observation of lepton pairs of invariant mass around* $95GeV/c^2$ *at the CERN SPS collider*, Phy. Lett. **B126** no. 5, (1983) 398 – 410. `http://inspirehep.net/record/190338?`

[31] The ATLAS Collaboration, *Observation of a new particle in the search for the Standard Model Higgs boson with the ATLAS detector at the LHC* , Phys. Lett. **B716** (2012) 1 – 29. `http://cds.cern.ch/record/1471031`.

[32] The CMS Collaboration, *Observation of a new boson at a mass of 125 GeV with the CMS experiment at the LHC*, Phys. Lett. **B716** (2012) 30–61, `arXiv:1207.7235 [hep-ex]`. `http://cds.cern.ch/record/1471016`.

[33] The ATLAS Collaboration, *Measurement of total and differential* W^+W^- *production cross sections in proton-proton collisions at* $\sqrt{s} = 8$ *TeV with the ATLAS detector and limits on anomalous triple-gauge-boson couplings*, `arXiv:1603.01702 [hep-ex]`. `http://inspirehep.net/record/1426515`.

[34] The CMS Collaboration, *Measurement of* W^+W^- *and* ZZ *production cross sections in pp collisions at* $\sqrt{s} = 8$ TeV, Phys. Lett. **B721** (2013) 190–211, `arXiv:1301.4698 [hep-ex]`. `https://inspirehep.net/record/1215317`.

[35] E. Commins and P. Bucksbaum, *Weak Interactions of Leptons and Quarks.* Cambridge University Press, 1983. `https://books.google.com/books?id=A15OvAvA7HAC`.

[36] F. Halzen and A. Martin, *Quarks and Leptons: An Introductory Course In Modern Particle Physics.* Wiley, 1984. `https://books.google.com/books?id=zwDvAAAAMAAJ`.

[37] R. Cahn and G. Goldhaber, *The Experimental Foundations of Particle Physics.* Cambridge books online. Cambridge University Press, 2009. `https://books.google.com/books?id=F2fwI-K2O7kC`.

[38] D. J. Gross and F. Wilczek, *Ultraviolet Behavior of Nonabelian Gauge Theories*, Phys. Rev. Lett. **30** (1973) 1343–1346. http://inspirehep.net/record/81238.

[39] H. D. Politzer, *Reliable Perturbative Results for Strong Interactions?*, Phys. Rev. Lett. **30** (1973) 1346–1349. http://inspirehep.net/record/81351.

[40] The LHCb Collaboration, *Observation of $J/\psi p$ Resonances Consistent with Pentaquark States in $\Lambda_b^0 \to J/\psi K^- p$ Decays*, Phys. Rev. Lett. **115** (2015) 072001, arXiv:1507.03414 [hep-ex]. https://inspirehep.net/record/1382595.

[41] S. Alekhin et al., *The PDF4LHC Working Group Interim Report*, arXiv:1101.0536 [hep-ph]. https://inspirehep.net/record/883198.

[42] R. D. Ball et al., *Parton distributions for the LHC Run II*, JHEP **04** (2015) 040, arXiv:1410.8849 [hep-ph]. http://cds.cern.ch/record/1966481.

[43] G. 't Hooft, *Renormalization of massless Yang-Mills fields*, Nucl. Phys. **B33** (1971) 173–199. http://inspirehep.net/record/68080.

[44] G. 't Hooft, *Renormalizable Lagrangians for massive Yang-Mills fields*, Nucl. Phys. **B35** (1971) 167 – 188. http://inspirehep.net/record/67962.

[45] C. S. Wu, E. Ambler, R. W. Hayward, D. D. Hoppes, and R. P. Hudson, *Experimental Test of Parity Conservation in Beta Decay*, Phys. Rev. **105** (1957) 1413–1415. http://link.aps.org/doi/10.1103/PhysRev.105.1413.

[46] R. L. Garwin, L. M. Lederman, and M. Weinrich, *Observations of the Failure of Conservation of Parity and Charge Conjugation in Meson Decays: The Magnetic Moment of the Free Muon*, Phys. Rev. **105** (1957) 1415–1417. http://journals.aps.org/pr/abstract/10.1103/PhysRev.105.1415.

[47] J. I. Friedman and V. L. Telegdi, *Nuclear Emulsion Evidence for Parity Nonconservation in the Decay Chain $\pi^+ \to \mu^+ \to e^+$*, Phys. Rev. **106** (1957) 1290–1293. http://link.aps.org/doi/10.1103/PhysRev.106.1290.

[48] J. H. Christenson, J. W. Cronin, V. L. Fitch, and R. Turlay, *Evidence for the 2π Decay of the K_2^0 Meson*, Phys. Rev. Lett. **13** (1964) 138–140. http://link.aps.org/doi/10.1103/PhysRevLett.13.138.

[49] N. Cabibbo, *Unitary Symmetry and Leptonic Decays*, Phys. Rev. Lett. **10** (1963) 531–533. http://link.aps.org/doi/10.1103/PhysRevLett.10.531.

[50] M. Kobayashi and T. Maskawa, *CP Violation in the Renormalizable Theory of Weak Interaction*, Prog. Theor. Phys. **49** (1973) 652–657. http://inspirehep.net/record/81350.

[51] The ATLAS and CMS Collaborations, *Combined Measurement of the Higgs Boson Mass in pp Collisions at $\sqrt{s} = 7$ and 8 TeV with the ATLAS and CMS Experiments*, Phys. Rev. Lett. **114** (2015) 191803, arXiv:1503.07589 [hep-ex]. http://journals.aps.org/prl/abstract/10.1103/PhysRevLett.114.191803.

[52] The ATLAS Collaboration, *Evidence for the spin-0 nature of the Higgs boson using ATLAS data*, Phys. Lett. **B726** (2013) 120 – 144.
`http://cds.cern.ch/record/1559925`.

[53] The CMS Collaboration, *Constraints on the spin-parity and anomalous HVV couplings of the Higgs boson in proton collisions at 7 and 8 TeV*, Phys. Rev. **D92** (2015) 012004, `arXiv:1411.3441 [hep-ex]`.
`http://cds.cern.ch/record/1969386`.

[54] The ATLAS Collaboration, *Determination of the off-shell Higgs boson signal strength in the high-mass ZZ and WW final states with the ATLAS detector*, Eur. Phys. J. **C75** (2015) 335, `arXiv:1503.01060 [hep-ex]`.
`http://cds.cern.ch/record/1995608`.

[55] The CMS Collaboration, *Constraints on the Higgs boson width from off-shell production and decay to Z-boson pairs*, Phys. Lett. **B736** (2014) 64–85, `arXiv:1405.3455 [hep-ex]`. `http://cds.cern.ch/record/1701344`.

[56] The ATLAS and CMS Collaborations, *Measurements of the Higgs boson production and decay rates and constraints on its couplings from a combined ATLAS and CMS analysis of the LHC pp collision data at $\sqrt{s} = 7$ and 8 TeV*, Tech. Rep. ATLAS-CONF-2015-044, CERN, Geneva, Sep, 2015.
`http://cds.cern.ch/record/2052552`.

[57] L. G. Almeida, S. J. Lee, S. Pokorski, and J. D. Wells, *Study of the standard model Higgs boson partial widths and branching fractions*, Phys. Rev. **D89** no. 3, (2014) 033006, `arXiv:1311.6721 [hep-ph]`. `https://inspirehep.net/record/1266287`.

[58] C. Degrande et al., *Effective Field Theory: A Modern Approach to Anomalous Couplings*, Ann. Phys. **335** (2013) 21–32, `arXiv:1205.4231 [hep-ph]`.
`https://inspirehep.net/record/1115311`.

[59] K. Hagiwara, S. Ishihara, R. Szalapski, and D. Zeppenfeld, *Low-energy effects of new interactions in the electroweak boson sector*, Phys. Rev. **D48** (1993) 2182–2203.
`http://journals.aps.org/prd/abstract/10.1103/PhysRevD.48.2182`.

[60] W. Buchmuller and D. Wyler, *Effective Lagrangian Analysis of New Interactions and Flavor Conservation*, Nucl.Phys. **B268** (1986) 621–653.
`http://cds.cern.ch/record/163116`.

[61] O. Eboli, M. Gonzalez-Garcia, and J. Mizukoshi, *$pp \rightarrow jje^{\pm}\mu^{\pm}\nu\nu$ and $jje^{\pm}\mu^{\pm}\nu\nu$ at $O(\alpha(em)^6)$ and $O(\alpha(em)^4\alpha(s)^2)$ for the study of the quartic electroweak gauge boson vertex at CERN LHC*, Phys. Rev. **D74** (2006) 073005, `arXiv:hep-ph/0606118 [hep-ph]`. `http://inspirehep.net/record/718973`.

[62] O. J. P. Eboli, M. C. Gonzalez-Garcia, and S. M. Lietti, *Bosonic quartic couplings at CERN LHC*, Phys. Rev. **D69** (2004) 095005, `arXiv:hep-ph/0310141 [hep-ph]`.
`http://inspirehep.net/record/630415`.

[63] M. Baak et al., *Working Group Report: Precision Study of Electroweak Interactions*, in *Community Summer Study 2013: Snowmass on the Mississippi (CSS2013) Minneapolis, MN, USA, July 29-August 6, 2013*. 2013. `arXiv:1310.6708 [hep-ph]`. `http://inspirehep.net/record/1261993`.

[64] W. Kilian, T. Ohl, J. Reuter, and M. Sekulla, *High-Energy Vector Boson Scattering after the Higgs Discovery*, Phys. Rev. **D91** (2015) 096007, `arXiv:1408.6207 [hep-ph]`. `https://inspirehep.net/record/1312375`.

[65] ATLAS Collaboration, *Evidence of $W\gamma\gamma$ Production in pp Collisions at* $\sqrt{s} = 8$ TeV *and Limits on Anomalous Quartic Gauge Couplings with the ATLAS Detector*, Phys. Rev. Lett. **115** (2015) 031802. `http://link.aps.org/doi/10.1103/PhysRevLett.115.031802`.

[66] The DELPHI Collaboration, *Measurement of the $e^+e^- \to W^+W^-\gamma$ cross-section and limits on anomalous quartic gauge couplings with DELPHI*, Eur. Phys. J. **C31** (2003) 139–147, `arXiv:hep-ex/0311004 [hep-ex]`. `http://cds.cern.ch/record/680543`.

[67] The OPAL Collaboration, *Constraints on anomalous quartic gauge boson couplings from $\nu\bar{\nu}\gamma\gamma$ and $q\bar{q}\gamma\gamma$ events at CERN LEP2*, Phys. Rev. **D70** (2004) 032005. `http://link.aps.org/doi/10.1103/PhysRevD.70.032005`.

[68] The D0 Collaboration, *Search for anomalous quartic $WW\gamma\gamma$ couplings in dielectron and missing energy final states in $p\bar{p}$ collisions at $\sqrt{s}$=1.96* TeV, Phys. Rev. **D88** (2013) 012005. `http://link.aps.org/doi/10.1103/PhysRevD.88.012005`.

[69] The CMS Collaboration, *Search for $WW\gamma$ and $WZ\gamma$ production and constraints on anomalous quartic gauge couplings in pp collisions at $\sqrt{s} = 8$* TeV, Phys. Rev. **D90** (2014) 032008. `http://link.aps.org/doi/10.1103/PhysRevD.90.032008`.

[70] The CMS Collaboration, *Study of exclusive two-photon production of W^+W^- in pp collisions at $\sqrt{s} = 7$ TeV and constraints on anomalous quartic gauge couplings*, JHEP **07** (2013) 116, `arXiv:1305.5596 [hep-ex]`. `http://cds.cern.ch/record/1550912`.

[71] The L3 Collaboration, *Study of the $W^+W^-\gamma$ process and limits on anomalous quartic gauge boson couplings at LEP*, Phys. Lett. **B527** (2002) 29–38, `arXiv:hep-ex/0111029 [hep-ex]`. `http://cds.cern.ch/record/525935`.

[72] The OPAL Collaboration, *Measurement of the $W^+W^-\gamma$ cross-section and first direct limits on anomalous electroweak quartic gauge couplings*, Phys. Lett. **B471** (1999) 293–307, `arXiv:hep-ex/9910069 [hep-ex]`. `http://cds.cern.ch/record/405987`.

[73] The OPAL Collaboration, *A Study of $W^+W^-\gamma$ events at LEP*, Phys. Lett. **B580** (2004) 17–36, `arXiv:hep-ex/0309013 [hep-ex]`. `http://cds.cern.ch/record/640531`.

[74] The L3 Collaboration, *The $e^+e^- \to Z\gamma\gamma \to q\bar{q}\gamma\gamma$ reaction at LEP and constraints on anomalous quartic gauge boson couplings*, Phys. Lett. **B540** (2002) 43–51, arXiv:hep-ex/0206050 [hep-ex]. http://cds.cern.ch/record/561994.

[75] The ATLAS Collaboration, *Evidence for Electroweak Production of $W^\pm W^\pm jj$ in pp Collisions at $\sqrt{s} = 8$ TeV with the ATLAS Detector*, Phys. Rev. Lett. **113** (2014) 141803. http://link.aps.org/doi/10.1103/PhysRevLett.113.141803.

[76] The CMS Collaboration, *Study of Vector Boson Scattering and Search for New Physics in Events with Two Same-Sign Leptons and Two Jets*, Phys. Rev. Lett. **114** (2015) 051801. http://link.aps.org/doi/10.1103/PhysRevLett.114.051801.

[77] The CMS Collaboration, *Study of vector boson scattering and search for new physics in events with two same-sign leptons and two jets*, Phys. Rev. Lett. **114** (2014) 051801. http://cds.cern.ch/record/1957133.

[78] The ATLAS Collaboration, *Measurements of $W^\pm Z$ production cross sections in pp collisions at $\sqrt{s} = 8$ TeV with the ATLAS detector and limits on anomalous gauge boson self-couplings*, arXiv:1603.02151 [hep-ex]. https://cds.cern.ch/record/2137188.

[79] L. Evans and P. Bryant, *LHC Machine*, JINST **3** (2008) S08001. http://cds.cern.ch/record/1129806.

[80] The ATLAS Collaboration, *Measurement of the total cross section from elastic scattering in pp collisions at $\sqrt{s} = 7$ TeV with the ATLAS detector*, Nucl. Phys. **B889** (2014) 486–548, arXiv:1408.5778 [hep-ex]. http://cds.cern.ch/record/1751527.

[81] The ATLAS Collaboration, *The ATLAS Experiment at the CERN Large Hadron Collider*, JINST **3** (2008) S08003. http://cds.cern.ch/record/1129811.

[82] The CMS Collaboration, *The CMS experiment at the CERN LHC*, JINST **3** (2008) S08004. http://cds.cern.ch/record/1129810.

[83] The ALICE Collaboration, *The ALICE experiment at the CERN LHC*, JINST **3** (2008) S08002. http://cds.cern.ch/record/1129812.

[84] The LHCb Collaboration, *The LHCb Detector at the LHC*, JINST **3** (2008) S08005. http://cds.cern.ch/record/1129809.

[85] M. Lamont, *Status of the LHC*, JPCS **455** (2013) 012001. https://cds.cern.ch/record/1709796.

[86] M. Hostettler and G. Papotti, *Luminosity Lifetime at the LHC in 2012 Proton Physics Operation*, in *Proceedings, 4th International Particle Accelerator Conference (IPAC 2013)*. 2013. http://JACoW.org/IPAC2013/papers/tupfi029.pdf.

[87] The ATLAS Collaboration, *Alignment of the ATLAS Inner Detector and its Performance in 2012*, Tech. Rep. ATLAS-CONF-2014-047, CERN, Geneva, Jul, 2014. `https://cds.cern.ch/record/1741021`.

[88] J. Alwall, P. Demin, S. de Visscher, R. Frederix, M. Herquet, F. Maltoni, T. Plehn, D. L. Rainwater, and T. Stelzer, *MadGraph/MadEvent v4: The New Web Generation*, JHEP **09** (2007) 028, `arXiv:0706.2334 [hep-ph]`. `http://cds.cern.ch/record/1041955`.

[89] The ATLAS Collaboration, *Improved luminosity determination in pp collisions at sqrt(s) = 7 TeV using the ATLAS detector at the LHC*, Eur. Phys. J. **C73** (2013) 2518, `arXiv:1302.4393 [hep-ex]`. `http://cds.cern.ch/record/1517411`.

[90] S. Agostinelli et al., *GEANT4: A Simulation toolkit*, Nucl. Instrum. Meth. **A506** (2003) 250–303. `http://cds.cern.ch/record/602040`.

[91] K. Arnold et al., *VBFNLO: A Parton Level Monte Carlo for Processes with Electroweak Bosons – Manual for Version 2.5.0*, `arXiv:1107.4038 [hep-ph]`. `http://cds.cern.ch/record/1369438`.

[92] K. Arnold et al., *Release Note – Vbfnlo-2.6.0*, `arXiv:1207.4975 [hep-ph]`. `http://cds.cern.ch/record/1463432`.

[93] T. Sjostrand, S. Mrenna, and P. Z. Skands, *A brief introduction to* PYTHIA *8.1*, Comput. Phys. Commun. **178** (2008) 852, `arXiv:0710.3820 [hep-ph]`. `http://cds.cern.ch/record/1064095`.

[94] P. Golonka and Z. Was, *PHOTOS Monte Carlo: A Precision tool for QED corrections in Z and W decays*, Eur. Phys. J. **C45** (2006) 97–107, `arXiv:hep-ph/0506026 [hep-ph]`. `http://cds.cern.ch/record/839598`.

[95] *ATLAS tunes of PYTHIA 6 and Pythia 8 for MC11*, Tech. Rep. ATL-PHYS-PUB-2011-009, CERN, Geneva, Jul, 2011. `http://cds.cern.ch/record/1363300`.

[96] J. Pumplin et al., *New generation of parton distributions with uncertainties from global QCD analysis*, JHEP **0207** (2002) 012, `arXiv:hep-ph/0201195 [hep-ph]`. `http://cds.cern.ch/record/534624`.

[97] H. Lai et al., *New parton distributions for collider physics*, Phys. Rev. **D82** (2010) 074024, `arXiv:1007.2241 [hep-ph]`. `http://journals.aps.org/prd/abstract/10.1103/PhysRevD.82.074024`.

[98] S. Alioli, P. Nason, C. Oleari, and E. Re, *NLO vector-boson production matched with shower in POWHEG*, JHEP **0807** (2008) 060, `arXiv:0805.4802 [hep-ph]`. `http://cds.cern.ch/record/1107190`.

[99] P. Nason, *A new method for combining NLO QCD with shower Monte Carlo algorithms*, JHEP **11** (2004) 040, `arXiv:hep-ph/0409146`. `http://inspirehep.net/record/659055`.

[100] S. Frixione, P. Nason, and C. Oleari, *Matching NLO QCD computations with parton shower simulations: the* POWHEG *method*, JHEP **0711** (2007) 070, `arXiv:0709.2092 [hep-ph]`. `http://cds.cern.ch/record/1056860`.

[101] S. Alioli et al., *A general framework for implementing NLO calculations in shower Monte Carlo programs: the* POWHEG *BOX*, JHEP **1006** (2010) 043, `arXiv:1002.2581 [hep-ph]`. `http://cds.cern.ch/record/1240986`.

[102] T. Sjostrand, S. Mrenna, and P. Skands, PYTHIA *6.4 physics and manual*, JHEP **05** (2006) 026, `arXiv:hep-ph/0603175`. `http://inspirehep.net/record/712925`.

[103] T. Gleisberg et al., *Event generation with SHERPA 1.1*, JHEP **0902** (2009) 007, `arXiv:0811.4622 [hep-ph]`. `http://cds.cern.ch/record/1142881`.

[104] M. Mangano et al., ALPGEN*, a generator for hard multiparton processes in hadronic collisions*, JHEP **07** (2003) 001, `arXiv:hep-ph/0206293`. `http://cds.cern.ch/record/565290`.

[105] J. M. Butterworth, J. R. Forshaw, and M. H. Seymour, *Multiparton interactions in photoproduction at HERA*, Z. Phys. **C72** (1996) 637, `arXiv:hep-ph/9601371`. `http://cds.cern.ch/record/295247`.

[106] T. Binoth, N. Kauer, and P. Mertsch, *Gluon-induced QCD corrections to* $pp \rightarrow ZZ \rightarrow l\bar{l}l'\bar{l}'$, in *Proceedings, 16th International Workshop on Deep Inelastic Scattering and Related Subjects (DIS 2008)*. 2008. `arXiv:0807.0024 [hep-ph]`. `http://inspirehep.net/record/789541/files/arXiv:0807.0024.pdf`.

[107] T. Binoth, M. Ciccolini, N. Kauer, and M. Kramer, *Gluon-induced W-boson pair production at the LHC*, JHEP **0612** (2006) 046, `arXiv:hep-ph/0611170 [hep-ph]`. `http://inspirehep.net/record/731635`.

[108] S. Frixione and B. R. Webber, *Matching NLO QCD computations and parton shower simulations*, JHEP **06** (2002) 029, `arXiv:hep-ph/0204244`. `http://cds.cern.ch/record/548281`.

[109] S. Hassani, L. Chevalier, E. Lancon, J. F. Laporte, R. Nicolaidou, and A. Ouraou, *A muon identification and combined reconstruction procedure for the ATLAS detector at the LHC using the (MUONBOY, STACO, MuTag) reconstruction packages*, Nucl. Instrum. Meth. **A572** (2007) 77–79. `https://inspirehep.net/record/754679`.

[110] The ATLAS Collaboration, *Measurement of the muon reconstruction performance of the ATLAS detector using 2011 and 2012 LHC protonproton collision data*, Eur. Phys. J. **C74** no. 11, (2014) 3130, `arXiv:1407.3935 [hep-ex]`. `https://cds.cern.ch/record/1743068`.

[111] The ATLAS Collaboration, *Electron and photon energy calibration with the ATLAS detector using LHC Run 1 data*, Eur. Phys. J. **C74** no. arXiv:1407.5063. CERN-PH-EP-2014-153, (2014) 51. `https://cds.cern.ch/record/1744017`.

[112] W. Lampl et al., *Calorimeter Clustering Algorithms: Description and Performance*, Tech. Rep. ATL-LARG-PUB-2008-002. ATL-COM-LARG-2008-003, CERN, Geneva, Apr, 2008. `http://cds.cern.ch/record/1099735`.

[113] M. Cacciari, G. P. Salam, and G. Soyez, *The Anti-k(t) jet clustering algorithm*, JHEP **04** (2008) 063, `arXiv:0802.1189 [hep-ph]`. `http://cds.cern.ch/record/1088021`.

[114] The ATLAS Collaboration, *Topological cell clustering in the ATLAS calorimeters and its performance in LHC Run 1*, `arXiv:1603.02934 [hep-ex]`. `https://cds.cern.ch/record/2138166`.

[115] D. W. Miller, A. Schwartzman, and D. Su, *Pile-up jet energy scale corrections using the jet-vertex fraction method*, Tech. Rep. ATL-PHYS-INT-2009-090, CERN, Geneva, Sep, 2009. `http://cds.cern.ch/record/1206864`.

[116] The ATLAS Collaboration, *Pile-up subtraction and suppression for jets in ATLAS*, Tech. Rep. ATLAS-CONF-2013-083, CERN, Geneva, Aug, 2013. `http://cds.cern.ch/record/1570994`.

[117] The ATLAS Collaboration, *Calibration of b-tagging using dileptonic top pair events in a combinatorial likelihood approach with the ATLAS experiment*, Tech. Rep. ATLAS-CONF-2014-004, CERN, Geneva, Feb, 2014. `http://cds.cern.ch/record/1664335`.

[118] A. Buckley et al., *Rivet user manual*, Comput. Phys. Commun. **184** (2013) 2803–2819, `arXiv:1003.0694 [hep-ph]`. `http://cds.cern.ch/record/1246848`.

[119] The ATLAS Collaboration, *Measurement of WZ production in proton-proton collisions at $\sqrt{s} = 7$ TeV with the ATLAS detector*, Eur. Phys. J. **C72** (2012) 2173, `arXiv:1208.1390 [hep-ex]`. `http://cds.cern.ch/record/1472179`.

[120] The ATLAS Collaboration, *A Measurement of WZ Production in Proton-Proton Collisions at $\sqrt{s} = 8$ TeV with the ATLAS Detector*, Tech. Rep. ATL-COM-PHYS-2014-144, CERN, Geneva, Feb, 2014. `http://cds.cern.ch/record/1663539`.

[121] The CMS Collaboration, *Measurement of WZ production rate*, Tech. Rep. CMS-PAS-SMP-12-006, CERN, Geneva, 2013. `http://cds.cern.ch/record/1564318`.

[122] M. Grazzini, S. Kallweit, and D. Rathlev, *$W\gamma$ and $Z\gamma$ production at the LHC in NNLO QCD*, JHEP **07** (2015) 085, `arXiv:1504.01330 [hep-ph]`. `http://inspirehep.net/record/1357993`.

[123] F. Cascioli et al., *ZZ production at hadron colliders in NNLO QCD*, Phys. Lett. **B735** (2014) 311–313, `arXiv:1405.2219 [hep-ph]`. `http://inspirehep.net/record/1295500`.

[124] The ATLAS Collaboration, *Measurements of $W\gamma$ and $Z\gamma$ production in pp collisions at $\sqrt{s} = 7\,TeV$ with the ATLAS detector at the LHC*, Phys. Rev. **D87** (2013) 112003, `arXiv:1302.1283 [hep-ex]`. `http://cds.cern.ch/record/1513670`.

[125] J. Baglio, L. D. Ninh, and M. M. Weber, *Massive gauge boson pair production at the LHC: a next-to-leading order story*, Phys.Rev. **D88** (2013) 113005, `arXiv:1307.4331`. `http://inspirehep.net/record/1242871`.

[126] A. Bierweiler, T. Kasprzik, and J. H. Khn, *Vector-boson pair production at the LHC to $\mathcal{O}(\alpha^3)$ accuracy*, JHEP **1312** (2013) 071, `arXiv:1305.5402 [hep-ph]`. `http://inspirehep.net/record/1235289`.

[127] The ATLAS Collaboration, *Measurements of Four-Lepton Production at the Z Resonance in pp Collisions at $\sqrt{s}$ =7 and 8 TeV with ATLAS*, Phys. Rev. Lett. **112** (2014) 231806, `arXiv:1403.5657 [hep-ex]`. `http://cds.cern.ch/record/1670332`.

[128] The ATLAS Collaboration, *Measurement of the $Z\gamma$ and $Z\gamma\gamma$ Production Cross Section in pp Collisions at $\sqrt{s}$ = 8 TeV with the ATLAS Detector at the LHC*, Tech. Rep. ATL-COM-PHYS-2013-1573, CERN, Geneva, Nov, 2013. `http://cds.cern.ch/record/1631102`.

[129] J. R. Gaunt, C.-H. Kom, A. Kulesza, and W. J. Stirling, *Same-sign W pair production as a probe of double parton scattering at the LHC*, Eur. Phys. J. **C69** (2010) 53–65, `arXiv:1003.3953 [hep-ph]`. `http://cds.cern.ch/record/1254601`.

[130] The ATLAS Collaboration, *Measurement of hard double-parton interactions in $W(\rightarrow l\nu)$+ 2 jet events at $\sqrt{s}$=7 TeV with the ATLAS detector*, New J. Phys. **15** (2013) 033038, `arXiv:1301.6872 [hep-ex]`. `http://cds.cern.ch/record/1510534`.

[131] The ATLAS Collaboration, *Measurement of the $t\bar{t}W$ and $t\bar{t}Z$ production cross sections in pp collisions at $\sqrt{s} = 8$ TeV with the ATLAS detector.*, Tech. Rep. ATLAS-CONF-2015-032, CERN, Geneva, Jul, 2015. `http://cds.cern.ch/record/2038143`.

[132] T. P. S. Gillam and C. G. Lester, *Improving estimates of the number of 'fake' leptons and other mis-reconstructed objects in hadron collider events: BoB's your UNCLE*, JHEP **11** (2014) 031, `arXiv:1407.5624 [hep-ph]`. `http://inspirehep.net/record/1307251`.

[133] The ATLAS Collaboration, *Search for strongly-produced superpartners in final states with two same-sign leptons or three leptons at $\sqrt{s} = 8$ TeV*, Tech. Rep. ATL-COM-PHYS-2013-887, CERN, Geneva, Jun, 2013. `http://cds.cern.ch/record/1558979`.

[134] The ATLAS Collaboration, *Background studies for top-pair production in lepton plus jets final states in $\sqrt{s} = 7$ TeV ATLAS data*, Tech. Rep. ATLAS-CONF-2010-087, CERN, Geneva, Oct, 2010. `http://cds.cern.ch/record/1298967`.

[135] G. Cowan, K. Cranmer, E. Gross, and O. Vitells, *Asymptotic formulae for likelihood-based tests of new physics*, Eur. Phys. J. **C71** (2010) 1554. `http://cds.cern.ch/record/1277304`.

[136] K. Cranmer, G. Lewis, L. Moneta, A. Shibata, and W. Verkerke, *HistFactory: A tool for creating statistical models for use with RooFit and RooStats*, Tech. Rep. CERN-OPEN-2012-016, New York U., New York, Jan, 2012. `http://cds.cern.ch/record/1456844`.

[137] S. S. Wilks, *The Large-Sample Distribution of the Likelihood Ratio for Testing Composite Hypotheses*, Ann. Math. Stat. **9** (1938) 60–62. `http://inspirehep.net/record/1247197`.

[138] M. Morii, M. Kagan, and S. Cole, *TGClim – Setting Frequentist Limits on Anomalous TGCs*, October, 2014. `https://svnweb.cern.ch/cern/wsvn/atlasphys/Physics/StandardModel/ElectroWeak/Common/Software/TGC/TGClim/trunk/docs/TGClimManual.pdf`.

[139] The ATLAS Collaboration, *Search for triboson $W^{\pm}W^{\pm}W^{\mp}$ production in pp collisions at $\sqrt{s} = 8$ TeV with the ATLAS detector*,. To be published in Phys. Lett. B.

Curriculum Vitae

Brian Alexander Long

Year of Birth: 1988

Contact:

Department of Physics, Boston University

Metcalf Science Center

590 Commonwealth Ave

Boston, MA 02215

Education

Boston University, Boston, Massachusetts

Ph.D. Candidate in Physics, Sep 2010 – Present

Boston University, Boston, Massachusetts

M.A. in Physics, Sep 2015

The University of North Carolina, Chapel Hill, North Carolina

B.S. in Physics and Astronomy, Sep 2006 – May 2010

Research Experience

The ATLAS Experiment, CERN, Meyrin, Switzerland

Graduate Research Fellow, High Energy Physics, Boston University, Sep 2010 – Present

Advisor: Prof. John Butler

- Conducting first search of WWW production using the fully leptonic decay channel using data collected at the LHC in 2012.

- Performed search for exotic heavy charged gauge bosons in the leptonic decay channel using data collected from the LHC in 2012. Significantly improves limits from previous searches within ATLAS.

- Studied the performance of the ATLAS muon trigger system during using data collected at the LHC in 2012. Demonstrated the robustness of the muon trigger system against pileup.

- Performed timing studies of new fast muon trigger algorithm to be used in LHC Run 2.

- Participated in upgrades and improvements to the ATLAS muon spectrometer system in preparation for LHC Run 2. Resulted in finally bringing the ATLAS muon system to the full Technical Design Report specifications. Also helped in first complete test of the Muon Drift Tube (MDT) gas system.

- Lead efforts to test custom ASD chips to be used in the MDT technology for future upgrades to the ATLAS muon system.

Triangle Universities Nuclear Laboratory (TUNL), Duke University

Undergraduate Research Assistant, Apr 2008 – May 2010

Advisor: Prof. Reyco Henning

- Built a muon veto system for a low background dark matter detector installed in the Kimballton Underground Research Facility.

- Performed Monte Carlo simulation of cosmogenically activated germanium in High-Purity Germanium detectors.

- Developed software for use in low-background gamma spectroscopy analysis.

Center for Beam Physics, LBNL, Berkeley, California

Undergraduate Research Assistant, Jun 2009 – Aug 2009

Advisor: Dr. Ji Qiang

- Developed software for the optimization of beam parameters in the design of the photo-injector for the Next Generation Light Source (NGLS) project at LBNL.

Publications

The ATLAS Collaboration, *Search for $W^{\pm}W^{\pm}W^{\mp}$ Production in pp collisions at $\sqrt{s} = 8$ TeV with the ATLAS detector*, to be submitted to Phys. Lett. B

The ATLAS Collaboration, *Search for new particles in events with one lepton and missing transverse momentum in pp collisions at $\sqrt{s} = 8$ TeV with the ATLAS detector*, JHEP **09** (2014) 037. https://cds.cern.ch/record/1746306.

The ATLAS Collaboration, *Performance of the ATLAS muon trigger in pp collisions at $\sqrt{s} = 8$ TeV*, Eur. Phys. J. **C75** (2015) 120. https://cds.cern.ch/record/1749694.

The ATLAS Collaboration, *Search for WZ resonance in the fully leptonic channel using pp collisions at $\sqrt{s} = 8$ TeV with the ATLAS detector*, Phys. Lett. **B737** 2014 223-243. https://cds.cern.ch/record/1709746.

Finnerty, P., Henning, R., Long, A., et al., *Low-background gamma counting at the Kimballton Underground Research Facility*, Nucl. Inst. Meth. **A642** (2011) 65-69. http://arxiv.org/abs/1007.0015.

Long, A., Qiang, J., *Parallel Optimization of Beam Energy for a Next Generation Lightsource Photoinjector*, Abstract, DOE Journal of Undergraduate Research 2009

Conference Experience & Citations

2016 Lake Louise Winter Institute, Lake Louise, AB, Canada

2015 Open Data Science Conference, Boston, MA

2015 American Physical Society April Meeting , Baltimore, MD

2014 Fermilab-CERN Hadron Collider Physics Symposium, Batavia, IL

2009 American Physical Society April Meeting, Denver, Colorado

2008 APS Division of Nuclear Physics Conference, Oakland, California

Honors & Awards

Outstanding Teaching Fellow 2010 – 2011

Boston University College of Arts and Sciences outstanding teaching fellow of the year in Physics.

DOE SULI Program Funding Award 2009

Full funding award for work with Center for Beam Physics at Lawrence-Berkeley National Lab.

APS CEU Full Travel Award 2008

2008 October Division of Nuclear Physics APS Meeting

Teaching Experience

Teaching Fellow, Department of Physics, Boston University Sep 2010 – May 2011

Teaching assistant for undergraduate physics courses. Topics covered: Mechanics, Electromagnetism, Thermodynamics, Modern physics.